

DTU



Technical
University of
Denmark

Numerical Solutions of Boussinesq Equations for Fully Nonlinear and Extremely Dispersive Water Waves

David R. Fuhrman
PhD thesis
May 2004

Department of
Mechanical
Engineering

MEK

Maritime
Engineering

NUMERICAL SOLUTIONS OF BOUSSINESQ EQUATIONS FOR FULLY NONLINEAR AND EXTREMELY DISPERSIVE WATER WAVES

David R. Fuhrman

TECHNICAL UNIVERSITY OF DENMARK
DEPARTMENT OF MECHANICAL ENGINEERING
MARITIME ENGINEERING
NOVEMBER 2004

Published in Denmark by
Technical University of Denmark

Copyright © D. R. Fuhrman 2004
All rights reserved

Maritime Engineering
Department of Mechanical Engineering
Technical University of Denmark
Studentertorvet, Building 101E, DK-2800 Kgs. Lyngby, Denmark
Phone +45 4525 1360, Telefax +45 4588 4325
E-mail: info.mt@mek.dtu.dk
WWW: <http://www.mek.dtu.dk/>

Publication Reference Data

Fuhrman, D. R.

NUMERICAL SOLUTIONS OF BOUSSINESQ EQUATIONS FOR FULLY NONLINEAR AND EXTREMELY DISPERSIVE WATER WAVES

PhD Thesis

Technical University of Denmark, Maritime Engineering.

November, 2004

ISBN 87-89502-41-8

Keywords: BOUSSINESQ EQUATIONS, BRAGG SCATTERING, COASTAL ENGINEERING, COMPUTATIONAL FLUID DYNAMICS, CRESCENT WAVES, DIFFRACTION, FINITE DIFFERENCE APPROXIMATIONS, ITERATIVE METHODS, NONLINEAR WAVES, OFFSHORE ENGINEERING, PRECONDITIONING, PSEUDOSPECTRA, SHORT-CRESTED WAVES, SPARSE MATRICES, STABILITY ANALYSIS, WAVE-STRUCTURE INTERACTIONS

To Hülya

Preface

This thesis is submitted as partial fulfillment for the degree of Doctor of Philosophy at the Technical University of Denmark (DTU), Lyngby, Denmark.

This work has been performed over the time period June 1, 2001–May 31, 2004. From June 1, 2001–December, 2002 work was carried out in the Informatics and Mathematical Modelling (IMM) Department, and from January, 2002–May 31, 2004 in the Mechanical Engineering (MEK) Department. The period August 5, 2002–December 20, 2002 was also spent as a visiting student at the Oxford University Computing Laboratory, Oxford, England. The study has been supervised by Dr. Harry B. Bingham (MEK), Prof. Per A. Madsen (MEK), and Prof. Per G. Thomsen (IMM).

In writing this thesis, I have attempted to make each chapter stand largely on its own. Indeed, many have arisen from papers which have been published or submitted elsewhere. I hope this modular structure will make the different parts of the thesis individually accessible. I have done my best to concentrate on what I feel are the most important achievements. This of course means that some details are inevitably left out, but I sincerely hope that I have reached a reasonable compromise between readability, complexity, and length. Some details, which are probably not necessary for the general understanding, but are nonetheless important and likely to be of interest to some, I have included as appendices.

Over the course of these three years I have had a chance to look into a large number of areas, and to meet a large number of people. While I specifically acknowledge certain individuals in the following section, I would here like to thank *all* those who have taken some time to discuss various problems with me along the way.

DAVID R. FUHRMAN

Lyngby, Denmark
May 28, 2004

The thesis was successfully defended August 9, 2004. In this official edition of the thesis minor improvements have been made to the text and Appendix F has been added.

DAVID R. FUHRMAN

Lyngby, Denmark
November 24, 2004

Acknowledgements

Below is an incomplete, but well-deserved list of people who have helped make this work possible.

I would firstly like to thank my primary supervisors Harry B. Bingham and Per A. Madsen for their daily guidance throughout this project. I have sincerely enjoyed the experience of working closely with you both. This thesis is in many ways a team effort.

I also thank my third supervisor Per Grove Thomsen for always lending a helping hand whenever asked. Your knowledge has been an immense help, particularly in the more numerical chapters.

I thank Iain Duff, Rutherford Appleton Laboratory, for sharing his knowledge and expertise on the solution of sparse matrices, as well as for recommending (and supplying!) the HSL MA41 direct factorization routine, which has been used extensively.

I also gratefully acknowledge the Oxford University Computing Laboratory, whom I had the pleasure of visiting for roughly five months, from August 5, 2002 – December 20, 2002. During this time some key breakthroughs were realized. In particular, I would like to thank Daniel Loghin for originally encouraging me to consider the Schur complement approach to preconditioning. I also thank Nick Trefethen for helpful discussions concerning the numerical stability analysis, in particular on the analysis of pseudospectra.

I would also like to thank various people for supplying data for comparison from their physical experiments. In particular I thank Diane Henderson (Penn State University) for supplying data from their experiments involving deep water rectangular (short-crested) wave patterns, and Bernard Molin and the entire group from the Hydrodynamics Department, Ecole Supérieure d'Ingénieurs de Marseille, France, for providing data from their plate run-up experiments.

I thank Benlong Wang, Shanghai Jiao Tong University, for his hard work and cooperation in the extension of the model to allow rapidly varying bathymetries.

I thank the Danish Center for Scientific Computing for supplying invaluable super-computing time on the NIFLHEIM cluster. Without this support it would have been difficult, if not impossible, to achieve the quality and quantity of the numerical simulations presented here.

To all the members of the IMM and MEK departments at DTU, thank you for your help and support at various times throughout this project. In particular I would like to thank my office mates at various times Henrik Bredmøse, Allan Engsig-Karup, Jesper Grooss, Jan Høgsberg, Boyan Lazarov, and Kristian Bendix Nielsen for creating a fun and productive working atmosphere. Thanks also to Kristian for setting up the NS3 model for an efficiency comparison.

Finally, to my friends and family, and especially to Hülya and my parents, thank you for your love, support, and encouragement. This would not have been possible without you.

This work was supported financially by the Danish Technical Research Council (STVF grant no. 9801635). Their support is greatly appreciated.

D. R. F.

Executive Summary

Numerical Solutions of Boussinesq Equations for Fully Nonlinear and Extremely Dispersive Water Waves

The objective of this work is to develop effective numerical techniques for solving a recently derived high-order Boussinesq formulation for the study of highly nonlinear and extremely dispersive water waves in two horizontal dimensions. For this purpose a numerical model is developed which combines finite difference spatial discretizations with high-order explicit Runge-Kutta time integration methods.

The dominant computational expense within the numerical model involves the solution of a (time variant) sparse, ill-conditioned matrix at each stage evaluation. The structure of the matrix is such that direct solution methods are computationally unattractive, and as a result Krylov subspace iterative solution methods are employed. The convergence of these basic methods is found to be prohibitively slow, however, and a number of novel preconditioning strategies are developed to significantly accelerate their convergence. Specifically, a matrix-free method in Fourier space (for solving flat-bottom problems) and a (generally applicable) approximate Schur complement approach are developed, which are shown to provide mesh-independent convergence, even in rather physically demanding circumstances. The end result is a robust numerical scheme which provides solutions that effectively scale linearly with the problem size.

A method of lines type numerical stability analysis of the discrete system is also undertaken, which combines standard Fourier analysis techniques with matrix-based methods in two horizontal dimensions. Necessary conditions for numerical stability of the linearized model are established for a number of different finite difference discretizations in combination with a variety of time stepping schemes, for both rotational and irrotational formulations. The matrix based approach is further extended to consider the local effects of the nonlinear terms, and it is shown that the irrotational formulation has significantly better stability properties when high nonlinearity is combined with large water depths or refined grids. The analysis is confirmed through a series of numerical experiments with both the linear and nonlinear models.

The numerical model is systematically validated, and then used to study a wide variety of nonlinear wave phenomena of both fundamental and practical interest. Firstly, (hexagonal) shallow and (rectangular) deep water short-crested wave patterns are investigated, which arise from the nonlinear interaction of wavefronts at oblique incident angles. In shallow water it is confirmed that the interaction is strong/weak when the incident angle is small/large.

Based on the model results for the deep water rectangular patterns, a new explanation for a number of features observed in recent physical experiments is provided. This involves the release of parasitic free first harmonics due to third-order discrepancies in the wavemaker conditions.

Secondly, a quantitative numerical study of crescent waves, arising from the instability of steep plane Stokes waves to three dimensional perturbations, is undertaken. The most-unstable phase-locked (so-called L2) patterns are firstly considered, and investigations into the unstable growth rate as well as the effects of nonlinearity are provided. The model results suggest that accelerated (compared with linearized theory) growth rates are possible during later stages of crescent formation. Secondly, the related oscillating crescent forms are studied, and the model results are in excellent agreement with recent physical experiments. Pre-existing analysis methods are extended to give accurate predictions of the oscillation period, while also providing a possible explanation of the selection mechanism in the experiments. The simulations also demonstrate previously observed L3 and L4 crescent patterns, which occur momentarily during model transitional states. Finally, the numerical model is used to investigate the initial competition of various instabilities to the breaking point. Simulations involving random perturbations match physical observations both in the form (*i.e.* two- or three-dimensional) and location of the initial instability.

Thirdly, the basic model is extended to incorporate domains having piecewise-rectangular, bottom-mounted structures. Analysis demonstrates that theoretically singular exterior corner points pose potential stability, as well as convergence problems. In practice these difficulties are overcome via repeated (local) applications of high-order smoothing filters. Simulations involving classical linear breakwater diffraction over a wide range of water depths demonstrate acceptable model accuracy. A case involving nonlinear gap diffraction is also simulated, and the results are shown to compare well with those from physical experiments. The model is finally used to simulate highly nonlinear wave run-up on a vertical plate. An excellent match with recent experimental measurements is obtained, even in cases where the wave steepness (waveheight divided by wavelength) exceeds 0.2.

Finally, an extension of the original formulation to allow for rapidly varying bathymetries is provided, and the resultant linearized model is validated through simulations involving shoaling and reflection from a plane shelf. Class I and II Bragg scattering, caused by the interaction of linear surface waves with undular sea bottoms, are also considered and the results compare well with both experiments and previous simulations. The nonlinear model is then used to study class III Bragg scattering, due to quartet interactions between nonlinear surface waves and an undular sea bottom. New computational results are presented which demonstrate a clear downshift/upshift for the reflected/transmitted class III resonance. These can be attributed to third-order interactions among the resultant wavefields.

This thesis establishes the present high-order Boussinesq-type approach as an effective means for the general study of highly nonlinear and extremely dispersive water waves, particularly in two horizontal dimensions. The computational results herein, combined with analysis, provide a deeper understanding of the many complicated physical processes involved in the various nonlinear wave phenomena considered.

Synopsis

Numeriske Løsninger af Boussinesq Ligninger for Fuldt Ikke-lineær og Extremt Dispersive Vandbølger

Formålet med dette arbejde er at udvikle en effektiv numerisk metode til løsning af en højere ordens Boussinesq formulering for ulineære vandbølger i to horizontale dimensioner, samt at studere diverse ikke-lineære bølgefænomener på lavt og dybt vand.

Den numeriske metode baseres på rumlige finite difference diskretiseringer kombineret med højere ordens eksplicit Runge-Kutta tidsintegrationer. For hvert tidsskridt skal der løses et matrix problem, som involverer en (tidsvarierende) *sparse, ill-conditioned* matrix. I en horizontal dimension kan direkte metoder overvejes men i to horizontale dimensioner er iterative metoder klart at foretrække. For at accelerere konvergen af den valgte iterative Krylov subspace metode, udvikles og aftestes et antal nye præ-konditionerings strategier. Der identificeres to attraktive metoder: En matrix-fri metode i Fourier domænet (til problemer med vandret bund) og en mere generelt anvendelig såkaldt *approximate Schur complement* metode. Den resulterende numeriske metode er robust og den skalerer lineært med antallet af beregningspunkter.

En numerisk stabilitetsanalyse, baseret på method of lines, udvikles for det diskrete system, og denne metode kombinerer standard Fourier analyse med matrix-baserede metoder i to horizontale dimensioner. Først etableres de nødvendige betingelser for lineær stabilitet for kombinationen af en række forskellige finite difference diskretiseringer og en række forskellige tids-integrations skemaer. Dernæst, udvides den matrix baserede analyse metode til at inkludere lokale ikke-lineære led i formuleringen. Det viser sig at en rotationsfri formulering af ligningerne er mere stabil end den generelle formulering, specielt hvis ikke-lineære effekter optræder på store vanddybder. Endelig bekræftes de teoretiske analyser af en række numeriske eksperimenter med både lineære og ikke-lineære bølger.

Den resulterende numeriske model testes først på en række kanoniske tilfælde. Dernæst, anvendes den til at studere en række ikke-lineære bølgefænomener, som har såvel fundamental som praktisk interesse.

Den første fundamentale undersøgelse involverer to-dimensionelle bølgemønstre i krydsende bølgetog. På lav vanddybde er interaktionen stærk/svag når vinklen mellem de to bølgetog er lille/stor og som resultat af de ikke-lineære interaktioner opnås sekskantede mønstre som er i fin overenstemmelse med observationer. På stor vanddybde fører de ikke-lineære interaktioner til rektangulære mønstre afbrudt af knudelinier. Igen er der glimrende overenstemmelse med modelforsøg, og i begge tilfælde konstateres diverse fluktationer og modulationer i

mønstrene, som hidtil ikke har været forklaret i litteraturen. For første gang gives der her en plausibel forklaring på de fleste af de observerede og beregnede modulationer: Årsagen er anvendelsen af lineær bølge-genererings teori, som er ufuldstændig i forbindelse med ikke-lineære bølger og derfor resulterer i de såkaldte parasit bølger.

Den anden fundamentale undersøgelse involverer udviklingen af tre-dimensionelle instabiliteter i stejle dybvandsbølger. Fænomenet simuleres ved at addere to små retningsspredte perturbationsbølger til en strømfunktions løsning. Først studeres de såkaldte *L2 crescent patterns* som resulterer i quasi-stationære hestesko formede bølgemønstre. Fænomenet beregnes for forskellige bølgestejlheder og forskellige perturbationsstyrker. Endvidere bestemmes vækstraten af instabiliteterne for forskellige numeriske filtre. Dernæst studeres de såkaldte oscillerende hestesko-mønstre, som opstår når de ustabile perturbationsbølger ikke er faselåst til hovedbølgen. Beregningerne viser sig at være i fremragende overensstemmelse med modelforsøgs-observationer, og indeholder bl.a. de såkaldte L3 og L4 mønstre, som er omtalt i litteraturen. For at forklare de observerede og beregnede oscillationsperioder, foretages en ikke-lineær stabilitetsanalyse. Endelig undersøges fænomener hvor forskellige to- og tre-dimensionelle instabiliteter konkurrerer.

Den tredje fundamentale undersøgelse involverer bølge interaktioner med rektangulære konstruktioner. Den numeriske kode udvides til at håndtere randbetingelser i forbindelse med hjørneeffekter. En numerisk analyse viser at disse hjørnebetingelser fører til potentielle stabilitets og konvergens problemer. I praksis løses disse problemer ved hjælp af lokale numeriske filtre. Modellen aftestes på det klassiske lineære diffraktionsproblem på dybt vand og lavt vand. Dernæst anvendes modellen til at studere ikke-lineær diffraktion igennem en snæver åbning, og resultaterne er i god overensstemmelse med modelforsøg. Endelig beregnes ikke-lineært run-up på en vertikal mole. Der opnås en fremragende overensstemmelse mellem beregning og forsøg, selv i tilfælde hvor bølgestejlheden (dvs bølgehøjde divideret med længde) overskrider 0.2.

Den fjerde og sidste fundamentale undersøgelse involverer bølgeudbredelse på hurtig varierende bund. Til dette formål implementeres nogle korrektionsled til den oprindelige formulering, og den resulterende lineariserede model verificeres på fænomener som refleksion og transmission over stejle sejlrender med forskellige geometrier. Endelig studeres fænomenet Bragg scattering, som opstår som interaktion mellem overfladebølger og stationære sandbølger på havbunden. Lineære interaktioner af typen class I og II simuleres og er i god overensstemmelse med målinger fra litteraturen. Dernæst simuleres den såkaldte class III, som involverer ikke-lineære overfladebølger. I dette tilfælde kan Bragg scatter resultere i såvel refleksion som transmission, og der konstateres en downshift/upshift af resonanspunktet for refleksion/transmission, som kan forklares ved hjælp af amplitude dispersion.

Denne afhandling konkluderer, at den anvendte Boussinesq formulering er en effektiv og nøjagtig metode til at beregne fuldt ikke-lineære og dispersive vandbølger i to horizontale dimensioner. De numeriske resultater og analyser som beskrives i denne rapport, giver en dybere forståelse af mange komplicerede ikke-lineære bølgeprocesser som foregår på dybt og lavt vand, så vel på vandret bund som på skrå bund samt i interaktion med konstruktioner.

Contents

Preface	iii
Acknowledgements	v
Executive Summary	vii
Synopsis (in Danish)	ix
Contents	xi
Symbols	xix
1 Introduction	1
1.1 Historical Background	2
1.2 Motivation	4
1.3 Thesis Outline	6
2 The Boussinesq Formulation	7
2.1 Introduction	7
2.2 Governing Equations	8
2.3 Infinite Series Solution to the Laplace Equation	9
2.4 Generalization to an Arbitrary z -Level	11
2.5 Finite Series Expansions Involving Padé Approximants	11
2.6 The Kinematic Condition at the Sea Bed	13
2.7 Fourier Analysis of Linear Dispersion	14
2.8 Conclusions	15

3	The Numerical Model	17
3.1	Introduction	17
3.2	Finite Difference Approximations	18
3.3	Boundary Conditions	19
3.4	Time Integration	19
3.5	Relaxation Zones	20
3.6	Savitzky-Golay Smoothing Filters	21
3.7	Computer Processors	22
3.8	Programming Language and Compilers	22
3.9	Conclusions	23
4	Preconditioned Iterative Solutions	25
4.1	Introduction	25
4.2	Rotational and Irrotational Formulations	27
4.3	Matrix Properties	28
4.4	Direct Matrix Factorizations	30
4.5	Krylov Subspace Method	31
4.6	Preconditioning Methods	31
4.6.1	Factored linear preconditioner	31
4.6.2	ILUT preconditioner	32
4.6.3	Fourier space preconditioner	32
4.6.4	Approximate Schur complement preconditioner	34
4.7	Comparison of Preconditioners	36
4.7.1	Performance versus relative water depth	36
4.7.2	Performance versus nonlinearity	37

4.7.3	Performance versus grid refinement	38
4.7.4	Storage comparison	40
4.7.5	Breakdown of computational expenses	40
4.7.6	Performance versus problem size	41
4.7.7	Discussion	42
4.8	Conclusions	43
5	Linear & Nonlinear Stability Analysis	45
5.1	Introduction	45
5.2	Stability of the Method of Lines	46
5.3	Linear Stability Regions	47
5.4	Linear Fourier Analysis	50
5.5	Linear Matrix-Based Analysis	53
5.5.1	Description	53
5.5.2	Comparison of rotational & irrotational formulations	54
5.6	Local Nonlinear Matrix-Based Analysis	56
5.6.1	The presence of nonlinear instabilities	57
5.6.2	The effect of numerical dissipation	59
5.6.3	Comparison of rotational and irrotational formulations	59
5.7	Analysis of Pseudospectra	60
5.8	Numerical Experiments	63
5.8.1	Linear experiments	63
5.8.2	Nonlinear experiments	63
5.9	Conclusions	66

6	Model Verification	69
6.1	Introduction	69
6.2	Linear Standing Wave	70
6.3	Nonlinear Standing Wave	73
6.4	Linear Shoaling	73
6.5	Nonlinear Refraction & Diffraction	75
6.6	A Brief Comparison of Computational Efficiency	78
6.6.1	Comparison with NS3	79
6.6.2	Comparison with MIKE 21	80
6.6.3	A mention of some other fully nonlinear models	81
6.7	Conclusions	82
7	Modeling of Short-Crested Waves	83
7.1	Introduction	83
7.2	Hexagonal Surface Patterns	84
7.3	Rectangular Surface Patterns	86
7.3.1	Model setup	86
7.3.2	Numerical results	88
7.3.3	Physical explanation	90
7.4	Conclusions	96
8	A Numerical Study of Crescent Waves	99
8.1	Introduction	100
8.2	Crescent Wave Generation	101
8.3	Phase-Locked Crescent Patterns	102
8.3.1	Model discretizations	102

8.3.2	The effects of smoothing filters on the growth rate	103
8.3.3	Characteristics of the L2 crescent patterns	105
8.3.4	The effects of nonlinearity	108
8.3.5	Discussion of physical processes	110
8.4	Oscillating Crescent Patterns	113
8.4.1	Transition from $(k'_{x1}, k'_{x2}) = (\frac{4}{3}, \frac{5}{3})k_0$ to $(1, 2)k_0$	114
8.4.2	Transition from $(k'_{x1}, k'_{x2}) = (\frac{5}{4}, \frac{7}{4})k_0$ to $(\frac{3}{4}, \frac{9}{4})k_0$	119
8.4.3	A quantitative explanation	122
8.4.4	On the selection of the Collard & Caulliez (1999) oscillating crescents	124
8.5	Competition Between Unstable Modes	126
8.5.1	Competition between isolated class II modes	126
8.5.2	Competition between isolated class I and II modes	127
8.5.3	Competition of random disturbances	128
8.6	Computational Efficiency	131
8.7	Conclusions	132
9	Nonlinear Wave-Structure Interactions	135
9.1	Introduction	135
9.2	Discretization Around Structures	136
9.3	Linear Stability Analysis	137
9.4	Linear Breakwater Diffraction	141
9.5	Linear & Nonlinear Gap Diffraction	143
9.6	Nonlinear Wave Run-Up on a Vertical Plate	146
9.7	Conclusions	150

10 Extension to Rapidly Varying Bathymetry	155
10.1 Introduction	156
10.2 Extension to Rapidly Varying Bathymetry	157
10.3 Fourier Analysis of Linear Dispersion	159
10.4 Linear Shoaling	161
10.5 Reflection from a Plane Shelf	161
10.6 Bragg Scattering	164
10.6.1 Class I Bragg resonance	165
10.6.2 Class II Bragg resonance	166
10.6.3 Class III Bragg resonance	168
10.7 Conclusions	171
11 Conclusions & Recommendations	173
11.1 Conclusions	173
11.2 Recommendations	176
References	179
A Differential Operators	193
B Finite Difference Approximations	195
B.1 One-Dimensional Derivative Approximations	195
B.2 Mixed Derivative Approximations	196
C Fourier Analysis of Savitzky-Golay Smoothing Filters	199
D The Jacobian Matrix	201

E	Stability Analysis of Finite Amplitude Deep Water Waves	203
E.1	Governing Equations	203
E.2	The Eigenvalue Problem	204
E.3	Analysis of Linear Waves	205
E.4	Analysis of Finite Amplitude Waves	206
F	Linear Accuracy Analysis	211
	List of PhD Theses Available from the Department	217

Symbols

Roman Symbols

a, a_i	Amplitude
a_0	Incident wave amplitude
A	Fourier amplitude; Amplification factor
\mathcal{A}	Continuous representation of \mathbf{A}
\mathcal{A}_i	Continuous operator
$\tilde{\mathcal{A}}_i$	Fourier space representation of \mathcal{A}_i
\mathbf{A}	A matrix
\mathbf{A}_i	A sub-matrix
b	Thickness
b_0	Shelf length
b_i	Amplitudes
\mathbf{b}	Right hand side vector
B	Fourier amplitude
\mathcal{B}_i	A continuous operator
$\tilde{\mathcal{B}}_i$	Fourier space representation of \mathcal{B}_i
\mathbf{B}	A matrix
\mathbf{B}_i	A sub-matrix
c	Wave celerity
c_i	A coefficient
c_g	Group velocity
c_r	Weighting coefficient for a relaxation zone
c_s	Stokes drift velocity
c_{Stokes}	Wave celerity according to Stokes first-order theory
\mathbf{c}	Coefficient vector in a Runge-Kutta Butcher tableau
C	Fourier amplitude

\mathbf{C}_i	A sub-matrix
\mathcal{C}_i	A continuous operator
CPU	Computer simulation time
d, d_i	Amplitude of bottom ripple
D	Diffusion coefficient
e	Natural number
E	Measure of computational efficiency
f, f_i, f^*	Discrete functions
\check{f}	Fourier amplitude of f
F	Operator representing a stage evaluation for a system of differential equations
\mathcal{F}	A Fourier transform operation
\mathbf{F}	Matrix of finite difference coefficients
g	Gravitational acceleration
G	A function
h	Still water depth
h_0	Average still water depth; Depth of incident wave
h_i	Characteristic height
H	Waveheight
i	An index
i	$\equiv \sqrt{-1}$, Imaginary unit
\mathbf{I}	Identity matrix
j	An index
J_i	Operator
\mathcal{J}_i	Block in continuous Jacobian operator
\mathbf{J}	Jacobian matrix
k	Wavenumber; Modulus of \mathbf{k}
k_0	Incident wavenumber
$k_{critical}$	Wavenumber of most numerically unstable mode
k_N	Modulus of \mathbf{k}_N
k_R	Critical wavenumber causing a singularity in the linear dispersion relation
\mathbf{k}	$\equiv (k_x, k_y)$, Wavenumber vector
\mathbf{k}_i	Wavenumber vector; Runge-Kutta stage evaluation
\mathbf{k}'	$\equiv (k'_x, k'_y)$, Perturbation wavenumber vector
\mathbf{k}'_i	$\equiv (k'_{ix}, k'_{iy})$, Perturbation wavenumber vector

\mathbf{k}_N	Nyquist wavenumber vector
K, K_i	Wavenumber of an undular sea bottom
\mathbf{K}	Wavenumber vector of an undular sea bottom
L	Wavelength; Operator on pseudo-velocity variables
L_x, L_y	Wavelengths in the x, y directions
m	An index
\mathcal{M}	A preconditioning operator
\mathbf{M}	Preconditioning matrix
n	An index
n_s	Number of successive smoothing applications
n_u	Time step where a simulation is deemed unstable
N	Number of grid points; Number of grid points per wavelength
N_r	Number of grid points in a relaxation zone
N_t	Number of time steps
N_x, N_y, N_z	Number of grid points in the x, y, z -directions
O	Order
p	Related to the longitudinal wavenumber perturbation
q	An index; Magnitude of normalized transversal wavenumber perturbation
r	Shape parameter for a relaxation zone; Relative residual tolerance
r_h	Hyperbolic Courant number
$r_{h,max}$	Maximum numerically stable hyperbolic Courant number
r_p	Parabolic Courant number
R	Root-mean-squared growth rate
s_i	A coefficient
s_{max}	Maximum free surface slope
\mathbf{s}	Smoothing stencil
\mathcal{S}	Schur complement operator
\mathcal{S}_0	Utility Schur complement operator
\mathbf{S}_0	Discrete representation of \mathcal{S}_0
t	Time
T	Wave period; Transpose
T^*	Oscillation period
\mathbf{u}	$\equiv (u, v)$, Horizontal velocity vector

$\tilde{\mathbf{u}}$	$\equiv (\tilde{u}, \tilde{v})$, Horizontal velocity vector at $z = \eta$
$\tilde{\mathbf{u}}'$	$\equiv (\tilde{u}', \tilde{v}')$, Perturbation of $\tilde{\mathbf{u}}$
\mathbf{u}_0	$\equiv (u_0, v_0)$, Horizontal velocity vector at $z = 0$
\tilde{u}_0	Fourier amplitude of u_0
$\hat{\mathbf{u}}$	$\equiv (\hat{u}, \hat{v})$, Horizontal velocity vector at $z = \hat{z}$
$\hat{\mathbf{u}}^*$	$\equiv (\hat{u}^*, \hat{v}^*)$, Horizontal pseudo-velocity vector at $z = \hat{z}$
\mathbf{u}_b	$\equiv (u_b, v_b)$, Horizontal velocity vector at $z = -h$; Eigenvector
$\tilde{\mathbf{U}}$	$\equiv (\tilde{U}, \tilde{V}) \equiv \nabla \tilde{\phi}$, Gradient of the velocity potential at $z = \eta$
$\tilde{\mathbf{U}}'$	$\equiv (\tilde{U}', \tilde{V}')$, Perturbation of $\tilde{\mathbf{U}}$
v_i	Element in \mathbf{v}
\mathbf{v}	Vector of time stepping variables in the eigenvector basis
\mathbf{V}	Matrix whose columns are eigenvectors
w	Vertical velocity
\tilde{w}	Vertical velocity at $z = \eta$
\tilde{w}'	Perturbation of \tilde{w}
w_0	Vertical velocity at $z = 0$
\hat{w}	Vertical velocity at $z = \hat{z}$
\hat{w}^*	Vertical pseudo-velocity at $z = \hat{z}$
w_b	Vertical velocity at $z = -h$
w_i	Element in \mathbf{w}
\mathbf{w}	Right hand size vector of preconditioning operation
\mathbf{w}_i	Component of \mathbf{w}
x	Horizontal Cartesian coordinate
x^*	Horizontal Cartesian coordinate in moving reference frame
\mathbf{x}	Vector of unknowns
y	Horizontal Cartesian coordinate
y^*	Horizontal Cartesian coordinate in moving reference frame
\mathbf{y}	Vector of time stepping variables
z	Vertical Cartesian coordinate; An element in the vector \mathbf{z}
\hat{z}	Vertical expansion point
z_i	Element in \mathbf{z}
\mathbf{z}	Vector of unknowns in a preconditioning operation
\mathbf{z}_i	Component of \mathbf{z}
\mathbf{Z}	Utility matrix
\mathcal{Z}	$= \mathcal{A}^{-1}$, A continuous operator

Greek symbols

α	Half-width of a smoothing stencil
α_i	A coefficient
α_r	Shape parameter for a relaxation zone
β	Phase shift
β_i	A coefficient
γ	A utility variable
Γ_w	$\nabla\hat{z}$ operator for the w velocity profile
Γ_u	$\nabla\hat{z}$ operator for the \mathbf{u} velocity profile
δ	A coefficient; Order parameter with respect to differentiation of \hat{z}
Δ	Change in
Δk	Wavenumber step
$\Delta x, \Delta y$	Spatial discretization
Δt	Time step
Δt_{max}	Maximum stable time step
ϵ	A coefficient; A perturbation strength
η	Free surface elevation above datum
$\bar{\eta}$	Unperturbed free surface
$\tilde{\eta}$	Fourier amplitude of η
η'	Perturbation of η
θ	Phase angle
θ_0	Incident wave angle
λ	Function argument; Eigenvalue
λ_i	Characteristic length
λ_{max}	Modulus of maximum imaginary eigenvalue
λ_ϵ	Pseudo-eigenvalue
Λ_ϵ	Matrix pseudospectrum
Λ	Diagonal matrix of eigenvalues
μ	Random number
μ_i	Coefficient
ν	Kinematic viscosity of water
π	Ratio of a circles circumference and diameter
Π	Product of a series

ρ	Utility variable
σ	Notation for $\equiv -\hat{z}/h$; Complex perturbation angular frequency
σ_0	Notation for $\equiv -\hat{z}/h_0$
Σ	Summation
ϕ	Velocity potential
$\bar{\phi}$	Unperturbed velocity potential
$\tilde{\phi}$	Velocity potential at $z = \eta$
χ	Spatial truncation error order parameter
ψ	Notation for $= (z - \hat{z})$; Function argument
ψ_b	Notation for $= -(h + \hat{z})$
ω	Angular frequency
ω', ω'_i	Perturbation frequency
ω^*	Angular oscillation frequency
ω_0	Angular frequency of incident wave
ω_N	Angular frequency of the Nyquist mode

Additional symbols

\Im	Imaginary part of
∇	$\equiv (\frac{\partial}{\partial x}, \frac{\partial}{\partial y})$, Horizontal gradient operator
\Re	Real part of

Chapter 1

Introduction

The mathematical description of nonlinear water waves involves the Laplace equation combined with nonlinear boundary conditions at the free-surface and at the sea bottom. This problem is complicated by the fact that the moving surface boundary is part of the solution. Direct numerical methods for solving the full equations exist but they are extremely time consuming and can only be applied to small scale problems. For this reason there is a strong interest in so-called Boussinesq-type formulations of the water wave problem.

The principle behind Boussinesq formulations is to incorporate the effects of non-hydrostatic pressure, while eliminating the vertical coordinate, thus significantly reducing the computational effort relative to a full three-dimensional solution. This principle was initially introduced by Boussinesq (1872)¹, who derived new governing equations (which now bear his name) under the assumption that the magnitude of the vertical velocity increases polynomially (in his case linearly) from the bottom to the free surface. This type of approximation inevitably leads to some form of depth limitation in the accuracy of the embedded dispersive and nonlinear properties. Hence, Boussinesq-type equations are conventionally associated with relatively shallow water.

Despite these physical limitations, history has proven the original ideas of Boussinesq extremely influential. Beginning in the late 1970s, commercial numerical models based on this concept have been developed to solve numerous practical engineering problems. Over the

¹Named after Joseph Valentin Boussinesq, 1842–1929. French physicist and mathematician who received his Ph.D. in 1867. He was professor of differential and integral calculus at the Faculty of Sciences of Lille (1872-86), and professor of physics and mechanics at Sorbonne, Paris (1886). He was a member of the French Académie des Sciences (1886), the teacher of mathematics at Agde, Le Vigan, and Gap (1866-1872), and retired in 1918. Boussinesq made important contributions to numerous branches of mathematical physics. His work on hydraulics was especially considerable. He studied whirlpools, liquid waves, the flow of fluids, the mechanics of pulverulent masses, the resistance of a fluid against a solid body, the cooling effect of a liquid flow, and turbulence. Among his more famous contributions is the ‘Boussinesq approximation’, which has become one of the most widely used simplifications in all of mathematical physics, and is the original inspiration for the present work. (This excerpt is taken largely from Weisstein, 2004).

past 20 years in particular, the international use of Boussinesq-type equations has steadily increased, as many researchers and engineers regard these formulations to be a balanced compromise between detailed results and affordable computational cost. Indeed, extended Boussinesq-type methods are now among those most widely used for predicting the propagation of nonlinear wind-generated waves in harbors and along coast-lines.

This concept has additionally inspired a wealth of research, much of it quite recent, attempting to overcome the physical limitations associated with the original derivation. This work continues to the present day (including this thesis!), and has met with much success. In particular, a recent breakthrough by Madsen, Bingham & Liu (2002) and Madsen, Bingham & Schäffer (2003) has resulted in a formulation having such high accuracy that the conventional shallow water and weakly nonlinear limitations have been effectively removed. Efficient numerical solutions of this system are far from trivial, however, and this thesis is primarily concerned with the development (and application) of a numerical model solving this particular formulation.

In this chapter a review of the background of the most important historical achievements in the development of extended Boussinesq formulations is provided in §1.1, leading up to the highly-accurate formulation considered throughout this thesis. In §1.2 we make clear the motivation and goals for the research detailed in the present work. The outline for the remaining thesis chapters is finally provided in §1.3.

1.1 Historical Background

In its classical form, Boussinesq wave theory represents a shallow-water approximation to the fully dispersive and nonlinear water wave problem, and the equations incorporate a balance between lowest-order dispersion and lowest-order nonlinearity (see *e.g.* Boussinesq, 1872; Madsen & Mei, 1969; Mei & LeMéhauté, 1966; Peregrine, 1967). The original use of the Boussinesq equations concentrated on the propagation of weakly nonlinear solitary waves (*e.g.* Madsen & Mei, 1969), but in the late 1970s, use of the equations started to become popular in coastal engineering, and the focus shifted towards regular cnoidal waves and irregular waves. With this shift of interest the underlying limitations in linear dispersion and nonlinearity for shorter waves became of concern.

As a result, relaxing the shallow water limitations within the framework of Boussinesq theory has received considerable attention, as stated previously, particularly over the past 20 years, see *e.g.* Kennedy *et al.* (2001); Madsen *et al.* (1991); Madsen & Schäffer (1998); Nwogu (1993); Witting (1984); Wu (1999, 2001) (see also the review of Madsen & Schäffer, 1999, and references therein). The historical progression of these advancements is summarized in Table 1.1. Here it can be seen that the earliest work rightly concentrated on improving the accuracy of the embedded linear dispersive properties. Among the more important developments, Witting (1984) was the first to demonstrate the efficiency of Padé approximants in connection with the linear celerity, and Madsen *et al.* (1991) used this idea to derive a new set of

Table 1.1: Historical relaxation of shallow water limitations within Boussinesq theory.

Property	Reference	Limiting kh
Linear dispersion	Boussinesq (1872); Peregrine (1967)	0.75
	Benjamin <i>et al.</i> (1972)	1.25
	Witting (1984)	3–6
	Madsen <i>et al.</i> (1991)	3
	Schäffer & Madsen (1995)	6
	Madsen <i>et al.</i> (2002, 2003)	25–40
Nonlinearity	Serre (1953)	0.7
	Wei <i>et al.</i> (1995)	1.2
	Madsen <i>et al.</i> (1996)	1.7
	Gobbi <i>et al.</i> (1998)	3 [†]
	Agnon <i>et al.</i> (1999)	6
	Madsen <i>et al.</i> (2002, 2003)	25–40
Velocity kinematics	Peregrine (1967)	0.5
	Nwogu (1993)	1.5
	Gobbi <i>et al.</i> (2000)	4
	Madsen <i>et al.</i> (2002, 2003)	12
	Lynett & Liu (2004 <i>b</i>)	6

[†]Accuracy of superharmonics.

extended lower-order equations having accurate linear dispersion to approximately the deep water limit (wavenumber times depth) $kh \approx 3$. This was later followed by the higher-order formulation of Schäffer & Madsen (1995), who further extended the limitation to $kh \approx 6$.

Weak nonlinearity is also a traditional shortcoming within Boussinesq theory, and as a result numerous so-called ‘fully nonlinear’ formulations have been recently developed, which means that they include all nonlinear terms up to the retained order of dispersion. These build on the early work of Serre (1953) and Su & Gardner (1969). However, despite these claims of full nonlinearity, analysis has shown that most of them have incorporated far better linear than nonlinear characteristics, see *e.g.* Gobbi *et al.* (2000); Madsen & Schäffer (1998, 1999); Wei *et al.* (1995).

A breakthrough in treating nonlinearity was achieved by Agnon, Madsen & Schäffer (1999). They presented a new procedure by which it is possible to achieve the same accuracy in nonlinear properties as in linear properties. Their procedure is based on an exact formulation of the boundary conditions at the free surface as well as at the sea bottom, combined with an approximate solution to the Laplace equation in the interior domain, which is given in terms of truncated series expansions about the still water datum. Unlike most conventional Boussinesq formulations, they also retained the vertical velocity variable as an unknown. As a result their formulation allows an accurate description of dispersive nonlinear waves out to $kh \approx 6$.

One problem that Agnon *et al.* (1999) did not resolve, however, is to provide an accurate

vertical distribution of the velocity field. As shown by Madsen & Agnon (2003), the difficulties in achieving accurate velocity kinematics are primarily due to restrictions caused by a finite convergence radius of the resulting expansions. This turns out to be a rather severe restriction to conventional Boussinesq formulations, and most existing formulations can only produce a reasonable velocity profile for $kh \leq 0.5$. Two exceptions are the formulations of Nwogu (1993) and Gobbi, Kirby & Wei (2000). Nwogu (1993) expanded the velocity field from an arbitrary (vertical) z -level, which was taken to be approximately mid-depth. The objective of Nwogu was not to improve the velocity profile, but rather the linear dispersion relation. Nevertheless, the profile obtained from his lower-order formulation is accurate up to $kh \approx 1.5$ and can be shown to converge up to $kh \approx 3.5$ (if higher-order terms are included). Recently, Gobbi *et al.* (2000) presented a higher-order formulation based on a linear combination of the velocities at two arbitrary z -levels. The linear velocity profile obtained from their method is applicable out to $kh \approx 4$, while their dispersion relation is applicable up to $kh \approx 6$. Recently, Lynett & Liu (2004*b*) have also proposed a two-layer approach, with reasonable velocity profiles to $kh \approx 6$ (see also Lynett & Liu, 2004*a*).

Inspired by the original idea of Nwogu (1993), and with the original aim of further increasing the accuracy of the velocity profile, Madsen, Bingham & Schäffer (2003) (also Madsen, Bingham & Liu, 2002) generalized the formulation of Agnon *et al.* (1999) to use an arbitrary vertical expansion level. The result, as can be gathered from Table 1.1, is a Boussinesq formulation with accuracy vastly superior to all previous derivations, capable of treating fully nonlinear waves out to $kh \approx 25$ –40 (depending on the chosen expansion point), with velocity profiles accurate to $kh \approx 12$. This corresponds to a major breakthrough in modern Boussinesq theory, as it is the first formulation to effectively remove the shallow water limitations conventionally associated with this approach. It is again this formulation which provides the basis for the present work.

As the accuracy of Boussinesq formulations has gradually improved, so has the variety of physical phenomena which have been incorporated into the various models, which is also worth mentioning. The major advancements in this regard are listed in Table 1.2, which includes an achievement of the present work. As can be seen, modern Boussinesq formulations are capable of treating a wide variety of coastal and offshore phenomena, which explains their popularity among scientists and engineers. Originally limited to shallow water, Boussinesq models have now successfully been used to study highly nonlinear deep water wave phenomena *e.g.* wave instabilities (see Fuhrman *et al.*, 2004*d*; Madsen *et al.*, 2002).

1.2 Motivation

As described previously, the Boussinesq equations of Madsen *et al.* (2002, 2003) represent a major step forward in the advancement of Boussinesq theory. The high accuracy unfortunately comes at the expense of a rather complicated system of partial differential equations (PDEs). Numerical (finite difference) solutions in a single horizontal dimension, as presented

Table 1.2: Historical milestones in incorporating various physical phenomena using Boussinesq-type formulations. The vertical line after the first four rows roughly divides the pioneering classical works with more modern developments.

Reference	New phenomena
Boussinesq (1872)	Original derivation
Rayleigh (1876)	Solitary waves
Korteweg & de Vries (1895)	Cnoidal waves
Peregrine (1967)	Uneven bottom
Abbott <i>et al.</i> (1978)	Irregular waves in harbors; Large scale numerical models
Freilich & Guza (1984)	Wave-wave interaction; Evolution of wave spectra
Yoon & Liu (1989)	Wave-current interaction
Madsen & Sørensen (1990)	Wave-ship interaction
Schäffer <i>et al.</i> (1993)	Breaking of regular waves
Madsen <i>et al.</i> (1997 <i>a</i>)	Breaking of irregular waves
Madsen <i>et al.</i> (1997 <i>b</i>)	Surf beat and net circulations
Rakha & Kamphuis (1997)	Beach profile evolution
Madsen & Schäffer (1998)	Wave blocking by currents
Madsen <i>et al.</i> (2002)	Side-band instability
Fuhrman <i>et al.</i> (2004 <i>d</i>) [†]	Crescent waves

[†]See Chapter 8.

in Madsen *et al.* (2002), are still in a sense trivial, requiring solutions of a banded linear system at each stage evaluation. This is a problem for which specialized direct methods (*i.e.* gaussian elimination) for sparse matrices are known to be well suited for (see *e.g.* Duff *et al.*, 1986; Golub & Van Loan, 1996; Meurant, 1999). When the system is extended to two horizontal dimensions, however, numerical solutions are much more complicated, which is the focus of the present work.

Hence, with this project we are faced with an exciting and challenging situation: A new system of partial differential equations for which *nobody* has yet seriously attempted numerical solutions. Extended Boussinesq equations have, of course, been solved before in two horizontal dimensions (*e.g.* Wei & Kirby, 1995), though their resemblance to the system considered herein is in fact not as large as one might think, as many of the ‘tricks’ used to obtain high accuracy have only been developed recently. The primary motivation for this thesis is to develop efficient numerical solutions in two horizontal dimensions for the high-order Boussinesq formulation of Madsen *et al.* (2002, 2003).

Directly related to this task is the overall development of a numerical (finite difference) model based on this system, for the realistic simulation of nonlinear water wave phenomena, which are important in coastal and offshore engineering. We ultimately consider problems involving (sometimes rapidly) varying water depths, extreme nonlinearities, and even semi-irregular domains. The focus is on problems which have been previously unamenable with Boussinesq

formulations. Through this work we aim to provide a more complete understanding of the many complicated physical processes involved within the areas investigated.

The original formulation of Madsen *et al.* (2003) is in many ways very diverse in terms of the potential applications, allowing for the treatment of fully nonlinear waves over a rather extreme range of water depths. As originally derived, however, it was limited to mildly sloping bottoms. A final aim of this thesis is to demonstrate an extension of the original derivation which removes this limitation, thus broadening the already wide application range of the model to include problems with rapidly varying bathymetries.

1.3 Thesis Outline

The outline for the remaining chapters of this thesis is as follows. A brief derivation of the system of PDEs of Madsen *et al.* (2002, 2003) starting from the standard Laplace problem for irrotational free surface flow is provided in Chapter 2. Chapter 3 describes various details of the basic numerical finite difference model used throughout this work. Various preconditioning methods, essential for efficient numerical solutions of this system, are developed and tested in Chapter 4. The linear and nonlinear stability of the numerical scheme is analyzed in Chapter 5. The basic model is systematically verified using a number of standard test cases in Chapter 6. The model is then used to study short-crested waves arising from the nonlinear interaction of wavefronts at oblique incident angles in Chapter 7. Chapter 8 details a rather extensive numerical study of the phenomenon of crescent waves, arising from the instability of steep deep water plane waves to three dimensional disturbances. Chapter 9 describes the extension of the basic model to include bottom mounted piecewise-rectangular structures, as well as numerous test cases involving nonlinear wave-structure interactions. Additionally, Chapter 10 describes the extension of the model to allow cases having rapidly varying bathymetry, and the model is used to investigate, among other things, the phenomenon of Bragg scattering from undular sea bottoms. Finally, conclusions are drawn in Chapter 11, where some recommendations for further research are also discussed.

Chapter 2

The Boussinesq Formulation

Chapter Summary

Starting from the standard fully nonlinear Laplace problem for inviscid, irrotational free surface flow, a brief derivation of the high-order Boussinesq formulation used throughout this work is provided. The formulation combines exact representations of the (dynamic and kinematic) surface and (kinematic) bottom boundary conditions with truncated solutions of the Laplace equation in the interior domain. Fourier analysis of the embedded linear dispersive properties is also provided, demonstrating excellent accuracy to (wavenumber times depth) $kh \approx 30$.

2.1 Introduction

In this chapter a brief review of the derivation of the Boussinesq formulation of Madsen *et al.* (2002, 2003) is provided. Starting from the standard fully nonlinear Laplace problem for inviscid, irrotational free surface flow, the main steps involved in the derivation process are included. For complete details on the derivation (as well as for a complete analysis of embedded linear and nonlinear properties for this system), the reader is referred to the original literature (Madsen *et al.*, 2002, 2003).

This chapter is organized as follows. The equations governing inviscid, irrotational free surface flow are outlined in §2.2, where the exact free surface conditions are also re-formulated in terms of variables directly on the free surface. The derivation of the Boussinesq formulation begins with an infinite series solution to the Laplace equation in §2.3, which is generalized to an arbitrary vertical expansion level in §2.4. The final truncated series solution involving Padé approximants is detailed in §2.5, with the corresponding expression of the kinematic bottom condition provided in §2.6. Fourier analysis of the embedded linear dispersion properties is given in §2.7, and conclusions are briefly re-stated in §2.8.

2.2 Governing Equations

We adopt a Cartesian coordinate system with the x - and y -axes located on the still water plane and the z -axis pointing vertically upwards. The fluid domain is bounded by the sea bed at $z = -h(x, y)$ and the free surface at $z = \eta(x, y, t)$, where t is time. Assuming irrotational flow, the velocity potential ϕ is related to the velocity components by the definition

$$\mathbf{u} \equiv \nabla\phi, \quad w \equiv \phi_z, \quad (2.1)$$

where subscripts denote partial differentiation and

$$\nabla \equiv \left(\frac{\partial}{\partial x}, \frac{\partial}{\partial y} \right), \quad (2.2)$$

is the two-dimensional gradient operator. The governing equations and boundary conditions for the irrotational flow of an incompressible inviscid fluid with a free surface (neglecting surface tension) are standard

$$\nabla^2\phi + \phi_{zz} = 0, \quad -h < z < \eta, \quad (2.3)$$

$$\eta_t - \phi_z + \nabla\eta \cdot \nabla\phi = 0, \quad z = \eta, \quad (2.4)$$

$$\phi_t + g\eta + \frac{1}{2}(\nabla\phi \cdot \nabla\phi + (\phi_z)^2) = 0, \quad z = \eta, \quad (2.5)$$

$$\phi_z + \nabla h \cdot \nabla\phi = 0, \quad z = -h, \quad (2.6)$$

where $g = 9.81 \text{ m/s}^2$ (unless otherwise noted) is the gravitational acceleration. Here (2.3) is the Laplace equation, which satisfies local continuity throughout the fluid; (2.4) is the kinematic free surface condition, stating that a fluid particle on the free surface will remain there; (2.5) is the dynamic free surface condition, stating that the pressure at the surface is constant; and (2.6) is the kinematic bottom condition, stating that the bed is impermeable.

Following Dommermuth & Yue (1987); Witting (1984); Zakharov (1968), we choose to reformulate the dynamic and kinematic boundary conditions at the free surface by introducing variables defined directly at the free surface, *i.e.*

$$\tilde{\mathbf{u}} \equiv (\tilde{u}, \tilde{w}) \equiv (\nabla\phi)_{z=\eta}, \quad \tilde{w} \equiv (\phi_z)_{z=\eta}, \quad \tilde{\phi} \equiv \phi_{z=\eta}. \quad (2.7)$$

Now spatial and temporal differentiation of the variables at the free surface involves the chain rule, giving the relations

$$\nabla\tilde{\phi} = (\nabla\phi)_{z=\eta} + \nabla\eta(\phi_z)_{z=\eta} = \tilde{\mathbf{u}} + \tilde{w}\nabla\eta, \quad (2.8)$$

$$\tilde{\phi}_t = (\phi_t)_{z=\eta} + \eta_t(\phi_z)_{z=\eta} = (\phi_t)_{z=\eta} + \tilde{w}^2 - \tilde{w}\nabla\eta \cdot \tilde{\mathbf{u}}, \quad (2.9)$$

where η_t has been eliminated by the use of (2.4). Using (2.7)–(2.9), the dynamic condition (2.5) can be expressed as

$$\tilde{\phi}_t + g\eta + \frac{1}{2}(\nabla\tilde{\phi} \cdot \nabla\tilde{\phi} - \tilde{w}^2(1 + \nabla\eta \cdot \nabla\eta)) = 0, \quad (2.10)$$

which is the form used by Dommermuth & Yue (1987). Applying the gradient operator to (2.10), we transform the equation into the velocity vector equation used by Witting (1984)

$$\tilde{\mathbf{U}}_t = -g\nabla\eta - \frac{1}{2}\nabla\left(\tilde{\mathbf{U}}\cdot\tilde{\mathbf{U}} - \tilde{w}^2(1 + \nabla\eta\cdot\nabla\eta)\right), \quad (2.11)$$

where

$$\tilde{\mathbf{U}} \equiv (\tilde{U}, \tilde{V}) \equiv \nabla\tilde{\phi} = \tilde{\mathbf{u}} + \tilde{w}\nabla\eta. \quad (2.12)$$

The kinematic surface condition (2.4) may similarly be expressed as

$$\eta_t = \tilde{w}(1 + \nabla\eta\cdot\nabla\eta) - \tilde{\mathbf{U}}\cdot\nabla\eta. \quad (2.13)$$

We note that (2.11) and (2.13) define the fully nonlinear time-stepping problem, and are used throughout this work. Finally, expressed in terms of velocity variables, the kinematic bottom condition (2.6) may be written as

$$w_b + \nabla h \cdot \mathbf{u}_b = 0, \quad (2.14)$$

where $w_b = w(x, y, -h, t)$ and $\mathbf{u}_b = \mathbf{u}(x, y, -h, t)$ are velocities defined directly at the sea bottom *i.e.* at $z = -h$.

2.3 Infinite Series Solution to the Laplace Equation

In order to establish a connection between the velocity variables at the free surface we need to solve the Laplace equation in the interior domain. As a starting point we follow the classical Boussinesq procedure and introduce an expansion of the velocity potential as a power series in the vertical coordinate

$$\phi(x, y, z, t) = \sum_{n=0}^{\infty} z^n \phi^{(n)}(x, y, t), \quad (2.15)$$

where

$$\phi^{(n)}(x, y, t) \equiv \phi^{(n)} \equiv \left. \frac{\partial^n \phi}{\partial z^n} \right|_{z=0}. \quad (2.16)$$

Inserting (2.15) this into the Laplace equation (2.3) leads a polynomial in z of the form

$$\nabla^2 \phi^{(0)} + z \nabla^2 \phi^{(1)} + \sum_{n=2}^{\infty} (n(n-1)z^{(n-2)}\phi^{(n)} + z^n \nabla^2 \phi^{(n)}) = 0. \quad (2.17)$$

By grouping powers of z this may be equivalently written as

$$\sum_{n=0}^{\infty} ((n+2)(n+1)\phi^{(n+2)} + \nabla^2 \phi^{(n)}) z^n = 0. \quad (2.18)$$

Requiring the coefficient for each power of z to vanish, then leads to the classical recurrence relation

$$\phi^{(n+2)} = -\frac{\nabla^2 \phi^{(n)}}{(n+1)(n+2)}. \quad (2.19)$$

Due to this recurrence, we may express the full series in terms of only two variables $\phi^{(0)}$ and $\phi^{(1)}$. From (2.16) these are equivalent to

$$\phi^{(0)} = \phi(x, y, 0, t), \quad \phi^{(1)} = \phi_z(x, y, 0, t), \quad (2.20)$$

i.e. the series may be expressed entirely in terms of the potential and its z -derivative, both taken at $z = 0$. Hence we may write (2.15) as

$$\phi(x, y, z, t) = \sum_{n=0}^{\infty} (-1)^n \left(\frac{z^{2n}}{(2n)!} \nabla^{2n} \phi^{(0)} + \frac{z^{2n+1}}{(2n+1)!} \nabla^{2n} \phi^{(1)} \right). \quad (2.21)$$

Following Madsen & Schäffer (1998), we introduce the still water variables

$$\mathbf{u}_0 \equiv (u_0, v_0) \equiv \nabla \phi(x, y, 0, t) = \nabla \phi^{(0)}, \quad w_0 \equiv \phi_z(x, y, 0, t) = \phi^{(1)}, \quad (2.22)$$

and obtain the following exact expressions for the velocity field

$$\mathbf{u}(x, y, z, t) = \cos(z\nabla) \mathbf{u}_0 + \sin(z\nabla) w_0, \quad (2.23)$$

$$w(x, y, z, t) = \cos(z\nabla) w_0 - \sin(z\nabla) \mathbf{u}_0. \quad (2.24)$$

Here the cos- and sin- operators are infinite Taylor series operators defined by

$$\cos(\lambda\nabla) \equiv \sum_{n=0}^{\infty} (-1)^n \frac{\lambda^{2n}}{(2n)!} \nabla^{2n}, \quad \sin(\lambda\nabla) \equiv \sum_{n=0}^{\infty} (-1)^n \frac{\lambda^{2n+1}}{(2n+1)!} \nabla^{2n+1}, \quad (2.25)$$

which is an elegant notation introduced by Rayleigh (1876). We emphasize that throughout this work the interpretation of the powers of ∇ depends on whether this operator is acting on a scalar or a vector, and in this context the following set of rules should be obeyed (see Madsen & Schäffer, 1999, Chapter 5)

$$\begin{aligned} \nabla^{2n} \mathbf{u} &= \nabla(\nabla^{2n-2}(\nabla \cdot \mathbf{u})), & \nabla^{2n+1} \mathbf{u} &= \nabla^{2n}(\nabla \cdot \mathbf{u}), \\ \nabla^{2n} w &= \nabla^{2n} w, & \nabla^{2n+1} w &= \nabla(\nabla^{2n} w). \end{aligned}$$

Note that (2.23) and (2.24) define the exact velocity profile in the entire water column $-h < z < \eta$ expressed in terms of the velocity variables at $z = 0$, and these expressions automatically satisfy the Laplace equation. Linear analysis of this system can be shown to recover the exact linear dispersion relation and the exact linear shoaling gradient (see Agnon *et al.*, 1999).

2.4 Generalization to an Arbitrary z -Level

We now generalize (2.23) and (2.24) in the following. The first step is to introduce the velocities $\hat{\mathbf{u}} \equiv (\hat{u}, \hat{v}) \equiv \mathbf{u}(x, y, \hat{z}, t)$, which are at an arbitrary level $\hat{z} = \hat{z}(x, y)$ in the fluid. Here \hat{z} is assumed to be a constant fraction σ of the (negative) still-water depth h *i.e.* $\hat{z} = -\sigma h$. This generalization of the formulation by Agnon *et al.* (1999) is inspired by Nwogu (1993), who was the first to formulate truncated Boussinesq equations in terms of the horizontal velocity vector defined at an arbitrary z -level.

From (2.23) and (2.24) we find the relations

$$\hat{\mathbf{u}} = \cos(\hat{z}\nabla)\mathbf{u}_0 + \sin(\hat{z}\nabla)w_0, \quad (2.26)$$

$$\hat{w} = \cos(\hat{z}\nabla)w_0 - \sin(\hat{z}\nabla)\mathbf{u}_0. \quad (2.27)$$

In order to invert (2.26) and (2.27) and determine \mathbf{u}_0, w_0 in terms of $\hat{\mathbf{u}}, \hat{w}$, we insert (2.25) in (2.26) and (2.27) and use successive approximations assuming high-derivative terms to be smaller than low-derivative terms. The inversion process involves higher derivatives of \hat{z} and in the following we shall include only terms which are $O(\nabla\hat{z})$, corresponding to a mild-slope approximation. Finally, we insert the inverted expressions for \mathbf{u}_0, w_0 into (2.23) and (2.24) and derive the following mild-slope expression for the velocity field

$$\mathbf{u}(x, y, z, t) = \cos((z - \hat{z})\nabla)\hat{\mathbf{u}} + \sin((z - \hat{z})\nabla)\hat{w} + \Gamma_u \nabla\hat{z}, \quad (2.28)$$

$$w(x, y, z, t) = \cos((z - \hat{z})\nabla)\hat{w} - \sin((z - \hat{z})\nabla)\hat{\mathbf{u}} + \Gamma_w \cdot \nabla\hat{z}, \quad (2.29)$$

where

$$\Gamma_u \equiv (z - \hat{z})(\cos((z - \hat{z})\nabla)\nabla \cdot \hat{\mathbf{u}} + \sin((z - \hat{z})\nabla)\nabla\hat{w}), \quad (2.30)$$

$$\Gamma_w \equiv (z - \hat{z})(\cos((z - \hat{z})\nabla)\nabla\hat{w} - \sin((z - \hat{z})\nabla)\nabla \cdot \hat{\mathbf{u}}). \quad (2.31)$$

This completes the formulation of the un-truncated system of equations, which consists of (2.11), (2.13), (2.14), (2.28), and (2.29). A linear analysis of this un-truncated system can be found in Madsen *et al.* (2003), and this again recovers the exact linear velocity profile, the linear dispersion relation, and the linear shoaling gradient.

2.5 Finite Series Expansions Involving Padé Approximants

For numerical solutions of this system to be possible, the infinite series operators previously introduced must of course be truncated. We now describe the method of truncation used

in the derivation of Madsen *et al.* (2002, 2003), which achieves the best possible accuracy for a given number of terms. As a starting point, we follow Agnon *et al.* (1999) and include the first three terms in both the cos- and the sin-series defined in (2.25). This leads to the approximations

$$\cos(\lambda\nabla) = 1 - \frac{\lambda^2\nabla^2}{2} + \frac{\lambda^4\nabla^4}{24} + O(\lambda^6\nabla^6), \quad (2.32)$$

$$\sin(\lambda\nabla) = \lambda\nabla - \frac{\lambda^3\nabla^3}{6} + \frac{\lambda^5\nabla^5}{120} + O(\lambda^7\nabla^7). \quad (2.33)$$

By inserting (2.32) and (2.33) into (2.28) and (2.29) and analyzing the resulting velocity profile, it can be shown that the accuracy will increase significantly by choosing $\hat{z} = -h/2$, rather than the $\hat{z} = 0$ used by Agnon *et al.* (1999) (for details see Madsen *et al.*, 2003). On the other hand, it turns out that an even better accuracy can be achieved by the procedure presented in the following.

First, we expand the physical velocity variables $\hat{\mathbf{u}}, \hat{w}$ in terms of pseudo-velocity variables $\hat{\mathbf{u}}^*, \hat{w}^*$ using the connection

$$\hat{\mathbf{u}} \equiv L(\hat{z}\nabla)\hat{\mathbf{u}}^*, \quad \hat{w} \equiv L(\hat{z}\nabla)\hat{w}^*, \quad (2.34)$$

where L is a linear operator to be determined. We note that there is some similarity between this approach and the previous ideas of Schäffer & Madsen (1995) and Gobbi *et al.* (2000) who also used generalized velocity variables rather than physical velocity variables. However, the choice of the L -operator is very important in this process, as shown below. We insert (2.34) in (2.28) and (2.29) and obtain

$$\mathbf{u}(x, y, z, t) = \cos((z - \hat{z})\nabla)L(\hat{z}\nabla)\hat{\mathbf{u}}^* + \sin((z - \hat{z})\nabla)L(\hat{z}\nabla)\hat{w}^*, \quad (2.35)$$

$$w(x, y, z, t) = \cos((z - \hat{z})\nabla)L(\hat{z}\nabla)\hat{w}^* - \sin((z - \hat{z})\nabla)L(\hat{z}\nabla)\hat{\mathbf{u}}^*. \quad (2.36)$$

Note that here the Γ_u, Γ_w terms have been dropped. This is consistent with the analysis of Madsen *et al.* (2002, 2003) who found that these terms have only a local effect on the velocity profile, and do not significantly affect linear shoaling properties¹.

With the objective of maximizing the formal accuracy of (2.35) and (2.36) applied at $z = 0$ for the number of terms included relative to the Taylor series expansions given in (2.32) and (2.33), Madsen *et al.* (2002, 2003) demonstrate that it is indeed possible to achieve a much higher order of accuracy without increasing the order of the derivatives if the L -operator is chosen to introduce Padé approximants in the truncated equations. This was achieved with

$$L(\lambda\nabla) = 1 + \frac{(\lambda\nabla)^2}{18} + \frac{(\lambda\nabla)^4}{504} + \frac{(\lambda\nabla)^6}{15,120} + \frac{(\lambda\nabla)^8}{362,880}, \quad (2.37)$$

¹It turns out, however, that these terms are important *e.g.* in cases involving partial reflection from bathymetric changes (see Madsen, Fuhrman & Wang, 2005). We will return to this issue in Chapter 10.

and consequently we obtain

$$\cos(\lambda\nabla)L(\lambda\nabla) = 1 - \frac{4}{9}(\lambda\nabla)^2 + \frac{1}{63}(\lambda\nabla)^4 + O(\lambda^{10}\nabla^{10}), \quad (2.38)$$

$$\sin(\lambda\nabla)L(\lambda\nabla) = \lambda\nabla - \frac{1}{9}(\lambda\nabla)^3 + \frac{1}{945}(\lambda\nabla)^5 + O(\lambda^{11}\nabla^{11}). \quad (2.39)$$

Note that now the accuracy has become twice the order of the terms included, which is a typical property of Padé approximants, and with this procedure the formal accuracy of (2.35) and (2.36) applied at $z = 0$ has increased from $O(\lambda^5\nabla^5)$ to $O(\lambda^9\nabla^9)$. Unfortunately, this requires that the L -, \cos -, and \sin -operators have the same argument, which is only the case at $z = 0$. Hence, in general the velocity profiles given by (2.35) and (2.36) are still $O(\lambda^5\nabla^5)$. Nevertheless, the analysis of Madsen *et al.* (2002, 2003) demonstrates that in practice the profiles of (2.35) and (2.36) are much more accurate than those from (2.28) and (2.29), and in addition this improvement spills over to the embedded linear and nonlinear properties.

By inserting (2.32), (2.33), and (2.37) into (2.35) and (2.36) and ignoring spatial derivatives higher than fifth order we arrive at the following expressions for the velocity profile

$$\mathbf{u}(x, y, z, t) = (1 - \alpha_2\nabla^2 + \alpha_4\nabla^4)\hat{\mathbf{u}}^* + (\psi\nabla - \beta_3\nabla^3 + \beta_5\nabla^5)\hat{w}^*, \quad (2.40)$$

$$w(x, y, z, t) = (1 - \alpha_2\nabla^2 + \alpha_4\nabla^4)\hat{w}^* - (\psi\nabla - \beta_3\nabla^3 + \beta_5\nabla^5)\hat{\mathbf{u}}^*, \quad (2.41)$$

where $\psi = (z - \hat{z})$ and

$$\begin{aligned} \alpha_2 &= \frac{\psi^2}{2} - \frac{\hat{z}^2}{18}, & \alpha_4 &= \frac{\psi^4}{24} - \frac{\hat{z}^2\psi^2}{36} + \frac{\hat{z}^4}{504}, \\ \beta_3 &= \frac{\psi^3}{6} - \frac{\hat{z}^2\psi}{18}, & \beta_5 &= \frac{\psi^5}{120} - \frac{\hat{z}^2\psi^3}{108} + \frac{\hat{z}^4\psi}{504}. \end{aligned} \quad (2.42)$$

These expressions are generally used throughout the present work. Note that this differs slightly from Madsen *et al.* (2002, 2003) who used (2.40) and (2.41) for $-h \leq z \leq 0$ combined with (2.23) and (2.24) from $0 < z \leq \eta$. Based on linear analysis, Madsen *et al.* (2003) found that optimal velocity distributions are obtained with $\hat{z} \approx -h/2$, and this value is also adopted throughout, unless otherwise noted.

2.6 The Kinematic Condition at the Sea Bed

The remaining condition which must be considered is the kinematic bottom condition (2.14). Substituting (2.40) and (2.41) applied at $z = -h$ into (2.14) and setting $\hat{z} = -h/2$ leads to

an expression of the form

$$\begin{aligned} & \left(1 - \frac{4}{9}\gamma^2\nabla^2 + \frac{1}{63}\gamma^4\nabla^4\right)\hat{w}^* + \left(\gamma\nabla - \frac{1}{9}\gamma^3\nabla^3 + \frac{1}{945}\gamma^5\nabla^5\right)\hat{\mathbf{u}}^* \\ & + \nabla h \cdot (1 - c_2\gamma^2\nabla^2 + c_4\gamma^4\nabla^4)\hat{\mathbf{u}}^* - \nabla h \cdot (\gamma\nabla - s_3\gamma^3\nabla^3 + s_5\gamma^5\nabla^5)\hat{w}^* = 0, \end{aligned} \quad (2.43)$$

where $\gamma = (h + \hat{z}) = h/2$. Here, the c_i and s_i slope coefficients have been left as free parameters, and used to optimize accuracy with respect to the exact linear shoaling gradient (see Madsen *et al.*, 2002, 2003). This leads to $c_2 = 0.357739$, $c_4 = 0.00663819$, $s_3 = 0.0753019$, and $s_5 = -6.31532 \times 10^{-5}$. These values have been shown to provide very accurate linear shoaling properties out to $kh \approx 30$.

2.7 Fourier Analysis of Linear Dispersion

A very thorough analysis of this system is presented in Madsen *et al.* (2003), and for brevity it is not repeated here. For completeness, however, the linear dispersive properties of the system will be examined, as this is perhaps the most fundamental property embedded in the system of equations.

The following Fourier analysis proceeds from (2.11), (2.13), (2.40), (2.41), and (2.43), which represents the fully nonlinear time stepping problem considered throughout this thesis. Linearization firstly gives $\tilde{\mathbf{U}} = \tilde{\mathbf{u}} = \mathbf{u}_0$ and $\tilde{w} = w_0$. Restricting the analysis to a single horizontal dimension and neglecting nonlinear terms, (2.11) and (2.13) simplify respectively to

$$u_{0t} + g\eta_x = 0, \quad \eta_t - w_0 = 0. \quad (2.44)$$

We look for solutions of the form

$$\eta(x, t) = Ae^{i\theta}, \quad \hat{u}^*(x, t) = Be^{i\theta}, \quad \hat{w}^*(x, t) = iCe^{i\theta}, \quad \theta = \omega t - kx, \quad (2.45)$$

where i is the imaginary unit, k is again the wavenumber, and ω is the angular frequency. These are firstly inserted into (2.44) as well as into the final velocity profiles (2.40) and (2.41). Evaluating (2.44) combined with (2.43) (setting $h_x = 0$) then yields a 3×3 system of equations in terms of the Fourier amplitudes A , B , and C . For non-trivial solutions we require that the determinant of this system is equal to zero. This yields the final dispersion relation

$$\frac{c^2}{gh} \equiv \frac{\omega^2}{ghk^2} = \frac{1}{kh} \left(\frac{sh(kh/2)ch(-kh/2) - ch(kh/2)sh(-kh/2)}{ch(kh/2)ch(-kh/2) - sh(kh/2)sh(-kh/2)} \right), \quad (2.46)$$

where

$$ch(\lambda) \equiv 1 + \frac{4}{9}\lambda^2 + \frac{1}{63}\lambda^4, \quad sh(\lambda) \equiv \lambda + \frac{1}{9}\lambda^3 + \frac{1}{945}\lambda^5. \quad (2.47)$$

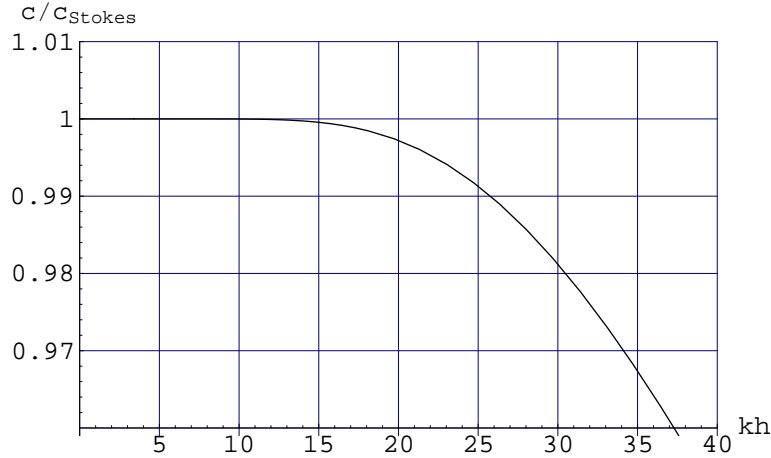


Figure 2.1: A plot showing the relative wave celerity compared with Stokes' target solution.

This can be compared with Stokes' target solution (*i.e.* the linear dispersion relation)

$$\frac{c_{Stokes}^2}{gh} = \frac{\omega^2}{ghk^2} = \frac{\tanh(kh)}{kh}. \quad (2.48)$$

A plot showing the relative embedded wave celerity with respect to the target solution can be found in Figure 2.1. Here it can be seen that this formulation contains excellent linear dispersive properties, as a 2% error is not exceeded until $kh > 30$.

It is again emphasized that Madsen *et al.* (2003) provide a complete analysis of this system (their Method III), including analysis of linear shoaling properties, accuracy of the velocity profile, and analysis of up to third-order (including amplitude dispersion) nonlinear properties. In each case the accuracy greatly exceeds that of all previous derivations, having accurate shoaling to $kh \approx 30$, accurate velocity profiles to $kh \approx 12$, and nonlinear properties to $kh \approx 25$. For complete details on the analysis the interested reader is again referred to the original derivation and analysis of Madsen *et al.* (2003) (see also Madsen *et al.*, 2002).

2.8 Conclusions

In this chapter the main details concerning the derivation of the Boussinesq formulation of Madsen *et al.* (2002, 2003) are reviewed, starting from the standard Laplace problem governing incompressible and irrotational free surface flow. The formulation combines exact representations of the dynamic and kinematic free surface conditions, as well as the kinematic bottom condition, with truncated (Boussinesq-type) solutions for the Laplace equation in the interior domain. The embedded linear dispersive properties of this system are analyzed on a flat bottom, demonstrating excellent agreement with Stokes' target solution out to dimensionless depths of $kh \approx 30$.

Chapter 3

The Numerical Model

Chapter Summary

This chapter describes a number of basic components comprising the numerical finite difference model, including details on the spatial and temporal discretizations. Other features of the numerical model are also introduced. These include a description of the boundary conditions imposed, the use of relaxation zones for generating and absorbing wave fields, and the use of smoothing filters for adding numerical dissipation. Some relevant details on the computer processors, programming language, and compilers used during this work are also provided.

3.1 Introduction

The construction of virtually any non-trivial numerical model requires the careful coordination of a variety of components. Of fundamental importance are of course the temporal and spatial discretizations, including boundary conditions. A number of additional elements must also typically be incorporated in a model suitable for practical simulations. The aim of this chapter is to provide a description of the most important features of the basic numerical finite difference model used to solve the system of high-order Boussinesq equations throughout this work.

This chapter is organized as follows. The basic finite difference discretizations are described in §3.2, with details on the corresponding boundary conditions provided in §3.3. The time stepping scheme used throughout this work is similarly presented in §3.4. The use of relaxation zones for both wave generation and absorption is explained in §3.5. Discussion on the application of smoothing filters used for introducing numerical dissipation (and their

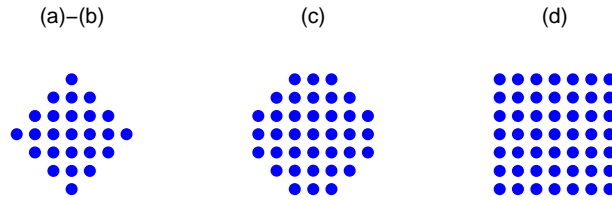


Figure 3.1: Stencils used for the various combinations of finite difference approximations. These stencils have (a)-(b) 25, (c) 37, and (d) 49 points.

corresponding Fourier analysis) is additionally provided in §3.6. Some details on the computer processors used throughout are given in §3.7, and on the programming language and compilers in §3.8. Conclusions are briefly re-stated in §3.9.

3.2 Finite Difference Approximations

To solve the system of PDEs numerically we replace each of the continuous derivatives (see Appendix A) with finite difference approximations. Note that due to the high-derivative nature of this system, the stencils required are inevitably rather large. A number of centered finite difference discretizations have been implemented. These are (a) second-order approximations for each partial derivative, (b) a 25-point (diamond) finite difference stencil, (c) a 37-point (octagon) stencil, and (d) a 49-point (square) stencil. Each of these stencils is shown in Figure 3.1. The actual finite difference approximations are all provided in Appendix B, along with the order of their respective truncation errors. With the exception of stencil (a), all finite difference approximations are allowed to have the maximum possible accuracy for the given stencil, which results in greater accuracy for the lower-order partial derivatives than for their higher-order counterparts. In particular, under finite difference stencil (b) cross-terms of a given order will tend to be less accurate than corresponding pure x - or y -derivatives. Alternatively, stencils (c) and (d) provide highly-accurate mixed derivative approximations. In fact the formal order of accuracy achieved by these two stencils is equivalent, despite the differences in their size. The coefficients for stencil (c) can be derived by considering the two-dimensional operator directly, whereas the coefficients in (d) can be derived via the superposition of the corresponding pure x - and y -derivatives. The minimum stencil that can be used to (centrally) discretize mixed fifth-order partial derivatives, arising from (2.40), (2.41), and (2.43), is the 25-point stencil, however the larger stencils do not significantly affect the overall structure (*i.e.* the bandwidth) of the resulting discrete operators. The relative merits of these various stencils will be investigated further in §6.2.

3.3 Boundary Conditions

In the numerical solution of any system of PDEs appropriate boundary conditions must be specified. In the present model combined Dirichlet and Neumann boundary conditions are used to create closed boundaries (*i.e.* fully reflecting walls) on a rectangular domain. Specifically, this corresponds to imposing $\eta_x = 0$, $u = 0$ (similarly for all even x -derivatives), $v_x = 0$ (similarly for all odd x -derivatives), and $w_x = 0$ (similarly for all odd x -derivatives) along x -boundaries; and $\eta_y = 0$, $u_y = 0$ (similarly for all odd y -derivatives), $v = 0$ (similarly for all even y -derivatives), and $w_y = 0$ (similarly for all odd y -derivatives) along y -boundaries. These conditions are imposed simply by reflecting the finite difference coefficients evenly for Neumann boundary conditions and oddly for Dirichlet boundary conditions. Note that this is equivalent to assuming that each variable is either symmetric or anti-symmetric about the wall. This strategy has the advantage of keeping the overall model structure very regular, as all equations are considered in some fashion at each individual grid point.

3.4 Time Integration

Throughout the present work the classical fourth-order, four-stage explicit Runge-Kutta method is used for time integration. Other explicit time-stepping methods have also been implemented, however this particular method has been found to give a good combination of accuracy and stability at reasonable computational costs. Considering a system of differential equations of the form

$$\mathbf{y}_t = F(\mathbf{y}), \quad (3.1)$$

where \mathbf{y} is a vector of time stepping variables with $F(\mathbf{y})$ representing a corresponding stage evaluation, this scheme is given by

$$\mathbf{k}_1 = \Delta t F(\mathbf{y}_n), \quad (3.2)$$

$$\mathbf{k}_2 = \Delta t F\left(\mathbf{y}_n + \frac{\mathbf{k}_1}{2}\right), \quad (3.3)$$

$$\mathbf{k}_3 = \Delta t F\left(\mathbf{y}_n + \frac{\mathbf{k}_2}{2}\right), \quad (3.4)$$

$$\mathbf{k}_4 = \Delta t F(\mathbf{y}_n + \mathbf{k}_3), \quad (3.5)$$

$$\mathbf{y}_{n+1} = \mathbf{y}_n + \frac{\mathbf{k}_1}{6} + \frac{\mathbf{k}_2}{3} + \frac{\mathbf{k}_3}{3} + \frac{\mathbf{k}_4}{6} + O(\Delta t^5). \quad (3.6)$$

Given the complexity of this system of PDEs implicit methods are not felt to be very attractive, and have not been attempted.

3.5 Relaxation Zones

In practical wave simulations a means of both generating and absorbing the resulting wave fields is required. A convenient method for both generating and absorbing waves within a numerical model is to use so-called *relaxation zones*. This involves simply ramping between discrete variables in space using the function

$$f^*(i) = c_r(i)f_1(i) + (1 - c_r(i))f_2(i), \quad (3.7)$$

where i is the grid point index, and $0 \leq c_r \leq 1$. Here we describe the method in terms of a general discrete function f , however in the numerical model relaxation zones are applied identically on each of the time stepping variables $\eta, \hat{\mathbf{U}}$. The variable f^* hence corresponds to the final values to be used in the numerical simulation after the relaxation zones are applied (this is done at each time step). For relaxing a function up and down we respectively use

$$c_r(i) = \alpha_r^{-r(i-1)}, \quad (3.8)$$

$$c_r(i) = \alpha_r^{-r(N_r-i)}, \quad (3.9)$$

for $i = 1, 2, \dots, N_r$, where N_r is the set number of grid points for the relaxation zone, and α_r and r are shape parameters. Typically, these functions are not extremely sensitive to the choice of α_r (values ranging from 6–9 are generally appropriate). The choice for the coefficient r is much more crucial, however. A proper choice for r depends on the number of grid points defining the relaxation zone, and for $N_r = 21, 51, 101$ we recommend $r = 0.6, 0.8, 0.9$, respectively. Experience has shown that zones covering a single wavelength are generally sufficient both for generation and absorption purposes. Note that with this method the first/last coefficients with (3.8)/(3.9) should be artificially set to zero.

A typical model setup with waves primarily traveling from left to right (in x) is illustrated in Figure 3.2, consisting of three relaxation zones: 1) a wavemaker region; 2) a region to absorb any backward reflected waves (*e.g.* from bathymetric changes); and 3) a sponge layer for absorbing the outgoing wave field. In region 1 (3.7) combined with (3.8) is applied to gradually ramp up the incident wave field, with f_1 typically corresponding to some analytical solution (*e.g.* a Stokes or stream function solution) and $f_2 = 0$. In region 2 this same combination is again applied, but with f_1 now corresponding to the actual numerical solution, and with f_2 being the same analytical function as used in region 1 (*i.e.* we gradually ramp from the analytical to the computed solution). In the sponge layer, region 3, (3.7) combined with (3.9) is applied, with f_1 being the computed solution and $f_2 = 0$. This basic setup is used throughout this work in all simulations involving progressive incident wave fields. In cases where there is not a wavefield reflected back to the wavemaker (typically the case on flat bottoms) it is not necessary to use region 2.

It is finally mentioned, that an example demonstrating the effectiveness of this approach for wave generation and absorption (using stream function incident waves reflected off a wall) in a single horizontal dimension can be found in Madsen *et al.* (2003) (see their Figures 10 and 11). See also Bingham & Agnon (2005).

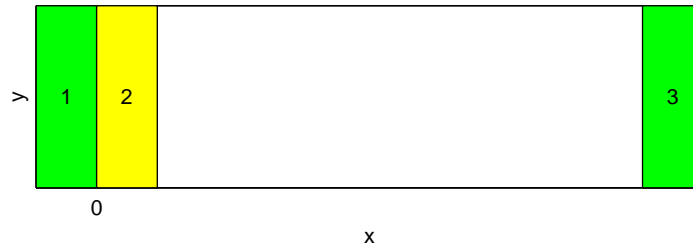


Figure 3.2: A sketch showing a typical setup of relaxation zones used in the numerical model. Region 1 is the wavemaker region, region 2 absorbs any backward reflected wave, and region 3 is the sponge layer.

3.6 Savitzky-Golay Smoothing Filters

An essential component of the numerical model for practical applications is some form of a *dissipative interface*. Such a means for introducing numerical dissipation is generally necessary to maintain numerical stability. On constant depths and regular domains the numerical model is indeed linearly stable (this is shown in Chapter 5). However it will be shown through the course of this work that mild levels of numerical dissipation become necessary in general applications involving nonlinearity, variable bathymetries, or irregular domains. Throughout most of this thesis we employ Savitzky & Golay (1964)-type smoothing filters (see also *e.g.* Press *et al.*, 1992) for this purpose, applied intermittently. These filters are particularly convenient as they can be easily derived to arbitrary polynomial order, with the high-order filters generally having lesser effects on well resolved modes. As implemented, the coefficients for a given two-dimensional filter stencil can be derived to arbitrary polynomial order within the numerical model. Unsurprisingly, it has been found that best results are achieved using relatively high-order filters, as these tend to minimize damage to modes of physical interest.

To more accurately quantify the effects of these filters, a number have been analyzed using standard Fourier techniques (a description of the analysis is provided in Appendix C). Each of these filters uses the minimum diamond shaped stencil possible for the given order, and prior to the analyses the filter coefficients have been summed by row (or equivalently by column, as they are symmetric), simplifying the analysis to a single dimension. The resulting amplification portraits for filters of order ranging from 2–10 are shown in Figure 3.3. As a reference value, discretizations typically use at least 20 grid points per primary wavelength, hence these filters will primarily only affect higher harmonics, which become important in nonlinear simulations. Experience has shown that the use of filters having order six or higher is sufficient for most applications, which is generally confirmed in Figure 3.3, where it is seen that the amplification factor for the higher-order filters rapidly approaches unity as the resolution is increased. The choice of filter, however, is inevitably somewhat case specific. The filter used for a given simulation will generally be mentioned throughout this work.

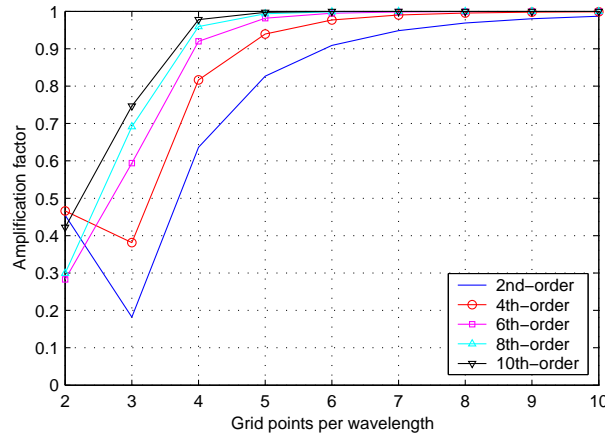


Figure 3.3: Amplification portrait for various Savitzky-Golay smoothing filters. The 2nd–10th-order filters originally arise from (diamond shaped) stencils with 13, 25, 41, 61, and 85 grid points, respectively.

3.7 Computer Processors

During this work two different computer processors have been used for all simulations. Firstly, a Dell Pentium 4 1.8 GHz processor with 1 GB DDR RAM has been used (this has been the author’s main workstation). Secondly, simulations have also been run on single nodes of the NIFLHEIM cluster supercomputer¹. Each node consists of a Pentium 4 2.26 GHz processor, also with 1 GB DDR RAM. Throughout this work (when it is deemed necessary) the processor used for a given simulation will be made clear.

3.8 Programming Language and Compilers

The numerical model is programmed using FORTRAN 90 (Metcalf & Reid, 1996), which remains popular with scientists and engineers. This choice is also convenient, as many of the more standard numerical software packages are also based in a FORTRAN language.

A somewhat surprisingly critical aspect in obtaining high performance, which is certainly worth mentioning, is that of the compiler. Originally an Absoft FORTRAN compiler was used. This was later changed to a freely available (for research purposes) Intel compiler. We refrain from making a detailed comparison. Speaking quite generally, however, (using similar levels of optimization), this resulted in a speed up by a factor of 2–3 in simulations! This is mentioned with the hope that others might also benefit from this experience.

¹The NIFLHEIM cluster supercomputer was installed on August 12, 2002 at Center for Atomic-scale Materials Physics (CAMP) at the Technical University of Denmark, with a grant from the Danish Center for Scientific Computing. The cluster consists of 480 PCs, and has a total peak performance of above 2.1 TeraFLOPS, making it one of the fastest computers in Europe at the time of installation.

3.9 Conclusions

This chapter describes a number of basic features making up the numerical model used throughout this thesis. This includes a description of various finite difference schemes implemented (and their corresponding boundary conditions), as well as of the time stepping scheme used throughout. A number of other important elements comprising the numerical model are also introduced. These include the use of relaxation zones for generating and absorbing wave fields, as well as the use of smoothing filters (and analysis of their effects) necessary for general stability purposes. Finally, some relevant details on the the processors used for simulations, as well as the programming language and compilers are presented.

Chapter 4

Preconditioned Iterative Solutions

Chapter Summary

This chapter investigates preconditioned iterative techniques involved in the finite difference solutions of the Boussinesq model in two horizontal dimensions. It is shown that the resultant system of equations requires that a sparse, unsymmetric, and often ill-conditioned matrix be solved at each stage evaluation within a simulation. Various preconditioning strategies are developed and investigated, including full factorizations of the linearized matrix, ILU factorizations, a matrix-free (Fourier space) method, and an approximate Schur complement approach. A detailed comparison of the methods is given for both rotational and irrotational formulations, and the strengths and limitations of each are discussed. Mesh-independent convergence is demonstrated with many of the preconditioners for solutions of the irrotational formulation, and solutions using the Fourier space and approximate Schur complement preconditioners are shown to require an overall computational effort that scales linearly with problem size (for large problems). Through combined physical and mathematical insight effective preconditioned iterative solutions are achieved for the full physical application range of the model.

4.1 Introduction

As is common in the solution of systems of PDEs, the dominant computational expense for numerical solutions of the high-order Boussinesq formulation involves solutions of sparse linear systems of the form

$$\mathbf{Ax} = \mathbf{b}. \tag{4.1}$$

Generally speaking there are two primary solution strategies for systems of this type. These are so-called *direct methods* (see *e.g.* Duff *et al.*, 1986), based on Gaussian elimination

techniques, and *iterative methods* (see *e.g.* Saad, 2003), where an initial guess is continually improved, eventually resulting in a suitable approximate solution. Both of these areas can truly be considered as fields in their own right (with some inevitable overlap), for which extensive literature is available. Direct methods for sparse matrices are attractive due to their inherent robustness. Unfortunately, their large storage demands and lack of scalability can make such solutions impossible when solving large problems, particularly in two and three dimensions. Alternatively, iterative methods generally have significantly lower storage demands, and at their best are both fast and scalable. However, they generally lack the robustness of direct methods, particularly when solving very difficult problems. Modern research is continually increasing the effectiveness of these iterative methods, however (see the recent review of Saad & van der Vorst, 2000), and they are becoming increasingly popular among scientists and engineers when solving large sparse matrix problems.

Of the various iterative strategies available today, Krylov subspace methods¹ are perhaps those most commonly used. This is due to their combined general effectiveness and relative ease of implementation (*e.g.* compared with more complicated multi-grid schemes). For non-trivial problems, however, these basic methods often provide prohibitively slow convergence. The key to efficient solution strategies therefore lies in *preconditioning* of the original system. The basic idea is to transform the original linear system (4.1) via an operation with a preconditioning matrix \mathbf{M} . For example, preconditioning from the left leads to

$$(\mathbf{M}^{-1}\mathbf{A})\mathbf{x} = \mathbf{M}^{-1}\mathbf{b}. \quad (4.2)$$

Hence the actual iterative procedure is applied conceptually using the matrix $\mathbf{M}^{-1}\mathbf{A}$, which is of course not explicitly formed (this would result in a dense matrix). This matrix should generally be well conditioned or have clustered eigenvalues, leading to enhanced convergence rates. Sparse matrix vector products of the form $\mathbf{z} = \mathbf{M}^{-1}\mathbf{A}\mathbf{v}$ inherent within the basic Krylov subspace methods are thus carried out by first forming $\mathbf{w} = \mathbf{A}\mathbf{v}$, followed by a solution of a system having the form

$$\mathbf{M}\mathbf{z} = \mathbf{w}. \quad (4.3)$$

Hence, a good preconditioner \mathbf{M} must satisfy the often-conflicting criteria of approximating \mathbf{A} well, while at the same time being somehow ‘easy’ to solve. This is a non-trivial task, as there is inevitably something about the matrix \mathbf{A} making it difficult to invert directly (otherwise it would not have been necessary to resort to iterative methods in the first place!). This paradox gives rise to the common phrase ‘the art of preconditioning’.

This chapter is primarily concerned with the development of efficient preconditioned iterative solutions for a rather difficult sparse matrix problem arising from the numerical solution of the previously introduced Boussinesq formulation. Here it will be shown that finite difference discretizations of the governing system of PDEs require a solution of a sparse and (usually) ill-conditioned linear system at each stage evaluation. The structure of the resulting matrix is such that direct methods for sparse matrices are uncompetitive in terms

¹Named after the Russian scientist Alexei Nikolaevich Krylov, 1863–1945.

of both time and storage demands. The development of effective preconditioning methods is therefore of paramount importance, and a number of strategies are developed. These include complete/incomplete factorizations of the linearized matrix, a matrix-free (Fourier space) method, and an approximate Schur complement approach. A detailed comparison of the methods is given for both rotational and irrotational formulations, and the strengths and limitations of each are discussed. Mesh-independent convergence is demonstrated with many of the preconditioners for solutions of the irrotational formulation, and solutions using the Fourier space and approximate Schur complement preconditioners are shown to require an overall computational effort that scales linearly with problem size (for large problems).

The outline of this chapter is as follows. The Boussinesq formulation is re-stated in both rotational and irrotational forms in §4.2. Relevant discussion on the sparse matrix software used with many of the developed methods is provided in §4.4, with the basic Krylov subspace method used given in §4.5. Various preconditioning strategies are described in §4.6, and a detailed comparison of these methods is given in §4.7. Conclusions are drawn in §4.8.

This chapter is published in a similar form in Fuhrman & Bingham (2003) (see also Fuhrman & Bingham, 2004).

4.2 Rotational and Irrotational Formulations

In this section the governing system of equations from the Boussinesq formulation is re-stated in a form more in-line with the actual numerical procedure used for their solution. From (2.11) and (2.13), the dynamic and kinematic free surface conditions are again

$$\tilde{\mathbf{U}}_t = -g\nabla\eta - \frac{1}{2}\nabla\left(\tilde{\mathbf{U}}\cdot\tilde{\mathbf{U}} - \tilde{w}^2(1 + \nabla\eta\cdot\nabla\eta)\right), \quad (4.4)$$

$$\eta_t = \tilde{w}(1 + \nabla\eta\cdot\nabla\eta) - \tilde{\mathbf{U}}\cdot\nabla\eta. \quad (4.5)$$

From these it can be seen that evolving η and $\tilde{\mathbf{U}}$ forward in time requires a means of computing the associated \tilde{w} , subject to the Laplace equation (2.3), which is inherently (approximately) satisfied by the velocity profiles (2.40) and (2.41), and the kinematic bottom condition (2.43). Combining (2.40) applied at $z = \eta$ with (2.43), while also invoking (2.12) gives a 3×3 system that can be solved for $\hat{\mathbf{u}}^*$, \hat{w}^* in terms of $\tilde{\mathbf{U}}$ and η . The resulting system of PDEs is given in matrix form as

$$\begin{bmatrix} \mathcal{A}_{11} - \eta_x \mathcal{B}_{11} & \mathcal{A}_2 - \eta_x \mathcal{B}_{12} & \mathcal{B}_{11} + \eta_x \mathcal{A}_1 \\ \mathcal{A}_2 - \eta_y \mathcal{B}_{11} & \mathcal{A}_{22} - \eta_y \mathcal{B}_{12} & \mathcal{B}_{12} + \eta_y \mathcal{A}_1 \\ \mathcal{A}_{01} + h_x \mathcal{C}_{11} + h_y \mathcal{C}_{21} & \mathcal{A}_{02} + h_x \mathcal{C}_{12} + h_y \mathcal{C}_{22} & \mathcal{B}_0 - h_x \mathcal{C}_{13} - h_y \mathcal{C}_{23} \end{bmatrix} \begin{bmatrix} \hat{u}^* \\ \hat{v}^* \\ \hat{w}^* \end{bmatrix} = \begin{bmatrix} \tilde{U} \\ \tilde{V} \\ 0 \end{bmatrix}. \quad (4.6)$$

Here the subscripts x and y denote partial differentiation. The system contains a number of operators, which are again given in their entirety in Appendix A. For now it is sufficient to

mention that each operator contains up to either fourth- or fifth-order mixed partial derivatives. This system of operators shall henceforth be referred to as \mathcal{A} , and upon discretization this system shall be referred to as $\mathbf{Ax} = \mathbf{b}$. Each evaluation of (4.4) and (4.5) will hence require a solution of this system. As stated previously, this chapter concentrates on iterative methods for solving discrete linear systems of this form. It is also worthwhile to note that under the assumption of potential (irrotational) flow such that

$$\frac{\partial u}{\partial y} - \frac{\partial v}{\partial x} = 0, \quad (4.7)$$

the system simplifies slightly to

$$\mathcal{A} = \begin{bmatrix} \mathcal{A}_1 - \eta_x \mathcal{B}_{11} & -\eta_x \mathcal{B}_{12} & \mathcal{B}_{11} + \eta_x \mathcal{A}_1 \\ -\eta_y \mathcal{B}_{11} & \mathcal{A}_1 - \eta_y \mathcal{B}_{12} & \mathcal{B}_{12} + \eta_y \mathcal{A}_1 \\ \mathcal{A}_{01} + h_x \mathcal{C}_1 & \mathcal{A}_{02} + h_y \mathcal{C}_1 & \mathcal{B}_0 - h_x \mathcal{C}_{13} - h_y \mathcal{C}_{23} \end{bmatrix}. \quad (4.8)$$

Note that (4.7) is a single component of the vorticity vector, and that the other elements (involving z -derivatives) have already been eliminated via the expansion of the velocity potential in the z -direction. This system has certain useful mathematical properties which shall be made apparent. Water wave models are commonly formulated in terms of a velocity potential, thus it can be argued that not much is lost physically under this assumption. Solutions involving \mathbf{A} stemming from (4.6) and (4.8) will both be considered in this work.

Having solved for the utility variables $\hat{\mathbf{u}}^*, \hat{\mathbf{w}}^*$ from (4.6) or (4.8), $\tilde{\mathbf{w}}$ can be computed from (2.41) applied at $z = \eta$. In terms of the previously introduced operators, this may be equivalently written as

$$\tilde{\mathbf{w}} = \mathcal{A}_1 \hat{\mathbf{w}}^* - \mathcal{B}_{11} \hat{\mathbf{u}}^* - \mathcal{B}_{12} \hat{\mathbf{v}}^*, \quad (4.9)$$

which closes the problem.

Writing the governing equations in this form perhaps gives a more clear impression of what is required to time step the system of PDEs. The operator notation introduced here will be maintained throughout this thesis.

4.3 Matrix Properties

In this section we will briefly discuss some of the inherent properties of the resulting matrix \mathbf{A} , arising upon discretization of \mathcal{A} (using centered finite difference approximations). These properties are useful in that they provide insight into potential difficulties which might be expected to arise when attempting solutions of the linear system.

The matrix \mathbf{A} is unsymmetric, but has a symmetric block structure. The matrix can have a variable sparsity pattern depending on the natural ordering of the equations (*i.e.* whether the

equations are grouped strictly by PDE or by grid point). Both scenarios are shown in Figure 4.1. It is seen that grouping the equations by PDE, as in Figure 4.1 (a), leads to a natural block structure as seen *e.g.* in (4.6). It is often useful to consider such a structure when implementing a preconditioner so that the natural operator structure is maintained. It is likewise seen that grouping the discretized equations by grid point results in a much smaller bandwidth as in Figure 4.1 (b). This ordering results in larger, more concentrated blocks, which allows for a more efficient implementation of sparse matrix-vector multiplication within various iterative solution strategies. Regardless of the ordering used, the matrix is generally far from diagonally dominant. The matrix is also somewhat unusual in that, while certainly sparse, it contains a substantial number of nonzeros per row. For example, a 37-point finite difference stencil results in up to $37 \cdot 3 = 111$ nonzeros per row.

The properties of the matrix also vary widely depending on the physical situation, with the most important parameter being the dimensionless number $k_N h$, where

$$k_N = \sqrt{\left(\frac{\pi}{\Delta x}\right)^2 + \left(\frac{\pi}{\Delta y}\right)^2}, \quad (4.10)$$

is the modulus of the two-dimensional Nyquist wavenumber vector. This dimensionless number governs the numerical significance of the Boussinesq terms². Note that under a constant discretization (in terms of grid points per wavelength) this is directly proportional to the dimensionless measure of water depth kh (this measure is used throughout this chapter to provide more physical relevance). To illustrate this dependence the spectrum of eigenvalues, λ , for two matrices having different depths (but with identical free surfaces) are shown in Figure 4.2. Both matrices are generated from the discretization of (4.6) on a 21×21 grid, with the free surface given by

$$\eta(x, y) = \frac{H}{2} \cos k_x x \cos k_y y, \quad (4.11)$$

with waveheight $H = 0.05$ m, wavenumbers $k_x = k_y = 2\pi \text{ m}^{-1}$, and $\Delta x = \Delta y = 0.05$ m. The shallow-water matrix, Figure 4.2 (a), uses $h = 0.07071$ m (*i.e.* $kh = \pi/5$, $H/h = 0.7071$), while the deep-water matrix, Figure 4.2 (b), uses $h = 0.7071$ m (*i.e.* $kh = 2\pi$, $H/L = 0.05$). Note that here $k = \sqrt{k_x^2 + k_y^2}$ and $L = L_x \equiv 2\pi/k_x = L_y \equiv 2\pi/k_y$ are used. Both matrices have a minimum eigenvalue near unity. The eigenvalues of the shallow-water matrix are reasonably well clustered, which gives evidence that preconditioning is perhaps not so crucial in these situations. The spectrum of the deep-water matrix is dramatically different, having a much larger spread of eigenvalues throughout the right half of the complex plane. Preconditioning deep-water problems therefore can be expected to be much more critical. These conclusions are further reflected in the respective condition numbers of the two matrices, which are 11.5 and 5.47×10^3 for the shallow- and deep-water matrices, respectively. The matrices become even more ill-conditioned as the depth is further increased (or the grid refined), but these matrices illustrate the general nature of this particular linear system. In practice condition numbers as high as 10^8 have been encountered.

²The dimensionless ratio of the depth and spatial discretization, $h/\Delta x$, has been previously deemed the ‘Abbott number’; see *e.g.* Abbott (1979); Abbott & Basco (1989); Abbott *et al.* (1984); Abbott & Minns (1998).

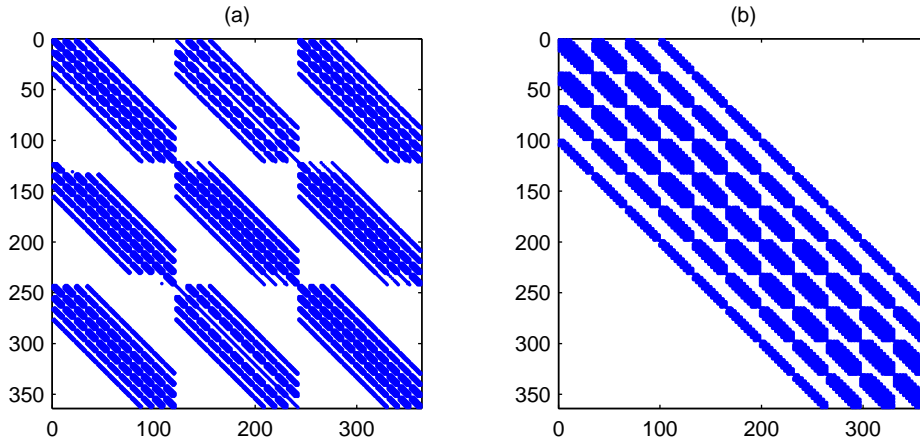


Figure 4.1: Sparsity patterns of \mathbf{A} using a 37-point finite difference stencil on an 11×11 grid when grouping the discrete equations (a) by PDE and (b) by grid point.

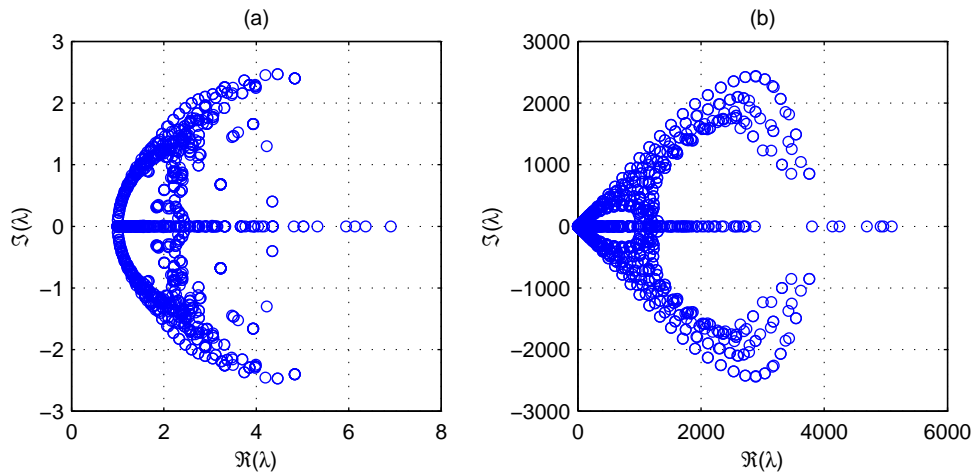


Figure 4.2: Eigenvalues of (a) a shallow-water matrix with $kh = \pi/5$ and (b) a deep-water matrix with $kh = 2\pi$.

4.4 Direct Matrix Factorizations

Due to the structure of \mathbf{A} (with a bandwidth that continually increases with problem size) direct matrix factorizations have been found to be uncompetitive as a general solution procedure. However, many of the strategies developed herein use direct methods within a greater iterative solution strategy. For all direct matrix factorizations and corresponding solutions the MA41 package from the well-known Harwell Subroutine Library (HSL) is employed. The factorization method used is a potentially parallel sparse multi-frontal variant of Gaussian elimination, which is particularly effective on matrices whose sparsity pattern is symmetric, or nearly so. The method chooses pivots from the diagonal using the approximate minimum degree algorithm of Amestoy *et al.* (1996). When solving systems with a single right hand side (RHS) the routine also makes efficient use of level 2 Basic Linear Algebra Subprograms

(BLAS), which have been optimized using the Automatically Tuned Linear Algebra Software (ATLAS, see *e.g.* Whaley *et al.*, 2000). For full details on the factorization method see Duff (1986, 1989); Duff & Reid (1984). In the present work only the serial version of the code is used (a parallel OpenMP version is also available), however, the potential for parallelism is duly noted here.

4.5 Krylov Subspace Method

Due to the large number of nonzeros per row in \mathbf{A} , the Krylov subspace method best suited to solving this linear system is arguably the Generalized Minimal RESidual (GMRES) algorithm of Saad & Schultz (1986). Indeed, as long as the number of iterations required are kept reasonable (through effective preconditioning), the additional storage required by GMRES is generally the same order of magnitude or less than the matrix itself. Furthermore, the number of iterations must become fairly large before an increase in the number of matrix-vector products can be warranted by restarting the iteration procedure. For these reasons unrestarted GMRES is used throughout this work.

4.6 Preconditioning Methods

This section introduces a number of preconditioning strategies that have proven to be effective in solving $\mathbf{A}\mathbf{x} = \mathbf{b}$. Throughout this chapter the preconditioning operation consists of solving systems of the form (4.3), where $\mathbf{z}^T = [\mathbf{z}_1, \mathbf{z}_2, \mathbf{z}_3]$ and $\mathbf{w}^T = [\mathbf{w}_1, \mathbf{w}_2, \mathbf{w}_3]$. All preconditioning in the present work is done from the left, as shown in (4.2). In limited testing preconditioning from the right has been found to be equally effective. For a recent review on preconditioning techniques for sparse matrices see Benzi (2002).

4.6.1 Factored linear preconditioner

A relatively straight-forward method for preconditioning \mathbf{A} is to simply neglect the nonlinear terms (with $\eta = 0$ in the remaining operators), which leaves for the rotational system

$$\mathbf{M} = \begin{bmatrix} \mathbf{A}_{11} & \mathbf{A}_2 & \mathbf{B}_{11} \\ \mathbf{A}_2 & \mathbf{A}_{22} & \mathbf{B}_{12} \\ \mathbf{A}_{01} + h_x \mathbf{C}_{11} + h_y \mathbf{C}_{21} & \mathbf{A}_{02} + h_x \mathbf{C}_{12} + h_y \mathbf{C}_{22} & \mathbf{B}_0 - h_x \mathbf{C}_{13} - h_y \mathbf{C}_{23} \end{bmatrix}, \quad (4.12)$$

and similarly for the irrotational system

$$\mathbf{M} = \begin{bmatrix} \mathbf{A}_1 & & \mathbf{B}_{11} \\ & \mathbf{A}_1 & \mathbf{B}_{12} \\ \mathbf{A}_{01} + h_x \mathbf{C}_1 & \mathbf{A}_{02} + h_y \mathbf{C}_{22} & \mathbf{B}_0 - h_x \mathbf{C}_{13} - h_y \mathbf{C}_{23} \end{bmatrix}. \quad (4.13)$$

The physical justification for neglecting the nonlinear terms is related to the fact that in deep water (where the matrix becomes ill-conditioned) the maximum wave steepness physically possible before breaking is $H/L \approx 0.141$ (Longuet-Higgins, 1975; Williams, 1985). This value gives a rough upper estimate for the relative significance of the nonlinear terms in deep water. More precisely, as h becomes large $(\eta - \hat{z}) \approx -\hat{z}$, and \mathbf{M} should quite closely resemble \mathbf{A} . Unfortunately, \mathbf{M} generally has the same structure as \mathbf{A} , and after factorization will have essentially the same storage demands as would a direct method. The advantage of this approach lies simply in the fact that \mathbf{M} is time-constant. The preconditioner can therefore be factored a single time at the beginning of a simulation, with the preconditioning operation consisting only of a solve step. This is quite significant, as a solve step for this system is much less expensive than a factorization step, typically by a factor 10-100 for the range of problem sizes considered in this work. To combat the sometimes excessive storage demands associated with this approach single precision (SP) factorizations of \mathbf{M} are also considered (still to precondition \mathbf{A} in double precision), thus reducing the storage by roughly a factor of two.

4.6.2 ILUT preconditioner

As a lower-storage alternative to the full factorizations described in §4.6.1, incomplete factorizations of \mathbf{M} in (4.12) or (4.13) will also be considered. For these purposes the well-known ILUT factorization of Saad (1994a) is used. This software uses a dual-threshold dropping strategy, and is freely available as part of the SPARSKIT package (Saad, 1994b). In earlier testing (incremental) incomplete factorizations of \mathbf{A} have also been considered. However, the use of incomplete factorizations of the time-constant linear matrix has proven to be a much more efficient alternative. Throughout this work a drop-tolerance of 0.005 is used, combined with a maximum fill-in of 200 elements per row (in the factors), which have been found to be good general parameters for this problem class.

4.6.3 Fourier space preconditioner

The linearized version of \mathbf{A} , as discussed in §4.6.1, should provide an effective preconditioner for this system. Unfortunately the high storage requirements for such complete factorizations can be quite limiting. In search of a more efficient means of applying this idea, we also consider an equivalent operation in Fourier space. In the linear sense (*i.e.* neglecting nonlinear terms), \mathcal{A} relates the pseudo-velocities at \hat{z} to the horizontal velocities at $z = 0$. According to Stokes' first-order theory for constant h , the relationship between $\hat{\mathbf{u}}$ and \mathbf{u}_0 is given as

$$\hat{\mathbf{u}} = \frac{\cosh(k(h + \hat{z}))}{\cosh kh} \mathbf{u}_0 = [\cosh(-k\hat{z}) + \sinh(-k\hat{z}) \tanh(k(h + \hat{z}))]^{-1} \mathbf{u}_0. \quad (4.14)$$

To gain an expression consistent with the embedded properties of the Boussinesq formulation, the infinite operators must first be replaced by Taylor series expansions. Further Padé-enhancement of the resultant expansions corresponds to transforming from $\hat{\mathbf{u}}$ to the utility velocities $\hat{\mathbf{u}}^*$. This procedure ultimately leads to the following replacement operations

$$\cosh(-k\hat{z}) \Rightarrow 1 + k^2\alpha_2 + k^4\alpha_4, \quad (4.15)$$

$$\sinh(-k\hat{z}) \Rightarrow -k\hat{z} + k^3\beta_3 + k^5\beta_5, \quad (4.16)$$

$$\tanh(k(h + \hat{z})) \Rightarrow \frac{k\gamma + \frac{1}{9}k^3\gamma^3 + \frac{1}{945}k^5\gamma^5}{1 + \frac{4}{9}k^2\gamma^2 + \frac{1}{63}k^4\gamma^4}, \quad (4.17)$$

where setting $z = 0$ in (2.42) gives $\alpha_2 = 4\hat{z}^2/9$, $\alpha_4 = \hat{z}^4/63$, $\beta_3 = -\hat{z}^3/9$, and $\beta_5 = -\hat{z}^5/945$, with $\gamma = (h + \hat{z})$. Inserting (4.15)-(4.17) into (4.14) and setting $\hat{z} = -h/2$ gives the final relationship

$$\hat{\mathbf{u}}^* = \left[1 + \frac{k^2h^2}{9} + \frac{k^4h^4}{1008} + \frac{(15, 120kh + 420k^3h^3 + k^5h^5)^2}{907, 200(1008 + 112k^2h^2 + k^4h^4)} \right]^{-1} \mathbf{u}_0. \quad (4.18)$$

The corresponding preconditioning operation consists of firstly transforming the components of the preconditioning RHS \mathbf{w}_1 , \mathbf{w}_2 , and \mathbf{w}_3 into Fourier space (treating each as two-dimensional arrays). For this operation two-dimensional combinations of fast sine and cosine transforms are used as appropriate for Dirichlet and Neumann boundary conditions, respectively. The preconditioning is applied entirely in Fourier space, which uses $\Delta k_x = \frac{\pi}{\Delta x(N_x-1)}$ and $\Delta k_y = \frac{\pi}{\Delta y(N_y-1)}$, where N_x and N_y are the number of grid points in the x - and y -directions, respectively. The complete operation is given in Algorithm 1, which is seen to include the truncated relationship from (4.18). Note also that solutions for $z_3(i, j)$ are found simply through spectral differentiation *i.e.* replacing $\frac{\partial}{\partial x}$ and $\frac{\partial}{\partial y}$ with ik_x and ik_y , respectively in the flat-bottom operators \mathcal{A}_{01} , \mathcal{A}_{02} , and \mathcal{B}_0 . Once the loops are complete, the two-dimensional arrays corresponding to \mathbf{z}_1 , \mathbf{z}_2 , and \mathbf{z}_3 are inverse-transformed back to physical space, completing the preconditioning operation.

This preconditioner should essentially provide the same operation as the factored (irrotational) linear matrix with constant h in (4.13). It is entirely matrix-free, however, thus any additional storage requirements are negligible. This preconditioner requires a global value for h to be applied in Fourier space. The hope was that simply taking an average value over the domain would still be effective in preconditioning the system on a variable bottom. Unfortunately this simple strategy does not appear to work, and it is not immediately clear how to apply the idea on a variable depth. Therefore, throughout this thesis applications of this preconditioner will be limited to cases having constant depth. Because this method stems from potential theory it is also expected to be more effective in preconditioning the irrotational system than the rotational system.

Algorithm 1 Algorithm for the Fourier space preconditioning operation.

```

 $\mathbf{w}_1 = \mathcal{F}\{\mathbf{w}_1\}; \mathbf{w}_2 = \mathcal{F}\{\mathbf{w}_2\}; \mathbf{w}_3 = \mathcal{F}\{\mathbf{w}_3\}$ 
for  $j = 1$  to  $N_y$  do
   $k_y = (j - 1)\Delta k_y$ 
  for  $i = 1$  to  $N_x$  do
     $k_x = (i - 1)\Delta k_x; k = \sqrt{k_x^2 + k_y^2}$ 
     $\epsilon = \left(1 + \frac{k^2 h^2}{9} + \frac{k^2 h^2}{1008} + \frac{(15,120kh + 420k^3 h^3 + k^5 h^5)^2}{907,200(1008 + 112k^2 h^2 + k^4 h^4)}\right)^{-1}$ 
     $z_1(i, j) = \epsilon w_1(i, j); z_2(i, j) = \epsilon w_2(i, j)$ 
     $\check{\mathcal{A}}_{01} = \frac{k_x h}{30,240}(15, 120 + 420k^2 h^2 + k^4 h^4)$ 
     $\check{\mathcal{A}}_{02} = \frac{k_y h}{30,240}(15, 120 + 420k^2 h^2 + k^4 h^4)$ 
     $\check{\mathcal{B}}_0 = 1 + \frac{k^2 h^2}{9} + \frac{k^4 h^4}{1008}$ 
     $z_3(i, j) = \frac{1}{\check{\mathcal{B}}_0}(w_3(i, j) - \check{\mathcal{A}}_{01} z_1(i, j) - \check{\mathcal{A}}_{02} z_2(i, j))$ 
  end for
end for
 $\mathbf{z}_1 = \mathcal{F}^{-1}\{\mathbf{z}_1\}; \mathbf{z}_2 = \mathcal{F}^{-1}\{\mathbf{z}_2\}; \mathbf{z}_3 = \mathcal{F}^{-1}\{\mathbf{z}_3\}$ 

```

4.6.4 Approximate Schur complement preconditioner

The derivation of an approximate Schur complement³ preconditioner shall begin with the irrotational, flat-bottom system given by

$$\begin{bmatrix} \mathcal{A}_1 & & \mathcal{B}_{11} \\ & \mathcal{A}_1 & \mathcal{B}_{12} \\ \mathcal{A}_{01} & \mathcal{A}_{02} & \mathcal{B}_0 \end{bmatrix}.$$

The justification for neglecting the slope terms is that the formulation inherently includes a mild slope assumption (see again Madsen *et al.*, 2002, 2003). Thus, terms multiplied by h_x and h_y in (4.6) and (4.8) should be of secondary importance. There is nothing preventing the application of preconditioners based on this formulation on variable depth problems, however. Note that in this version, the upper-left 2×2 system is block diagonal, with the \mathcal{A}_1 operator on both diagonals. This rather unique structure will be taken advantage of in the following. The Schur complement with respect to this upper left 2×2 system is

$$\mathcal{S} = \mathcal{B}_0 - \mathcal{A}_{01}\mathcal{A}_1^{-1}\mathcal{B}_{11} - \mathcal{A}_{02}\mathcal{A}_1^{-1}\mathcal{B}_{12}. \quad (4.19)$$

It seems natural to first simplify \mathcal{S} through multiplication by \mathcal{A}_1 , which leaves

$$\mathcal{S}_0 = \mathcal{A}_1\mathcal{B}_0 - \mathcal{A}_{01}\mathcal{B}_{11} - \mathcal{A}_{02}\mathcal{B}_{12}. \quad (4.20)$$

This operation assumes commutivity for all the operators in \mathcal{S} , which is strictly true only when h is constant (*i.e.* on a flat bottom). However, experience has shown that it is still

³Named after the German mathematician Issai Schur, 1875–1941.

reasonable for preconditioning purposes on mildly sloping bathymetries. In full form \mathcal{S}_0 is the following 10th-order operator

$$\mathcal{S}_0 = 1 - \frac{17h^2\nabla^2}{36} + \frac{16h^4\nabla^4}{567} - \frac{h^6\nabla^6}{2240} + \frac{29h^8\nabla^8}{15,240,960} - \frac{h^{10}\nabla^{10}}{914,457,600}. \quad (4.21)$$

At first glance inverting the discrete sub-matrix \mathbf{S}_0 might seem an insurmountable task (here a sub-matrix refers to a matrix with order equal to the number of grid points N , *i.e.* $1/3$ that of \mathbf{A}); however it turns out, quite remarkably, that the operator can be factored into five second-order modified Helmholtz operators *i.e.*

$$\mathcal{S}_0 = \prod_{i=1}^5 (1 - a_i h^2 \nabla^2), \quad (4.22)$$

where $a_1 = 0.4052847276166189$, $a_2 = 0.04500344115884187$, $a_3 = 0.01558017599415051$, $a_4 = 0.005675885605119240$, and $a_5 = 0.0006779918474916520$. Such a factorization can be shown to exist by considering (4.21) as a polynomial in $h^2\nabla^2$, which can in-turn be shown to have all real roots. Similarly, \mathcal{A}_1 can be factored as

$$\mathcal{A}_1 = \left(1 - \frac{h^2\nabla^2}{4(14 - \sqrt{133})}\right) \left(1 - \frac{h^2\nabla^2}{4(14 + \sqrt{133})}\right). \quad (4.23)$$

Thus, the preconditioning operation can be simplified to the quite-manageable task of inverting nine second-order sub-matrices and three sub-matrix-vector multiplications! The preconditioner is given by

$$\mathbf{M} = \begin{bmatrix} \mathbf{A}_1 & & \\ & \mathbf{A}_1 & \\ \mathbf{A}_{01} & \mathbf{A}_{02} & \mathbf{S}_0\mathbf{A}_1^{-1} \end{bmatrix}, \quad (4.24)$$

where \mathbf{S}_0 and the two upper-left \mathbf{A}_1 sub-matrices correspond to discrete forms of (4.22) and (4.23), respectively. It should be stressed that the three \mathbf{A}_1 sub-matrices in (4.24) all have different boundary conditions corresponding to their respective column position. It is interesting to mention that the preconditioned (linear, irrotational, flat-bottom) system (maintaining operator form) becomes

$$\mathcal{M}^{-1}\mathcal{A} = \begin{bmatrix} 1 & 0 & \mathcal{A}_1^{-1}\mathcal{B}_{11} \\ 0 & 1 & \mathcal{A}_1^{-1}\mathcal{B}_{12} \\ 0 & 0 & 1 \end{bmatrix}. \quad (4.25)$$

Thus, even though \mathbf{M}^{-1} in no sense approximates \mathbf{A}^{-1} , it should still have a similar clustering effect on the eigenvalues of \mathbf{A} (the eigenvalues of an upper-triangular matrix are simply the diagonals). All sub-matrices in \mathbf{M} are again time-constant, and can be built and (if necessary) factored a single time at the beginning of a simulation. Second-order (five-point) finite difference approximations for all Laplacian operators are used in practice as MA41 is extremely effective in limiting fill-in in matrices having a single outer band. As a result,

this preconditioner should have very low storage demands, and as no truncations have been imposed, should not be limited by problem depth. It is again expected that this approach will be more effective in preconditioning the irrotational matrix than the full rotational matrix, however it shall be applied in either case.

Discussion on the use of Schur complement preconditioners on matrices with reasonably similar (2×2) block structures is given in Ipsen (2001); Murphy *et al.* (2000). For other applications see *e.g.* Loghin & Wathen (2002, 2003).

4.7 Comparison of Preconditioners

To compare the preconditioning strategies outlined in §4.6 nonlinear simulations using linear standing wave initial conditions (in two horizontal dimensions) given by (4.11) and $\tilde{\mathbf{U}}(x, y, 0) = 0$, shall be used, with $k_x = k_y = 2\pi \text{ m}^{-1}$ (*i.e.* $L = L_x = L_y = 1 \text{ m}$). This provides a simple means for varying the nonlinearity, water depth, and discretization. For ease of interpretation, all results will be reported in this section in terms of the dimensionless variables kh , and either H/h or H/L for shallow- and deep-water cases, respectively. As reference values, $kh \approx \pi$ is often taken as the practical deep-water limit, and (as noted previously in §4.6.1) the maximum deep-water wave steepness physically possible for a progressive wave train (before wave breaking) is $H/L \approx 0.141$. Similarly, at the shallow water limit breaking occurs at $H/h \approx 0.8$. All computations are performed on the 1.8 GHz processor with 1 GB RAM, using the Absoft FORTRAN compiler (recall that the CPU times reported here could likely be significantly reduced using the Intel compiler; see §3.8). All iterative solutions use a relative residual error tolerance $r = \|\mathbf{b} - \mathbf{Ax}\|_2 / \|\mathbf{b}\|_2$ of 10^{-6} . This tolerance is used throughout this thesis, unless otherwise noted. Within all simulations the previously found solution vector \mathbf{x} is used as the starting guess for each successive iterative solution.

4.7.1 Performance versus relative water depth

Figure 4.3 demonstrates how the relative water depth, kh , affects the performance of the various preconditioning strategies under a constant discretization. These simulations use a 33×33 grid, are for 101 time steps, with $H/L = 0.05 \text{ m}$, $\Delta x = \Delta y = 0.0625 \text{ m}$ (*i.e.* 16 grid points per wavelength), and $\Delta t = 0.03365 \text{ s}$. The domain covers two wavelengths in both horizontal directions. Table 4.1 also provides a summary of the simulations at both the shallow and deep extremes, giving the range of iterations required with each method. In quite shallow water it can be seen that preconditioning is perhaps not so critical, as even the results with no preconditioning are reasonable. This is consistent with the expectations from §4.3. As kh increases (even moderately), however, it is seen that some form of preconditioning becomes absolutely necessary. The ILUT preconditioner works quite well in shallow to intermediately deep water, however it rapidly loses effectiveness as the depth is

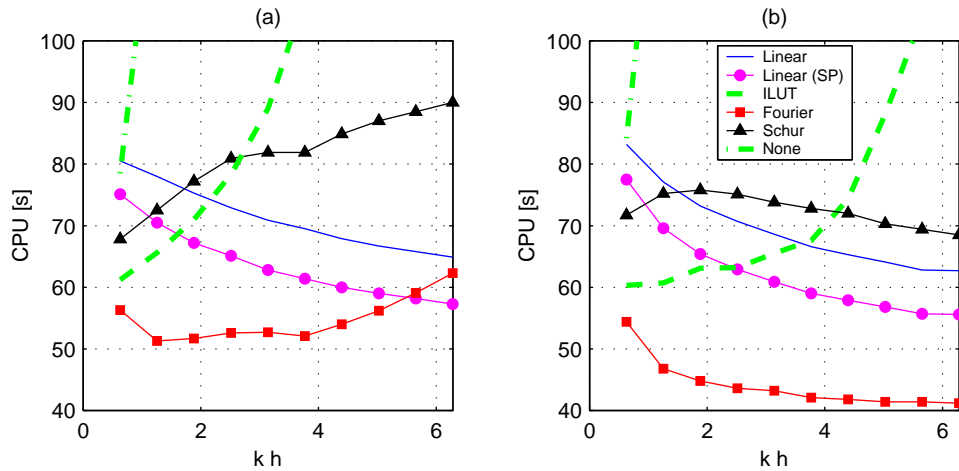


Figure 4.3: CPU times (101 time steps, $H/L = 0.05$) under variable depth for solving (a) the rotational system and (b) the irrotational system.

further increased. This trend is more exaggerated when solving rotational problems, but the method eventually fails in either case. A somewhat similar loss in effectiveness is seen with the Schur complement and (to some degree) with the Fourier space preconditioner for the rotational matrix. The observed increase in CPU time is much more controlled in these instances, however. Both provide noticeably more efficient solutions for irrotational simulations, which was expected from §4.6.3 and §4.6.4. Somewhat remarkably, many of the preconditioners actually become more effective as the depth is increased. This can again easily be explained physically by the fact that as h increases $(\eta - \hat{z}) \approx -\hat{z}$. Put another way, when the depth is large the variations of the water surface become relatively insignificant with respect to the entire water column. These results will inevitably change under different discretizations, nonlinearity, and problem size, however the trends seen here remain very consistent. Experience has shown that the results in Figure 4.3 are quite representative.

It is finally mentioned that in Table 4.1 simulation times for the same problem using direct solution methods for $\mathbf{Ax} = \mathbf{b}$ are also reported. Here it is clearly seen that such methods are uncompetitive with the best of the preconditioned iterative approaches, even for this rather small problem.

4.7.2 Performance versus nonlinearity

Figure 4.4 provides a similar comparison of CPU times for simulations where the deep-water nonlinearity (or wave steepness), H/L , is varied. These simulations are again on a 33×33 grid, for 101 time steps, with $kh = 2\pi$, $\Delta x = \Delta y = 0.0625$ m, and $\Delta t = 0.03365$ s. As Figure 4.3 has shown simulations with the ILUT preconditioner to be uncompetitive at this depth, this preconditioner is not considered in the remainder of this section. As Figure 4.4 demonstrates, all of the preconditioning methods gradually lose some effectiveness as the

Table 4.1: A summary of the simulations having the minimum and maximum kh values from Figure 4.3. All simulations are on a 33×33 grid, for 101 time steps, with $\Delta x = \Delta y = 0.0625$ m, and $\Delta t = 0.03365$ s. The description column corresponds to the entire list of simulations to the right.

Description	Preconditioner	Rotational		Irrotational	
		Iterations	CPU [s]	Iterations	CPU [s]
Shallow water: $kh = \pi/5$ $H/h = 0.7071$	Linear	3-12	80.5	3-13	83.2
	Linear (SP)	3-12	75.1	2-13	77.5
	ILUT	3-14	61.2	3-16	60.3
	Fourier	5-14	56.3	4-15	54.4
	Schur	4-13	67.8	5-15	71.7
	None	8-23	78.5	9-27	84.2
Deep water: $kh = 2\pi$ $H/L = 0.05$	Linear	2-9	64.9	2-9	62.7
	Linear (SP)	2-10	57.3	2-9	55.6
	ILUT	14-40	309	7-21	128
	Fourier	2-21	62.3	2-10	41.2
	Schur	3-20	90.0	4-14	68.5
	None	94-206	747	85-129	513
Direct method	—	—	269	—	268

nonlinearity is increased. This is expected, as the nonlinear terms have been neglected in the preconditioners. The growth is very acceptable, however, and the simulation time grows roughly linearly with the wave steepness. As can be seen, the preconditioners remain effective even when the nonlinearity is quite high (results up to $H/L = 0.12$ are shown). Consistent with previous observations, the Fourier space and Schur complement methods are more sensitive to increases in nonlinearity when solving the rotational system, as characterized by their steeper slopes.

4.7.3 Performance versus grid refinement

Figure 4.5 demonstrates how the preconditioning strategies perform when the mesh is refined under a constant depth and nonlinearity. These simulations use $kh = 2\pi$, $H/L = 0.08$, and a constant fraction $\Delta x/\Delta t = \Delta y/\Delta t = 1.857$ m/s. Each simulation uses a domain covering a single wavelength in each horizontal direction, and covers the equivalent of a linear period *i.e.* to $t = 0.6730$ s. The reported iterations are the average from each simulation. These tests are quite demanding, as refinements in the mesh make \mathbf{A} increasingly ill-conditioned. Solutions for the rotational system using the Schur complement and linear (SP) preconditioners can be seen to be rather sensitive to refinements in the mesh, as the number of required iterations increases significantly. The linear (SP) preconditioner is fairly robust with discretizations up to around 48 grid points per wavelength, however. The results for the irrotational system are most impressive, as the required number of iterations actually

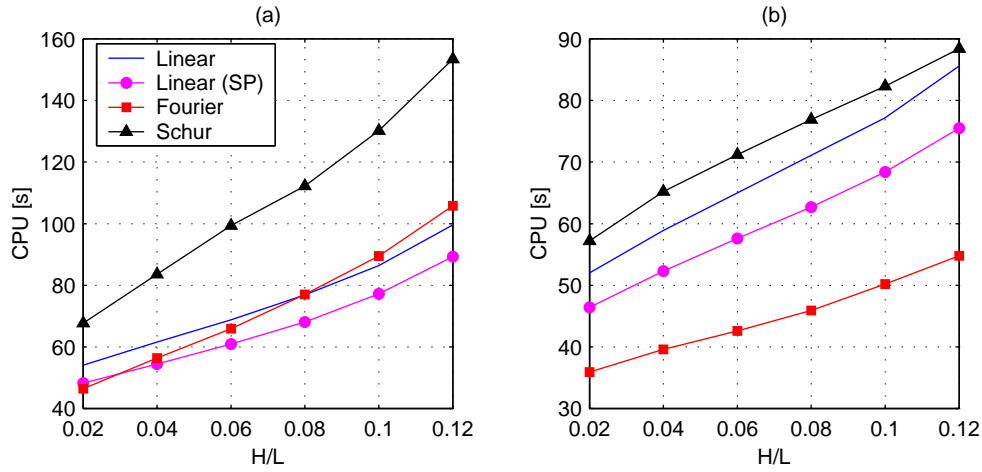


Figure 4.4: CPU times (101 time steps, $kh = 2\pi$) under variable deep-water nonlinearity when solving (a) the rotational system and (b) the irrotational system.

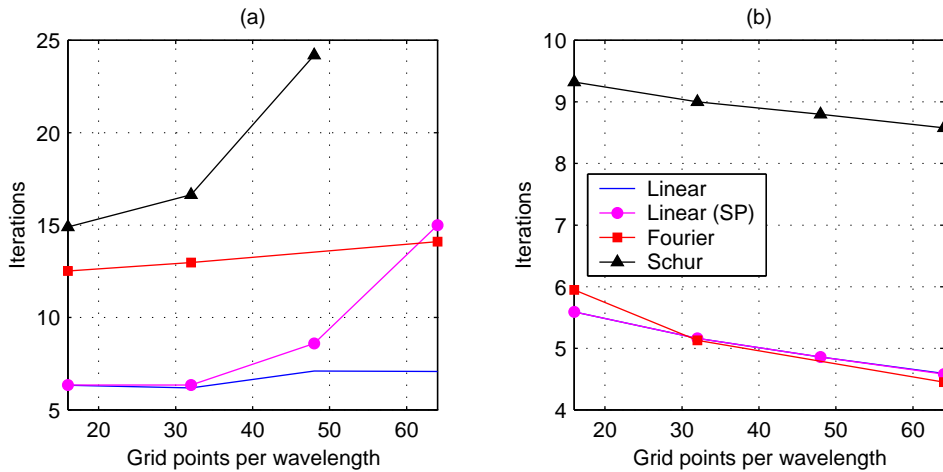


Figure 4.5: Average number of iterations required over a linear period ($kh = 2\pi$, $H/L = 0.08$) when solving (a) the rotational system and (b) the irrotational system. The domain in each simulation covers a single wavelength in each horizontal direction, and the time step is varied such that $\Delta x/\Delta t = \Delta y/\Delta t = 1.857$ m/s is constant. Note that the curves for both linear preconditioners in (b) are visually indistinguishable from one another.

decreases as the mesh is refined. This decrease is simply due to the use of smaller time steps as Δx and Δy are reduced, thus the starting guess for each iterative solution becomes better as the mesh is refined. The results with both linear preconditioners are virtually indistinguishable from one another in Figure 4.5 (b). Over this quite realistic discretization range the convergence using each of the preconditioners for solving the irrotational system appears to be mesh independent. The linear and (somewhat surprisingly) Fourier space preconditioners seem to be the most robust when solving the rotational system. In practice (see *e.g.* §6.2) solutions using as few as 15-20 grid points per wavelength have been found

Table 4.2: Length of real storage allocated for the various preconditioners compared with the matrix \mathbf{A} for a wide range of problem sizes.

Grid	N	\mathbf{A}	Linear	Fourier	Schur
17×17	289	8.1×10^4	4.0×10^5	8.7×10^2	1.1×10^5
33×33	1089	3.3×10^5	2.3×10^6	3.3×10^3	4.9×10^5
65×65	4225	1.3×10^6	1.5×10^7	1.3×10^4	2.3×10^6
129×129	16,641	5.4×10^6	8.4×10^7	5.0×10^4	1.1×10^7
257×129	33,153	1.1×10^7	1.8×10^8	9.9×10^4	2.4×10^7
257×257	66,049	2.2×10^7	4.3×10^8	2.0×10^5	5.3×10^7

to give sufficient accuracy, perhaps making such fine discretizations unnecessary with this model. Mesh independence is a very desirable property nonetheless, and is rarely achieved with conventional (ILU or approximate inverse) preconditioning techniques (Benzi, 2002). The use of complete factorizations within the greater iterative strategy seems to have made this achievement possible.

4.7.4 Storage comparison

As hinted in §4.6, the storage required by each of the preconditioners varies significantly. To illustrate this point, Table 4.2 shows the length of real storage that must be allocated for each preconditioner for a variety of problem sizes. Also shown for comparison is the length of the real array required to store \mathbf{A} . The linear preconditioners can be seen to have quite large storage demands, which are generally an order of magnitude more than for the matrix itself. The use of single precision factorizations has proven to be an effective method for reducing these demands, however even in this case the storage can be quite limiting. The Fourier and Schur complement methods, on the other hand, have much lower storage requirements. These results show that the additional storage required by the Fourier space preconditioner is essentially negligible, while that of the Schur complement preconditioner is roughly double that of \mathbf{A} (for large problems), which is still very reasonable.

4.7.5 Breakdown of computational expenses

Given the large differences in the storage demands (and therefore in the corresponding number of required floating point operations per iteration), it might seem surprising that the linear preconditioning methods are competitive at all with the Fourier and Schur complement approaches, as the required number of iterations do not differ nearly as significantly. The explanation is apparent upon a profiling of the simulations, a sample of which is given in Table 4.3. Here a breakdown of the computational expense of the major operations (in percentages) is provided for solutions with each preconditioner. The results shown are from

Table 4.3: Percentage CPU time spent in major operations during irrotational simulations (101 time steps, $kh = 2\pi$, $H/L = 0.05$) on a 129×129 grid using the various preconditioners. The numbers in parentheses correspond to the percentage of the preconditioning operation spent in level 2 BLAS. The total CPU time for each simulation is also provided.

Operation	Linear	Linear (SP)	Fourier	Schur
Mat.-vec. prod.	19.8	24.6	50.5	40.3
Build \mathbf{A}	12.3	15.1	28.4	15.3
Preconditioning	63.1 (89.0)	54.7 (88.7)	13.8	38.6 (25.1)
GMRES	1.2	1.8	3.7	2.9
Time int.	1.2	1.4	2.7	1.5
Misc.	2.4	2.4	0.9	1.4
Total CPU [s]	1587	1295	679	1268

irrotational simulations using 101 time steps on a 129×129 grid, with $kh = 2\pi$, $H/L = 0.05$, $\Delta x = \Delta y = 0.0625$ m, and $\Delta t = 0.03365$ s. It is seen that the preconditioning operation dominates the time spent in solutions using the linear preconditioners. Quite remarkably, nearly 90 percent of this operation is spent inside level 2 BLAS routines. Thus, with these preconditioning strategies a high flop rate more closely associated with direct methods is achieved. Alternatively, the Fourier space preconditioning method is seen to be dominated by the sparse matrix-vector product, which is an inherently slower operation. Solutions using the Schur complement preconditioner require roughly the same time for the preconditioning operation and the sparse matrix-vector product, with a much smaller portion of the preconditioning operation spent in level 2 BLAS. Also noteworthy is the fairly small portion spent inside GMRES (regardless of the preconditioner), which seemingly confirms the arguments from §4.5. We stress that the information in Table 4.3 is only meant to provide a comparison of the relative expense of the major operations for simulations using each preconditioner. To obtain the overall expense of each operation, the percentages can be multiplied by the total CPU time given at the bottom of the table.

4.7.6 Performance versus problem size

To gain insight into how solutions using the various preconditioning strategies scale with problem size, Figure 4.6 shows the results of simulations where the number of grid points, N , is continually increased. Note that the rank of \mathbf{A} is actually $3N$, as each grid point houses velocity variables in three directions. All simulations are for 101 time steps, with $kh = 2\pi$, $H/L = 0.10$, $\Delta x = \Delta y = 0.0625$ m, and $\Delta t = 0.03365$ s. Results solving both the rotational and irrotational systems are shown. Solutions with each preconditioner are carried out roughly to the maximum problem size possible on this machine (with 1 GB RAM). The average number of iterations required for each simulation is essentially identical to that presented in Figure 4.4 for this nonlinearity. The degree of nonlinearity does not

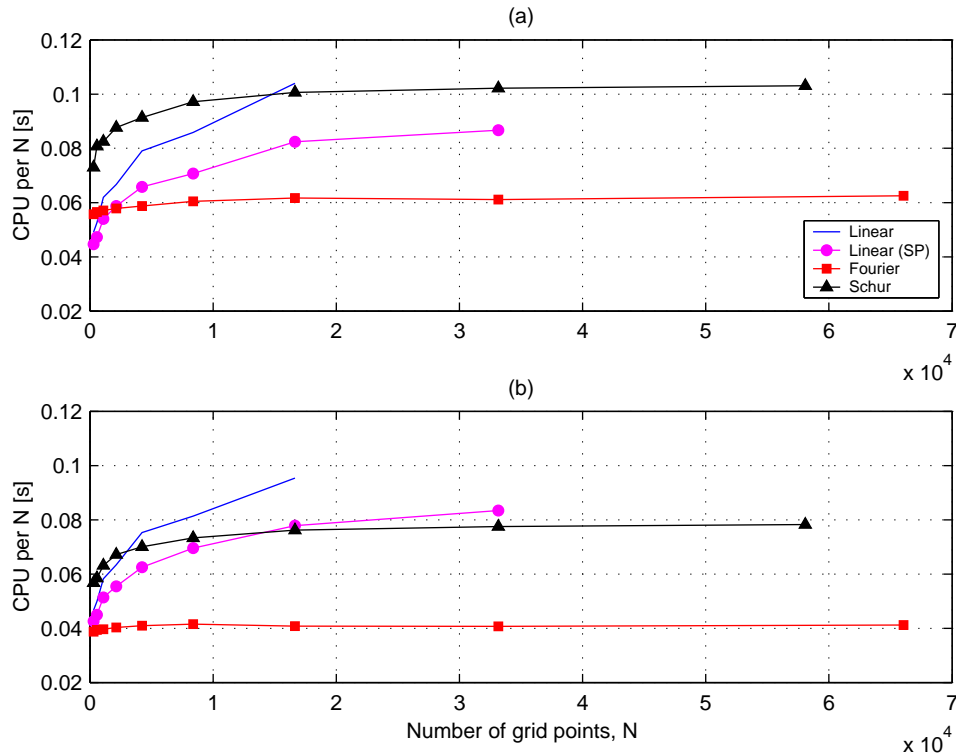


Figure 4.6: CPU time per grid point (101 time steps, $kh = 2\pi$, $H/L = 0.10$) for solving (a) the rotational system, and (b) the irrotational system.

affect the general shape of the curves – it does, however, affect the relative solution times of the various methods, as should also be expected from Figure 4.4. Perhaps the most impressive of the methods considered is the Fourier space preconditioner, which gives a constant solution time per grid point for virtually any size of problem. The relative expense of the other preconditioning methods gradually flattens as the problem size is increased, which is perhaps more typical. Also noteworthy is the performance of the Schur complement preconditioner (especially in the irrotational simulations), which levels off much faster than the linear preconditioners. Indeed, it is seen that although this method is slower for small problems, it becomes the fastest of the variable-depth preconditioners for large potential flow problems. As mentioned previously, the method is less effective in preconditioning the rotational matrix, but for large variable depth problems (moderately deep, where the non-linearity is not too large) it still seems to be a viable alternative. The linear preconditioners are equally effective in preconditioning both the rotational and irrotational systems, making them perhaps the most robust of the schemes devised.

4.7.7 Discussion

As demonstrated throughout this section, each of the preconditioning methods presented has its own respective strengths and weaknesses. It is when viewed as complementary that they

are seen to be very robust, as they efficiently cover the entire physical range of applicability of the Boussinesq model. Interestingly, many of the methods also serve as quite modern examples of the combined use of direct and iterative methods for sparse matrices, and as a result are robust in situations where more conventional ILU-based methods fail. In short, through combined physical and mathematical insight, the preconditioning methods successfully transform an extremely difficult problem to one ‘whose solution can be approximated rapidly’ (Trefethen & Bau, 1997), even in the most physically demanding situations. This is, of course, the very essence of preconditioning.

4.8 Conclusions

In this chapter it is shown that numerical solutions of the high-order Boussinesq formulation in two horizontal dimensions require that an ill-conditioned sparse matrix arising from the nonlinear system of PDEs be solved at each stage evaluation. Direct factorization methods are found to be uncompetitive in terms of both time and storage demands, making iterative solution strategies necessary. A number of different preconditioning strategies designed to greatly accelerate iterative solutions for this problem are subsequently developed. These include complete factorizations of the linearized matrix, ILU factorizations, a matrix-free (Fourier space) method, and an approximate Schur complement approach. The preconditioners are tested under a variety of physical situations (*i.e.* varying the depth, discretization, and nonlinearity), as well as on both rotational and irrotational formulations.

With the exception of the ILU-based method, all preconditioners are found to be very effective in solving deep-water problems, which are by far the most difficult. In particular it is shown that the factored linear preconditioners are perhaps the most robust of the methods devised, as they are equally effective in solving both the rotational and irrotational systems. Their high storage demands, however, can limit the problem size to some degree. Alternatively, the Fourier space preconditioner has essentially negligible storage demands, and consistently produces the fastest solutions (for irrotational simulations) when it is applicable. Unfortunately, it is seemingly limited to solving constant depth problems on regular domains. Finally, the approximate Schur complement method has low storage demands, and is particularly effective in solving large potential-flow problems. Mesh-independent convergence is demonstrated with many of the preconditioners for solutions of the irrotational formulation, and solutions using the Fourier space and approximate Schur complement preconditioners are shown to require an overall computational effort that scales linearly with the problem size (for large problems).

As is evident, each of the methods have their own respective strengths and weaknesses, and should therefore be viewed as complementary. In general, the methods are quite robust, and are effective for the full physical range of applicability of the model. The effectiveness of the preconditioners developed in this chapter will be further demonstrated in numerous test cases (involving both highly nonlinear waves and variable depths) throughout this thesis.

Chapter 5

Linear & Nonlinear Stability Analysis

Chapter Summary

This chapter considers a method of lines stability analysis for finite difference discretizations of the high-order Boussinesq method. The analysis demonstrates the near-equivalence of classical linear Fourier (von Neumann) techniques with matrix-based methods for formulations in both one and two horizontal dimensions. The matrix-based method is also extended to show the local de-stabilizing effects of the nonlinear terms, as well as the stabilizing effects of numerical dissipation. A comparison of the relative stability of rotational and irrotational formulations in two horizontal dimensions provides evidence that the irrotational formulation has significantly better stability properties when the deep-water nonlinearity is high, particularly on refined grids. Computation of matrix pseudospectra shows that the system is only moderately non-normal, suggesting that the eigenvalues are likely suitable for analysis purposes. Numerical experiments demonstrate excellent agreement with the linear analysis, and good qualitative agreement with the local nonlinear analysis. The various methods of analysis combine to provide significant insight into the numerical behavior of this rather complicated system of nonlinear PDEs.

5.1 Introduction

In this chapter, we undertake a *method of lines* stability analysis for finite difference discretizations of the high-order Boussinesq formulation. Such an analysis is extremely important in solving systems of PDEs, as it provides critical information *e.g.* for the maximum time step possible for a formally convergent scheme. The method of lines approach has been adopted, as it conveniently allows for combinations of multiple spatial and temporal discretizations to be analyzed simultaneously.

Herein, we consider the numerical stability of a number of finite difference discretizations of the high-order Boussinesq formulation, as introduced in §3.2. The methods used include a classical linear Fourier (von Neumann) analysis in a single horizontal dimension, as well as a matrix-based method in two horizontal dimensions (for both rotational and irrotational formulations), with all of the analyses providing similar results. While the rotational and irrotational systems exhibit similar linear properties, experience has shown that their nonlinear behavior can be quite different. We therefore extend the matrix-based method to include the temporally local effects of the nonlinear terms. As will be demonstrated, the addition of the nonlinear terms tends to de-stabilize the the resulting eigenvalue distributions, while numerical dissipation is demonstrated to have a stabilizing effect. A comparison of the two formulations provides clear evidence that the irrotational formulation has significantly better stability properties in highly-nonlinear, deep-water situations, consistent with observations. Computation of matrix pseudospectra also demonstrates that the system is only moderately non-normal (with increased eigenvalue sensitivity for the rotational formulation), giving confidence that the eigenvalues reasonably characterize the discrete systems. To confirm the results from the analysis, a series of numerical experiments are conducted using explicit fourth-order, four stage Runge-Kutta time integration. The results demonstrate excellent quantitative agreement with the linear analyses, and good qualitative agreement with the local nonlinear analysis. This work serves as an example of the combined use of many widely-applicable analysis techniques, with each providing significant insight into the numerical behavior of this complicated system.

The outline of this chapter is as follows. The method of lines approach for numerical stability is briefly described in §5.2, and stability regions for numerous popular time stepping schemes are provided in §5.3. In §5.4 a classical linear Fourier (von Neumann) stability analysis is undertaken in a single horizontal dimension for two separate sets of finite difference approximations. An alternative matrix-based linear stability analysis is used in §5.5 in two horizontal dimensions, which is further extended to include the temporally local effects of the nonlinear terms in §5.6. This section also demonstrates the effects of numerical dissipation on the system, and includes a comparison of rotational and irrotational formulations. Analysis of matrix pseudospectra is provided in §5.7. A series of numerical experiments with both the linear and nonlinear models is detailed in §5.8. Conclusions are drawn in §5.9.

This work is published in a similar form by Fuhrman *et al.* (2004a).

5.2 Stability of the Method of Lines

A method of lines approach allows for separate consideration of the time integration scheme and the spatial discretization. This has the advantage that stability criterion for any number of time stepping schemes can be obtained simultaneously. The justification is widely known and can be explained by considering a general system of linear differential equations having

the form

$$\frac{\partial \mathbf{y}}{\partial t} = \mathbf{J} \mathbf{y}, \quad (5.1)$$

where \mathbf{y} is a vector of time stepping variables, and \mathbf{J} is the linear Jacobian matrix. Substituting the spectral factorization $\mathbf{J} = \mathbf{V} \mathbf{\Lambda} \mathbf{V}^{-1}$ (where \mathbf{V} is a matrix whose columns contain the eigenvectors of \mathbf{J} , and $\mathbf{\Lambda}$ is a diagonal matrix of corresponding eigenvalues λ_i) into (5.1) leads directly to $\frac{\partial \mathbf{y}}{\partial t} = \mathbf{V} \mathbf{\Lambda} \mathbf{V}^{-1} \mathbf{y}$. Multiplying both sides by \mathbf{V}^{-1} and considering that \mathbf{V} is time independent gives $\frac{\partial}{\partial t}(\mathbf{V}^{-1} \mathbf{y}) = \mathbf{\Lambda}(\mathbf{V}^{-1} \mathbf{y})$. Finally, defining a new variable $\mathbf{v} = \mathbf{V}^{-1} \mathbf{y}$, the system becomes $\frac{\partial \mathbf{v}}{\partial t} = \mathbf{\Lambda} \mathbf{v}$ *i.e.* the original system (5.1) can identically be considered as a number of independent scalar linear ordinary differential equations of the form

$$\frac{\partial v_i}{\partial t} = \lambda_i v_i. \quad (5.2)$$

This diagonalized system can be interpreted as a representation of the original system (5.1) in the basis of eigenvectors of \mathbf{J} (Trefethen, 2000). As a result of this diagonalization the semi-discrete system can be analyzed for stability based on the eigenvalues of \mathbf{J} alone. When applied to systems of PDEs, the eigenvalue spectrum of the matrix \mathbf{J} thus fully characterizes the discrete spatial representation.

5.3 Linear Stability Regions

By considering a single scalar linear test equation of the form (5.2), it can likewise be shown (see *e.g.* Fornberg, 1998; Hirsch, 1988; Iserles, 1996; Trefethen, 1996, 2000) that for a given time stepping scheme a region of absolute stability can be constructed – often simply called its *stability region*. As a demonstration we will consider the explicit fourth-order, four-stage Runge-Kutta scheme outlined in §3.4. Applied to a single equation of the form (5.2) the algorithm can in fact be equivalently written as the following one-step method

$$v_{n+1} = \left[1 + \Delta t \lambda + \frac{(\Delta t \lambda)^2}{2} + \frac{(\Delta t \lambda)^3}{6} + \frac{(\Delta t \lambda)^4}{24} \right] v_n, \quad (5.3)$$

where n is the time level. Clearly, the quantity in the brackets defines the amplification of the variable v from one time step to the next, hence to prevent an exponential growth (*i.e.* an instability) we must require that

$$\left| 1 + \Delta t \lambda + \frac{(\Delta t \lambda)^2}{2} + \frac{(\Delta t \lambda)^3}{6} + \frac{(\Delta t \lambda)^4}{24} \right| \leq 1. \quad (5.4)$$

This defines the stability region (in terms of $\Delta t \lambda$) in the complex plane for this method. Relating back to the original system (5.1), it follows that as a necessary condition for stability, all eigenvalues of \mathbf{J} , when amplified by the time step Δt , must lie within the stability region of the respective time stepping scheme.

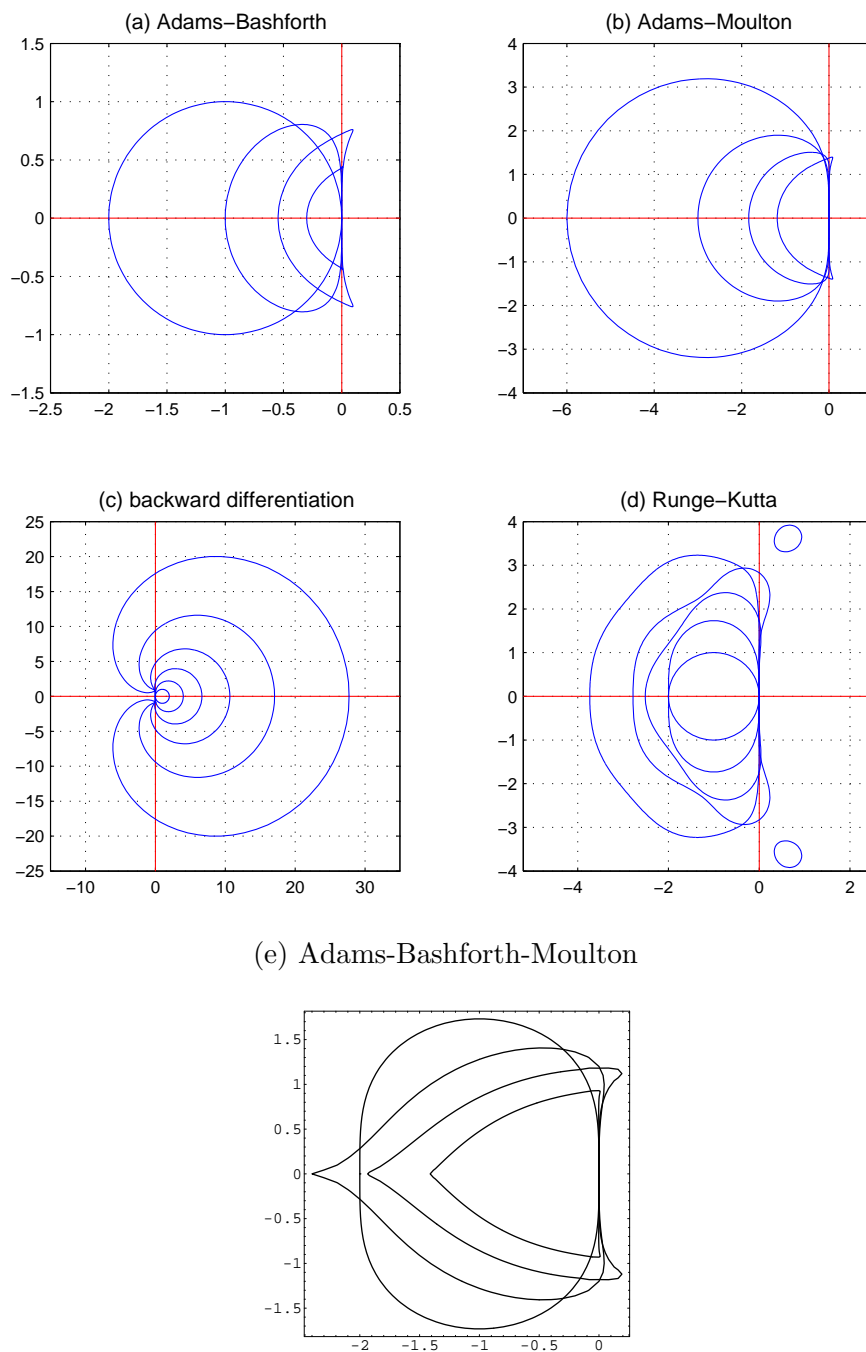


Figure 5.1: Stability regions for (a) explicit Adams-Bashforth schemes of order 1–4, (b) implicit Adams-Moulton schemes of order 3–6, (c) implicit backward differentiation formulae of order 1–6, (d) explicit Runge-Kutta methods of order 1–5 (the fifth-order method corresponds to the six-stage scheme of Cash & Karp, 1990), and (e) Adams-Bashforth-Moulton predictor corrector schemes of order 2–5. Figures (a)–(d) have been made using slightly modified MATLAB[®] code from Trefethen (2000).

Table 5.1: Real and imaginary limits for selected stability regions. The Runge-Kutta schemes are assumed to be explicit and to have a number of stages equal to the order. The Adams-Bashforth-Moulton schemes are assumed to use a predictor one order less than the corrector.

Time integration	Order	Imaginary limits	Real limit
Adams-Bashforth	3	± 0.7236	-0.5455
	4	± 0.4300	-0.3
Runge-Kutta	3	± 1.7321	-2.5128
	4	± 2.8284	-2.7853
Adams-Bashforth-Moulton	3	± 1.2	-2.4
	4	± 1.1785	-1.9346
	5	± 0.9363	-1.4115

Stability regions for numerous popular time stepping schemes (including the fourth-order Runge-Kutta method) are shown in Figure 5.1. As can be seen both implicit and explicit methods are considered. With the exception of Figure 5.1 (c) the stability regions are the interior of the plotted lines. Also, with the exception of Figure 5.1 (d) the regions generally become smaller with increasing order (with the explicit Runge-Kutta methods the regions become larger).

It is easy to show that a centrally discretized (linear) hyperbolic system will result in a Jacobian matrix having purely imaginary eigenvalues (this is demonstrated for our particular system in §5.4 and §5.5). By inspection of the various linear stability regions it can immediately be seen that such a scheme will only be conditionally stable under certain time stepping schemes *i.e.* those whose stability region contains some portion of the imaginary axis. By inspecting the stability regions in Figure 5.1 it can be seen that many of the implicit schemes considered have far worse stability criterion than many of the explicit methods for systems of this type! It should be stressed, however, that certain implicit schemes will in fact lead to unconditional linear stability *e.g.* the trapezoidal rule or backward Euler methods. Due to the complexity of this system of PDEs, however, implicit schemes are not felt to be very attractive. The real and imaginary limits for some explicit time stepping schemes felt to be best suited for this particular system are summarized in Table 5.1 (note that Fornberg, 1998, p. 209, also discusses methods suitable for systems having purely imaginary eigenvalues). The real limits become relevant with the introduction of numerical dissipation.

As was previously stated in Chapter 3, we will consider the classical explicit fourth-order, four stage Runge-Kutta time stepping scheme throughout this work, and the analysis in this chapter will concentrate on this particular method. We stress, however, that the analysis herein can easily be applied to any number of time integration methods (both explicit and implicit), simply by considering the eigenvalue spectra in the following sections with the stability region of interest.

5.4 Linear Fourier Analysis

The system of PDEs in the Boussinesq formulation will now be considered in its simplest form *i.e.* considering linear wave propagation in a single horizontal dimension on a flat bottom. The linearized kinematic and dynamic free surface conditions respectively read

$$\frac{\partial \eta}{\partial t} = w_0, \quad \frac{\partial u_0}{\partial t} = -g \frac{\partial \eta}{\partial x}. \quad (5.5)$$

Here u_0 and w_0 are velocities at the still water level $z = 0$ in the x - and z -directions, respectively. Similar to §4.2, w_0 is found via a solution of the implicit (flat-bottom) relationship

$$\begin{bmatrix} \mathcal{A}_1 & \mathcal{B}_{11} \\ \mathcal{A}_{01} & \mathcal{B}_0 \end{bmatrix} \begin{bmatrix} \hat{u}^* \\ \hat{w}^* \end{bmatrix} = \begin{bmatrix} u_0 \\ 0 \end{bmatrix}, \quad (5.6)$$

combined with the expression

$$w_0 = \mathcal{A}_1 \hat{w}^* - \mathcal{B}_{11} \hat{u}^*. \quad (5.7)$$

The operators in (5.6) and (5.7) are simply one-dimensional representations of those in Appendix A, and contain up to fifth-order partial derivatives in x . Note that in this linearized form, each operator arises from (2.40) and (2.41) applied at $z = 0$. It can be seen that \hat{u}^* and \hat{w}^* can be eliminated by inserting the solution of (5.6) directly into (5.7), which gives an expression for w_0 in terms of u_0

$$w_0 = \left(\frac{\mathcal{A}_1 \mathcal{A}_{01} + \mathcal{B}_0 \mathcal{B}_{11}}{\mathcal{A}_{01} \mathcal{B}_{11} - \mathcal{A}_1 \mathcal{B}_0} \right) u_0. \quad (5.8)$$

The Fourier (von Neumann) analysis begins by firstly considering each differential operator in discrete form, as stability is purely a property of the discretized equations. In this analysis we consider two centered spatial discretizations. These are the use of second-order finite-difference approximations for each derivative, as well as the use of high-order seven-point approximations for each derivative (order ranging from two to six). Through further substitution of individual Fourier components

$$\eta(j) \Rightarrow \check{\eta} e^{ij\theta}, \quad u_0(j) \Rightarrow \check{u}_0 e^{ij\theta}, \quad (5.9)$$

(where j is the grid point, and $\theta = 2\pi/N$, with N the number of grid points per wavelength) and by inserting (5.8) into w_0 in (5.5) the system can be transformed to a semi-discrete form

$$\frac{\partial}{\partial t} \begin{bmatrix} \check{\eta} \\ \check{u}_0 \end{bmatrix} = \begin{bmatrix} 0 & \mathcal{J}_{12} \\ \mathcal{J}_{21} & 0 \end{bmatrix} \begin{bmatrix} \check{\eta} \\ \check{u}_0 \end{bmatrix}. \quad (5.10)$$

Note that in this form the time stepping variables have changed from η and u_0 to their respective Fourier amplitudes $\check{\eta}$ and \check{u}_0 . It should also be mentioned that the insertion of

the Fourier components (5.9) involves the assumption of periodic boundary conditions. This is often interpreted simply as being applicable to the modeled regions which are sufficiently far from the boundaries such that their effects are minimal (Hirsch, 1988). After invoking the Eulerian identity

$$e^{i\theta} = \cos \theta + i \sin \theta, \quad (5.11)$$

it can be shown that $\mathcal{J}_{21} = -\frac{ig \sin \theta}{\Delta x}$ under discretization with second-order finite difference approximations and $\mathcal{J}_{21} = -\frac{ig}{\Delta x} \left(\frac{3 \sin \theta}{2} - \frac{3 \sin 2\theta}{10} + \frac{\sin 3\theta}{30} \right)$ under discretization with high-order (seven-point) finite difference approximations. These expressions are simply Fourier space representations of the discrete $-g \frac{\partial}{\partial x}$ operator. Under both discretizations the representation of \mathcal{J}_{12} is extremely long and will not be given here (it is in fact the Fourier space representation of the discretized factor for u_0 in (5.8)). Given the complexity of this term, the analysis is only practical with a symbolic manipulator (the current analysis has been performed using *Mathematica*TM). Note that (5.10) is precisely of the form (5.1), and thus it is the eigenvalues of this matrix which will govern the linear stability. In the current analysis only integer values for N are considered, which has been found to give reasonable results. As suggested earlier, the eigenvalues are indeed purely imaginary and the maximum computed values are given (non-dimensionalized) in Figure 5.2 for both discretizations for a wide range of $k_N h$, where $k_N = \pi/\Delta x$ is the Nyquist wavenumber. The eigenvalues have been non-dimensionalized using the celerity of the Nyquist mode c_N , which is computed using the embedded linear dispersion relation given in Madsen *et al.* (2002, 2003) as

$$c = \sqrt{\frac{g}{k} \left(\frac{sh(kh/2)ch(-kh/2) - ch(kh/2)sh(-kh/2)}{ch(kh/2)ch(-kh/2) - sh(kh/2)sh(-kh/2)} \right)}, \quad (5.12)$$

with

$$ch(\psi) = \left(1 + \frac{4}{9}\psi^2 + \frac{1}{63}\psi^4 \right), \quad sh(\psi) = \left(\psi + \frac{1}{9}\psi^3 + \frac{1}{945}\psi^5 \right). \quad (5.13)$$

Note that the y -axis of this figure could identically be replaced with λ_{max}/ω_N , where ω_N is the angular frequency of the Nyquist mode. This plot is given in terms of k_N (rather than *e.g.* just Δx), to allow for a more direct comparison with the matrix-based analysis (in two horizontal dimensions) in §5.5.

From the Fourier analysis it has been found that the maximum eigenvalue generally occurs with $\theta = \pi/2$ (*i.e.* a mode having four grid points per wavelength, or twice the Nyquist wavelength, thus $k_{critical} = k_N/2$). This has been found to be generally true under discretization with second-order finite difference approximations, and true for $k_N h < 100$ with high-order finite difference approximations. For $k_N h > 100$ under the high-order discretization the critical mode shifts to $\theta = 2\pi/3$ *i.e.* one having three grid points per wavelength. The highest frequency (Nyquist) mode actually results in a zero eigenvalue, and is thus *always* linearly stable under these discretizations (this can readily be seen *e.g.* by inserting $\theta = \pi$ into the

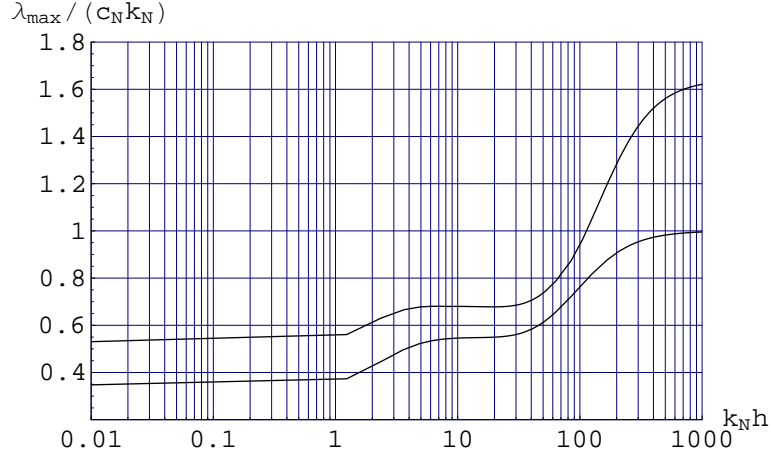


Figure 5.2: Non-dimensionalized maximum eigenvalues as a function of $k_N h$ from the Fourier analysis in a single horizontal dimension. The top and bottom lines correspond to using high-order (seven-point) and second-order finite difference approximations, respectively.

previously given expressions for \mathcal{J}_{21}). In general it is seen that the high-order spatial discretization results in larger eigenvalues, and will consequently have more restrictive stability properties. These differences are more dramatic in very shallow water, and become less pronounced (percentage-wise) as $k_N h$ increases, at least up to $k_N h \approx 100$. We stress that as shown in §6.2, this does not necessarily result in greater overall efficiency, as the use of the higher-order finite difference approximations can allow for significant reductions in the number of grid points required for a desired accuracy.

Upon closer examination of Figure 5.2 some distinct regions can be observed. With $k_N h < 1$ it is seen that the non-dimensionalized eigenvalue flattens, corresponding to the point where the most critical mode becomes non-dispersive. Within the range $1 < k_N h < 2\pi$ a transition region is apparent, as the critical mode gradually moves from shallow water to the practical deep-water limit. In the range $2\pi < k_N h < 40$ the curves again level, as the celerity of the critical mode becomes insensitive to changes in the depth. Finally, at $k_N h > 40$ the curves again begin to rise, corresponding roughly to the point where the linear dispersive properties of the critical mode begin to fail with respect to linear wave theory (c_N becomes significantly underestimated). Note that in most practical applications $k_N h > \pi$ *i.e.* at least the highest resolved frequency mode is beyond the practical deep-water limit. Practical applications in intermediate to very deep water are typically in the range $10 < k_N h < 500$.

The maximum time step Δt_{max} that can be taken due to stability constraints is found as follows: Given a spatial discretization, k_N can readily be computed, as can c_N from (5.12). With k_N and c_N known, the maximum eigenvalue λ_{max} can be obtained from Figure 5.2. The (hyperbolic) Courant number is then

$$r_h = \lambda_{max} \Delta t. \quad (5.14)$$

Thus, the maximum Courant number $r_{h,max}$ allowable for stability is simply the point where

the stability region of the time stepping scheme of interest crosses the imaginary axis. Hence, Δt_{max} can easily be computed from (5.14) *i.e.* $\Delta t_{max} = \frac{r_{h,max}}{\lambda_{max}}$. From this section linear stability criterion can be established for both finite difference discretizations considered in combination with any number of time stepping methods.

5.5 Linear Matrix-Based Analysis

5.5.1 Description

As an alternative to the Fourier techniques used in §5.4 an entirely numerical, matrix-based approach can be adopted – the actual Jacobian matrix \mathbf{J} can be constructed and its eigenvalues computed directly. This approach has the advantage of being very general *e.g.* any effects from boundary conditions are inherently included in the analysis. It is even fairly straight-forward to extend the analysis to include the effects of the nonlinear terms (at least locally), which is the ultimate motivation here. Note that for the remainder of this chapter combined Dirichlet and Neumann boundary conditions are used to create closed boundaries on a rectangular domain, as described in §3.3. Although the approach in this section is completely numerical, for convenience the differential operators are given in continuous form in much of what follows.

To begin the linearized flat-bottom system in two horizontal dimensions will be considered. The free surface conditions now consist of (5.5) combined with

$$\frac{\partial v_0}{\partial t} = -g \frac{\partial \eta}{\partial y}. \quad (5.15)$$

To form the Jacobian matrix \mathbf{J} it is necessary to express the linearized free surface equations explicitly in terms of the time stepping variables η , u_0 , and v_0 . With this system, however, w_0 is normally found via an implicit relationship *i.e.* a solution of the system $\mathbf{Ax} = \mathbf{b}$, where $\mathbf{x}^T = [\hat{u}^*, \hat{v}^*, \hat{w}^*]$ and $\mathbf{b}^T = [\mathbf{u}_0, \mathbf{v}_0, \mathbf{0}]$, combined with

$$w_0 = \mathcal{A}_1 \hat{w}^* - \mathcal{B}_{11} \hat{u}^* - \mathcal{B}_{12} \hat{v}^*, \quad (5.16)$$

which is simply the linearized form of (4.9). This can easily be converted into an explicit expression, however, simply by taking $\mathbf{Z} = \mathbf{A}^{-1}$, which leads obviously to $\mathbf{x} = \mathbf{Zb}$. Note that here \mathbf{Z} is a dense matrix. Considering \mathbf{Z} in block form, this operation can be written as

$$\begin{bmatrix} \hat{u}^* \\ \hat{v}^* \\ \hat{w}^* \end{bmatrix} = \begin{bmatrix} \mathcal{Z}_{11} & \mathcal{Z}_{12} & \mathcal{Z}_{13} \\ \mathcal{Z}_{21} & \mathcal{Z}_{22} & \mathcal{Z}_{23} \\ \mathcal{Z}_{31} & \mathcal{Z}_{32} & \mathcal{Z}_{33} \end{bmatrix} \begin{bmatrix} u_0 \\ v_0 \\ 0 \end{bmatrix}. \quad (5.17)$$

Inserting (5.17) into (5.16) gives the following explicit expression for the determination of w_0 from u_0 and v_0

$$w_0 = \mathcal{A}_1 \mathcal{Z}_{31} u_0 + \mathcal{A}_1 \mathcal{Z}_{32} v_0 - \mathcal{B}_{11} \mathcal{Z}_{11} u_0 - \mathcal{B}_{11} \mathcal{Z}_{12} v_0 - \mathcal{B}_{12} \mathcal{Z}_{21} u_0 - \mathcal{B}_{12} \mathcal{Z}_{22} v_0. \quad (5.18)$$

Thus, the linearized system can now indeed be written in a semi-discrete form as

$$\frac{\partial}{\partial t} \begin{bmatrix} \eta \\ u_0 \\ v_0 \end{bmatrix} = \begin{bmatrix} 0 & \frac{\partial}{\partial u_0} \left(\frac{\partial \eta}{\partial t} \right) & \frac{\partial}{\partial v_0} \left(\frac{\partial \eta}{\partial t} \right) \\ -g \frac{\partial}{\partial x} & 0 & 0 \\ -g \frac{\partial}{\partial y} & 0 & 0 \end{bmatrix} \begin{bmatrix} \eta \\ u_0 \\ v_0 \end{bmatrix}, \quad (5.19)$$

where substituting (5.18) into w_0 from (5.5) leads to

$$\frac{\partial}{\partial u_0} \left(\frac{\partial \eta}{\partial t} \right) = \mathcal{A}_1 \mathcal{Z}_{31} - \mathcal{B}_{11} \mathcal{Z}_{11} - \mathcal{B}_{12} \mathcal{Z}_{21}, \quad (5.20)$$

$$\frac{\partial}{\partial v_0} \left(\frac{\partial \eta}{\partial t} \right) = \mathcal{A}_1 \mathcal{Z}_{32} - \mathcal{B}_{11} \mathcal{Z}_{12} - \mathcal{B}_{12} \mathcal{Z}_{22}. \quad (5.21)$$

Note that the 3×3 system in (5.19) (when discretized) is the Jacobian matrix \mathbf{J} for this system, and in this linearized form is time constant.

5.5.2 Comparison of rotational & irrotational formulations

As shown in §4.2, this Boussinesq method can be written in either rotational or irrotational form in two horizontal dimensions, and both will be considered here. The analyses are quite similar, however, with the only difference being in the form of the matrix \mathbf{A} . Figure 5.3 plots computed maximum (non-dimensionalized) eigenvalues (computed using the MATLAB[®] `eig` function) for both the rotational and irrotational formulations under all four finite difference discretizations considered with the Boussinesq model in §3.2. These again include the use of all second-order finite difference approximations, as well as stencils containing 25, 37, and 49 points, where each approximation is allowed to have the maximum formal accuracy possible on each stencil. All computations use a $21 \times 21 \cdot 3 = 1323$, which has been found in practice to be sufficiently large for the purposes of this analysis. This grid provides three full stencil widths in both horizontal directions, and comparisons with systems arising from larger grids have been found to result in essentially the same spread of eigenvalues. In two horizontal dimensions k_N is the modulus of the Nyquist wavenumber vector $\mathbf{k}_N = \left(\frac{\pi}{\Delta x}, \frac{\pi}{\Delta y} \right)$, defined as

$$k_N = \sqrt{\left(\frac{\pi}{\Delta x} \right)^2 + \left(\frac{\pi}{\Delta y} \right)^2}. \quad (5.22)$$

Note that this two-dimensional modulus will tend to be larger than in a single dimension for a given spatial discretization (for example, with $\Delta x = \Delta y$ the two-dimensional k_N will always be larger than that from a single horizontal dimension with equivalent Δx by a factor $\sqrt{2}$). Again the high-order finite difference approximations are somewhat more restrictive (*i.e.* result in larger eigenvalues) than are second-order finite difference approximations. The differences between the other finite difference stencils, as well as in the two formulations are relatively minor, with slight differences becoming apparent at higher values of $k_N h$. The

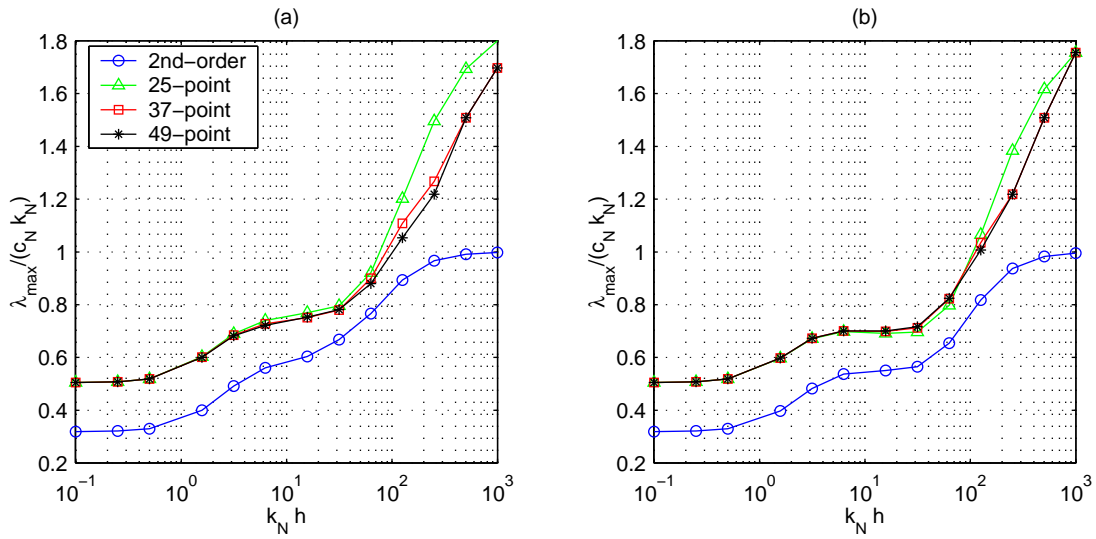


Figure 5.3: Non-dimensionalized maximum eigenvalues for the linear system (in two horizontal dimensions) as a function of $k_N h$ for (a) the rotational formulation and (b) the irrotational formulation.

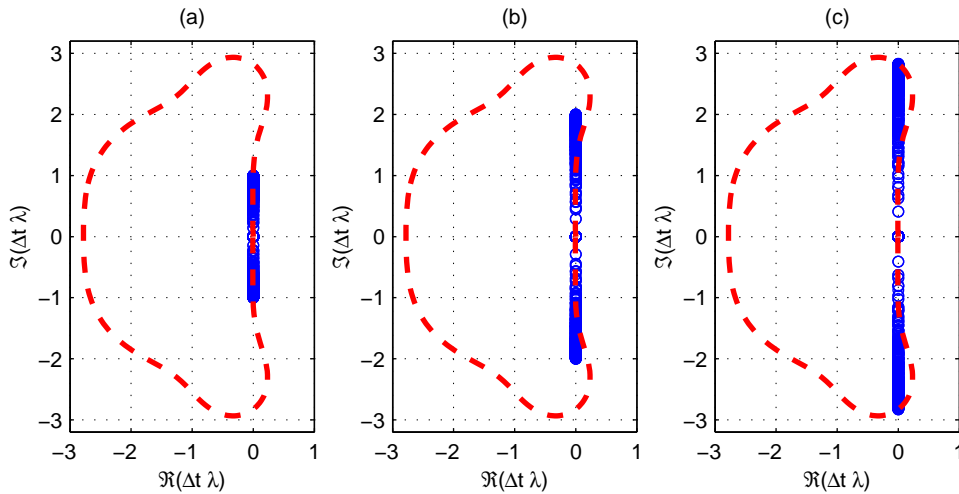


Figure 5.4: Eigenvalues of $\Delta t \mathbf{J}$ for the linear rotational formulation with $k_N h = 20\pi$ and (a) $r_h = 1$, (b) $r_h = 2$, and (c) $r_h = 2.8284$.

resulting figures (especially for the irrotational formulation) are remarkably similar to Figure 5.2, as the two-dimensionality and the closed boundary conditions seem to play a relatively minor role as far as the overall numerical stability is concerned. Values for the eigenvalues (and thus for the determination of r_h) will be taken directly from Figure 5.3 for the remainder of this chapter.

As examples from the linearized system Figure 5.4 shows the eigenvalue distributions for three different values of r_h arising from a rotational system using the 37-point finite difference

stencil with $k_N h = 20\pi$. From these plots it can once again be seen that the eigenvalues are indeed purely imaginary, as discussed previously in §5.4. For demonstration purposes, the stability region from the explicit fourth-order Runge-Kutta time stepping scheme is shown (likewise on all remaining figures), and the maximum (and minimum) eigenvalues can be seen to lie on the curve at the limiting $r_h = 2.8284$. This stability limit is also confirmed using the numerical model in §5.8.1.

5.6 Local Nonlinear Matrix-Based Analysis

While numerical experiments confirm the previous findings for the linearized system, experience with the nonlinear model has shown that in the absence of numerical dissipation, simulations are generally *unstable*. Thus the linear analyses, perhaps unsurprisingly, do not give a complete account of the nonlinear behavior. In other words, the linear constraints are no doubt *necessary*, but by no means are they *sufficient* for the general stability of nonlinear simulations. In an attempt to gain insight into this behavior, the matrix-based stability analysis from §5.5 is extended to include the nonlinear terms in this section.

We begin by re-writing the dynamic and kinematic free surface conditions from (2.11) and (2.13) in the scalar forms

$$\frac{\partial \tilde{U}}{\partial t} = -g \frac{\partial \eta}{\partial x} - \frac{1}{2} \frac{\partial}{\partial x} \left(\tilde{U}^2 + \tilde{V}^2 - \tilde{w}^2 \left(1 + \left(\frac{\partial \eta}{\partial x} \right)^2 + \left(\frac{\partial \eta}{\partial y} \right)^2 \right) \right) + D \nabla^2 \tilde{U}, \quad (5.23)$$

$$\frac{\partial \tilde{V}}{\partial t} = -g \frac{\partial \eta}{\partial y} - \frac{1}{2} \frac{\partial}{\partial y} \left(\tilde{U}^2 + \tilde{V}^2 - \tilde{w}^2 \left(1 + \left(\frac{\partial \eta}{\partial x} \right)^2 + \left(\frac{\partial \eta}{\partial y} \right)^2 \right) \right) + D \nabla^2 \tilde{V}, \quad (5.24)$$

$$\frac{\partial \eta}{\partial t} = \tilde{w} \left(1 + \left(\frac{\partial \eta}{\partial x} \right)^2 + \left(\frac{\partial \eta}{\partial y} \right)^2 \right) - \tilde{U} \frac{\partial \eta}{\partial x} - \tilde{V} \frac{\partial \eta}{\partial y} + D \nabla^2 \eta. \quad (5.25)$$

Note that diffusive terms with diffusion coefficient D have been added to each of the free surface equations (5.23)-(5.25). This serves as a convenient means of adding numerical dissipation to the system, the effect of which will be demonstrated in §5.6.3. These diffusive terms also necessitate an additional stability criterion based on the parabolic Courant number, defined here as

$$r_p = \delta D k_N^2 \Delta t. \quad (5.26)$$

This definition for r_p is convenient, as it corresponds precisely to the (negative) real spread of the linear eigenvalue spectrum. Calculations with the linearized system have shown that reasonable values for the coefficient δ are 0.4053 and 0.6124 when using second-order and higher-order finite difference approximations, respectively. Note that when $r_p = 0$ the system is free of any added dissipation.

For nonlinear analysis purposes it is common to investigate the eigenvalues of the Jacobian matrix using temporally local coefficients. Hence, we inherently assume that the local behavior of the system is modeled well by the variational equation $\frac{\partial \mathbf{y}}{\partial t} = \frac{\partial \mathbf{y}_n}{\partial t} + \mathbf{J}_n(\mathbf{y} - \mathbf{y}_n)$, where n is the local time level. The 3×3 Jacobian matrix \mathbf{J} is now generally defined as

$$\mathbf{J} = \begin{bmatrix} \frac{\partial}{\partial \eta} \left(\frac{\partial \eta}{\partial t} \right) & \frac{\partial}{\partial \tilde{U}} \left(\frac{\partial \eta}{\partial t} \right) & \frac{\partial}{\partial \tilde{V}} \left(\frac{\partial \eta}{\partial t} \right) \\ \frac{\partial}{\partial \eta} \left(\frac{\partial \tilde{U}}{\partial t} \right) & \frac{\partial}{\partial \tilde{U}} \left(\frac{\partial \tilde{U}}{\partial t} \right) & \frac{\partial}{\partial \tilde{V}} \left(\frac{\partial \tilde{U}}{\partial t} \right) \\ \frac{\partial}{\partial \eta} \left(\frac{\partial \tilde{V}}{\partial t} \right) & \frac{\partial}{\partial \tilde{U}} \left(\frac{\partial \tilde{V}}{\partial t} \right) & \frac{\partial}{\partial \tilde{V}} \left(\frac{\partial \tilde{V}}{\partial t} \right) \end{bmatrix}. \quad (5.27)$$

The determination of the individual components of this matrix is rather complicated, and is addressed in Appendix D. It should be stressed that such an extension of linear theory to a nonlinear setting is far from an exact practice, and due care should be taken in the interpretation of the results. Adding to the complication, it is impossible to examine every possible physical situation. Despite these drawbacks, it is often possible to demonstrate qualitative tendencies using such a local analysis, and this is the aim here.

All results in this section use linear standing wave initial conditions on a flat bottom with waveheight H and wavelength (in both x - and y -directions) $L = 1$ m. This gives a linear deep-water period $T = 0.6730$ s. Each simulation uses $\Delta x = \Delta y = L/20 = 0.05$ m, and $\Delta t = T/20 = 0.03365$ s, and the results shown are from the 22nd time step (frozen in time), which has been chosen arbitrarily to provide conditions roughly in mid-cycle. Computations are again on a 21×21 grid, and use the 37-point finite difference stencil. Results using the other stencils, as well as at other time levels have been found to be qualitatively similar. All results in this section will be given in terms of the dimensionless quantities kh (the relative depth of the primary wave), either H/h or H/L (the shallow- or deep-water nonlinearity, respectively), and $k_N h$ (the spatial discretization). As reference values, the practical deep water limit is again conventionally $kh = \pi$, and upper limits for the respective nonlinearities (before wave breaking) are $H/h \approx 0.8$ and $H/L \approx 0.14$ in shallow and deep water. Experience has shown that the rotational and irrotational formulations behave somewhat differently in cases having significant nonlinearity, particularly in deep water where the irrotational formulation has been found to be much more stable. Both systems will therefore be analyzed independently in what follows.

5.6.1 The presence of nonlinear instabilities

Figure 5.5 shows eigenvalue distributions from both the rotational and irrotational formulations under a variety of physical situations (*i.e.* varying depth and nonlinearity) with $r_h = 1.5$ and $r_p = 0$ (*i.e.* no added dissipation). Here it is clearly seen that the addition of the nonlinear terms has produced scattered eigenvalues protruding into the right half of the complex plane, indicating the presence of local exponentially growing modes. This suggests that under these discretizations the system may indeed be susceptible to nonlinear instabilities, which is in fact the case in practice. This analysis indicates that in both formulations

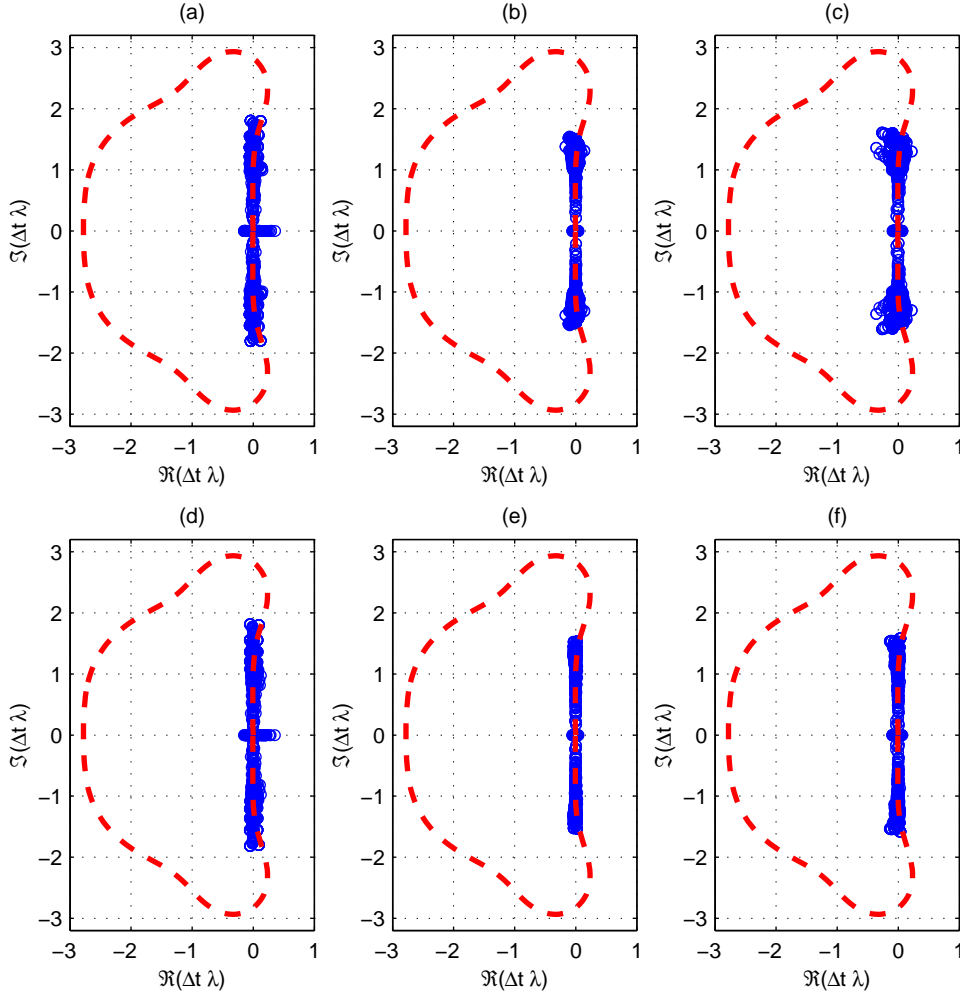


Figure 5.5: Eigenvalues of $\Delta t\mathbf{J}$ with $r_h = 1.5$ for the rotational (top) and irrotational (bottom) formulations with (a),(d) $kh = \pi/5$, $H/h = 0.7071$, $k_N h = 2\pi$; (b),(e) $kh = 2\pi$, $H/L = 0.05$, $k_N h = 20\pi$; and (c),(f) $kh = 2\pi$, $H/L = 0.10$, $k_N h = 20\pi$.

the strength of the instabilities increases with nonlinearity, with the rotational system exhibiting faster growth of the locally unstable modes (*i.e.* eigenvalues farther away from the linear stability region) in deep water. Note also that the imaginary spread of eigenvalues is somewhat greater than would be expected from the linear analysis, and that this trend is amplified as the nonlinearity is increased. This is particularly apparent in Figures 5.5 (a),(c) and (d),(f), which have the strongest nonlinearity (recall that the hyperbolic Courant number r_h refers to the expected imaginary spread of eigenvalues from the linear analysis). This trend is consistent with the amplitude dispersion characteristics of nonlinear waves – nonlinear waves travel faster than linear waves having the same wavelength and water depth.

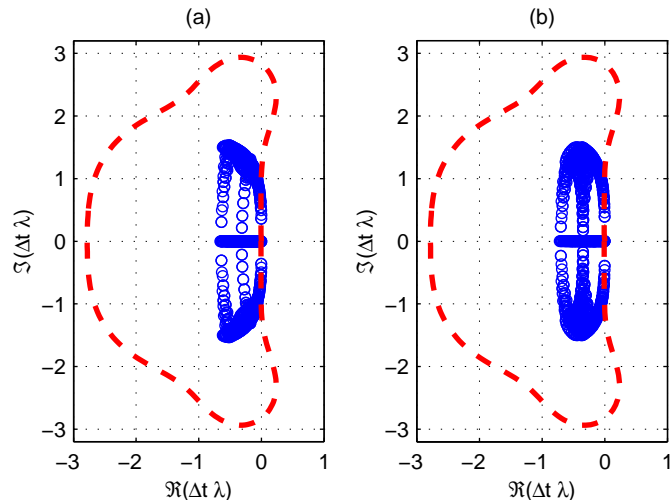


Figure 5.6: Eigenvalues of $\Delta t \mathbf{J}$ with $kh = 2\pi$, $H/L = 0.05$, $k_N h = 20\pi$, $r_h = 1.5$, and $D = 0.002 \text{ m}^2/\text{s}^2$ for (a) the rotational ($r_p = 0.6338$) and (b) the irrotational formulation ($r_p = 0.6934$).

5.6.2 The effect of numerical dissipation

The eigenvalue distributions shown in Figure 5.5 for the nonlinear model indicate that simulations are locally unstable. In practice, however, we find that the addition of minor levels of numerical dissipation will generally stabilize the nonlinear simulations. The effect of such dissipation on the eigenvalue spectra is demonstrated in Figure 5.6, where now the diffusion coefficient has been increased to $D = 0.002 \text{ m}^2/\text{s}$. These plots can be compared with Figures 5.5 (b) and (e) with $D = 0 \text{ m}^2/\text{s}$. Clearly (as should be expected) the diffusive terms tend to move the eigenvalue distributions to the left half of the complex plane, stabilizing the schemes (at least locally). The chosen value for D in Figure 5.6 is roughly the necessary value to locally stabilize each of the distributions.

The use of similar *dissipative interfaces* is commonplace in the numerical modeling community, and is discussed *e.g.* in Abbott & Minns (1998); Hirsch (1988). In general it is felt that the effects shown in Figure 5.6 on the eigenvalue distributions are qualitatively representative for any number of dissipative interfaces. Other methods for introducing numerical dissipation include Fischer-type semi-discretization (Fischer, 1959), which has been considered in the numerical analysis of an alternative form of Boussinesq equations in Houwen *et al.* (1991), as well as the application of Savitzky-Golay smoothing filters, which will be used extensively throughout this thesis.

5.6.3 Comparison of rotational and irrotational formulations

As noted previously, rotational simulations having high deep-water nonlinearity have been found in practice to be much more difficult to stabilize than those using the irrotational

formulation. This is especially true on refined grids *i.e.* where $k_N h$ is relatively large. In an attempt to provide insight into this observation Figure 5.7 shows eigenvalue distributions for both formulations with $kh = 4\pi$, $k_N h = 40\pi$, and $H/L = 0.12$. Clearly, both simulations appear locally unstable in the absence of any numerical dissipation, as seen in Figures 5.7 (a) and (d), though this is much less pronounced for the irrotational system, Figure 5.7 (d). Figures 5.7 (b)-(c) and (e)-(f) give quite dramatic evidence that the rotational system is much more difficult to stabilize in these highly nonlinear, deep-water situations. Indeed, as shown in Figures 5.7 (b)-(c), the rotational formulation still retains some locally unstable eigenvalues at relatively high levels of dissipation *i.e.* up to $D = 0.005 \text{ m}^2/\text{s}$. Closer (visual) inspection of the associated eigenvectors has revealed that these modes seemingly contain somewhat lower frequencies, and thus are not as easily damped by the diffusive terms. The irrotational formulation, on the other hand, is locally stabilized under much lower values of D , as shown in Figures 5.7 (e)-(f). This analysis provides a possible explanation for these difficulties with the rotational formulation, and shows at least locally that the irrotational formulation is much more receptive to dissipation. Based on this analysis (as well as experience) the irrotational formulation is seemingly preferable in simulations having high deep-water nonlinearity, so long as the formulation is applicable. Remarkably, Figure 5.7 (f), with $H/L = 0.12$ and $kh = 4\pi$ shows that the necessary value for the diffusion coefficient in this example is roughly $D = 5 \cdot 10^{-4} \text{ m}^2/\text{s}$ – significantly less than the necessary value of $0.002 \text{ m}^2/\text{s}$ in Figure 5.6 (b) with $H/L = 0.05$ and $kh = 2\pi$. This suggests that the nonlinear stability properties of the irrotational formulation actually improve with increasing $k_N h$!

5.7 Analysis of Pseudospectra

In recent years the concept of the *pseudospectra* of a matrix has arisen as a tool to help understand the behavior of non-normal matrices (*i.e.* matrices whose eigenvectors do not form an orthogonal basis). This is important, as cases having severe non-normality can result in behavior that is not always consistent with what is predicted by an analysis of eigenvalues alone. If λ is an eigenvalue of \mathbf{J} , then $\|(\lambda\mathbf{I} - \mathbf{J})^{-1}\|$ is conventionally regarded to be infinite. This begs the question: What if $\|(\lambda_\epsilon\mathbf{I} - \mathbf{J})^{-1}\|$, $\lambda_\epsilon \neq \lambda$ is finite, but very large? This pattern of thinking leads to the following definition for the pseudospectra of a matrix (Embree & Trefethen, 2004)

$$\Lambda_\epsilon(\mathbf{J}) = \{\lambda_\epsilon \in \mathbb{C} : \|(\lambda_\epsilon\mathbf{I} - \mathbf{J})^{-1}\| \geq \epsilon^{-1}\}. \quad (5.28)$$

The pseudospectra of a matrix are thus useful in describing the sensitivity of the eigenvalues to minor perturbations in the original matrix. If a matrix is normal then its two-norm ϵ -pseudospectrum consists of closed balls of radius ϵ surrounding the eigenvalues (Trefethen, 1997). As the non-normality increases, however, the pseudospectra may deviate far more significantly from the eigenvalues, sometimes by many orders of magnitudes. Pseudospectra have provided valuable insight into numerous issues *e.g.* that of hydrodynamic stability (Baggett *et al.*, 1995; Baggett & Trefethen, 1995; Trefethen *et al.*, 1999, 1993). Issues concerning their computation can be found *e.g.* in Wright (2002); Wright & Trefethen (2001).

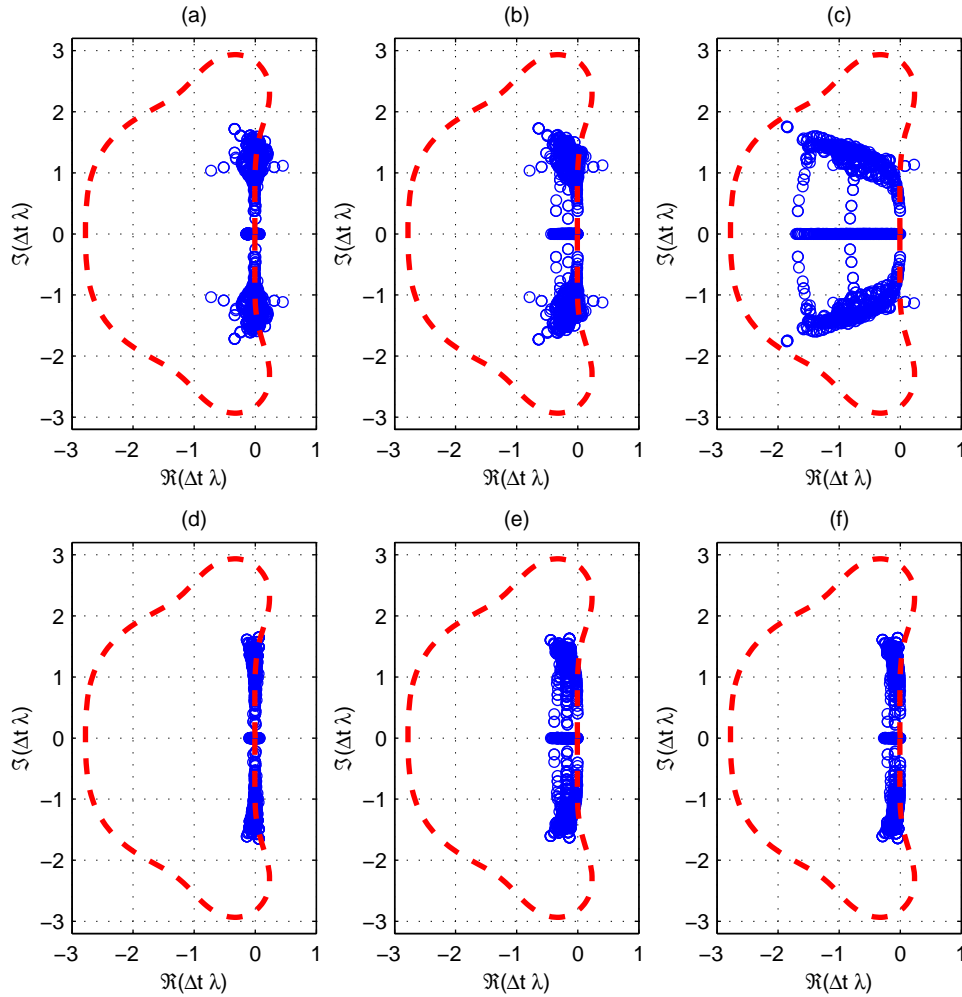


Figure 5.7: Eigenvalues of $\Delta t \mathbf{J}$ for the rotational (top) and irrotational (bottom) formulations with $kh = 4\pi$, $H/L = 0.12$, $k_N h = 40\pi$, $r_h = 1.5$, and (a),(d) $D = 0 \text{ m}^2/\text{s}$; (b),(e) $D = 0.001 \text{ m}^2/\text{s}$ ($r_p = 0.3327, 0.3561$); (c) $D = 0.005 \text{ m}^2/\text{s}$ ($r_p = 1.6636$); and (f) $D = 5 \cdot 10^{-4} \text{ m}^2/\text{s}$ ($r_p = 0.1780$).

For more detailed discussions of pseudospectra as well as numerous examples see Embree & Trefethen (2004); Trefethen (1997, 2000); Wright (2002).

This issue is explored for the current system using the EigTool package for MATLAB[®]. A detailed description of this package can be found in Wright (2002); Wright & Trefethen (2001). Pseudospectra from a number of matrices for both rotational and irrotational formulations are shown in Figure 5.8. From these plots it can be seen that these matrices are only moderately non-normal, which is itself comforting and useful information. This can be seen *e.g.* by considering that the contours corresponding to $\epsilon = 10^{-1}$ deviate from the original spread of eigenvalues typically by a length of $10^0 = 1$, or roughly 10 times what would be expected for a normal matrix. Pseudospectra from the linear models in quite deep water (Figures 5.8 (a) and (d) with $k_N h = 40\pi$) show that the eigenvalues from the rotational system are

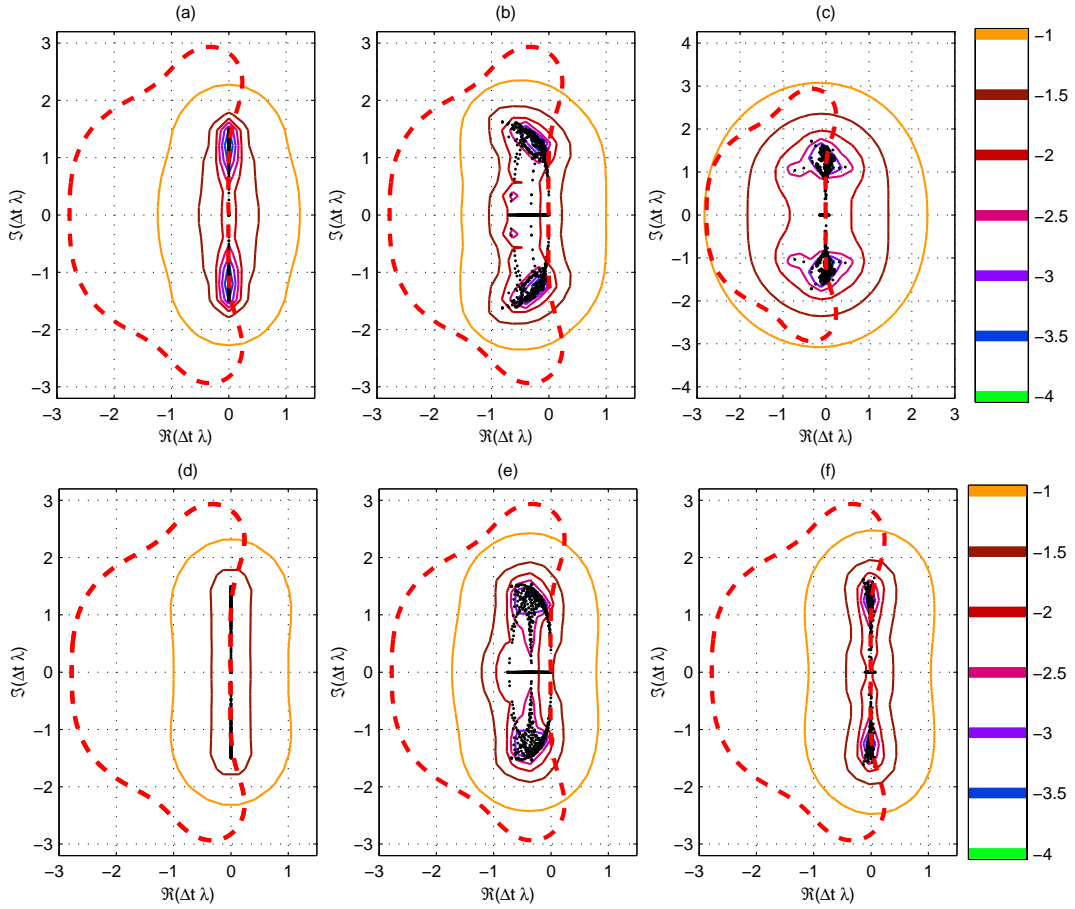


Figure 5.8: Pseudospectra ($r_h = 1.5$) of $\Delta t \mathbf{J}$ for the (top) rotational and (bottom) irrotational formulations for (a),(d) linear matrices with $k_N h = 4\pi$; (b),(e) nonlinear matrices with $kh = 2\pi$, $H/L = 0.10$, $k_N h = 20\pi$, $D = 0.002 \text{ m}^2/\text{s}$ ($r_p = 0.6338, 0.6934$); and (c),(f) nonlinear matrices with $kh = 4\pi$, $H/L = 0.12$, $k_N h = 40\pi$, $D = 0 \text{ m}^2/\text{s}$. The values for the colorbars correspond to the base-10 power of ϵ *i.e.* $\epsilon = 10^{-4}, \dots, 10^{-1}$.

slightly more sensitive to perturbations than from the irrotational formulation, deviating noticeably from the eigenvalues at much lower values of ϵ . Interestingly, the problematic area in the (nonlinear) rotational spectrum seems to already be properly identified in the linearized pseudospectrum in Figure 5.8 (a). In practice we do not observe deviations from the eigenvalue analysis with either system, suggesting that the eigenvalues reasonably characterize the discrete systems at this moderate level of non-normality. Figures 5.8 (b) and (e) show pseudospectra arising from locally stabilized matrices in moderately deep water ($kh = 2\pi$, $k_N h = 20\pi$) with high nonlinearity ($H/L = 0.10$). The differences between the two formulations are again not too severe, with the rotational formulation having a slightly larger spread. Notably, while the eigenvalues from Figures 5.8 (a)-(b) and (d)-(e) lie within the stability region, the pseudospectra protrude to the right half of the complex plane, at least for the larger values of ϵ . However, as the non-normality of the systems in Figures 5.8 (b) and (e) is roughly equivalent to that from Figures 5.8 (a) and (d), we do not expect

significant deviations from the eigenvalue analysis with these discretizations. More dramatic differences become apparent when $k_N h$ is increased, as can be seen in a comparison of Figures 5.8 (c) and (f), with $k_N h = 40\pi$, $kh = 4\pi$, $H/L = 0.12$. As Figure 5.8 (f) demonstrates, the irrotational formulation exhibits virtually no dependence on increasing $k_N h$, whereas the rotational system, Figure 5.8 (c), demonstrates a significant increase in its non-normality (the real pseudospectral radius roughly doubles). This suggests that the non-normality of the rotational formulation may play an increasing role in de-stabilizing highly nonlinear deep-water simulations as the grid is refined. However, as shown in §5.6.3 (Figure 5.7), the eigenvalues already suggest stability problems in these instances.

5.8 Numerical Experiments

The previous findings from both the linear and nonlinear analyses will now be tested in a series of numerical experiments. All experiments in this section use linear standing wave initial conditions, and results are again presented in terms of the previously introduced dimensionless quantities. The experiments use a 21×21 grid, and consider a single wavelength $L = 1$ m in both x - and y -directions, with $\Delta x = \Delta y = L/20 = 0.05$ m. All simulations use the 37-point finite difference stencil combined with the explicit fourth-order, four-stage Runge-Kutta time stepping scheme. Results from Figure 5.3 are again used for the determination of the hyperbolic Courant number r_h .

5.8.1 Linear experiments

Table 5.2 provides a summary of a series of experiments with the linear model for both rotational and irrotational formulations. Simulations are deemed ‘stable’ after running 10,000 time steps with no sign of instabilities. Recall that the necessary stability limits for this scheme are $r_h < 2.8284$ (corresponding to the imaginary limit) and $r_p < 2.7853$ (corresponding to the negative real limit), assuming the eigenvalues span either the imaginary or (negative) real axes separately. This is controlled in these experiments through the choice of time step Δt and diffusion coefficient D *i.e.* when r_h is varied $r_p = 0$, and when r_p is varied r_h is kept small. Here it can clearly be seen that the numerical results match extremely well with the linear stability criterion outlined previously in §5.4 and §5.5 for both hyperbolic and parabolic Courant numbers. Simulations with the same unstable Courant numbers for both formulations can in fact be seen to go unstable at approximately the same time. These models behave as predicted by the analysis, and the results are not discussed further.

5.8.2 Nonlinear experiments

Tables 5.3 and 5.4 provide results from a series of nonlinear simulations, where the depth and nonlinearity are varied for both rotational and irrotational formulations, respectively. These

Table 5.2: Summary of numerical experiments with the linear model. The column heading S/U refers to the simulation being either stable/unstable. The variable n_u refers to the time step where the simulations go unstable (taken here as when a NaN is detected).

$k_N h$	r_h	r_p	S/U	Rotational			Irrotational		
				Δt [s]	D [m ² /s]	n_u	Δt [s]	D [m ² /s]	n_u
2π	2.8	0	S	0.1304	0	—	0.1355	0	—
2π	2.9	0	U	0.1350	0	448	0.1403	0	456
20π	2.8	0	S	0.1223	0	—	0.1338	0	—
20π	2.9	0	U	0.1267	0	435	0.1386	0	430
40π	2.8	0	S	0.1284	0	—	0.1375	0	—
40π	2.9	0	U	0.1330	0	421	0.1424	0	420
20π	0.1	2.7	S	0.004369	0.1278	—	0.004780	0.1168	—
20π	0.1	2.9	U	0.004369	0.1373	461	0.004780	0.1255	461

simulations use an unrestarted GMRES (Saad & Schultz, 1986) algorithm for solutions of $\mathbf{Ax} = \mathbf{b}$ (preconditioned with the linearized matrix, as described in §4.6.1), with a relative residual error tolerance $r = \|\mathbf{b} - \mathbf{Ax}\|_2 / \|\mathbf{b}\|_2$ of 10^{-6} . Simulations are deemed ‘stable’ after progressing 5000 time steps with no noticeable evidence of instabilities. For all of the nonlinear experiments $r_h = 1.0$ is used to prevent numerical dissipation from the time stepping scheme (at approximately this level lobes from the stability region extend to the right half of the complex plane, effectively resulting in a dissipative scheme).

From these experiments it can be seen that the results match qualitatively with the local nonlinear analysis of §5.6. As predicted in §5.6.1, although linearly stable, the simulations generally suffer from nonlinear instabilities in the absence of numerical dissipation. Consistent with §5.6.2 (see Figure 5.6), simulations with either formulation require roughly the same level of dissipation for stabilization in cases with moderate deep-water nonlinearity (consider the cases with $kh = 2\pi$, $H/L = 0.05$). Consistent with §5.6.3, it is also shown that the irrotational formulation is much easier to stabilize than is the rotational formulation when the deep-water nonlinearity is high, particularly with large $k_N h$. For example, the irrotational simulations with $k_N h = 40\pi$, $kh = 4\pi$ surprisingly require no added dissipation to maintain stability, while similar rotational simulations quickly go unstable. The numerical experiments also indicate that the rotational formulation is somewhat easier to stabilize in shallow water (consider the results with $kh = \pi/5$). Note that these shallow-water simulations are actually very nonlinear, with $H/h = 0.7071$. This difference is not as severe as in deep water, however, and was not detected in the local analysis. Further investigation of Tables 5.3 and 5.4 confirms an important trend – the nonlinear stability properties of the rotational formulation deteriorate with increasing $k_N h$, whereas for the irrotational formulation the stability properties actually improve! This was also suggested in §5.6.3. This is quite significant, as many of the practical applications of this model involve highly nonlinear waves in deep water.

Table 5.3: Summary of numerical experiments with the nonlinear rotational model. All simulations use $r_h = 1.0$. The column headings are the same as used in Table 5.2. Here the variable n_u refers to first time step where a solution of $\mathbf{Ax} = \mathbf{b}$ exceeds 200 iterations.

$k_N h$	kh	H/L	Δt [s]	D [m ² /s]	r_p	S/U	n_u
2π	$\pi/5$	0.05	0.04655	0	0	U	2310
2π	$\pi/5$	0.05	0.04655	10^{-6}	$2.25 \cdot 10^{-4}$	U	2440
2π	$\pi/5$	0.05	0.04655	10^{-5}	$2.25 \cdot 10^{-3}$	S	—
20π	2π	0.05	0.04369	0	0	U	2960
20π	2π	0.05	0.04369	10^{-5}	$2.11 \cdot 10^{-3}$	U	3620
20π	2π	0.05	0.04369	10^{-4}	$2.11 \cdot 10^{-2}$	S	—
20π	2π	0.10	0.04369	0	0	U	510
20π	2π	0.10	0.04369	10^{-4}	$2.11 \cdot 10^{-2}$	U	980
20π	2π	0.10	0.04369	10^{-3}	$2.11 \cdot 10^{-1}$	S	—
20π	2π	0.12	0.04369	0	0	U	360
20π	2π	0.12	0.04369	10^{-4}	$2.11 \cdot 10^{-2}$	U	560
20π	2π	0.12	0.04369	10^{-3}	$2.11 \cdot 10^{-1}$	S	—
40π	4π	0.10	0.04587	0	0	U	650
40π	4π	0.10	0.04587	10^{-5}	$2.22 \cdot 10^{-3}$	U	700
40π	4π	0.10	0.04587	10^{-4}	$2.22 \cdot 10^{-2}$	S	—
40π	4π	0.12	0.04587	0	0	U	230
40π	4π	0.12	0.04587	10^{-4}	$2.22 \cdot 10^{-2}$	U	570
40π	4π	0.12	0.04587	10^{-3}	$2.22 \cdot 10^{-1}$	S	—

Table 5.4: Summary of numerical experiments with the nonlinear irrotational model. Column headings are as in Table 5.3.

$k_N h$	kh	H/L	Δt [s]	D [m ² /s]	r_p	S/U	n_u
2π	$\pi/5$	0.05	0.04838	0	0	U	1030
2π	$\pi/5$	0.05	0.04838	10^{-5}	$2.34 \cdot 10^{-3}$	U	1180
2π	$\pi/5$	0.05	0.04838	10^{-4}	$2.34 \cdot 10^{-2}$	S	—
20π	2π	0.05	0.04780	0	0	U	2270
20π	2π	0.05	0.04780	10^{-5}	$2.31 \cdot 10^{-3}$	U	2520
20π	2π	0.05	0.04780	10^{-4}	$2.31 \cdot 10^{-2}$	S	—
20π	2π	0.10	0.04780	0	0	U	1030
20π	2π	0.10	0.04780	10^{-5}	$2.31 \cdot 10^{-3}$	U	1100
20π	2π	0.10	0.04780	10^{-4}	$2.31 \cdot 10^{-2}$	S	—
20π	2π	0.12	0.04780	0	0	U	460
20π	2π	0.12	0.04780	10^{-4}	$2.31 \cdot 10^{-2}$	U	830
20π	2π	0.12	0.04780	10^{-3}	$2.31 \cdot 10^{-1}$	S	—
40π	4π	0.10	0.04909	0	0	S	—
40π	4π	0.12	0.04909	0	0	S	—

It can be seen from the experiments that the necessary values for the diffusion coefficient D are typically $O(10^{-5}) - O(10^{-3})$ m²/s. These are often somewhat lower than the values $O(10^{-4}) - O(10^{-3})$ m²/s that might be inferred from the local nonlinear analysis in §5.6. This discrepancy is likely, at least in part, due to the dissipative nature of these simulations. The diffusive terms inevitably result in an energy loss, thus the waveheight (and correspondingly the degree of nonlinearity) continually decreases during a simulation. This occurs quite rapidly *e.g.* with $D = 10^{-3}$ m²/s, effectively making it impossible to test the performance of high nonlinearity combined with larger diffusion coefficients for an extended time period. This discrepancy with the local nonlinear analysis is not of great concern, given that the original intent was to gain qualitative knowledge for this system. Note also that these necessary values for D are one to three orders of magnitude larger than the kinematic viscosity of water $\nu \approx 10^{-6}$ m²/s. Thus, the numerical dissipation required for numerical stability is in most cases significantly greater than what might be included for purely physical reasons. The resulting values for r_p are in all cases significantly lower (typically by orders of magnitude) than the corresponding stability limit, perhaps making this limit of little practical significance (at least for this particular time stepping scheme).

The general numerical stability for this nonlinear system is an extremely complicated issue, and a full account has certainly not been presented here. These results should, however, provide useful guidelines for future applications of the nonlinear model for the general study of water waves.

5.9 Conclusions

This chapter investigates the numerical stability of method of lines discretizations of the high-order Boussinesq formulation. It is shown through linear analyses that centered finite difference schemes are conditionally stable for time stepping schemes whose stability regions contain some portion of the imaginary axis. From the results presented here necessary stability criterion can be established for numerous time integration schemes in combination with a number of finite difference spatial discretizations. Linear analyses using conventional Fourier (von Neumann) techniques in a single horizontal dimension and matrix-based methods in two horizontal dimensions (for both rotational and irrotational formulations) give very similar results, with both indicating that the high-order discretizations result in more restrictive stability constraints than do second-order finite difference approximations.

The matrix-based method is also extended to include the local effects of the nonlinear terms. The general de-stabilizing effects of these terms are demonstrated, as are the stabilizing effects of numerical dissipation. The analysis provides clear evidence that the numerical model becomes increasingly unstable as the nonlinearity becomes stronger. Although the linear analyses show only minor differences between the rotational and irrotational formulations, much more dramatic differences are demonstrated in the local nonlinear analysis. Specifically, it is shown (locally) that the eigenvalues from the rotational system are much

less receptive to numerical dissipation than are those from the irrotational formulation when high nonlinearity is combined with large water depths and/or refined grids (*i.e.* large $k_N h$). Alternatively, the analysis suggests that the stability properties of the irrotational formulation actually improve with increasing $k_N h$. Computation of matrix pseudospectra shows that the system is generally only moderately non-normal, giving confidence that the eigenvalues reasonably characterize the discrete systems. Increased non-normality is, however, demonstrated for the rotational formulation when high nonlinearity is combined with large $k_N h$, providing yet further evidence of deteriorating stability properties for this formulation in these circumstances.

A series of numerical experiments demonstrates excellent agreement with the linear analyses, and good qualitative agreement with the local nonlinear analysis. These experiments provide further insight, indicating that the rotational formulation has slightly better stability properties in highly nonlinear shallow-water situations. The experiments confirm that the irrotational formulation has significantly better stability properties in cases having high deep-water nonlinearity, particularly with large $k_N h$. From this analysis it can confidently be concluded that the irrotational formulation is preferable from a stability standpoint in these circumstances. The experiments also demonstrate that the nonlinear stability properties of the irrotational formulation improve with increasing $k_N h$, consistent with the local nonlinear analysis. These conclusions are significant, as many of the practical applications of this model involve highly nonlinear waves in deep water.

This work serves as an example of the combined use of many widely-applicable numerical analysis techniques, with each providing valuable insight into the numerical behavior of this complicated system of PDEs (including up to fifth-order spatial derivatives). Extension beyond classical linear methods of analysis has proven essential for the understanding of this system, as the behavior of the nonlinear model deviates significantly from what might be expected from a strictly linear analysis. This work has proven essential in obtaining convergent numerical solutions for this important high-order system of nonlinear PDEs.

Chapter 6

Model Verification

Chapter Summary

This chapter describes the systematic verification of the Boussinesq model using simulations of idealized test cases for which analytic solutions exist. Simulations involving linear standing waves, nonlinear standing waves, and linear shoaling are used to independently test the basic linear terms, the nonlinear terms, and the variable bottom terms, respectively. In each case a (nearly) perfect agreement with theoretical solutions confirms their correct implementation. Additionally, computed results involving nonlinear refraction and diffraction are shown to compare well with experimental measurements, demonstrating the application of the model in more realistic circumstances. A brief comparison of the computational costs with a full three dimensional Navier-Stokes solution suggest that the use of the Boussinesq model within its physical limitations is justified from an efficiency standpoint.

6.1 Introduction

In the development of any numerical model idealized test cases, for which analytical (or semi-analytical) solutions exist, are invaluable. Without such test cases, verifying the correct implementation of a numerical model and testing its performance is, at best, extremely difficult. This is particularly true when solving complicated systems of PDEs, as in this thesis, as the opportunities for making mistakes are abundant.

This chapter describes the verification of the Boussinesq model using such idealized test cases. The cases have been selected so that the various terms within the model can be systematically and independently tested. Specifically, simulations involving linear standing waves, nonlinear standing waves, and linear shoaling are used to test the basic linear (including mixed-derivative), nonlinear, and variable bottom terms, respectively. Computed

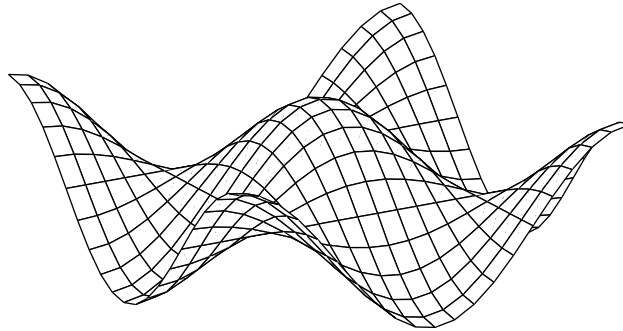


Figure 6.1: The computed free surface of a linear standing wave at $t = 6.730 = 10T$.

results involving nonlinear refraction and diffraction also compare well with measurements, highlighting the accuracy of the model in realistic circumstances. Simulations throughout the chapter using the various preconditioners developed in Chapter 4 further demonstrate their effectiveness on variable depth problems. A brief comparison of the computational efficiency of the Boussinesq model compared to a full three-dimensional Navier-Stokes solution as well as a nonlinear shallow-water model is also provided. The results suggests that applications of the Boussinesq model (within its physical limitations) are justified from an efficiency standpoint.

This chapter is organized as follows. Model verification with respect to linear and nonlinear standing waves is presented in §6.2 and §6.3, respectively. Verification with respect to linear shoaling is presented in §6.4. Verification with respect to nonlinear refraction and diffraction are presented in §6.5. A brief comparison of the computational efficiency when compared to other modeling alternatives is presented in §6.6. Conclusions are briefly re-stated in §6.7.

6.2 Linear Standing Wave

As a first means of model verification we consider linear standing wave simulations, given by the initial conditions

$$\tilde{\mathbf{U}}(x, y, 0) = 0, \quad (6.1)$$

$$\eta(x, y, 0) = \frac{H}{2} \cos k_x x \cos k_y y, \quad (6.2)$$

where H is the wave height, and k_x and k_y are components of the wavenumber vector $\mathbf{k} = (k_x, k_y) = (2\pi/L_x, 2\pi/L_y)$ (where L_x and L_y are wavelengths in the x - and y -directions, respectively). The initial free surface elevation is shown in Figure 6.1.

We will firstly consider the relative merits of each of the finite difference discretizations introduced in §3.2. These are again (a) second-order approximations for each partial derivative, (b) a 25-point (diamond) finite difference stencil, (c) a 37-point (octagon) stencil, and

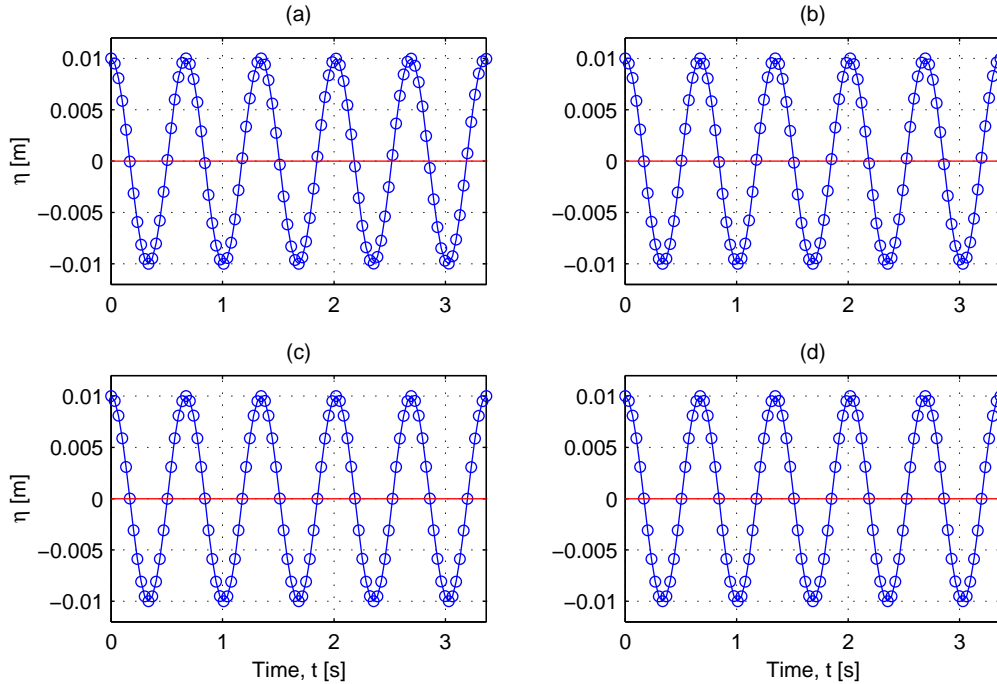


Figure 6.2: Computed time series of free surface elevations (at the center-point) from linear standing wave simulations using (a) second-order finite difference approximations, (b) a 25-point stencil, (c) a 37-point stencil, and (d) a 49-point stencil.

(d) a 49-point (square) stencil (see Figure 3.1). For comparison we use simulations on a 21×21 computational grid, with $H = 0.02$ m, $h = 0.7071$ m, $k_x = k_y = 2\pi \text{ m}^{-1}$ (*i.e.* $L_x = L_y = L = 1$ m, $kh = 2\pi$), and $\Delta x = \Delta y = L/20 = 0.05$ m. Using the linear dispersion relation

$$\omega^2 = gk \tanh(kh), \quad (6.3)$$

gives a linear period $T = 2\pi/\omega = 0.6730$ s, and the time step is taken to be $\Delta t = T/20 = 0.03365$ s. Nonlinear terms are switched off for the simulations so that results should match linear theory. Note that in the linear sense $\tilde{\mathbf{U}} = \mathbf{u}_0$, where $\mathbf{u}_0 = (u_0, v_0)$ are again horizontal velocity variables at $z = 0$. Resulting time series of surface elevations at the center-point under each finite difference stencil are shown in Figure 6.2. Here particular attention should be paid to the zero crossings, as these should theoretically correspond to a point from the time series. In Figures 6.2 (a) and (b) the period is seen to be noticeably off, whereas in (c) and (d) it is visually exact under this discretization. Table 6.1 gives quantitative results of the root-mean-squared-error (RMSE) over the entire domain at $t = 4.75T$ and at $t = 5T$, where the free surface should theoretically be flat and back to its initial condition, respectively. It is again seen that the 37- and 49-point stencils give a substantial reduction in the accumulated error. Indeed, achieving similar accuracy with stencils (a) and (b) requires roughly 15 and 4 times as many grid points, respectively! Note that as this case is in deep water ($kh = 2\pi$) all of the spatial derivatives are important for this problem. In shallow water this trend becomes even more exaggerated, as the leading order spatial derivatives

Table 6.1: RMSE of computed free surface elevations (compared with linear theory) using various finite difference approximations in linear standing wave simulations. The simulations are on the 1.8 GHz machine, and use the factored linear preconditioner from §4.6.1 (thus each solution of $\mathbf{Ax} = \mathbf{b}$ requires a single iteration).

Stencil	Grid	$t = 4.75T$	$t = 5T$	CPU [s]
2nd-order	21×21	3.94×10^{-4}	2.00×10^{-5}	5.99
25-point	21×21	1.74×10^{-4}	6.68×10^{-6}	5.98
37-point	21×21	7.59×10^{-6}	3.46×10^{-6}	8.41
49-point	21×21	1.08×10^{-5}	3.46×10^{-6}	8.60
2nd-order	81×81	1.31×10^{-5}	3.36×10^{-6}	158
25-point	41×41	3.24×10^{-5}	3.50×10^{-6}	29.8

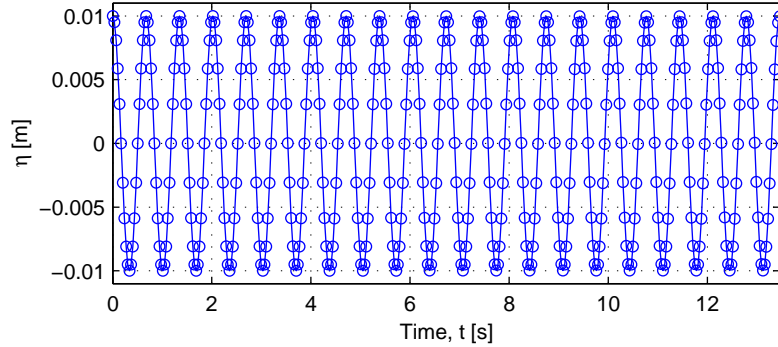


Figure 6.3: Time series of surface elevations for a linear standing wave simulation covering the first 20 periods.

are accurate to sixth-order with stencils (c) and (d), see again Appendix B. Due to the inclusion of mixed fifth-order partial derivatives, this model inevitably requires a fairly large finite difference stencil. Correspondingly, it rather naturally lends itself to higher-order finite difference approximations (for lower-order terms), which can give significant reductions in the overall computational expense (as well as the storage) required for a desired accuracy. Because the 37-point stencil seems to provide essentially the same accuracy as the 49-point stencil, it will be used exclusively in the remainder of this work.

The resulting time series from an extended simulation (covering 20 periods) using the 37-point stencil is also shown in Figure 6.3. Here it can be seen that this discretization maintains a visually (nearly) perfect match with the theoretical period over the entire duration. The essentially perfect results presented in this section confirm the correct implementation of the linear, flat-bottom terms, including mixed-derivative terms.

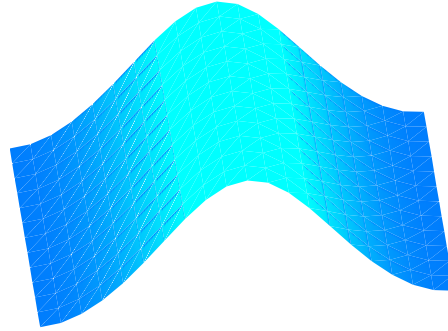


Figure 6.4: The computed free surface from a nonlinear standing wave simulation at $t = 9.5T$ s. Note that the vertical scale in this figure is exaggerated 10 times.

6.3 Nonlinear Standing Wave

As a second means of model verification we simulate the eighth-order nonlinear standing wave of Agnon & Glozman (1996) with $H = 0.05$ m, $h = 2$ m, and $L = 2$ m ($H/L = 0.025$, $kh = 2\pi$). This problem in fact contains no variation in the y -direction, however it is still useful to test the basic nonlinear terms. Using $g = 9.82$ m/s² gives a nonlinear period $T = 1.1341$ s. The problem is discretized using $\Delta x = \Delta y = L/20 = 0.10$ m on a 21×13 grid with $\Delta t = T/20 = .056704$ s. The simulation was run for 1001 time steps (*i.e.* 50 full periods) and was preconditioned using the factored linear preconditioner. The results shown are from the irrotational formulation, however results from the irrotational formulation are virtually identical. The simulation required between 1–8 iterations (with an average of 3.51), and required 119 s on the 1.8 GHz machine (Absoft compiler).

The computed free surface after $9.5T$ is shown in Figure 6.4. A time series of the surface elevation at the center point is also shown in Figure 6.5, covering the first 20 periods. Here the nonlinear effects can clearly be seen, as the time series is no longer centered about $z = 0$ (as in Figure 6.3), but is rather shifted slightly upwards. In this figure a nearly perfect match with the theoretical period is again observed (this can again be seen from the zero crossings), confirming the correct implementation of the basic nonlinear terms.

6.4 Linear Shoaling

To test the variable bottom terms, we will now consider simulations involving linear shoaling of waves over the bathymetry shown in Figure 6.6 (a), having depths ranging from $h = 10$ m to 0.2 m. The simulation uses sinusoidal incident waves at the deep water region with wavelength $L = 20$ m and $H = 0.002$ m. Using $g = 9.81$ m/s² gives a linear period $T = 3.586$

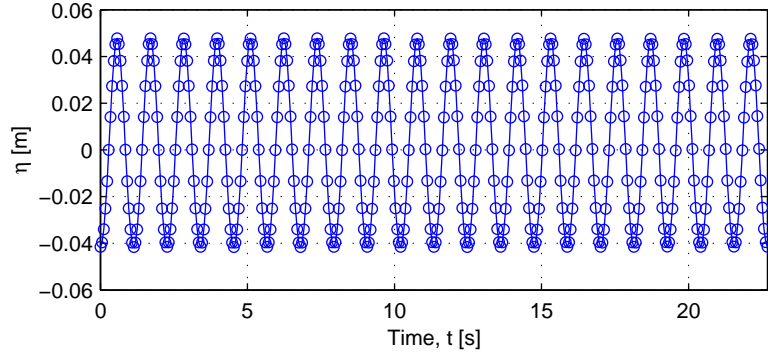


Figure 6.5: Time series of surface elevations for a nonlinear standing wave simulation covering the first 20 periods.

s. The simulation thus involves dimensionless depths ranging from $kh = \pi$ to $kh = 0.253$ *i.e.* deep to quite shallow water. The time step is taken as $\Delta t = 0.15$ s, and for the spatial discretization we use $\Delta x = \Delta y = 0.2$ m (note that there is again no variation in the y -direction). Nonlinear terms are switched off for this simulation. Results are shown from an irrotational simulation using the Schur complement preconditioner. This case is interesting in-part because it demonstrates the effectiveness of this preconditioner on a problem with vastly different depths. A 1701×9 computational grid is used, and the simulation was run for 2001 time steps, requiring 3.14 hr on a 2.26 GHz processor. The simulation required between 4–9 iterations (with an average of 6.74). For stability purposes (necessary because of the variable bottom), a sixth-order, 57-point smoothing filter was applied after each full time step. For comparison a rotational simulation preconditioned with the factored linear matrix required 1.14 hr, and gave virtually identical results. Note that this preconditioner can be very efficient when solving small linear problems since then $\mathbf{M} = \mathbf{A}$, hence GMRES always converges in a single iteration! Of course, direct solution methods are also efficient in these cases.

The computed shoaling envelope is presented in Figure 6.6 (b). Also shown for comparison is the envelope based on conservation of energy flux from linear theory (see *e.g.* Svendsen & Jonsson, 1976). This is computed by solving

$$\frac{a(x)}{a_0} = \left[\frac{k(x) \left(1 + \frac{2k_0 h_0}{\sinh(2k_0 h_0)} \right)}{k_0 \left(1 + \frac{2k(x)h(x)}{\sinh(2k(x)h(x))} \right)} \right]^{0.5}, \quad (6.4)$$

in combination with the linear dispersion relation, which must be satisfied for all x . Here a_0 and k_0 are the amplitude and wavenumber of the incident wave. In Figure 6.6 (b) a perfect match between the computed results and the theory is again observed, confirming the correct implementation of the variable depth terms.

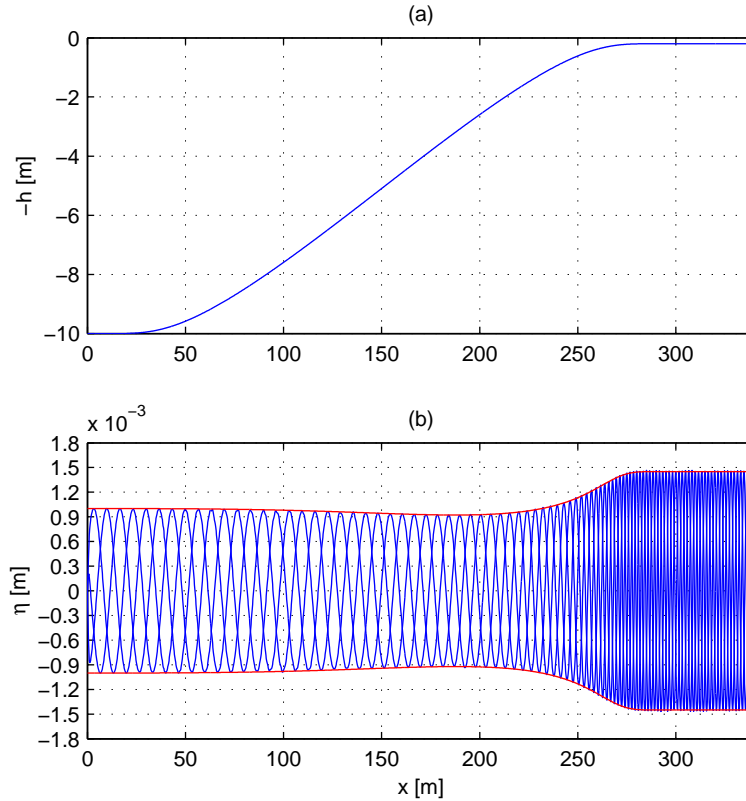


Figure 6.6: Plots showing (a) the bathymetry, and (b) the computed (blue) and theoretical (red) linear shoaling envelope.

6.5 Nonlinear Refraction & Diffraction

Having systematically confirmed the linear, nonlinear, and variable depth terms in the previous three sections, we will now consider their combined effects in simulating the experiments of Whalin (1971) involving nonlinear refraction and diffraction. These simulations will hence demonstrate the performance of the nonlinear model on a three-dimensional bathymetry. The topography used connects deep and shallow regions with a semi-circular shoaling region that acts as a focusing lens, and is described (in meters) by

$$h(x, y) = \begin{cases} 0.4572 & \text{if } 0 \leq x \leq 10.67 - G \\ 0.4572 + \frac{1}{25}(10.67 - G - x) & \text{if } 10.67 - G \leq x \leq 18.29 - G \\ 0.1524 & \text{otherwise} \end{cases} \quad (6.5)$$

where

$$G(y) = \sqrt{y(6.096 - y)}. \quad (6.6)$$

Gradients of h in both horizontal directions are calculated analytically. Because the bathymetry is symmetric about the centerline (*i.e.* at $y = 3.048$ m) only half of the domain is modeled, as shown in Figure 6.7.

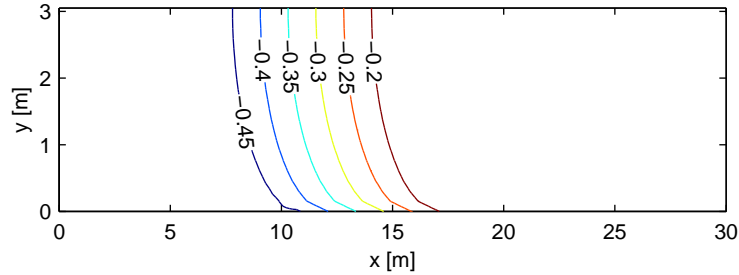


Figure 6.7: Bathymetry ($-h$ in m) used when simulating the experiments of Whalin (1971).

Table 6.2: Description of the incident wave (at $h = 0.4562$ m) and model setup for the simulations modeling the experiments of Whalin (1971).

T [s]	H [m]	L [m]	kh	Grid	Δx [m]	Δy [m]	Δt [s]
1.0	0.0390	1.50	1.92	467×21	0.0762	0.1524	0.03906
2.0	0.0150	3.91	0.73	276×21	0.1524	0.1524	0.03906
3.0	0.0136	6.14	0.47	291×21	0.1524	0.1524	0.03516

We consider three separate cases, having periods $T = 1, 2,$ and 3 s. The model setup for each of the cases is described in Table 6.2. Note that these same three cases have also been considered *e.g.* in Madsen & Sørensen (1992). In each case stream function (Fenton, 1988) incident waves are used, with Stokes' drift (or mean transport) velocity $c_s = 0$, to match the conditions of a closed flume. These incident waves are relaxed over a wavemaker region (in the negative x -region) consisting of approximately a single wavelength. A second relaxation zone having the same length is placed after the wavemaker region to absorb the reflected wavefield (see §3.5). A sponge layer consisting of 50 grid points is also applied for $x > 30$ m to absorb the outgoing wavefield. In each simulation a 10th-order, 109-point (octagon) Savitzky-Golay smoothing filter is applied every 20 time steps, which is necessary to remove high-frequency instabilities caused by the nonlinear and variable bottom terms (the discretizations satisfy the linear stability criterion outlined in Chapter 5). The end result is a very minor loss of accuracy. Each simulation was run for approximately 2000 time steps, using the 1.8 GHz processor on code compiled with the Absoft FORTRAN compiler.

Specific attention will be paid to the physical processes involved in the deep water test case (*i.e.* with $T = 1$ s). Figure 6.8 (a) shows the measured and computed harmonic amplitudes along the centerline (*i.e.* at $y = 3.048$ m). The harmonic analysis has been made using a linear least-squares fit from the final 500 time steps. Here a strong focusing effect is very apparent behind the shoal, resulting in a major increase in amplitudes. At the wavemaker the incident waves are nearly linear. During the shoal, however, there is a build up of bound second harmonics due to nonlinear effects. After the shoal, when the depth is again constant, there is a release of free second harmonics. Hence, in the shallow region the wavefield consists of both bound and free second harmonics, which propagate not only with different speeds, but also with different directions. This in turn causes the observed modulation in the second harmonic amplitude behind the shoal. There is a considerable scattering in the data in

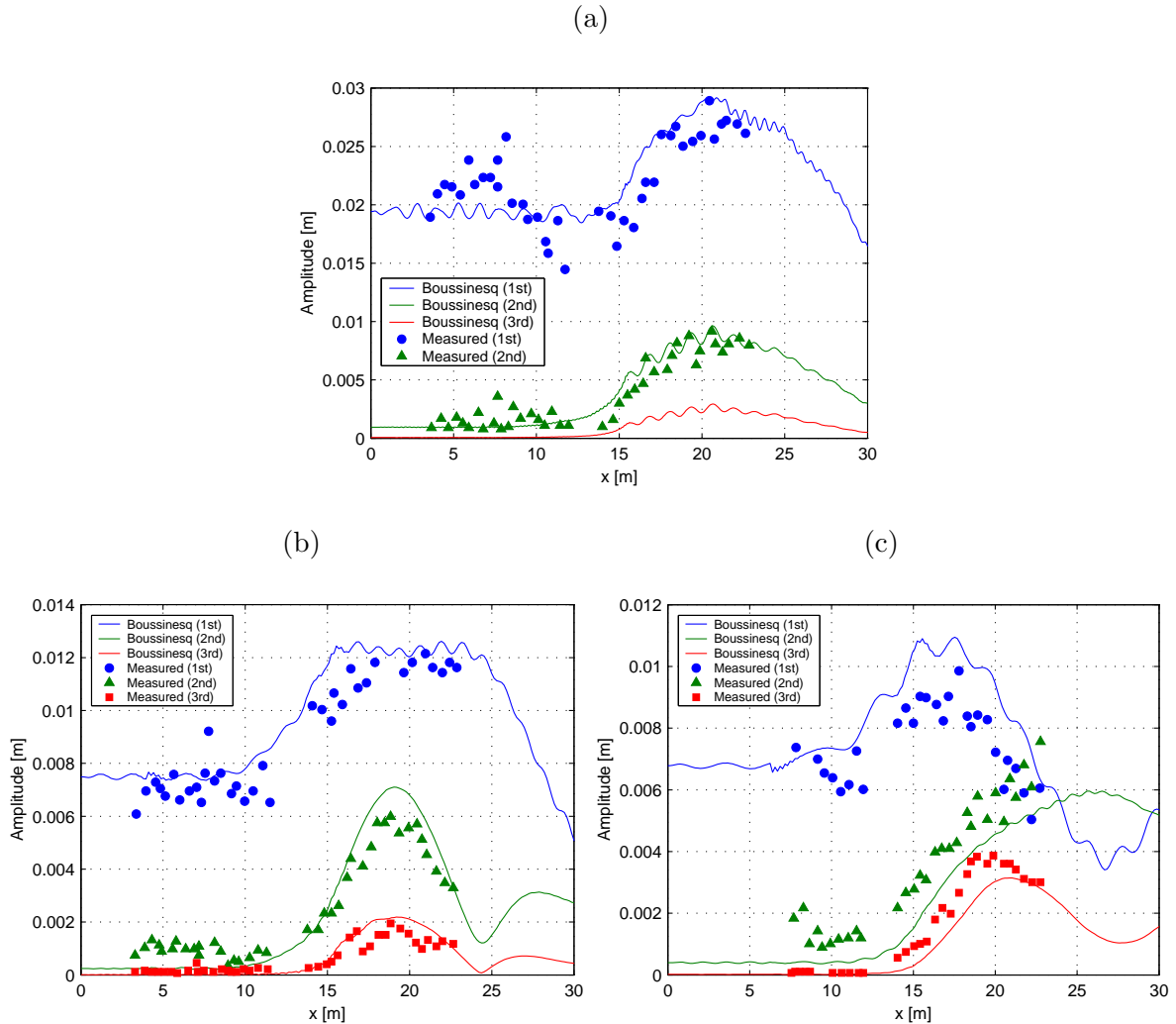


Figure 6.8: Computed and measured harmonic amplitudes for simulations modeling the experiments of Whalin (1971) with (a) $T = 1$ s, (b) $T = 2$ s, and (c) $T = 3$ s.

front of the shoal, but behind the shoal the agreement between the measured and computed results is quite impressive. Indeed, even the modulations in the second harmonic seem to be well modeled.

We will also use this case (again with $T = 1$ s), which is the most computationally demanding of the three, to investigate the effectiveness of the various preconditioning methods developed in Chapter 4 on a more realistic problem. Table 6.3 provides a summary of simulations using the various preconditioning strategies for both rotational and irrotational simulations. As this problem is not extremely deep, all of the preconditioning methods are seen to be very effective. Solutions of this problem are far from trivial, however, and some form of preconditioning is necessary to achieve reasonable solution times. Notably, the Schur complement preconditioner remains effective on this nonlinear variable-depth problem, even though it has neglected both the nonlinear and bottom slope terms. Curiously, the results using the

Table 6.3: Summary of simulations modeling the experiment of Whalin (1971) with $T = 1$ s.

Formulation	Preconditioner	Iterations	CPU [h]
Rotational	Linear	4-10	4.39
Rotational	Linear (SP)	3-10	6.59
Rotational	ILUT	4-10	4.57
Rotational	Schur	6-17	5.13
Irrotational	Linear	3-10	4.75
Irrotational	Linear (SP)	3-10	6.39
Irrotational	ILUT	4-10	4.16
Irrotational	Schur	6-13	5.09

linear (single precision, SP) preconditioner are slower than with the double precision alternative, which contradicts previous findings. These simulations confirm the effectiveness of each of these solution strategies on a realistic case involving both nonlinearity and variable bathymetry.

Harmonic analyses are likewise shown in Figures 6.8 (b) and (c) for the additional cases with $T = 2$ and 3 s. The agreement in both cases between the computed and measured harmonic amplitudes is again most acceptable. The results from the three test cases compare particularly well with others from the literature (see *e.g.* Chen & Liu, 1995; Li & Fleming, 1997; Liu & Tsay, 1984; Liu *et al.*, 1985; Madsen *et al.*, 1991; Madsen & Sørensen, 1992; Rygg, 1988), further confirming the accuracy of the Boussinesq model.

6.6 A Brief Comparison of Computational Efficiency

The cases presented previously have all focused on the accuracy of the Boussinesq model in some idealized cases, which is of course of the utmost importance. Also relevant in terms of the validity of the model, however, is the relative computational efficiency when compared to other water wave models. In this section we briefly compare the computational demands of the Boussinesq model to those of a full three-dimensional model, as well as with a shallow water model. The hope is, of course, that numerical solutions are significantly cheaper than with a three-dimensional model, while perhaps being justifiably more costly than a shallow water alternative. For simplicity we focus almost entirely on CPU demands for a given problem size, and make very little effort at comparing accuracy, relying only on discretizations used previously from the literature to gain some idea. Hence the comparison is admittedly incomplete. A much more detailed (and perhaps proper) methodology for the comparison of models can be found *e.g.* in Bredmøse (2002), who compared model efficiencies (for frequency domain models vs. MIKE 21) for a given accuracy, measured with respect to their own highly-converged results. Such comparisons are rather complicated

and inevitably depend on a large number of parameters, particularly when variable-order convergence rates are involved, inevitably making firm conclusions difficult. The intent of this section is therefore not to provide a detailed comparison of the methods considered, but rather only to gain a rough idea of the relative computational expenses required for the various models on a grid point basis.

6.6.1 Comparison with NS3

For a comparison with a three-dimension model we use the NS3 model described *e.g.* in Mayer *et al.* (1998); Nielsen (2003); Nielsen & Mayer (2004). This model solves the Navier-Stokes¹ equations using a volume of fluid (VOF) scheme, and is second-order accurate in both space and time. For simplicity we consider simulations of plane stream function (Fenton, 1988) incident waves on a depth $h = 0.8$ m, with wavelength $L = 0.8$ m, and waveheight $H = 0.064$ m (*i.e.* $kh = 2\pi$, $H/L = 0.08$). This yields a period $T = 0.6968$ s. With both models $\Delta x = \Delta y = L/30 = 0.0267$ m is used, with a total of 400 points/cells taken in the x -direction. Two- and three-dimensional problems are considered, with 24 points/cells taken in the y -direction for the three-dimensional cases. Simulations in two and three dimensions are run for $30T$ and $10T$, respectively. For the NS3 simulations the built in adaptive time stepping scheme is used, whereas with the Boussinesq model a constant $\Delta t = T/30 = 0.0232$ s is used. The Boussinesq model is compiled with the Intel FORTRAN compiler, whereas the NS3 code was pre-compiled using the gcc compiler. All simulations are run on the 1.8 GHz machine. Solutions with the Boussinesq model (in two-horizontal dimensions) use the Schur complement preconditioner of §4.6.4, whereas the NS3 simulations use multi-grid iterative methods (see *e.g.* Briggs *et al.*, 2000). For the NS3 simulations three different discretizations in the vertical direction are considered *i.e.* 16, 32, and 64 cells. These simulations hopefully give some indication of the relative expenses of solving shallow and deep water problems with this model.

A summary of the CPU time and storage required for the various simulations is provided in Table 6.4. For the two-dimensional simulations it can be seen that the Boussinesq model is roughly two orders of magnitude faster than the corresponding NS3 simulations, with approximately a single order of magnitude savings in storage. Alternatively, for the three-dimensional simulations, the Boussinesq model is roughly a single order of magnitude more efficient in terms of CPU times, with a factor of roughly 1–4 savings in storage. The reason for the relative loss in efficiency when going from a single to two horizontal dimensions with the Boussinesq model is simply because simulations in a single horizontal dimension only require solutions of banded linear systems (involving far fewer non-zero elements, see Madsen *et al.*, 2002), which is a trivial task.

While we again refrain from directly comparing accuracy of the simulations, some idea of the required resolution for the NS3 model can be obtained from the literature. In two-

¹Named after the French engineer Claude Louis Marie Henri Navier, 1785–1836, and the Irish mathematician George Gabriel Stokes, 1819–1903.

Table 6.4: Summary of the comparison between Boussinesq and NS3 simulations. Each computational domain uses $N_x = 400$ grid points/cells in the x -direction.

Model	N_y	N_z	N_t	CPU [s]	$\overline{\Delta t}$	Storage [MB]
NS3	1	16	1378	477	0.0152	11
NS3	1	32	2187	1078	0.00956	15
NS3	1	64	2499	1614	0.00837	23
Boussinesq	1	—	901	12.4	0.0232	2.2
NS3	24	16	728	12,715	0.00957	204
NS3	24	32	1094	37,555	0.006369	361
NS3	24	64	—	—	—	676
Boussinesq	24	—	301	1453	0.0232	174

dimensional simulations using the nonlinear standing wave of Agnon & Glozman (1996), the NS3 model presented in Mayer *et al.* (1998) obtains reasonably similar results to those presented here in §6.3 using a 64×32 grid (in the x - and z -directions), with roughly 100 time steps per period. Alternatively, in §6.3, visually perfect results were obtained using 20 points per wavelength and period. Nielsen & Mayer (2004) also demonstrate accurate propagation of stream function incident waves using roughly 50 cells per wavelength. Thus, at least at first glance the discretizations used in this section appear to be reasonable, and the computational savings implied by Table 6.4 for the Boussinesq model are likely conservative estimates for a given accuracy (since equivalent discretization in space for the two models was used). Note that the larger time steps used by the Boussinesq model are warranted due to the use of a fourth-order time stepping scheme, compared with the second-order accuracy of the NS3 model. Similar arguments can also be made with regard to the savings in the spatial discretization (see again the comparison in §6.2 using the different discretizations with the Boussinesq model).

Based on this simple comparison, the use of the high-order Boussinesq model over a full three-dimension solution seems justified for particular classes of problems. It must be stressed that the NS3 model is capable of solving much more complicated problems, and has been previously used to study *e.g.* wave breaking by Mayer & Madsen (2000), and green water loads on ships by Nielsen (2003); Nielsen & Mayer (2004). The comparison here is in no way meant to downplay the impressive achievements made using this approach, but merely to justify the computational demands of the Boussinesq model for solving problems within its own inherent physical limitations.

6.6.2 Comparison with MIKE 21

To get an idea of the relative computational efficiency with respect to a simpler model, we will briefly compare with the well-known MIKE 21 model from DHI Water & Environment, Hørsholm, Denmark, capable of simulating nonlinear shallow water waves. This finite

difference model solves two-dimensional variants of the Saint-Venant² equations, using an alternating direction implicit (ADI) algorithm, and is second-order accurate in both space and time. The basic numerical algorithm is explained *e.g.* in Abbott & Minns (1998). Numerous modules in addition to the basic hydrodynamic scheme have also been incorporated into this model, see *e.g.* Babovic & Fuhrman (2002).

This basic model (with slight modifications) has been used recently by Madsen *et al.* (2004) to simulate the fascinating tidal bore in Huangzhou Bay and Qiantang River in China, which we will use for comparative purposes. Their model consists of 375,000 grid points, 55,000 of which are water points. They report that a simulation using 7600 time steps required no more than 55 min (3300 s) on a 2.66 GHz Dell PC (*i.e.* the processors are of reasonably similar speed). Dividing this time by the number of grid points and time steps gives $3300/7600/55,000 = 7.9 \times 10^{-6}$ s per grid point per time step. Considering the Boussinesq simulation in two horizontal dimensions from Table 6.4 similarly gives $1453/301/24/400 = 5.0 \times 10^{-4}$ s per grid point per time step. Hence, based on this simple comparison, the MIKE 21 model would appear to be roughly two orders of magnitude more efficient than the present Boussinesq model on a grid point basis. We note that due to the use of higher-order space and time discretizations in the Boussinesq model, the differences in practical simulations would likely be somewhat less; recall that our scheme is fourth-order accurate in time, with the leading-order spatial derivatives accurate to sixth-order (in shallow water only the leading-order terms are important). Note also that in shallow water preconditioning is generally not necessary, see again Chapter 4, though it was used in Table 6.4. In any event, despite these additional factors, the MIKE 21 model is (unsurprisingly) significantly less computationally demanding than the Boussinesq model.

6.6.3 A mention of some other fully nonlinear models

This comparison is by no means exhaustive in terms of the models considered, as we restrict attention to only the NS3 and MIKE 21 models from the previous two sub-sections. It is felt that some other models at least merit a mention. In particular, the pseudo-spectral methods of Dommermuth & Yue (1987) (see also Liu & Yue, 1998) and Smith (1998), based on Fourier expansions, have demonstrated an ability to efficiently treat highly nonlinear waves on variable bathymetries. See also the recently proposed Fourier-Boussinesq method of Bingham & Agnon (2005), which uses a combined finite difference-FFT approach. The fully nonlinear pseudo-spectral approaches of Craig & Sulem (1993) (extended recently to two horizontal dimensions by Bateman, Swan & Taylor, 2001) and Clamond & Grue (1995) are also attractive for the study of highly nonlinear water waves, though applications on variable depth problems have yet to be demonstrated with these methods. Future comparisons with these various models would certainly be of interest.

²So-named after the French engineer Adhémar Jean Claude Barré de Saint-Venant, 1797–1886.

6.7 Conclusions

This chapter presents numerical simulations of some preliminary test cases designed to systematically verify the implementation of the high-order Boussinesq model. Firstly, results using a simple linear standing wave in two horizontal dimensions are presented, and visually perfect results are achieved using a discretization of 20 points per wavelength and period. Using this test case it is also demonstrated that significant savings in grid points required for a given accuracy can be achieved by using the larger finite difference stencils presented earlier in §3.2, as opposed to using *e.g.* all second-order accurate approximations, despite some additional overhead. Correct implementation of the nonlinear terms is also demonstrated through a similar simulation of a nonlinear standing wave. The variable bottom terms are likewise verified through a linear shoaling test case, where a perfect match with linear theory is again achieved. Good agreement with experimental measurements involving nonlinear refraction and diffraction are also presented, demonstrating quantitative accuracy with a first realistic application in two horizontal dimensions.

The issue of computational efficiency is also briefly addressed via comparisons with a three-dimensional Navier-Stokes VOF model, NS3, as well as with the nonlinear shallow water model, MIKE 21, from DHI Water & Environment. Computational savings (in terms of CPU times) of roughly two and one orders of magnitude are demonstrated with the Boussinesq model when solving problems in one and two horizontal dimensions, respectively, when compared with similar NS3 solutions. MIKE 21 simulations are also expectedly much faster than with the Boussinesq model on a grid point basis. We expect the comparison to be even more favorable if accuracy were taken into account, though this is not demonstrated here. From this comparison, applications of the Boussinesq model within its physical limitations seem warranted from an efficiency standpoint, confirming the adequacy of the numerical solution methods presented in Chapter 4. For shallow water (or weakly dispersive) problems, there are clearly cheaper alternatives.

Chapter 7

Modeling of Short-Crested Waves

Chapter Summary

This chapter details a study of short-crested wave patterns, created by the nonlinear interaction of wave fronts at symmetric incident angles. These interactions are considered in both shallow and deep water, which respectively result in characteristic hexagonal and rectangular wave forms. In shallow water it is confirmed that the interaction is strong/weak when the incident angle is small/large. For the study of the rectangular forms an identical setup as with some recent physical experiments is considered, and the computed results share many common features with the observations. Among these, the most pronounced feature is a curious modulation in the direction of propagation. It is explained, for the first time, that this is due to the release of parasitic free first harmonics, which are the result of third-order discrepancies in the three-dimensional wavemaker conditions.

7.1 Introduction

Some of the most fundamental three-dimensional water wave patterns occur due to the oblique interaction of wave fronts, which lead to perhaps the simplest short-crested wave forms. These nonlinear interactions are known to create quite spectacular hexagonal and rectangular patterns in shallow and deep water, respectively. Extensive research has been performed in the study of these patterns, historically as well as very recently.

The phenomena of oblique interaction of wave fronts in finite depth has been studied experimentally by *e.g.* Hammack *et al.* (1995, 1989); and Kimmoun *et al.* (1999) (see also Hammack *et al.*, 1991), analytically by *e.g.* Hsu *et al.* (1979); Kimmoun *et al.* (1999); Segur & Finkel (1985), and numerically by *e.g.* Chen & Liu (1995); Craig & Nicholls (2002); Nicholls (1998, 2001). Such hexagonal patterns have also been observed in nature, see *e.g.* the photographs

in Hammack *et al.* (1995). The related rectangular deep water patterns have also received much attention. These have been studied experimentally by *e.g.* Hammack & Henderson (2002, 2003) and Hammack, Henderson & Segur (2005), analytically by *e.g.* Bryant (1985) and Roberts (1983), and numerically by *e.g.* Nicholls (2001) and Craig & Nicholls (2002). Proofs of existence theorems for capillary gravity water waves in three dimensions have also recently been put forth by Craig & Nicholls (2000). As can be seen, much of this work is quite recent, and is still ongoing.

In the present chapter we add to the investigations of these short-crested wave patterns, both in shallow and deep water, which provide an interesting medium to demonstrate applications of the Boussinesq model over a wide range of water depth. In shallow water we repeat earlier simulations of Chen & Liu (1995), who studied the effects of the incident angle on interacting cnoidal waves. Alternatively, in deep water we repeat numerically a series of experiment from Hammack & Henderson (2002, 2003) and Hammack *et al.* (2005). Our simulations share a number of common features with their physical experiments, and we provide a new explanation of the root cause of many of these features.

This chapter is organized as follows. Simulations involving the interaction of wave fronts at oblique incident angles in shallow water, resulting in hexagonal surface patterns are presented in §7.2. Similarly, simulations of their deep-water analogue, resulting in rectangular forms are presented and discussed in §7.3. Conclusions are provided in §7.4.

Parts of this chapter can be found in Fuhrman *et al.* (2004*b*) and Fuhrman *et al.* (2004*c*).

7.2 Hexagonal Surface Patterns

We begin by studying the influence of the directed wave angle on the oblique interaction of identical wave fronts propagating over a slope connecting two constant depths. For our study, we use a similar model setup as in Chen & Liu (1995), with depth defined by

$$h(x) = \begin{cases} 0.3 & x \leq 0, \\ 0.3 - 0.015x & 0 < x \leq 12, \\ 0.12 & x > 12, \end{cases} \quad (7.1)$$

where $x = 0$ is here defined as at the end of the second relaxation zone (each consisting of 25 points), which is again used to absorb the reflected wave field, see §3.5. A 50-point sponge layer is used at the end of the domain to absorb the outgoing wave field. Rather than use cnoidal waves as in Chen & Liu (1995), we simply impose two stream function (Fenton, 1988) waves at incident angles in the wavemaker region, each having period $T = 2.55$ s, waveheight $H = 0.02$ m, and wavelength $L = 4.25$ m. Two different incident angles (between the front and the y -axis) are considered, $\theta_0 = 22.5^\circ$ and 45° , which represent small and large directed wave angles, respectively. We use a 381×33 computational grid, in each case covering a full wavelength in the y -direction. For the spatial discretization we use $\Delta x = 0.1$ m,

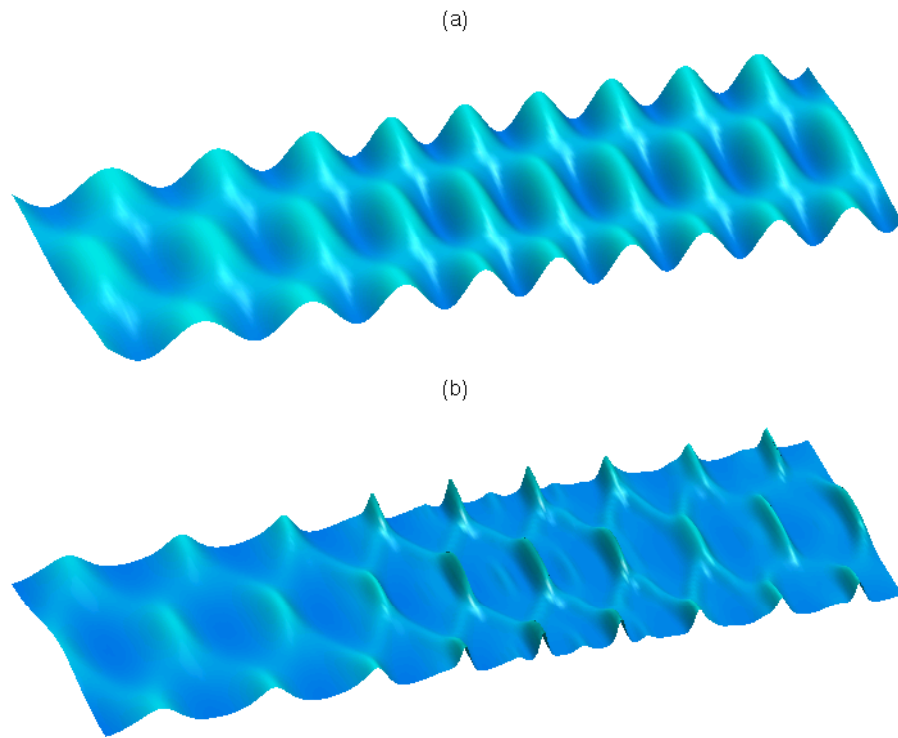


Figure 7.1: Mach stem interactions at an incident angle of 22.5° for (a) a linear and (b) a nonlinear simulation. In (b) the vertical scale is exaggerated 20 times.

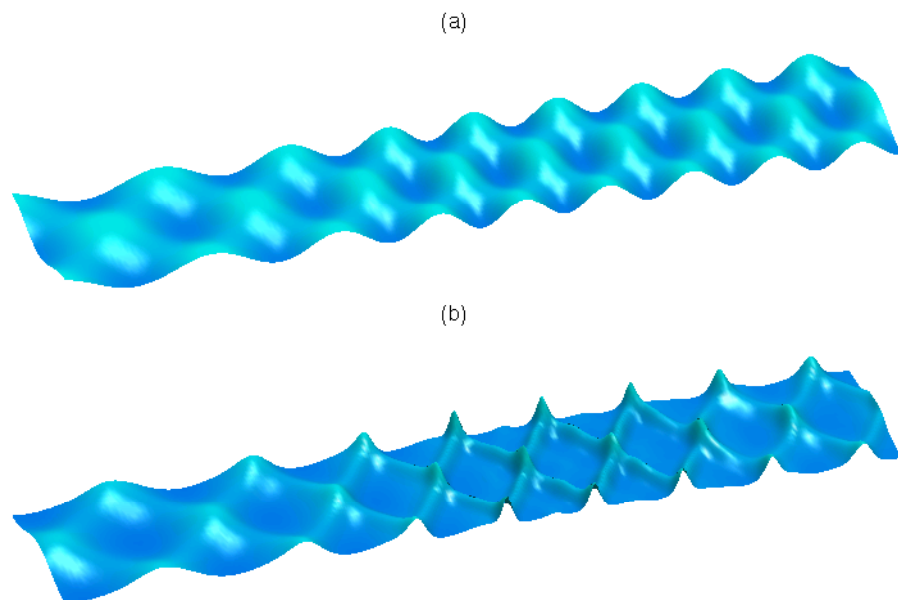


Figure 7.2: Mach stem interactions at an incident angle of 45° for (a) a linear and (b) a nonlinear simulation. In (b) the vertical scale is exaggerated 20 times.

and $\Delta y = 0.347$ m and 0.188 m with $\theta_0 = 22.5^\circ$ and 45° , respectively. For the temporal discretization we set $\Delta t = 0.085$ s, and simulations are run for 1000 time steps. A 10th-order, 85-point Savitzky-Golay smoothing filter is applied every 15 time steps.

Linear and nonlinear simulations near the end state are shown in Figure 7.1 for the case with $\theta_0 = 22.5^\circ$, and in Figure 7.2 for the case with $\theta_0 = 45^\circ$. In the deep regions, before the shoaling takes place, the differences between the linear and nonlinear simulations are rather small. On the other hand, large differences can be seen in the short-crested patterns after the step, when the waves have steepened. The case with $\theta_0 = 22.5^\circ$, Figure 7.1 (b), shows a strong interaction between the wavefronts, resulting in significantly increased transversal crest lengths. This results in the characteristic hexagonal surface patterns. The interaction is much weaker with $\theta_0 = 45^\circ$, though it is still apparent. The free surface in Figure 7.2 (b) is reasonably similar to the superposition of two cnoidal wave trains, and is distinctly different than the linear simulation, Figure 7.2 (a).

In his study of Mach reflection of a cnoidal wave from a vertical wall, Kirby (1990) showed that if the angle of incidence is small, a Mach stem¹ (Wiegel, 1964) evolves along the reflected wall. In contrast, when the angle of incidence is about 45° , the wave field exhibits an almost regular (*i.e.* superimposed) reflection pattern. This is consistent with our results, as well as with others. Figures 7.1 (b) and 7.2 (b) compare very well with similar plots in Chen & Liu (1995), see their Figure 8.

7.3 Rectangular Surface Patterns

We will now turn our attention to the deep water analogue to the hexagonal forms presented in the previous section, which result in surface patterns of a rectangular form. In the following we repeat numerically a series of physical experiments from Hammack *et al.* (2005) (see also Hammack & Henderson, 2002, 2003).

7.3.1 Model setup

For the simulations we simply use the superposition of two linear waves at incident angles with the free surface given as

$$\eta(x, y, t) = \frac{a}{2} \cos(\omega t - k_x x - k_y y) + \frac{a}{2} \cos(\omega t - k_x x + k_y y). \quad (7.2)$$

¹The phrase *Mach stem* has its origin in the field of explosives. It can be defined as the front formed by the fusion of the incident and reflected shocks from an explosion. The term is generally used with reference to a blast wave, propagated in the air, and reflected at the surface of the Earth. In the ideal case, the Mach stem is perpendicular to the reflecting surface and slightly convex (forward). The analogue within water waves arises from the nonlinear interaction between wave fronts at oblique incident angles, resulting in the extended crests apparent *e.g.* in Figure 7.1 (b).

Table 7.1: Parameters for the experiments of Hammack & Henderson (2002, 2003) for variable nonlinearity. Note: These simulations use the Fourier space preconditioner and have been run on a 2.26 GHz processor with the Absoft compiler.

Experiment	a [m]	ak	H/L	CPU [hr]	Avg. Iterations
C9	0.0024	0.15	0.048	5.85	5.79
C10	0.0032	0.20	0.064	6.17	6.41
C11	0.0039	0.24	0.078	6.58	7.05
C12	0.0047	0.29	0.094	7.23	8.21
C13	0.0055	0.34	0.110	8.25	9.92
C14	0.0063	0.39	0.126	9.48	11.95

This may be equivalently written as

$$\eta(x, y, t) = a \cos(k_y y) \cos(\omega t - k_x x). \quad (7.3)$$

Hence $a = H/2$ is the total amplitude of the incident wavefield, which consists of a stationary standing mode in the y -direction, and is progressive in the x -direction. The corresponding horizontal velocities are then

$$u_0(x, y, t) = \frac{a\omega k_x}{k} \frac{\cosh kh}{\sinh kh} \cos(k_y y) \cos(\omega t - k_x x), \quad (7.4)$$

$$v_0(x, y, t) = \frac{a\omega k_y}{k} \frac{\cosh kh}{\sinh kh} \sin(k_y y) \sin(\omega t - k_x x). \quad (7.5)$$

In nonlinear simulations we use $\tilde{\mathbf{U}} = \mathbf{u}_0$, hence the the wavemaker conditions satisfy the fully nonlinear water wave problem to first order, and are exact progressive solutions at the limit of small amplitudes. These incident conditions are particularly warranted, as they precisely match the experimental setup used by Hammack *et al.* (2005). Hence the simulations should be useful in explaining some of their observations.

Hammack *et al.* (2005) performed a number of physical experiments varying both the incident angle and wave steepness. A typical free surface from their experiments is shown in Figure 7.3, demonstrating the spectacular characteristic doubly (nearly) periodic rectangular forms. Note that from the image the patterns may actually appear hexagonal in shape, however time series measurements have confirmed that they are indeed rectangular in form, see Hammack *et al.* (2005). In this chapter we will only consider their experiments C9–C14, which use a constant incident angle with variable nonlinearity, though other simulations have also been made. The experimental setup for each case is summarized in Table 7.1. The simulations use $h = L = 0.10$ m (*i.e.* $k = 20\pi$, $kh = 2\pi$), which gives a linear period of $T = 0.253$ s ($\omega = 3.953$ s⁻¹). The wavenumbers in the two horizontal directions are chosen as $k_x = 62.03$ m⁻¹ and $k_y = 10.00$ m⁻¹ (*i.e.* $L_x = 0.1013$ m, $L_y = 0.6280$ m). Thus each wave front has an incident angle with the y -axis of $\theta_0 = \tan^{-1}(k_y/k_x) = 9.166^\circ$. For each simulation a 513×33 grid is used with the spatial discretization $\Delta x = L_x/32 = 0.003165$ m, $\Delta y = L_y/32 = 0.01963$ m,



Figure 7.3: Typical free surface from the physical experiments of Hammack *et al.* (2005). Photograph courtesy of Diane Henderson.

and the temporal discretization $\Delta t = 0.005$ s. Simulations C9-C11 use a 10th-order, 109-point smoothing filter applied every 50 time steps, while it is applied every 10 and 5 time steps for simulations C12-C13 and C14, respectively. Simulations begin with an initially flat free surface, and are run for 3501 time steps (roughly 69.2 periods) which is more than enough to reach an equilibrium. In each case the incident wave is ramped over a single period at the beginning of the simulation, and a 100-point sponge layer is used to absorb the outgoing wavefield. As the simulations are on a flat bottom, the matrix-free Fourier space preconditioner is used. Details on the required CPU times and average iterations for each simulation are also given in Table 7.1. This series of simulations is yet another clear demonstration on the effectiveness of this preconditioner, even in highly nonlinear, deep water situations.

7.3.2 Numerical results

Before discussing the nonlinear simulations, we will first demonstrate a simulation with the linearized model. The developed free surface after equilibrium is reached is shown in Figure 7.4. Here a doubly periodic wavefield propagating in a constant form for the entire length of the domain can be seen, as should be expected from linear theory. This is in contrast to the nonlinear simulations presented in what follows.

Computed free surface elevations from nonlinear simulations of cases C9, C11, and C13 are alternatively shown in Figure 7.5. A computed free surface from case C14 (at two viewing

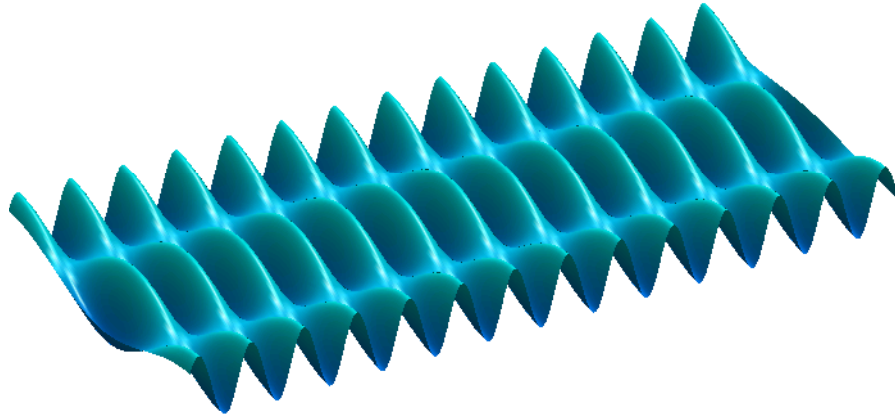


Figure 7.4: Computed water surface from a linear simulation.

angles), which is the most nonlinear case considered, is also shown in Figure 7.6. From these figures, it can be seen that the basic wave patterns are indeed rectangular in nature, consistent with known previous observations. This is characterized by the essentially flat and straight nodal regions along the channel, in contrast to the hexagonal patterns from §7.2. The rectangular patterns are also persistent *i.e.* they hold their basic form for the full length of the domain, consistent with the experiments.

From Figures 7.5 and 7.6 some interesting features can be seen. Namely, at various positions we can see both a curving and flattening of the crest-lines in the y -direction, as well as dips along the centerline. It is also clear that the waves no longer propagate in a constant form, but rather seem to modulate regularly along the x -direction of propagation. These features can most clearly be seen in Figure 7.6 (b), and become less pronounced as the wave steepness is decreased. Each of these features were also observed in the experiments of Hammack *et al.* (2005), see their Table 6.

To more clearly demonstrate the modulation in the x -direction, computed surface envelopes along the tank centerline are shown in Figure 7.7 for cases C9, C11, and C14. The first three corresponding harmonic amplitudes are also shown in Figure 7.8, which clearly shows that the long modulation is curiously due to variations in the first harmonic amplitude. We can also see a much shorter beat in the second and third harmonic amplitudes. For comparison with the experiments a time series taken from a gauge traversing along the centerline (at a velocity of 0.1059 m/s) from experiment C14 is also shown in Figure 7.9, which also clearly shows the modulating behavior in the physical experiments. From this plot the modulation takes between 6–7 s, corresponding to a length of roughly 0.64–0.74 m, which is reasonably close to what is observed in Figure 7.7. This modulating behavior of our simulations, as well as from the experiments of Hammack *et al.* (2005), is in contrast to the purely progressive (but similar) nonlinear forms computed by *e.g.* Craig & Nicholls (2002), as well as in the linear simulation from Figure 7.4.

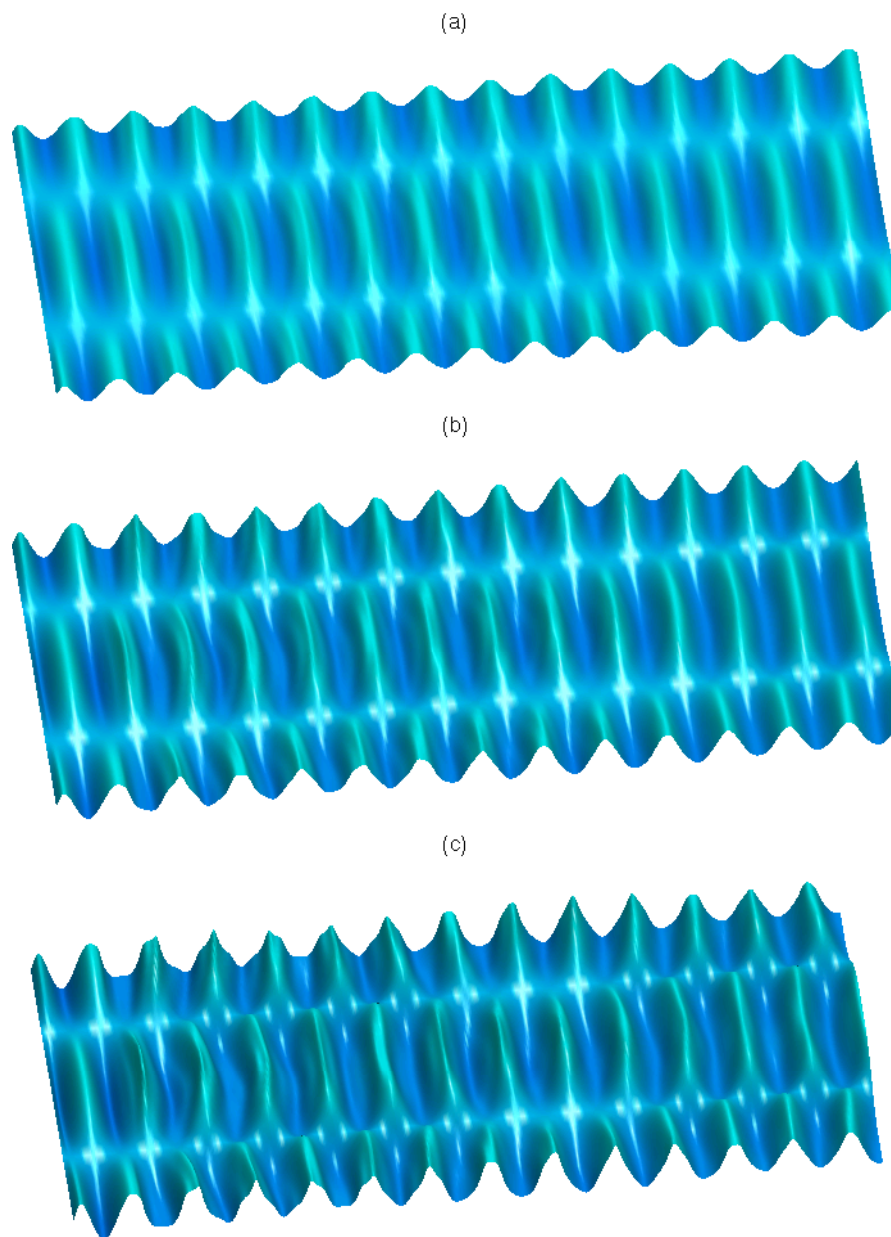


Figure 7.5: Computed water surfaces at the end of each simulation ($t = 17.48$ s). Figures (a)-(c) correspond to tests C9, C11, and C13, respectively. The vertical scale is exaggerated 10 times in these figures, and similarly for the remaining surface plots in this chapter.

7.3.3 Physical explanation

Using simple analysis concepts we will now explain the dominant features observed from the previously presented simulations, many of which have not been previously explained. We will start by considering the modulation of the second harmonic amplitude, as seen in Figure 7.8. The beat of the second harmonic is in fact a well-known artifact of using first-order

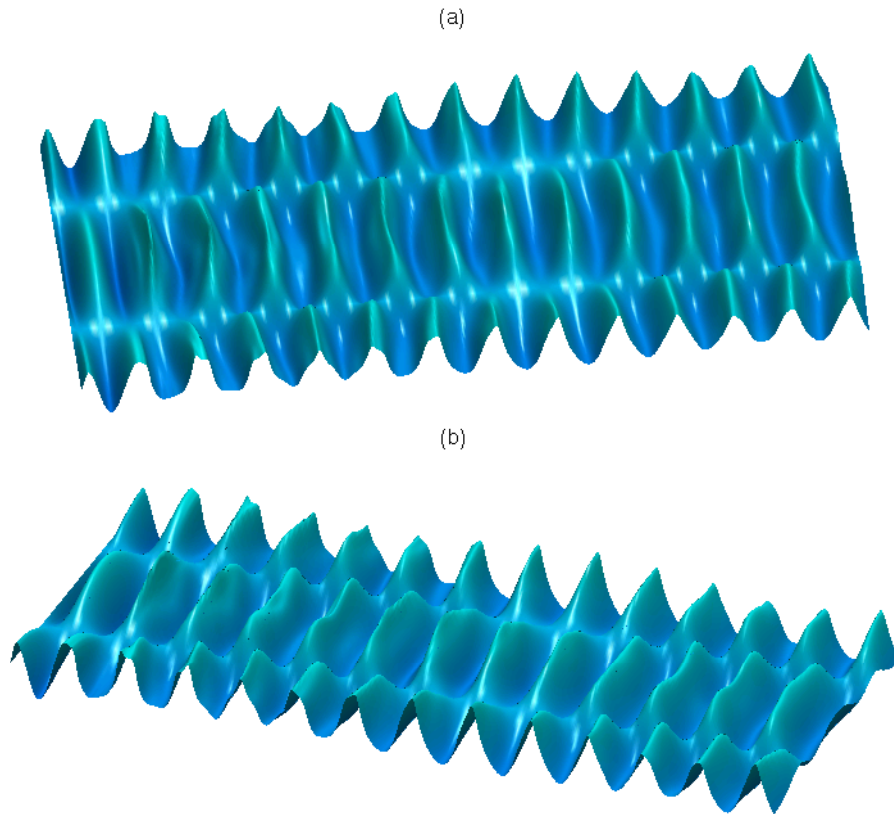


Figure 7.6: Computed free surface for experiment C14 at the end of the simulation ($t = 17.48$ s). Figures (a) and (b) show the same free surface at two different viewing angles.

incident waves in nonlinear simulations/experiments, which also occurs in a single horizontal dimension. This phenomenon has been studied experimentally by *e.g.* Boczar-Karakiewicz (1972); Buhr-Hansen & Svendsen (1974); and Chapalain *et al.* (1992); theoretically by *e.g.* Bryant (1973); Mei & Ünlüata (1972); and Mei (1983); and numerically by *e.g.* Madsen & Sørensen (1993). We will review the mechanism here, as it is somewhat more complicated when two horizontal dimensions are considered.

The second order problem can be fully characterized simply by taking a quadratic nonlinearity of the incident wave (7.3), which results in terms having the following form

$$\frac{\eta(x, y, t)^2}{O(a^2)} = \cos^2(k_y y) + \cos(2\omega t - 2k_x x) + \cos(2k_y y) \cos(2\omega t - 2k_x x). \quad (7.6)$$

Here the first term represents a set-up, which is constant in x as well as in time, while the second and third terms represent bound second harmonics. The second term is a plane wave traveling in the pure x -direction, while the third term has the same directionality as the incident wave. If these last two terms are absent in the prescribed incident wave (as is the case here, as well as in the physical experiments), the model will respond by releasing parasitic higher harmonics, which will propagate as free wave components. These will have equal amplitude but opposite phase compared to the bound waves at the wavemaker boundary.

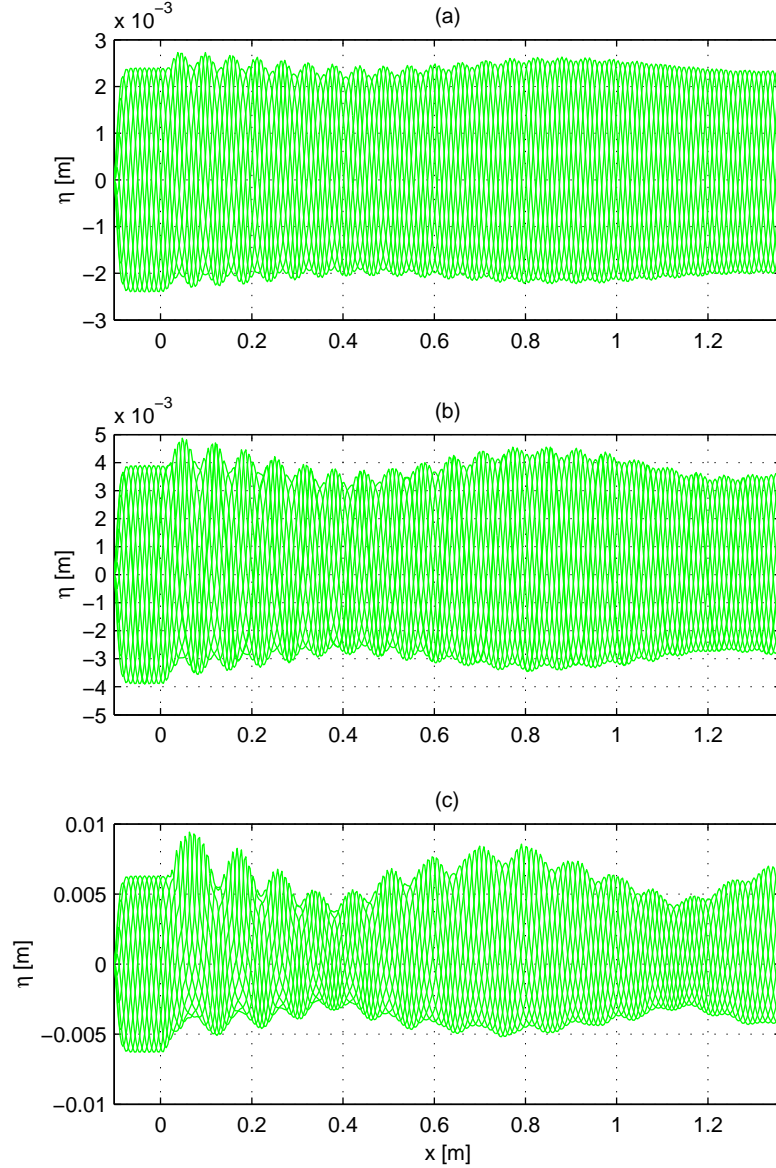


Figure 7.7: Envelope of free surface elevations along the centerline for experiments (a) C9, (b) C11, and (c) C14. The wavemaker covers the negative x region.

The free waves will match the frequency and transversal wavenumbers of the corresponding bound waves, with an adjustment to the x -wavenumber component. The second-order free wavefield will thus be of the form

$$\eta_{2f}(x, y, t) = \cos(2\omega t - 2k_{21x}x) + \cos(2k_y y) \cos(2\omega t - 2k_{22x}x). \quad (7.7)$$

As a first estimate we can assume that the free waves satisfy the linear dispersion relation, which ultimately yields $k_{21x} = 251.3 \text{ m}^{-1}$ and $k_{22x} = 248.1 \text{ m}^{-1}$. Note that $k_{21x}h \approx 25$ *i.e.* these free waves are near the upper dispersive limit of the Boussinesq model. Using simple

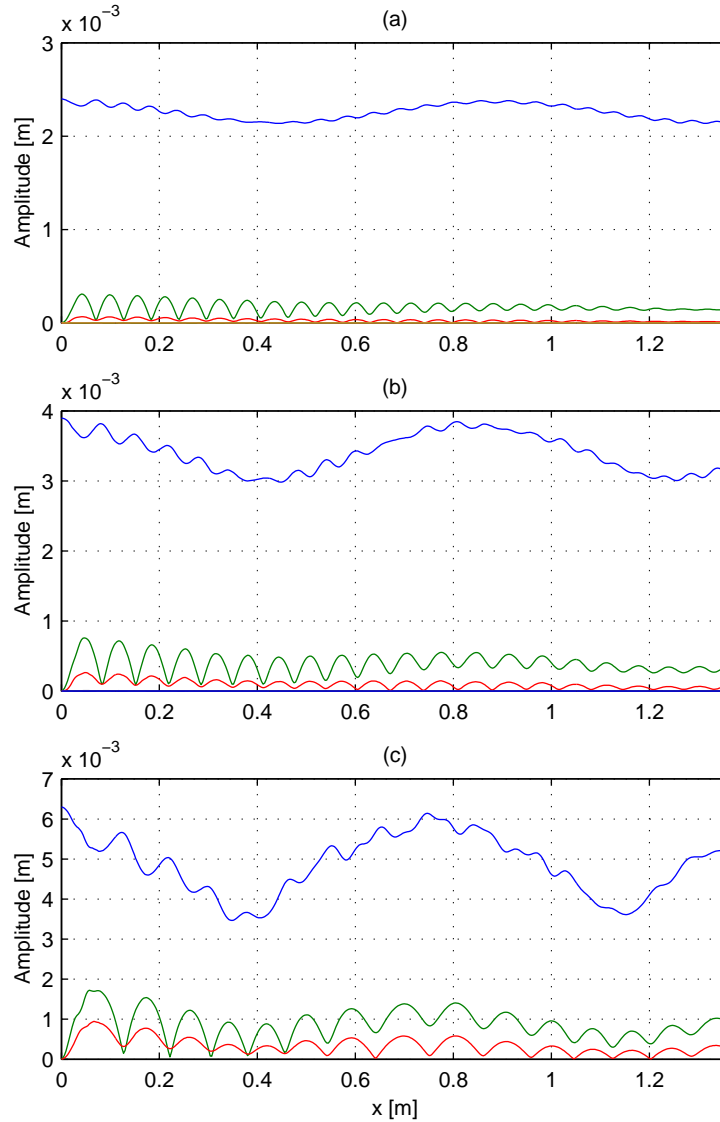


Figure 7.8: Evolution of the first three harmonic amplitudes along the centerline for experiments (a) C9, (b) C11, and (c) C14.

superposition arguments, this particular model setup in principle yields three second harmonic beat lengths. The first two are due to the difference in the x -wavenumber components of the bound and the free waves, which can be estimated as

$$\lambda_{B21} = \frac{2\pi}{2k_x - k_{21x}} = 0.0494 \text{ m}, \quad \lambda_{B22} = \frac{2\pi}{2k_x - k_{22x}} = 0.0497 \text{ m}. \quad (7.8)$$

These are almost identical, and correspond to roughly half the incident x -wavelength. The third is potentially due to the difference between the free wave components, giving

$$\lambda_{B23} = \frac{2\pi}{k_{22x} - k_{21x}} = 7.88 \text{ m}, \quad (7.9)$$

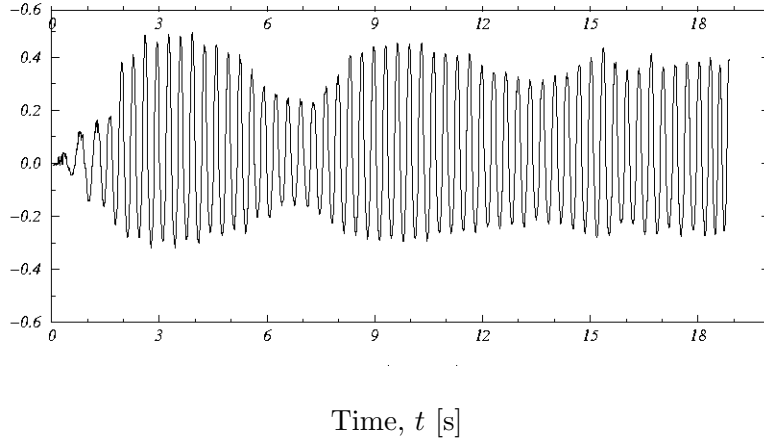


Figure 7.9: Measured surface elevation time series (in cm) from (physical) experiment C14 from a centerline traverse (taken from Hammack *et al.*, 2005). The measurements were taken from a gauge moving in the x -direction along the centerline at 0.01059 m/s.

which is much longer, spanning more than 77 x -wavelengths. The short beat in the second harmonic can clearly be seen in Figure 7.8, especially near the wavemaker. As should be expected, the beat length from the weakly nonlinear case C9, Figure 7.8 (a), nearly matches the estimates from (7.8). As $\lambda_{B21} \approx \lambda_{B22}$ it is not possible to distinguish their difference in the present simulations. It is difficult to notice the effects of the long beat in the current setup, in part due to the relatively short length of the domain. Similar simulations with a longer domain have revealed that the discretization in the x -direction is not sufficient to properly discretize the short wavelengths of the free second harmonics (*e.g.* $2\pi/k_{21x}/\Delta x \approx 7.9$ grid points per wavelength). As a result, the beat gradually decreases along the length of the channel, apparently due to numerical dissipation of the free waves (the bound harmonic persists). Direct confirmation of the longer beat will require additional future effort.

This does not, however, explain the modulation of the first harmonic, which is in many ways a much more pronounced feature of these experiments, seemingly driving many of the previously mentioned features of the wave crests. Note that Hammack *et al.* (2005) speculated that this modulation is due to a Benjamin & Feir (1967) type instability, though we do not believe this to be the case. To explain this modulation we must look to third order, which can similarly be characterized by taking a cubic nonlinearity of (7.3), yielding terms of the form

$$\begin{aligned} \frac{\eta(x, y, t)^3}{O(a^3)} = & \cos(k_y y) \cos(\omega t - k_x x) + \\ & \cos(3k_y y) \cos(3\omega t - 3k_x x) + \cos(k_y y) \cos(3\omega t - 3k_x x) + \\ & \cos(3k_y y) \cos(\omega t - k_x x). \end{aligned} \quad (7.10)$$

Here the first term satisfies the linear dispersion relation, and hence leads to secular terms (this particular component is in fact responsible for amplitude dispersion). This will be

discarded in the following, as it is not necessary to explain the phenomena of interest. The final three terms again represent bound waves. Similar to before, neglecting the last three terms in the wave generation (as we have done) will lead to the release of three corresponding free waves. These will again match the frequencies and y -wavenumbers of the corresponding bound waves, but with adjusted x -wavenumber components. Those stemming from the neglect of the second and third terms in the incident conditions will result in modulations of the third harmonic, which we will not discuss further for brevity (these free waves will in fact have kh too large for the Boussinesq model). Free waves stemming from the last term in (7.10) are more interesting, however, and will be of the form

$$\eta_{3f} = \cos(3k_y) \cos(\omega t - k_{31x}x). \quad (7.11)$$

Hence, these will indeed lead to a modulation of the first harmonic, potentially explaining the behavior seen in Figure 7.8.

To quantify the effects we will estimate the beat length for the particular model setup used in this section, again assuming that the linear dispersion relation is valid. Because these particular free waves share the incident frequency they will have identical wavenumber modulus $k = 20\pi$. The x -wavenumber component from the free wave can then be estimated directly by

$$k_{31x} = \sqrt{k^2 - (3k_y)^2} = 55.2 \text{ m}^{-1}. \quad (7.12)$$

The beat length of the first harmonic will be due to the difference in x -wavenumber components of the incident and free waves, which is due solely (at least to first order) to differences in their directionality *i.e.*

$$\lambda_{B31} = \frac{2\pi}{k_x - k_{31x}} = 0.920 \text{ m}. \quad (7.13)$$

Thus, this beat is due to the three dimensionality of the problem, and will disappear at the plane wave limit (*i.e.* when $\theta_0 = 0$). From Figure 7.8 (a) we measure a beat length of the first harmonic of $\lambda_{B31} = 0.912 \text{ m}$, a nearly perfect match. This confirms our explanation of this phenomenon.

Although these modulational effects have apparently been observed *e.g.* by Hammack *et al.* (2005), and perhaps by others, to the author's knowledge this is the first proper explanation as to their cause. Hammack *et al.* (2005) correctly predict that many of the features are indeed third-order in nature, but did not account for the release of free first harmonics as a consequence of using first-order wavemaker conditions. As can be seen from Figures 7.7 (b)–(c), 7.8 (b)–(c), and 7.9 the effects due to this third-order contribution can in fact be quite pronounced (in some cases even dominant), particularly when the wave steepness becomes moderately large. Generally, the effects on the first harmonic appear to be much more pronounced than *e.g.* the beat of the third harmonic, indicating that these three-dimensional effects are more important than corresponding two-dimensional third-order effects. That it

affects the primary frequency and results in long modulations are also particularly troublesome from an experimental viewpoint. Hammack *et al.* (2005) list (in their Table 6) a large number of features observed in their experiments, the most important of which have also been mentioned here. With the exception of their observed persistence, rectangular cell geometry, small-scale wave effects (probably due to surface tension), and perhaps oscillations in the nodal region (perhaps due to minor experimental error), it seems likely that most of these additional features can be attributed in some way to these artifacts.

The implications are in fact rather important. The recognition and understanding of the modulating phenomenon is of fundamental importance to experimentalists and modelers alike. Based on our numerical results (which are likewise supported by the physical experiments), it is seemingly *impossible* to generate steady progressive short-crested waves (of even moderate steepness) without taking into account third-order effects in the incident wavefield. This is again a direct consequence of the three-dimensionality of the problem, and the modulating effects on the first harmonic will disappear at the limit where the incident waves become plane in the y -direction. This work makes apparent the need for a complete third-order (three-dimensional) wavemaker theory, before the phenomena of truly progressive finite-amplitude short-crested waves can be properly studied in experimental wavetanks. Currently, wavemaker theory has only been developed to second-order (see *e.g.* Schäffer, 1996; Schäffer & Steenberg, 2003), which is already rather complicated. On this topic, it should finally be mentioned that Hammack *et al.* (2005) also describe an additional series of experiments using a Jacobi elliptic sine function in the transversal direction, which seems to reduce, but not eliminate these modulations in the x -direction.

7.4 Conclusions

In this chapter short-crested waves, created by superimposing two wavetrains at symmetric incident angles, are studied in both shallow and deep water. These respectively result in characteristic hexagonal and rectangular forms. Simulations in shallow water compare well with those from Chen & Liu (1995), demonstrating the ability of the Boussinesq model to treat this phenomena. In particular we confirm that the interaction of cnoidal wave fronts is strong/weak when the angle of incidence is small/large.

Deep water rectangular patterns are studied by repeating numerically a series of physical experiments from Hammack & Henderson (2002, 2003) and Hammack *et al.* (2005). A number of features observed in the experiments are very apparent in the simulations. In addition to the general persistent nature of the rectangular patterns, we clearly demonstrate both curving (forwards as well as backwards) and flattening crest-lines in the y -direction, as well as dips along the centerline, all consistent with experimental observations. These features are apparently driven by a previously unexplained modulation along the (traveling) x -direction, which our analysis clearly shows is from a corresponding modulation in the first harmonic amplitude.

The most important finding of this chapter is the new explanation that this modulation of the first harmonic is in fact an artifact of neglected third-order effects in the wave generation. At second order there is a release of parasitic free waves, causing a well-known beat of the second harmonic amplitude, which we have explained for the three-dimensional case. At third-order there is a similar release of free waves which will create modulations in both the third as well as the first harmonic. The first harmonic modulation has not been previously explained to the author's knowledge, and is likely responsible for a large number of the observed experimental features. This modulation will only occur when the generation is three dimensional, and disappears at the plane wave limit. The recognition of this phenomenon allows for a much more complete understanding of the previous physical experiments. This work also points to inadequacies of current wavemaking practice, and makes clear the need for a third-order (three-dimensional) wavemaker theory. We believe this to be necessary before (reasonably) steady progressive short-crested waves with moderate to large steepness can be produced in experimental wavetanks.

Chapter 8

A Numerical Study of Crescent Waves

Chapter Summary

In this chapter the high-order Boussinesq model is used to conduct a systematic numerical study of crescent (or horseshoe) water wave patterns in a tank, arising from the instability of steep deep-water waves to three-dimensional disturbances. The most unstable phase-locked (L2) crescent patterns are firstly investigated, and comparisons with experimental measurements confirm the quantitative accuracy of the model. The unstable growth rate is also investigated, as are the effects of variable nonlinearity. The dominant physical mechanism is clearly demonstrated (through time and space series analysis) to be the established quintet resonant interaction, involving the primary wave with a pair of symmetric satellites. A numerical investigation into oscillating crescent patterns is also included, and a detailed account of the complicated oscillation cycle is presented. These patterns are shown to arise from quintet resonant interactions involving the primary wave with two unsymmetric satellite pairs. Pre-existing methods for analyzing the stability of steep deep-water plane waves subject to three-dimensional perturbations are extended to provide accurate quantitative estimates for the oscillation period. A possible explanation for their selection in experiments is also provided. Finally, the model is used to conduct a series of experiments involving competition between various unstable modes. The results generally show that multiple instabilities can grow simultaneously, provided that they are of roughly equivalent strength. Results using random perturbations also match observations in physical experiments both in the form (*i.e.* two- or three-dimensional), as well as the location of the initial instability. The computational results further demonstrate applications of the model for the study of highly nonlinear (to the breaking point), deep-water waves in two horizontal dimensions. The efficiency of the model has allowed for a quantitative study of these phenomena at significantly larger spatial and temporal scales than have been demonstrated previously, providing new insight into the complicated physical processes involved.

8.1 Introduction

This chapter presents a numerical study of the fascinating phenomenon of ‘crescent’ or ‘horseshoe’ water wave patterns, which occur readily on the sea surface *e.g.* from the action of a fresh wind (examples in nature can be seen in the photographs from Shrira, Badulin & Kharif, 1996). Such patterns have been observed experimentally in wave tanks in the absence of wind in Melville (1982), Su *et al.* (1982), and Su (1982), as well as in its presence in Kusaba & Mitsuyasu (1986) and Collard & Caulliez (1999). These patterns are of interest for more than purely academic purposes. As noted in Annenkov & Shrira (1999), the patterns are very important from the ocean science perspective, since they modify the airflow above the surface and thus affect the air-sea momentum transfer, while also changing in a specific way radar scattering from the sea surface (Shrira, Badulin & Voronovich, 2000). Furthermore, conceptually new models for statistically describing wind-wave field dynamics become necessary in their presence (Shrira *et al.*, 1996). Such patterns are of additional interest from the nonlinear science perspective (Annenkov & Shrira, 1999). They are also important from an engineering standpoint, as they are part of the natural evolution of steep deep-water wave trains, which are commonly used as design waves for ships and other offshore structures.

These spectacular patterns have drawn the attention of numerous scientists in recent years. The inception mechanism is generally acknowledged to be the class II (three-dimensional) instability of McLean (1982*b*) (see also McLean *et al.*, 1981), who numerically analyzed the stability of steep deep-water wave trains subject to periodic disturbances. The dominant physical processes have also been recently confirmed as quintet resonant interactions using the qualitative model of Shrira *et al.* (1996), based on a modified Zakharov equation. An investigation using the model of Dommermuth & Yue (1987) can also be found in Skandrami (1997). Additional qualitative studies into the long-term sporadic nature of crescent waves can be found in Annenkov & Shrira (1999, 2001). While the two-dimensional (Benjamin & Feir, 1967), class I instability is well understood, quantitative investigations into the three-dimensional class II instability are rare. This is likely a consequence of the high computational costs associated with the three-dimensional nature of the patterns in combination with the high nonlinearity at which they occur. Recent numerical simulations with a boundary element model in Xue *et al.* (2001) have, however, demonstrated quantitatively accurate crescent forms, arising naturally from the nonlinear evolution of a perturbed plane incident wave. This ground-breaking investigation is unfortunately limited to relatively small domains and short time scales, making detailed investigations into the physical processes rather difficult.

Largely inspired by this work, the purpose of the present chapter is to perform a more extensive fully nonlinear numerical study of the class II instabilities leading to crescent wave patterns on the free surface. For this purpose the previously described numerical model based on the fully nonlinear and highly dispersive Boussinesq formulation of Madsen, Bingham & Liu (2002) and Madsen, Bingham & Schäffer (2003) is used, as described in Chapter 2. We consider significantly larger spatial and temporal scales than in Xue *et al.* (2001), paying particular attention to the complicated physical processes involved in each of the

simulations presented. Firstly, we investigate the most common phase-locked L2 patterns (as denoted in Su, 1982; Su *et al.*, 1982). The model is verified both qualitatively and quantitatively through comparison with experimental measurements. Detailed investigations into the unstable growth rate, the effects of nonlinearity, as well as the physical processes involved during the crescent wave evolution to breaking are also provided. Secondly, we present a detailed numerical investigation into the more recently observed oscillating crescent wave patterns. Through direct numerical simulation we obtain excellent qualitative and quantitative agreement with the oscillating forms observed by Collard & Caulliez (1999), while also demonstrating distinct L3 and L4 crescent patterns noted in Su *et al.* (1982) and Su (1982). Furthermore, the stability analysis of McLean (1982*b*) is extended, resulting in a quantitative explanation for each of the oscillating cases considered. A possible explanation for their selection in the experiments is also provided. Finally, we present a series of numerical experiments involving the competition of various unstable modes during their initial growth to the breaking point. These include competition between isolated symmetric (phase-locked) and unsymmetric (oscillating) class II modes, between isolated class I and II modes, as well as with random (white noise) disturbances.

The remainder of the chapter is organized as follows. The periodic perturbation of steady plane waves used to generate the crescent patterns is described in §8.2. The dominant (L2) phase-locked crescent patterns are investigated both qualitatively and quantitatively in §8.3. The different, but related oscillating patterns are investigated in §8.4. A series of numerical experiments involving the competition of various unstable modes is presented in §8.5. The issue of computational efficiency is addressed in §8.6. Finally, conclusions are drawn in §8.7.

This chapter is published in a similar form in Fuhrman, Madsen & Bingham (2004*d*). Some of the results are also presented in Madsen & Fuhrman (2004).

8.2 Crescent Wave Generation

Crescent waves are generated in this chapter by superimposing the following three-dimensional perturbations

$$\eta' = \frac{\epsilon H}{2} \sin(k'_x x - \omega' t + \beta) \cos(k'_y y), \quad (8.1)$$

$$\tilde{\mathbf{U}}' = \tilde{\mathbf{u}}' + \tilde{w}' \nabla \eta, \quad (8.2)$$

where

$$\tilde{u}' = \frac{\epsilon \sqrt{g} H k'_x}{2 (k'^2_x + k'^2_y)^{1/4}} \sin(k'_x x - \omega' t + \beta) \cos(k'_y y) \exp(\sqrt{k'^2_x + k'^2_y} \eta), \quad (8.3)$$

$$\tilde{v}' = \frac{\epsilon \sqrt{g} H k'_y}{2 (k'^2_x + k'^2_y)^{1/4}} \cos(k'_x x - \omega' t + \beta) \sin(k'_y y) \exp(\sqrt{k'^2_x + k'^2_y} \eta), \quad (8.4)$$

$$\tilde{w}' = -\frac{\epsilon\sqrt{gH}}{2} (k_x'^2 + k_y'^2)^{1/4} \cos(k_x'x - \omega't + \beta) \cos(k_y'y) \exp(\sqrt{k_x'^2 + k_y'^2}\eta), \quad (8.5)$$

over a stream function solution (Fenton, 1988) for a plane wave traveling in the $+x$ -direction, having a peak at $x = 0$ at $t = 0$. For the stream function solution we set Stokes' drift (or mean fluid transport) velocity to $c_s = 0$, to match the conditions of a closed flume. This plane incident wave has wavenumber k_0 and angular frequency ω_0 , with celerity $c = \omega_0/k_0$. In the preceding a prime superscript corresponds to a perturbation of the previously defined base variables, with $\tilde{\mathbf{U}}' = (\tilde{U}', \tilde{V}')$ and $\tilde{\mathbf{u}}' = (\tilde{u}', \tilde{v}')$. The values (k_x', k_y') are the wavenumbers of the three-dimensional perturbation. The perturbations correspond to two superimposed traveling components with equal k_x' and opposite k_y' (resulting in a stationary standing wave structure in the y -direction). Unless otherwise noted, the generated perturbation is assumed to be bound to the unperturbed wave, having angular frequency

$$\omega' = \frac{k_x'}{k_0} \omega_0. \quad (8.6)$$

This satisfies that the wavemaker region is repeated every $\left(\frac{k_x'}{k_0} - 1\right)^{-1}$ basic periods.

This method of generation has been inspired by Xue *et al.* (2001), who used similar perturbations of the free surface and velocity potential over an exact plane Stokes wave in a boundary element model. Their simulations used doubly periodic boundary conditions, thus the perturbations were applied only as initial conditions. Equations (8.1)–(8.5) generalize this idea to our particular time stepping variables and time-variant wavemaker. In all simulations the initial conditions are set to be this perturbed incident wave across the entire computational domain. Xue *et al.* (2001) found that the phase shift β had no significant effect on the overall crescent development. We have confirmed this finding (provided that ϵ is sufficiently small), and throughout this chapter we set $\beta = 0$.

8.3 Phase-Locked Crescent Patterns

8.3.1 Model discretizations

We begin the study of crescent waves by generating the common phase-locked (L2) patterns observed by Su *et al.* (1982), Su (1982), Melville (1982), Collard & Caulliez (1999), and others. The base incident wave throughout this chapter corresponds to a stream function solution with $k_0 = 1 \text{ m}^{-1}$ (*i.e.* with wavelength $L = 2\pi/k_0 = 2\pi \text{ m}$). The spatial discretization in the x -direction is taken to be $\Delta x = L/40 = 0.1571 \text{ m}$. For the water depth we use $h = L = 2\pi \text{ m}$, giving an incident wave having $k_0 h = 2\pi$, *i.e.* well beyond the practical deep-water limit. The resulting discretizations for a number of nonlinearities used in this chapter are given in Table 8.1. Each case listed corresponds to the most unstable transversal class II mode according to McLean (1982*b*) for the respective nonlinearities, and discretizations use $\Delta t = T/40$ (where T is the basic period) and $\Delta y = L_y/32$. All simulations for a given

Table 8.1: Discretizations used for crescent wave simulations with variable nonlinearity.

H [m]	H/L	T [s]	ω_0 [s^{-1}]	Δt [s]	k'_y [m^{-1}]	Δy [m]
0.4021	0.064	1.972	3.186	0.04930	1.54	0.1275
0.5969	0.095	1.931	3.254	0.04828	1.33	0.1476
0.6032	0.096	1.929	3.257	0.04824	1.32	0.1488
0.6600	0.105	1.914	3.283	0.04786	1.23	0.1596
0.6974	0.111	1.903	3.302	0.04759	1.15	0.1707
0.7980	0.127	1.873	3.355	0.04682	0.79	0.2485
0.8231	0.131	1.865	3.369	0.04663	0.65	0.3021

nonlinearity throughout this chapter use the parameters from Table 8.1. We stress that each of the discretizations satisfy linear stability criterion (see the analysis in Chapter 5, as well as Fuhrman *et al.*, 2004a), with Δt small enough to avoid potential dissipative effects from the time stepping scheme. Throughout §8.3 $k'_x = 1.5k_0$ is used for the perturbation, with $\omega' = 1.5\omega_0$.

8.3.2 The effects of smoothing filters on the growth rate

Crescent waves are a highly nonlinear phenomena, and though the discretizations used are *linearly* stable, some form of a dissipative interface is still generally necessary to maintain numerical stability. The resulting numerical instabilities (usually occurring as sawtooths at the wave crests) are due to the nonlinear terms, which tend to shift some eigenvalues of the discrete Jacobian matrix to the right half of the complex plane, as demonstrated locally in the numerical stability analysis of Fuhrman *et al.* (2004a), also presented in Chapter 5. There it is also shown that the system can be stabilized through the addition of relatively minor amounts of dissipation. Throughout this chapter we apply Savitzky & Golay (1964) smoothing filters (see also Press *et al.*, 1992) for this purpose, which have been used successfully in a number of other water wave studies (see *e.g.* Fuhrman & Bingham, 2004; Madsen *et al.*, 2002; Xue *et al.*, 2001). Fourier analysis of some of these filters is again provided in §3.6.

Although their use is commonplace, investigations into the relative effects of such smoothing filters are rarely presented. Our experience has shown, however, that it is important to recognize these effects, as they can have a profound influence on the solution, particularly on any higher harmonics which inevitably become important in nonlinear simulations. Here we present one such investigation on the effects on the growth rate of the instability, ultimately leading to crescent wave formation. We consider waves with steepness $H/L = 0.105$ on a 513×17 grid, with $\epsilon = 0.16$. Because the crescent patterns are symmetric about their centerline, it is only necessary to include half of a crescent width in the computational domain. Following Longuet-Higgins & Cokelet (1978) and Xue *et al.* (2001), we present

results in the form of a growth curve, where a root-mean-square growth rate $R(t)$ is defined as

$$R(t) = \left[\frac{\int \int \eta'(x, y, t)^2 dx dy}{\int \int \eta'(x, y, 0)^2 dx dy} \right]^{1/2}. \quad (8.7)$$

We consider the use of filters with polynomial order two, four, six, and eight; having 13, 37, 57, and 81 grid points, respectively (note that the second-order filter has a diamond shaped stencil, while the others have an octagon shaped stencil). In all simulations the filter is applied at every time step. Fourier analysis of various order filters (see again §3.6) has shown that the higher-order smoothing filters (order greater than two) have a much less pronounced effect on high frequency modes (discretized roughly with 10 or fewer grid points per wavelength), thus they provide the cleanest evolution based solely on the system of nonlinear PDEs. For each test a domain covering half a crescent width in y (17 grid points) and two full incident wavelengths in x (81 grid points) is used for the determination of $R(t)$, starting at $x = 7L$. Values for η' are obtained by subtracting the computed values for η in each simulation from those from a similar simulation using unperturbed stream function incident waves.

The resulting growth curves are presented in Figure 8.1 for the first $7T$, as is the theoretical curve based on the linear stability analysis of McLean (1982*b*). Xue *et al.* (2001) present a similar growth curve from a simulation with the same nonlinearity and ϵ using a second-order, 13-point filter (applied intermittently), which matches the theoretical curve very well. Figure 8.1 confirms their finding, demonstrating an excellent match for the first $4T$. Interesting deviations occur at later stages of growth, however. A comparison of the various smoothing filters clearly shows that the second-order smoothing filter hampers the long-term growth of the instability. This can be remedied to some degree by applying the filter intermittently *e.g.* at every other time step, however our experience has shown that the use of higher-order filters results in less interference. As demonstrated by the simulations with the higher-order filters, when the fully nonlinear evolution of these patterns is *uninhibited* (or nearly so) we obtain an accelerated growth rate for $t \geq 4T$, which significantly exceeds that predicted by the linear analysis. We remark that there is no fundamental reason to expect the fully nonlinear growth to precisely follow the theoretical linear curve after the onset of the instability, as the growth itself is due to nonlinear interactions. The very sudden appearance of these patterns as described in physical experiments supports this contention. Such an acceleration is even stated in Su *et al.* (1982), though it is doubtful that this observation is based on any quantitative information. Based on our results, we consider such an acceleration of the growth likely in the fully nonlinear evolution of these patterns. The results of all the filters with polynomial order four or higher are reasonably similar, and have a much less pronounced influence on the growth rate than does the second-order filter. We therefore adopt the fourth-order filter for the remainder of this section, unless otherwise noted. A more complete investigation of the physical processes can be found in §8.3.5, where we investigate the growth into a developed crescent wave field.

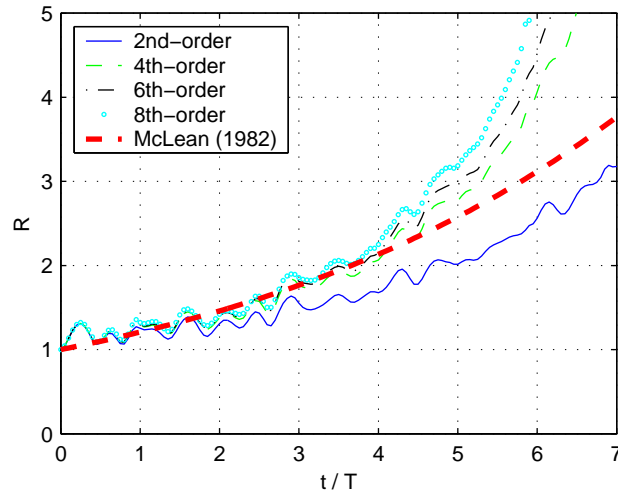


Figure 8.1: Growth rate $R(t)$ of the initial disturbance for simulations using smoothing filters with polynomial order ranging from two to eight. Also shown is the theoretical curve from the linear stability analysis of McLean (1982b), given by $e^{0.0316\sqrt{gk_0}t}$.

8.3.3 Characteristics of the L2 crescent patterns

In this section the characteristics of the phase-locked L2 crescent pattern are investigated. All results again use $H/L = 0.105$ with the fourth-order smoothing filter applied at every time step. Figure 8.2 shows computed surface elevations from simulations using $\epsilon = 0.05$ and 0.16 near their final state (*i.e.* $t = 11.45T$ and $7.45T$, respectively). Multiple widths of the computed free surface are obtained throughout simply by repeatedly reflecting the results over the y -axis. The perturbed incident waves develop very rapidly into crescent-shaped patterns, particularly with $\epsilon = 0.16$. The main effect of smaller ϵ is simply to slow the crescent growth (similar findings are discussed in Xue *et al.*, 2001). Other differences are also apparent, however. Notably, the crescents with $\epsilon = 0.16$ develop a much flatter face than do those with $\epsilon = 0.05$. Slightly after the states shown in Figure 8.2 the waves become extremely steep, and the simulations break down, almost certainly due to wave breaking. This process is consistent with the observations of Su *et al.* (1982), who repeatedly refer to the crescent patterns as ‘spilling breakers’. Throughout this chapter these computational breakdowns are characterized by a significant increase in the number of iterations required for solutions of $\mathbf{Ax} = \mathbf{b}$, and simulations are stopped after 200 iterations are reached without convergence. Figure 8.3 also shows a smaller portion of the final L2 pattern in more detail from the case with $\epsilon = 0.05$. From these figures many of the distinguishable features described by Su *et al.* (1982) and Su (1982) can clearly be seen: The waves have noticeable front-back asymmetry – with the steepest part of the wave occurring on the front face, the crests are shifted by one-half the width of the crescents on successive rows (*i.e.* the L2 pattern), deep troughs appear in front of the crescent face, and flattened troughs are evident directly behind the crests.

Figure 8.4 shows contour plots at two locations from the simulation with $\epsilon = 0.16$. The

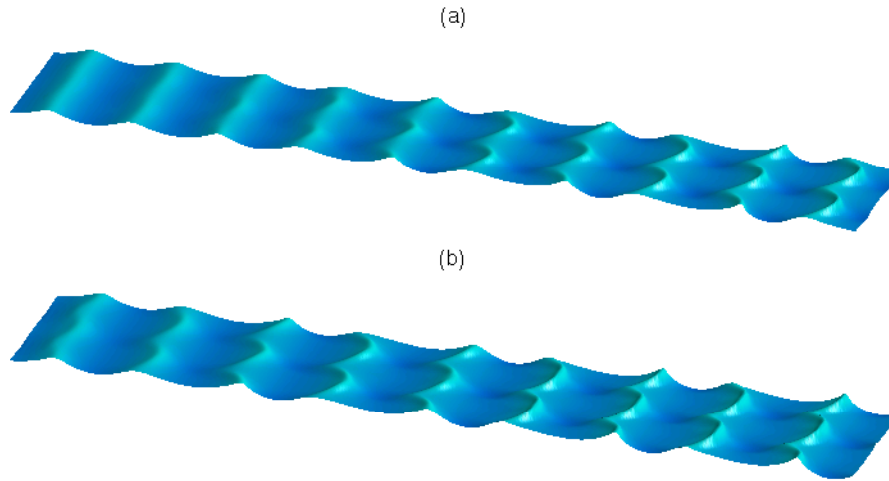


Figure 8.2: Computed free surfaces (to scale) for L2 crescent waves with $H/L = 0.105$ for (a) $\epsilon = 0.05$ at $t = 11.45T$, and (b) $\epsilon = 0.16$ at $t = 7.45T$.

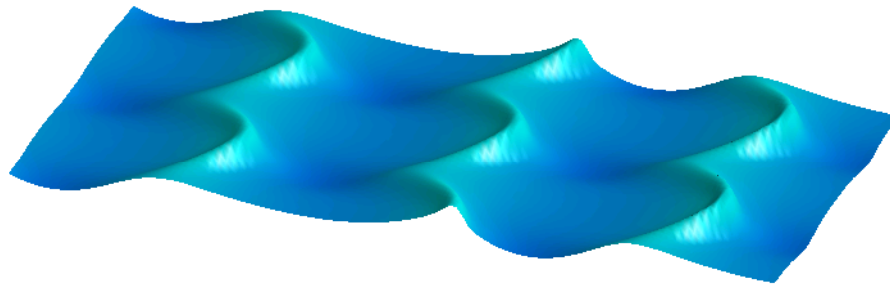


Figure 8.3: Computed free surface (to scale) for L2 crescent waves with $H/L = 0.105$ and $\epsilon = 0.05$ at $t = 11.45T$.

flattened troughs behind each crescent, and the deep troughs in front of each crescent face are again very apparent. Figure 8.4 (a) demonstrates some additional interesting features – namely a steepening of the crescent ‘shoulders’, and a rising ‘Delta’ region in front of the crescent face. Similar features were also observed in the simulations of Xue *et al.* (2001), just prior to breaking, and this figure compares qualitatively quite well with their Figure 12. These features have disappeared in the state shown in Figure 8.4 (b), however, with the steepest part of the wave occurring along the crescent center. This is consistent with the description of Su *et al.* (1982), who clearly report spilling breakers over the front (central) face of the wave. Contour plots from the simulation with $\epsilon = 0.05$ are similar to Figure 8.4 (b), again having a less flattened face, with the steepest part of the wave at the center.

Having established that the model results are qualitatively similar to those observed in physical experiments and in previous computations, we now attempt to validate the model in a more quantitative manner. As noted in Shrira *et al.* (1996), despite their seemingly common character and easiness of observation, quantitative experimental information available for

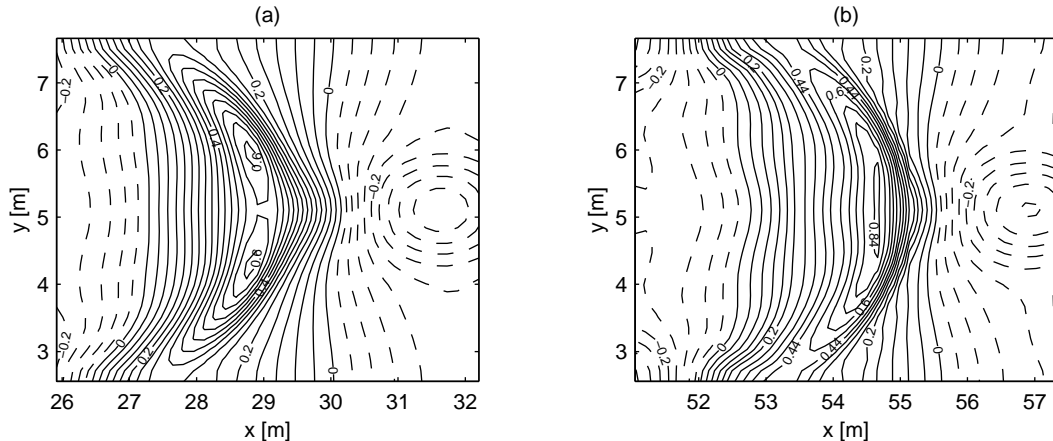


Figure 8.4: Contour plots from simulations with $H/L = 0.105$ and $\epsilon = 0.16$ at $t = 7.45T$ beginning at (a) $x = 4.125L$ and (b) $x = 8.125L$. Note that in (b) the contour interval varies for $\eta > 0.2$ (it is constant between each labeled contour).

such patterns is rather meager. Su (1982), however, does give some characteristic ratios for a typical L2 crescent wave generated using an incident wave of this nonlinearity. Note that there is seemingly a mistake in the definition for h_{12} in Su (1982), Figure 12. We adopt the measures used in Su *et al.* (1982) and Xue *et al.* (2001) for comparison here, which are shown in Figure 8.5 (a) along $y = L_y/2$. Also shown in Figure 8.5 (b) is the free surface along $y = L_y/4$, which is qualitatively similar in form to a plane Stokes wave and compares well with similar plots in Su (1982) and Xue *et al.* (2001).

Table 8.2 gives a quantitative comparison of the characteristic ratios from Figure 8.5 (a) with those reported in Su (1982) for both simulations, *i.e.* with $\epsilon = 0.05$ and 0.16 . As we have shown, our simulations result in continually developing patterns, thus measurements are taken at full-period intervals for comparison. As can be seen in Table 8.2, the results from both simulations compare with the experimental measurements quite well. The computed results are similar in quality to those obtained from the boundary element model of Xue *et al.* (2001). Notable exceptions are the results for λ_2/λ_1 , which match the experiments better than those of Xue *et al.* (2001), who attributed this to possible lower accuracy in the measurements (another possible explanation is their use of periodic boundaries in x , which do not allow for free adjustment of the lengths in this direction). The computed results for the maximum slope of the water surface s_{max} (calculated here using a centered second-order finite difference approximation) initially match quite well with the first (lower) value of $s_{max} = 0.65$ given by Su (1982) (as well as those obtained in Xue *et al.*, 2001). As the simulations progress the waves steepen significantly, and surface slopes closer to the second (and significantly higher) reported value of $s_{max} = 1.02$ are obtained. A precise indication of where breaking occurs is unfortunately beyond the capabilities of the present model, though we speculate that it roughly corresponds to the point of computational breakdown. In general the computed results are quite acceptable, and give confidence that the Boussinesq model is capable of reproducing this deep-water, highly nonlinear phenomenon accurately.

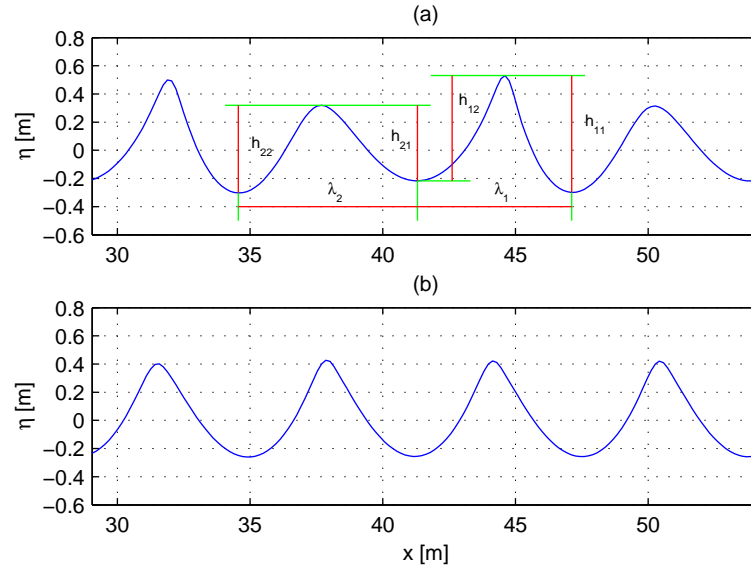


Figure 8.5: Computed free surface elevations at $t = 10T$ with $H/L = 0.105$ and $\epsilon = 0.05$ along (a) the crescent centerline $y = L_y/2$ and (b) $y = L_y/4$.

Table 8.2: Characteristic ratios for measured and computed phase-locked L2 crescent wave patterns with $H/L = 0.105$ (at full-period intervals).

	Su (1982)	$\epsilon = 0.05$				$\epsilon = 0.16$			
		$t/T = 8$	9	10	11	4	5	6	7
λ_2/λ_1	1.28	1.16	1.16	1.22	1.29	1.22	1.26	1.16	1.22
h_{11}/h_{12}	1.10	1.11	1.11	1.18	1.19	1.13	1.23	1.15	1.30
h_{21}/h_{22}	0.88	0.89	0.86	0.78	0.74	0.86	0.77	0.81	0.67
h_{11}/h_{21}	1.66	1.36	1.55	1.80	2.05	1.44	1.62	1.79	2.11
s_{max}	0.65, 1.02	0.51	0.66	0.79	1.42	0.62	0.59	0.83	0.92

8.3.4 The effects of nonlinearity

We will now use the model to demonstrate the effects of variable nonlinearity on the general features of the phase-locked L2 class of crescent pattern. We consider cases with $H/L = 0.096, 0.111, 0.127,$ and 0.131 . The simulation with $H/L = 0.096$ uses $\epsilon = 0.16$, while the others use $\epsilon = 0.05$. Each simulation uses the spatial and temporal discretizations from Table 8.1, again corresponding to the most unstable transversal class II mode for each nonlinearity according to McLean (1982*b*). Such a demonstration is quite demanding given the high wave steepness of even the incident carrier waves, and a model with excellent nonlinear characteristics in deep water is essential for this task.

Figure 8.6 shows computed free surface elevations near the end of each simulation (with the exception of the case with $H/L = 0.096$, due to severe steepening of the wave fronts). We

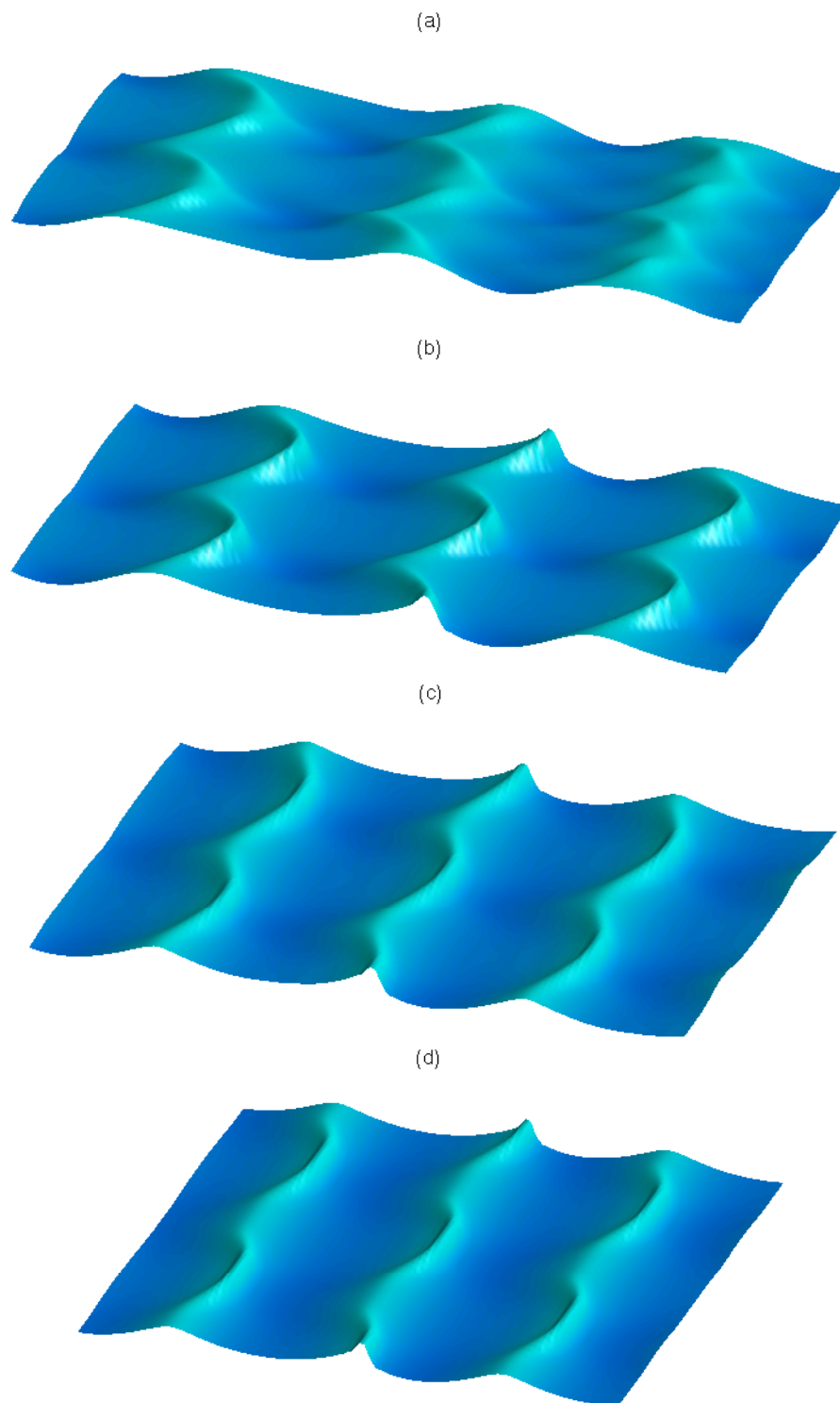


Figure 8.6: Computed free surfaces (to scale) for phase-locked L2 crescent wave patterns with (a) $H/L = 0.096$, $t = 50T$; (b) $H/L = 0.111$, $t = 8.7T$; (c) $H/L = 0.127$, $t = 4.2T$; and (d) $H/L = 0.131$, $t = 3.95T$.

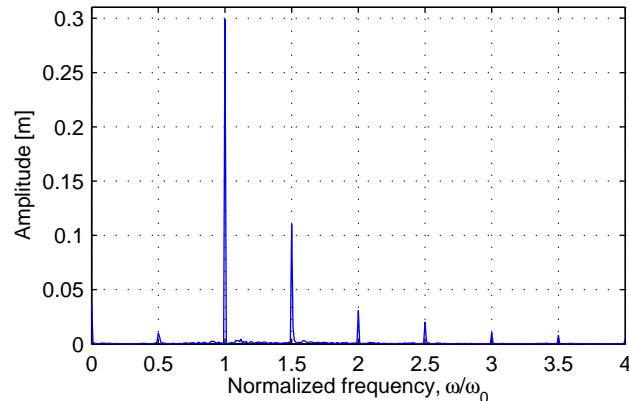


Figure 8.7: Computed Fourier amplitudes from an L2 crescent wave simulation ($H/L = 0.096$, $\epsilon = 0.16$) from a time series at $(x, y) = (5L, L_y/2)$ using time steps 1001-5001.

mention that this point is reached very quickly with simulations having $H/L = 0.127$ and 0.131 , after $4.2T$ and $3.95T$, respectively. The results with $H/L = 0.096$ are noticeably less defined than the others, presumably due to the relative weakness of the instability at this nonlinearity. Interestingly, the rising crescent shoulders noted previously in §8.3.3 are again apparent in this simulation. The results with $H/L = 0.111$ are quite similar to the previously shown results in Figure 8.3 (with $H/L = 0.105$). As the nonlinearity is further increased the dominant instability significantly increases its length in the y -direction (as predicted by McLean, 1982*b*, and indicated in Table 8.1), resulting in much wider patterns with less pronounced crescent tails, as can be seen in Figures 8.6 (c) and (d). The deepened trough regions in front of the crescent faces are also nearly absent in these patterns. This may simply be due to a lack of overall development before computational breakdown, however.

8.3.5 Discussion of physical processes

To provide an indication of the physical processes involved in the phase-locked L2 crescent patterns, computed Fourier amplitudes from the simulation with $H/L = 0.096$ and $\epsilon = 0.16$ are shown in Figure 8.7. We mention that, as pointed out by McLean (1982*b*), the three-dimensional class II instability does not become dominant until $H/L \approx 0.10$. However, the nonlinearity used here is close enough to this value to be physically relevant. Moreover, this simulation is quite useful, as it does not result in a computational breakdown within the model domain. Hence, enough data is available to perform an accurate time series analysis, providing insight into the dominant physical processes involved. The current simulation is stopped after 5000 time steps (*i.e.* $125T$). As seen in Figure 8.7, in addition to the primary wave and its higher (bound) harmonics ($\omega/\omega_0 = 1, 2, 3$), the figure shows very clear spikes at $\omega/\omega_0 = 0.5, 1.5, 2.5$, and 3.5 , with the amplitude at $\omega = 1.5\omega_0$ being by far the largest. This provides very strong evidence that the dominant physical process for the modeled L2 crescent patterns is indeed the established quintet resonant condition identified in Shrira

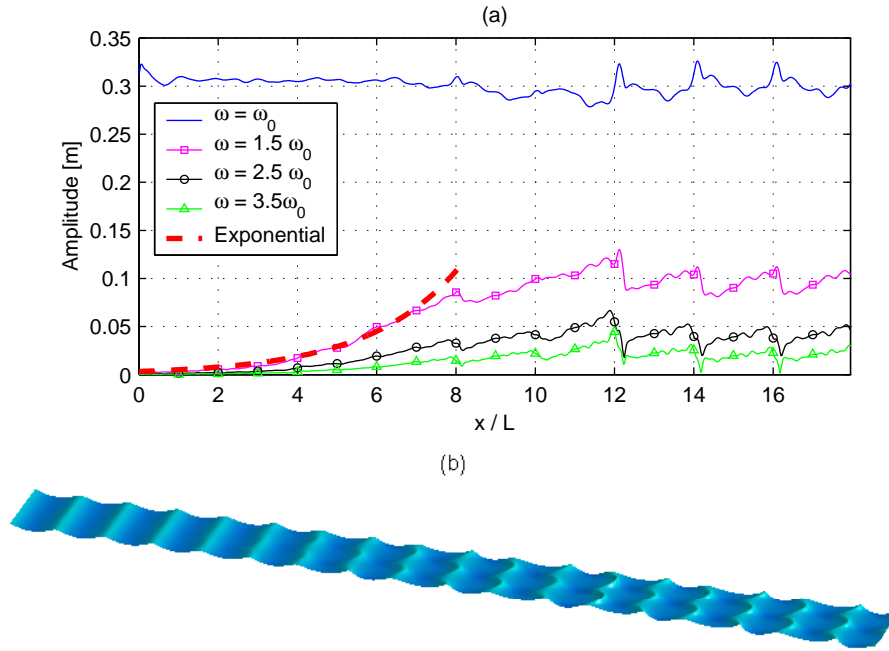


Figure 8.8: Computed (a) harmonic amplitudes and (b) free surface (to scale) at $t = 17.95T$ from an L2 crescent wave simulation with $H/L = 0.105$ and $\epsilon = 0.01$. The exponential curve in (a) is given by $\frac{\epsilon H}{2} e^{1.15 - 0.0316\sqrt{gk_0}(x/c_g)}$.

et al. (1996). This condition satisfies

$$\mathbf{k}'_1 + \mathbf{k}'_2 = 3\mathbf{k}_0, \quad \omega'_1 + \omega'_2 = 3\omega_0, \quad (8.8)$$

where $\mathbf{k}_0 = (k_0, 0)$. In the general L2 case this corresponds to a symmetric pair of satellites, *i.e.* $\mathbf{k}'_1 = (1.5k_0, k'_y)$ and $\mathbf{k}'_2 = (1.5k_0, -k'_y)$, with $\omega'_1 = \omega'_2 = 1.5\omega_0$. Additional triad interactions between the primary wave and the $\omega = 1.5\omega_0$ and $2.5\omega_0$ harmonics, as well as with the $\omega = 2.5\omega_0$ and $3.5\omega_0$ harmonics are also apparent. These interactions are of secondary importance, however they likely become more significant as the evolution progresses and the waves steepen. Figure 8.7 compares particularly well with the spectrum given in Collard & Caulliez (1999) (also those from Su, 1982) for an experimentally observed L2 pattern, giving further confidence in the Boussinesq model. Fourier amplitudes from other x -locations have been found to be very similar. Also noteworthy is the relative insignificance of the $\omega = 0.5\omega_0$ subharmonic. This is consistent with triad interactions in deep water for which the subharmonic energy transfer is less than the superharmonic transfer.

To gain even further insight, Figure 8.8 shows computed harmonic amplitudes and the free surface at the end state from a simulation using $H/L = 0.105$ and $\epsilon = 0.01$ on a 1025×17 computational grid, again with the fourth-order smoothing filter. The small value for ϵ likely provides a development more in line with a truly infinitesimal disturbance. This simulation lasts for $17.95T$, and the harmonic analysis uses a linear-least-squares fit from data covering

the final $2T$ to give an indication of the final evolved state. We stress that by analyzing the evolution at the end of the simulation rather than at the beginning (as was in part done in §8.3.2), we are now demonstrating the nonlinear growth into an existing wave field, which results in some rather interesting behavior.

In Figure 8.8 (a) an initial exponential growth along the channel for each of the higher harmonics is clearly demonstrated for $0 < x < 7L$. The close match with the exponential curve for the $\omega = 1.5\omega_0$ harmonic suggests a fully nonlinear growth rate near the end of the simulation of roughly 1.15 times larger than that predicted by the linear analysis of McLean (1982*b*). This is consistent with the accelerated growth at the later stages in Figure 8.1. It should be mentioned that the stability analysis corresponds specifically to infinitesimal perturbations of a plane progressive wave train, thus the deviation presented here (involving progression into a developed wave field) may not be altogether surprising. The development in these circumstances is equally important, however, as it corresponds to the state most often observed in wave tank experiments. Note that the growth of the $\omega = 1.5\omega_0$ harmonic for $x < 4L$ follows the theoretical growth quite closely, thus we can still confirm growth rates near the inception similar to the theoretical value of $0.0316\sqrt{gk_0}$ (see Table 8.3 in §8.4.3). Similar harmonic analyses using data from earlier time spans have shown that the $\omega = 1.5\omega_0$ harmonic gradually climbs the exponential curve along x at a rate approximately equal to the deep-water group velocity $c_g = c/2$, *i.e.* roughly matching the curve up to $x = c_g t$ as time progresses. The strength of the harmonic effectively levels downstream of this location. For example, in the present simulation this suggests a deviation from the exponential curve at the end state at $x \approx c_g 17.95T \approx 9L$. As mentioned previously, the deviation in Figure 8.8 begins at $x \approx 7L$, the difference being precisely the equivalent length of the time span used in the harmonic analysis. Just after the point shown in Figure 8.8 (b) the wave front at $x \approx 12L$ steepens, and the simulation breaks down.

Figure 8.8 also provides interesting insight into the harmonic composition of the crescent waves at various stages in their development. In Figure 8.8 (b) crescent patterns have clearly emerged at $x \approx 7L$, but they are not so well defined. For $7L < x < 12L$ the higher harmonics maintain a slowed evolution, sharpening the characteristics of the crescent patterns. From Figure 8.8 (a) the fully nonlinear physical process is again seen to be a complicated combination of resonant quintet interactions, with quadratic nonlinearities forcing additional $\omega = 2.5\omega_0$ and $3.5\omega_0$ harmonics. The basic quintet interaction results in the characteristic crescent patterns, while the higher harmonics add definition to the observed forms. Computed Fourier amplitudes from a space series of free surface elevations are also shown in Figure 8.9 along $y = L_y/2$. Spikes are again apparent at $k = 1.5k_0$, $2.5k_0$, and $3.5k_0$, clearly indicating that each of the higher harmonics is bound to the carrier wave (*i.e.* each having the same celerity $\omega/k'_x = \omega_0/k_0$).

We finally remark, that there is some contention in the literature on the role of dissipation in the formation of crescent wave patterns. Shrira *et al.* (1996) concluded that, within the framework of their Hamiltonian system, it is not possible to explain the emergence of any long-lived three-dimensional patterns. In a re-appraisal of their system, however, Craig (2001) found that three-dimensional crescent-shaped waves indeed occur, and that these

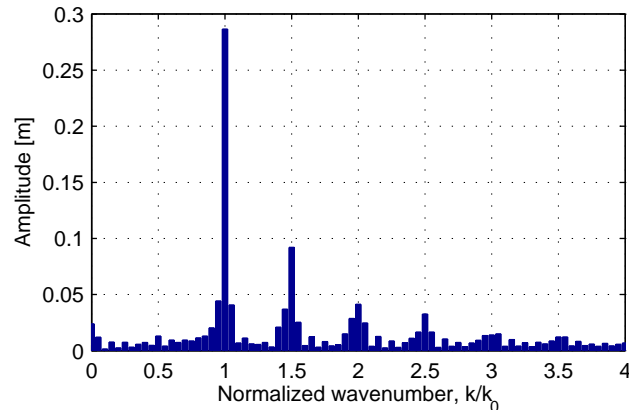


Figure 8.9: Computed Fourier amplitudes from an L2 crescent wave simulation with $H/L = 0.105$, and $\epsilon = 0.01$ from a space series at $t = 17.95T$, along $y = L_y/2$. The analysis uses grid points 126–925.

solutions are of permanent form, without the presence of breaking or other mechanisms of dissipation. Xue *et al.* (2001) also argue that crescent patterns arise naturally from nonlinear wave evolutions, which in our view seems quite logical given that they are initiated by the class II instability (which assumes no dissipation). In the present numerical study (as well as in Xue *et al.*, 2001), we do add light numerical smoothing to prolong our simulations in these highly nonlinear circumstances, therefore one may argue that we can hardly discriminate between conservative and dissipative cases. We have, however, also made simulations without smoothing, which lead to essentially similar crescent patterns (albeit noisy and less developed). Hence, we are convinced that the smoothing plays a relatively minor role in the developments presented here (in line with §8.3.2), and agree with Xue *et al.* (2001) and Craig (2001), that crescent waves can indeed develop without dissipation. In none of our simulations do they take a permanent form, however. The present model suggests a complicated evolution of the crescent waves, consisting of three distinct periods: (1) An initial linear growth (initiated by the class II instability), (2) an accelerated nonlinear growth fueled by resonant quintet interactions, and (3) a breaking stage. Thus, we feel it is likely the dissipation due to breaking that ultimately counteracts the unstable growth, resulting in waves of relatively constant form as observed *e.g.* in Su *et al.* (1982).

8.4 Oscillating Crescent Patterns

Having examined the phase-locked crescent wave patterns, we now turn our attention to those with an oscillating nature – where well-defined crescents no longer propagate in a quasi-steady form, but emerge and disappear repeatedly, shifting by a half-width in the y -direction with each successive emergence. Such oscillating patterns have been recently observed in a wave tank in a very pure form by Collard & Caulliez (1999). Deviations from the ‘standard’ L2 pattern were also reported in the experiments of Melville (1982), as

well as in Su *et al.* (1982) and Su (1982) (*i.e.* the L3 and L4 patterns). In this section we investigate the long-term evolution of crescent wave forms initiated by a double perturbation. All simulations in this section use a 513×17 computational grid.

8.4.1 Transition from $(k'_{x1}, k'_{x2}) = (\frac{4}{3}, \frac{5}{3})k_0$ to $(1, 2)k_0$

For the generation of oscillating crescent waves we first consider a simulation using a double perturbation (both as described in §8.2), with $k'_{x1} = \frac{4}{3}k_0$, $k'_{x2} = \frac{5}{3}k_0$, and $k'_{y1} = k'_{y2} = 1.32k_0$, superimposed over stream function incident waves with $H/L = 0.096$. Such a perturbation initially excites quintet resonant interactions involving the primary wave and two sets of un-symmetric satellites. Recall that the perturbation in §8.2 is equivalent to the superposition of two traveling components with $\pm k'_y$, thus two sets of resonant conditions are indeed satisfied. For both perturbations $\epsilon = 0.08$ is used, and the corresponding frequencies are defined according to (8.6), *i.e.* $\omega'_1 = \frac{4}{3}\omega_0$ and $\omega'_2 = \frac{5}{3}\omega_0$, which again assumes bound perturbations. The perturbation wavenumbers define the initial conditions throughout the computational domain, while the frequency perturbations are only imposed at the wavemaker. Thus, if the two do not satisfy a naturally occurring quintet resonant interaction we can expect a transition to occur. We wish to investigate the long-term nature of this generation, thus we use an extended simulation run for 5000 time steps (*i.e.* $125T$). The fourth-order smoothing filter is again applied at each time step.

Computed free surfaces are shown in Figure 8.10 at six instants, which give a good indication of the overall model development. Consistent with the observations from a reasonably similar simulation in Xue *et al.* (2001) (lasting for slightly more than $4T$), our simulations indicate that unlike the L2 case (with $k'_x = 1.5k_0$), the initial patterns are no longer bound to the carrier waves. Rather, the individual crescents oscillate. Figures 8.10 (a) and (b) show typical free surfaces early in the simulation (at $t = 4.1T$ and $8.8T$, respectively), which compare reasonably well to Figure 19 in Xue *et al.* (2001). Note that at this point in the simulation the pattern at the downstream end of the domain is repeated every $3L$, as specified by the initial conditions with $(k'_{x1}, k'_{x2}) = (\frac{4}{3}, \frac{5}{3})k_0$. By following the marked carrier wave from Figure 8.10 (a) to (b) it is seen that half of a complete oscillation cycle takes roughly $4.7T$, implying a full oscillation period of $T^* \approx 9.4T$. An explanation of the wavenumber and frequency combinations involved in the oscillating patterns is provided at the end of the current section.

Figure 8.10 (c) shows a slightly more evolved state (at $t = 14.2T$), where the model is in a transitional period *i.e.* the pattern generated from the initial conditions is indeed transitioning to one forced from the frequency disturbance at the wavemaker. Near the wavemaker region in Figure 8.10 (c) the crescent patterns are repeated roughly every carrier wavelength, and are beginning to oscillate in phase with one another. Near the end of the domain a distinct L3 pattern having the high-high-low (HHL) structure reported in Su *et al.* (1982) and Su (1982) is apparent. This is the first clear computation of such a pattern to the authors'

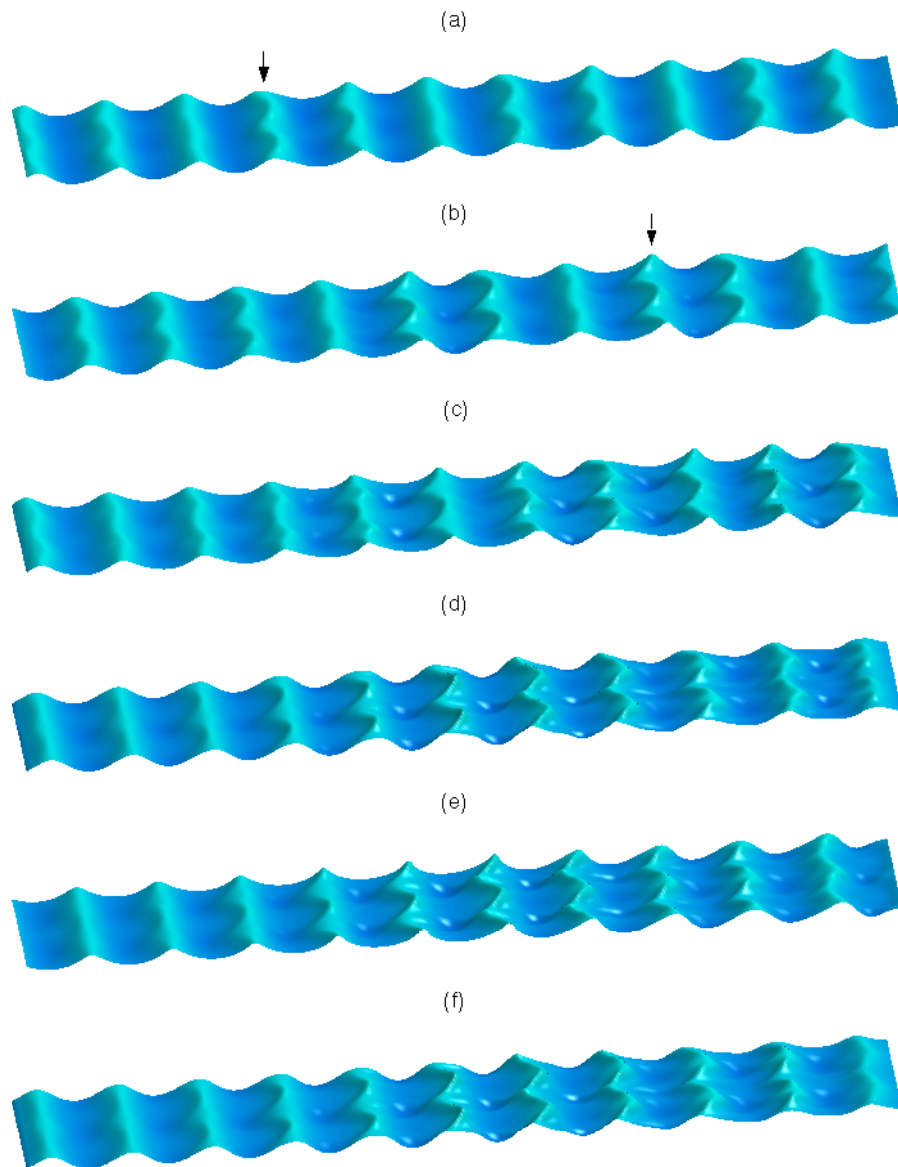


Figure 8.10: Evolution of oscillating crescent waves (transitioning from $(k'_{x1}, k'_{x2}) = (\frac{4}{3}, \frac{5}{3})k_0$ to $(1, 2)k_0$) at (a) $t = 4.1T$, (b) $t = 8.8T$, (c) $t = 14.2T$, (d) $t = 30.3T$, (e) $t = 31.8T$, and (f) $t = 33.3T$. The vertical scale is exaggerated two times.

knowledge. We stress that this formation occurs momentarily, and does not progress as a constant form.

As time evolves further the initial conditions become washed out of the computational domain, and the structured oscillations prevail throughout the computational region, as shown in Figure 8.10 (d). At this point the resulting patterns are strikingly similar to the recently observed oscillating crescent patterns of Collard & Caulliez (1999), which have a similar arrangement, and are reported to oscillate with a period of $T^* \approx 3T$. This resemblance could in fact be expected, as the perturbation frequencies at the wavemaker are reasonably close to the measured values from Collard & Caulliez (1999) of $1.36\omega_0$ and $1.64\omega_0$. Computed free surfaces are shown again $1.5T$ later during the next clear instance of crescent formation in Figure 8.10 (e). Here the crescents have shifted by one-half a crescent width in the y -direction from the formation in Figure 8.10 (d), in agreement with the description of Collard & Caulliez. Finally, Figure 8.10 (f) shows the computed free surface after another $1.5T$, where the crescents have shifted back to their original position shown in Figure 8.10 (d). This type of oscillating pattern prevails for the remainder of the simulation. A complete oscillation cycle as seen from Figures 8.10 (d) to (e) to (f) is indeed $T^* \approx 3T$ – in excellent agreement with the physical experiments.

Each crescent in the oscillating formation follows a complicated modulation pattern, which has not been previously detailed. In an attempt to fill this gap, the modulation of a single crescent wave is provided in Figure 8.11, beginning at $x = 5.25L$ and $t = 33T$. At this point in time the initial conditions are completely washed out of the computational domain, and the model is clearly in a repeating state of dynamic equilibrium. Figure 8.11 (a) begins just after the formation of a newly developed crescent, having peaks at $y = 0$, L_y , and $2L_y$. Notably, at this point in the evolution – where the crescent is near its most developed state – the deepened trough regions in front of and behind the crests are nearly absent. The waves pass through this state very quickly, providing a good means for a more precise estimation of the oscillation period. Soon after this state the crescent tails rise slightly and the crests begin to flatten, as shown in Figure 8.11 (b). Note that here deepened troughs are beginning to emerge following the crescent tails. The crests continue to flatten, until becoming nearly level, as shown in Figure 8.11 (c). At roughly this point the troughs following the crescent tails are at their most defined state. The crests continue to flatten until becoming nearly straight, as shown in Figure 8.11 (d). The tails then begin to push forward, fueling small spikes emerging from the wave crests, as shown in Figure 8.11 (e). The tails continue their collapse and the spikes enlarge, eventually forming entirely new crescents, as seen in Figure 8.11 (f). The trough regions following the crescent tails are again nearly absent in this figure, as was the case in Figure 8.11 (a). Note also that the crescent forms in Figure 8.11 (f) have shifted one-half a crescent width in the y -direction from the beginning form seen in Figure 8.11 (a).

From the point shown in Figure 8.11 (f), the waves follow a similar process, eventually arriving back to a state resembling that shown in Figure 8.11 (a). This can be seen in the evolution from Figure 8.11 (f) to (j). From Figure 8.11, this particular cycle in fact takes slightly longer than the previously mentioned $3T$. Our results indicate that this figure

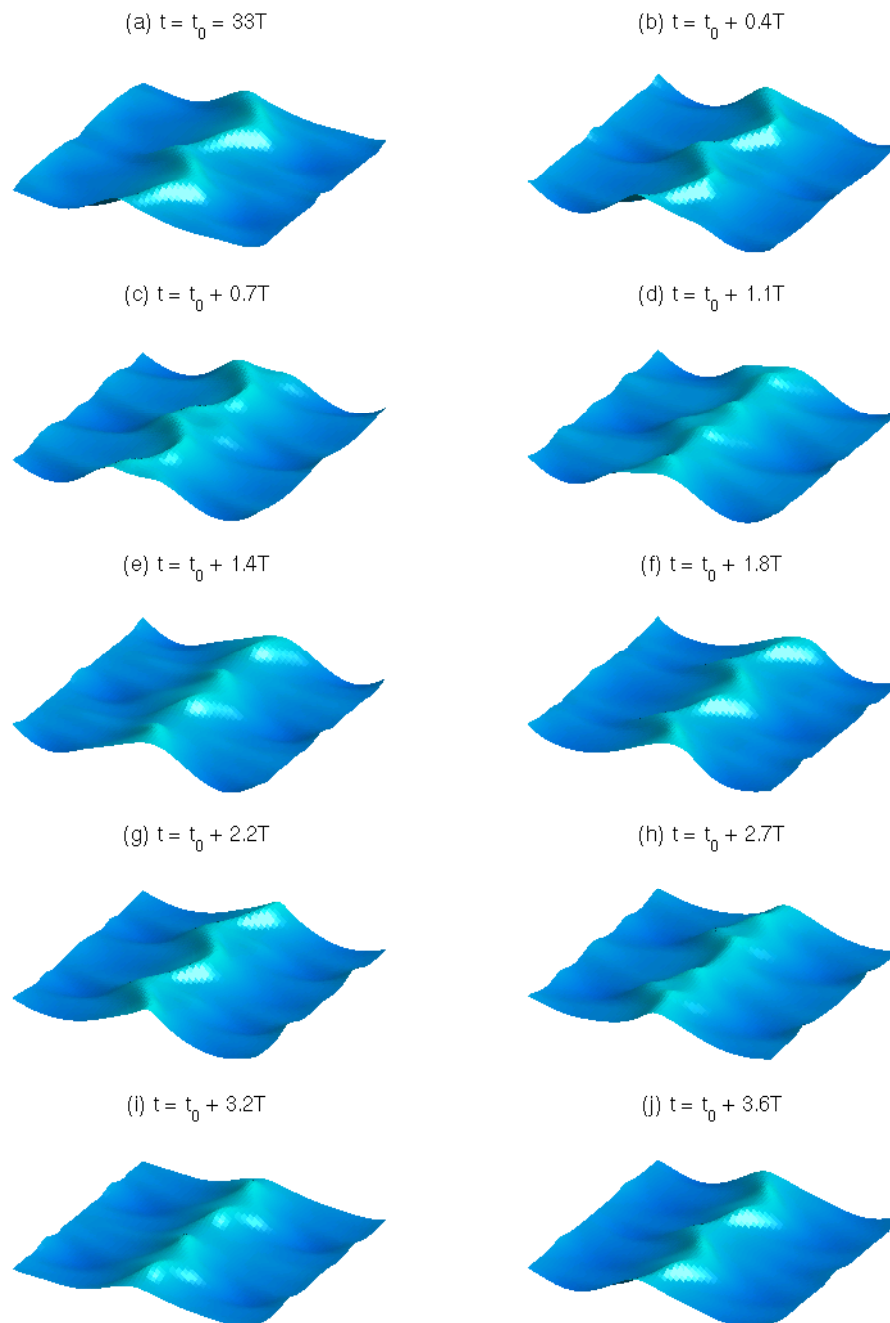


Figure 8.11: The evolution of an oscillating crescent wave starting at $t_0 = 33T$ and $x = 5.25L$. The vertical scale is exaggerated 1.5 times.

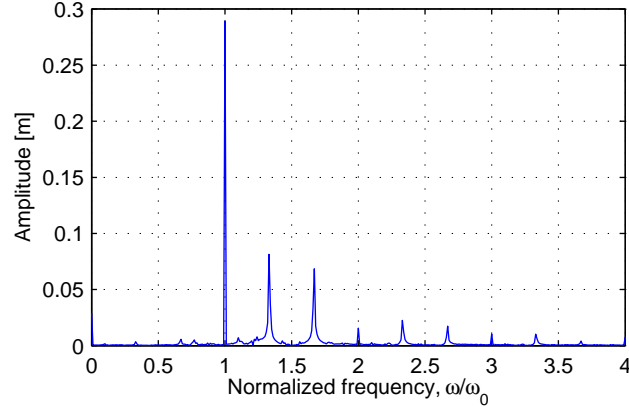


Figure 8.12: Computed Fourier amplitudes based on a time series from the oscillating crescent simulation from §8.4.1 at $(x, y) = (8L, L_y/2)$. The analysis uses time steps 1001-5001.

is closer to $3.6T$, though estimates vary slightly depending on the precise location where they are measured. Specifically, estimates ranging from $T^* = 3.1T$ near the left of the computational domain to the illustrated $3.6T$ near the right end have been measured (the latter is shown, as these are the most defined). These are still quite similar to the estimated $3T$ of Collard & Caulliez (1999) (note also that they do not specify a value for H/L).

To gain knowledge of the physical processes involved in the modeled oscillating crescent wave patterns, computed Fourier amplitudes from a time series taken at $(x, y) = (8L, L_y/2)$ are shown in Figure 8.12. The analysis uses time steps 1001-5001, when the initial conditions are completely washed out of the computational domain. Plots from other x -positions have been found to be qualitatively similar. After the primary wave, two significant spikes can be observed in the spectrum at $\omega = 1.33\omega_0$ and $1.67\omega_0$. As expected, these correspond precisely to the frequencies imposed at the wavemaker region. Additional higher harmonics are also clearly present. As the patterns at the end of the simulation are repeated roughly every primary wavelength, the corresponding wavenumbers can be estimated as $k'_{x1} \approx k_0$ and $k'_{x2} \approx 2k_0$, as discussed by Collard & Caulliez. These are clearly different from the initial conditions. The y wavenumbers can obviously be obtained from the transversal width of the computational domain. This combination clearly satisfies the quintet resonant condition (8.8) with two unsymmetric satellite pairs. This condition is illustrated graphically (for the wavenumbers) in Figure 8.13 for both symmetric and unsymmetric cases. For clarity, the first quintet resonant interaction involves $\mathbf{k}'_{1a} = (k_0, k'_y)$ and $\mathbf{k}'_{2a} = (2k_0, -k'_y)$, while the second involves $\mathbf{k}'_{1b} = (2k_0, k'_y)$ and $\mathbf{k}'_{2b} = (k_0, -k'_y)$. The corresponding frequencies are $\omega'_{1a} = \omega'_{2b} = \frac{4}{3}\omega_0$ and $\omega'_{1b} = \omega'_{2a} = \frac{5}{3}\omega_0$.

The relationship between the oscillation period and the combination of satellite frequencies and wavenumbers can be explained using simple linear superposition arguments. Consider a linear uni-directional carrier wave $\eta = a \cos(\omega_0 t - k_0 x)$ subject to the sinusoidal perturbation $\eta' = \epsilon \cos(\omega' t - k'_x x - k'_y y)$. In a frame of reference moving with the carrier wave *i.e.* letting $x = x^* + \frac{\omega_0}{k_0} t$ and $y = y^*$ (where x^* and y^* are the coordinates measured from this moving

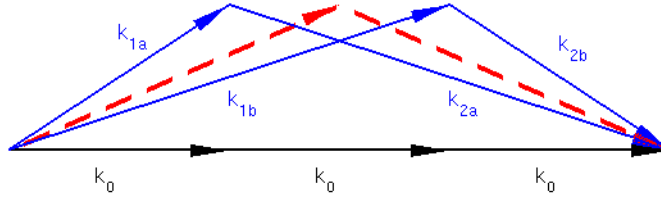


Figure 8.13: Resonant wavevector quintets for the phase-locked L2 (dashed) and the oscillating crescent (solid) patterns. A similar figure can be found in Collard & Caulliez (1999).

reference frame), the perturbation wave reads

$$\eta' = \epsilon \cos \left(\left(\frac{\omega'}{\omega_0} - \frac{k'_x}{k_0} \right) \omega_0 t - k'_x x^* - k'_y y^* \right). \quad (8.9)$$

Hence, the oscillation period can be expressed as

$$\frac{T^*}{T} = \left| \frac{\omega'}{\omega_0} - \frac{k'_x}{k_0} \right|^{-1}. \quad (8.10)$$

Using the observed $T^* \approx 9.4T$, from Figures 8.10 (a) and (b), in combination with the initial perturbation wavenumbers $k'_{x1} = \frac{4}{3}k_0$ and $k'_{x2} = \frac{5}{3}k_0$ yields estimates for the initial satellite frequencies of $\omega'_1 \approx 1.44\omega_0$ and $\omega'_2 \approx 1.56\omega_0$. As expected, these are entirely different from those imposed at the wavemaker. Similarly (after the transition), using the observed $T^* \approx 3.1T$ and the known frequencies $\omega'_1 = \frac{4}{3}\omega_0$ and $\omega'_2 = \frac{5}{3}\omega_0$ yields satellite wavenumbers $k'_{x1} \approx 1.01k_0$ and $k'_{x2} \approx 1.99k_0$, in almost perfect agreement with the previous estimations. These values will be re-confirmed in §8.4.3.

8.4.2 Transition from $(k'_{x1}, k'_{x2}) = (\frac{5}{4}, \frac{7}{4})k_0$ to $(\frac{3}{4}, \frac{9}{4})k_0$

We now turn our attention to another simulation resulting in oscillating crescent patterns which are not so distinctly arranged. This simulation uses the same model setup as in §8.4.1 (*i.e.* $H/L = 0.096$, $\epsilon = 0.08$, $k'_y = 1.32$), but with $k'_{x1} = \frac{5}{4}k_0$ and $k'_{x2} = \frac{7}{4}k_0$. The perturbation frequencies at the wavemaker are again obtained from (8.6), *i.e.* $\omega'_1 = \frac{5}{4}\omega_0$ and $\omega'_2 = \frac{7}{4}\omega_0$.

Figure 8.14 shows six computed free surfaces, which give a good account of the overall development. The evolution of this system is initially similar to that described in §8.4.1. Figures 8.14 (a) and (b) show computed free surfaces relatively early in the simulation. Following the marked carrier wave from Figures 8.14 (a) to (b) reveals an initial half-cycle of roughly $3.1T$, implying an oscillation period of $T^* \approx 6.2T$. From (8.10) this yields initial perturbation frequencies of $\omega'_1 = 1.41\omega_0$ and $\omega'_2 = 1.59\omega_0$, which will also be confirmed in §8.4.3. Figure 8.14 (c) shows the computed free surface during the transition from the incident cycle to that imposed by the frequency disturbance at the wavemaker. At this instant a distinct L4 pattern is apparent, having the high-high-low-low (HHLL) structure

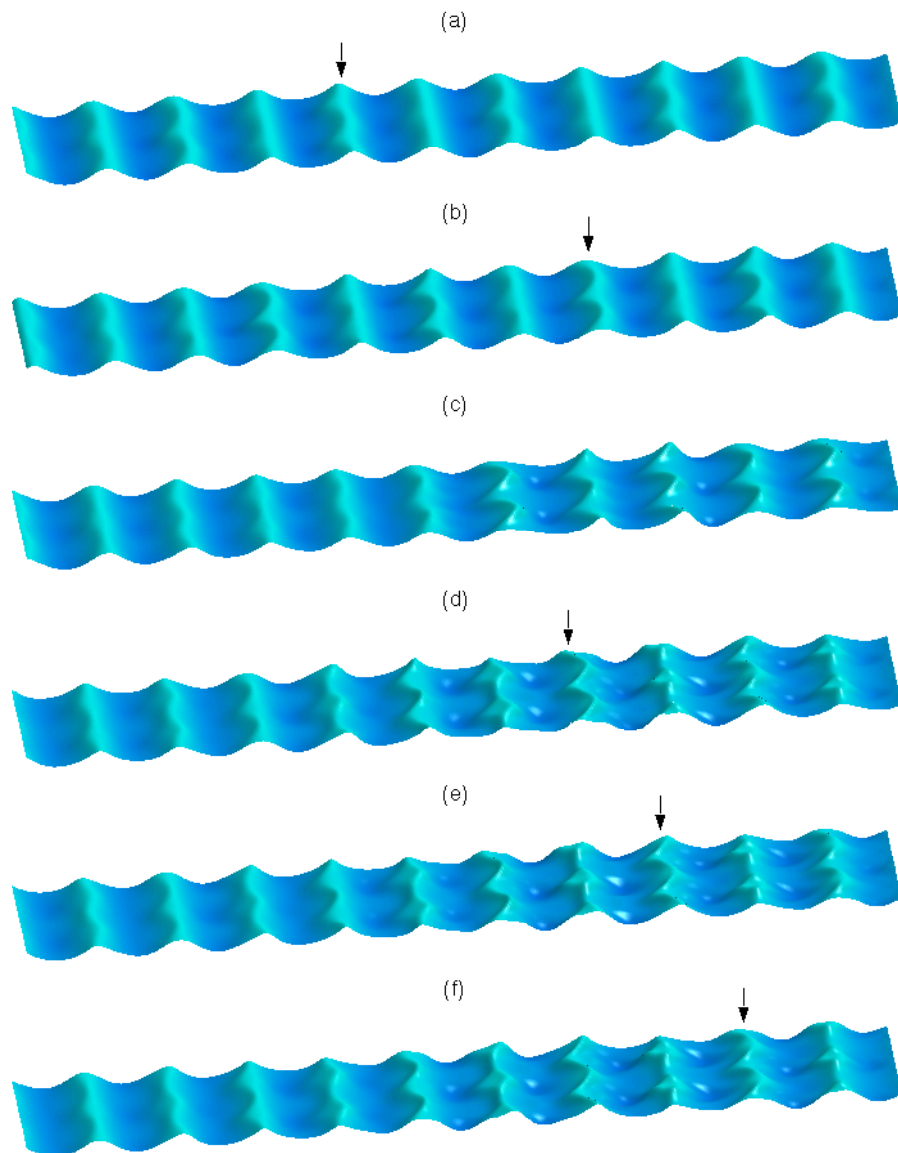


Figure 8.14: Evolution of oscillating crescent waves (transitioning from $(k'_{x1}, k'_{x2}) = (\frac{5}{4}, \frac{7}{4})k_0$ to $(\frac{3}{4}, \frac{9}{4})k_0$) at (a) $t = 3T$, (b) $t = 6.1T$, (c) $t = 12.2T$, (d) $t = 40.9T$, (e) $t = 41.9T$, and (f) $t = 42.9T$. The vertical scale is exaggerated two times.

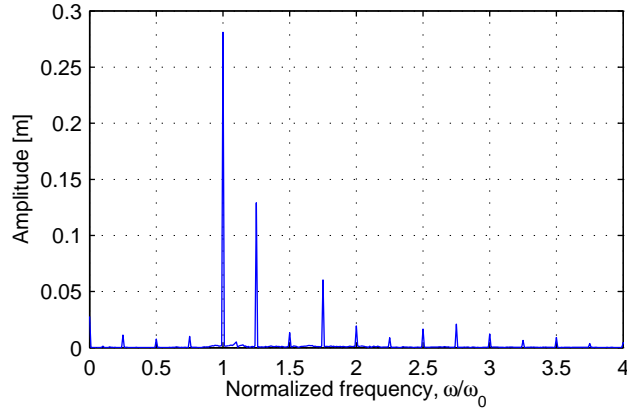


Figure 8.15: Computed Fourier amplitudes from the oscillating crescent wave simulation from §8.4.2 from a time series at $(x, y) = (7L, L_y/2)$. The analysis uses time steps 1001–5001.

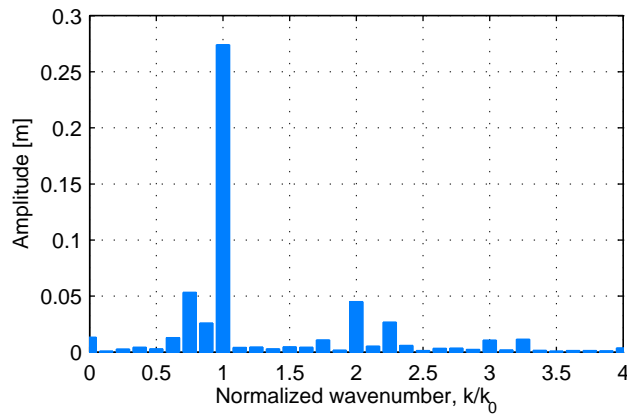


Figure 8.16: Computed Fourier amplitudes from an oscillating crescent wave simulation (as shown in §8.4.2 but using a second-order smoothing filter) from a space series at $t = 48T$, $y = L_y/2$. The analysis uses grid points 101–420.

described by Su *et al.* (1982) and Su (1982). This is the first computation of such a pattern to the authors' knowledge. As the model continues to evolve the initial conditions become completely washed out of the computational domain, and the patterns again adopt an entirely different oscillation period. Following the marked carrier wave in Figures 8.14 (d) to (e) to (f), a complete oscillation cycle is now seen to be $T^* \approx 2T$. This cycle persists for the remainder of the simulation. Contrary to §8.4.1, these oscillating crescent patterns do not become aligned in straight rows.

To demonstrate the physical processes involved in the final evolved patterns shown in Figures 8.14 (d)–(f), we first present computed Fourier amplitudes from a time series in Figures 8.15. This figure again clearly shows the presence of those frequencies imposed at the wavemaker region, *i.e.* $\omega'_1 = \frac{5}{4}\omega_0$ and $\omega'_2 = \frac{7}{4}\omega_0$. The wavenumbers associated with the oscillating process

in Figures 8.14 (d)–(f) can be estimated from (8.10) using the known satellite frequencies in combination with the observed $T^* \approx 2T$. This yields $k'_{x1} = \frac{3}{4}k_0$ and $k'_{x2} = \frac{9}{4}k_0$. Computed Fourier amplitudes from a space series along $y = L_y/2$ are shown in Figure 8.16 (from a similar simulation using a second-order smoothing filter). This does not allow for a precise estimation of the wavenumbers, however it does clearly show spikes at roughly the estimated values, which suffices as confirmation.

This simulation thus illustrates a quite general oscillating crescent wave pattern *i.e.* where the crescents do not become aligned in straight rows as seen in §8.4.1. The patterns arranged in straight rows in §8.4.1 are merely a special case (visually), owing their aligned nature to the fact that $k'_{x1} \approx k_0$, and $k'_{x2} \approx 2k_0$.

8.4.3 A quantitative explanation

We now pose the question: Is it possible to predict the oscillation period given only a set of perturbation wavenumbers satisfying the quintet resonant condition? Such a method for quantitatively explaining the oscillating crescent wave forms has not been previously presented to the authors' knowledge. The explanation essentially requires a means for estimating the satellite frequencies corresponding to the unstable perturbation wavenumbers *i.e.* a dispersion relation of sorts. Note that Collard & Caulliez (1999) use the linear dispersion relation as a rough estimate. When the incident wave has high steepness, however, this is not very useful in providing accurate quantitative estimations. It turns out that the required information is embedded in the stability analysis of McLean (1982*b*). Unfortunately, his analysis concentrates primarily on the dominant class II instability (resulting in the phase-locked L2 patterns), giving little quantitative information for those interactions involving unsymmetric satellite pairs.

We therefore undertake a similar analysis, analyzing numerically the stability of deep-water carrier waves generated from the stream function solution of Fenton (1988) to infinitesimal periodic disturbances resolved on an equidistant spatial grid. To allow for direct comparison with the values of McLean (1982*b*) (who used g and k_0 equal to unity) we present eigenvalues σ which are non-dimensionalized with respect to $\sqrt{gk_0}$. The analyses use up to 30 Fourier modes for the stream function solution, with the resulting wave discretized with up to 60 equidistant points in space for the corresponding stability analysis. The result is a generalized eigenvalue problem (see McLean, 1982*b*, for details). In the present analysis this is first converted to a standard eigenvalue problem before solving. Details on the analysis can be found in Appendix E. Specific attention is paid to those eigenvalues with non-zero imaginary part as these correspond to exponential growth of the unstable modes. The imaginary part determines the growth rate of the initial disturbance, while the real part corresponds to the frequency of the perturbation as seen from a moving frame of reference traveling with the unperturbed wave. A purely imaginary eigenvalue thus indicates an exponentially growing perturbation bound to the carrier wave, as in the general L2 case. Note that in this analysis

Table 8.3: Computed unstable class I and II eigenvalues having maximum imaginary part. Also shown for comparison are those from McLean (1982*b*).

H/L	Class I				Class II			
	p	q	σ	McLean (1982 <i>b</i>)	p	q	σ	McLean (1982 <i>b</i>)
0.032	0.18	0	$-0.088 + 0.00412i$	$-0.086 + 0.00409i$	0.5	1.64	$0 + 0.00059i$	$0 + 0.0006i$
0.064	0.32	0	$-0.146 + 0.0134i$	$-0.146 + 0.0133i$	0.5	1.54	$0 + 0.00531i$	$0 + 0.00523i$
0.095	0.47	0	$-0.189 + 0.0225i$	$-0.189 + 0.0226i$	0.5	1.33	$0 + 0.0210i$	$0 + 0.0215i$
0.096	0.47	0	$-0.188 + 0.0227i$	—	0.5	1.32	$0 + 0.0219i$	—
0.105	0.54	0	$-0.204 + 0.0236i$	—	0.5	1.23	$0 + 0.0316i$	—
0.111	0.60	0	$-0.215 + 0.0228i$	$-0.214 + 0.0227i$	0.5	1.15	$0 + 0.0406i$	$0 + 0.0413i$
0.127	0.84	0	$-0.229 + 0.0119i$	Stable	0.5	0.79	$0 + 0.0875i$	$0 + 0.0888i$
0.131	0.90	0	$-0.206 + 0.0073i$	Stable	0.5	0.65	$0 + 0.11i$	$0 + 0.11i$
0.131	—	—	—	—	0.5	0	$0 + 0.079i$	$0 + 0.067i$

Table 8.4: Computed unstable class II eigenvalues corresponding to the modeled oscillating crescent wave patterns.

\S	H/L	p	q	σ	T^*/T	ω'_1/ω_0	ω'_2/ω_0
8.4.1	0.096	0.667	1.32	$-0.111 + 0.0213i$	9.37	1.56	1.44
8.4.1	0.096	1.0	1.32	$-0.335 + 0.0171i$	3.10	1.68	1.32
8.4.2	0.096	0.75	1.32	$-0.166 + 0.0205i$	6.26	1.59	1.41
8.4.2	0.096	1.25	1.32	$-0.509 + 0.0117i$	2.04	1.76	1.24

the perturbation wavenumbers correspond to $\mathbf{k}'_1 = (p+1, q)k_0$ and $\mathbf{k}'_2 = (1-p, -q)k_0$ for the class I instabilities, and $\mathbf{k}'_1 = (p+1, q)k_0$ and $\mathbf{k}'_2 = (2-p, -q)k_0$ for the class II instabilities.

Computed eigenvalues for the most unstable class I and II instabilities are shown in Table 8.3, as are those from McLean (1982*b*) for comparison. As can be seen the two analyses generally compare well with one another, giving confidence in the computed values. In contrast to McLean (1982*b*), however, we detect class I instabilities for $H/L \geq 0.127$. This is consistent with the analysis of Kharif & Ramamonjariisoa (1988, 1990), who found that the class I instability is not stabilized until $H/L > 0.137$. For $H/L < 0.127$ the values shown are converged to at least the three digits shown, while for the higher nonlinearities the convergence becomes somewhat more erratic.

Table 8.4 shows computed eigenvalues corresponding to the initial and final stages of the two oscillating crescent wave simulations in §8.4.1 and §8.4.2. As the real part of σ is non-zero in these cases, the corresponding perturbations will no longer be bound as in the L2 case, explaining the oscillatory nature of the patterns. This information can thus be used to provide an estimate for the oscillation period. Recall that the eigenvalues are non-dimensional, and must thus be multiplied by $\sqrt{gk_0}$ to gain physical relevance for the present

simulations. The resulting oscillating period can hence be estimated as

$$\frac{T^*}{T_0} = \frac{\omega_0}{\sqrt{gk_0|\Re\sigma|}}. \quad (8.11)$$

These values are also tabulated in Table 8.4. In each case it is seen that the predicted oscillation period matches extremely well with the numerical simulations. In particular we note that the case with $p = 1.0$ predicts $T^* = 3.10T$, which is very close to the estimation of $3T$ given by Collard & Caulliez (1999). The prediction is also in essentially perfect agreement with the previously mentioned estimate from the model of $3.1T$ occurring nearest the wavemaker (*i.e.* before the perturbations reach significant amplitude). We mention that the frequencies corresponding to the perturbation wavenumbers can be obtained from

$$\frac{\omega'_1}{\omega_0} = \frac{k'_{x1}}{k_0} + \frac{\sqrt{gk_0}\Re\sigma}{\omega_0}, \quad \frac{\omega'_2}{\omega_0} = \frac{k'_{x2}}{k_0} - \frac{\sqrt{gk_0}\Re\sigma}{\omega_0}. \quad (8.12)$$

These values are also tabulated in Table 8.4. The cases having $H/L = 0.096$ with $p = 1.0$ and $p = 1.25$ result in perturbation frequencies very close to those imposed at the wavemaker regions in §8.4.1 and §8.4.2, respectively. The other values (with $p = 0.667$ and 0.75) also confirm the predicted frequencies using (8.10) in §8.4.1 and §8.4.2. This analysis has proven to be a very useful means for quantitatively explaining the modeled oscillating crescent wave patterns.

We also mention that a simulation using $H/L = 0.096$, $k'_{x1} = 2k_0$ and $k'_{x2} = k_0$ with $\omega'_1 = 1.68\omega_0$ and $\omega'_2 = 1.32\omega_0$ (as suggested in Table 8.4) indeed results in the development of oscillating crescent patterns aligned in straight rows from the very beginning of the simulation, which then persist indefinitely (within the computational domain). The resulting patterns are essentially the same as those in Figure 8.10 (d)–(f), thus they are not shown here. This simulation further confirms the accuracy of the stability analysis in quantitatively explaining these oscillating crescent wave patterns.

8.4.4 On the selection of the Collard & Caulliez (1999) oscillating crescents

While the previous subsection provides a quantitative explanation of the physics involved in the oscillating crescent wave phenomenon, it does not explain the selection of the specific unsymmetric satellite pair observed in the experiments of Collard & Caulliez (1999), again resulting in the striking alignment of the crescents in straight rows. In the following we propose that the selection of the observed satellites could in part be an artifact of the tank width, combined with a possible suppression of the class I instability.

Collard & Caulliez (1999) demonstrate their oscillating crescent waves at a carrier frequency $f = 1.3$ Hz ($T = 1/f = 0.769$ s, $\omega_0 = 8.17$ s⁻¹) in a tank with depth $h = 0.9$ m and width

$w = 2.6$ m. They report an estimated value of $q = |k'_y/k_0| = 1.32$, but unfortunately they do not provide the specific waveheight in the experiment. In an attempt to explain their observations we choose the waveheight of the carrier wave to be $H = 0.0682$ m. A stream function solution then yields the wavelength $L = 0.963$ m ($H/L = 0.0708$, $k_0 = 6.52$ m⁻¹, $k_0 h = 5.87$). Due to the tank width, we will assume that the transversal wavenumbers are limited to the discrete possibilities

$$|k'_y| = \frac{\pi n}{w}, \quad (8.13)$$

where n is an integer specifying the number of half transverse wavelengths spanning the width of the tank. Of these we consider $n = 7$ and 8 , giving $|k'_y| = 8.46$ m⁻¹, $q = |k'_y/k_0| = 1.30$, and $|k'_y| = 9.67$ m⁻¹, $q = |k'_y/k_0| = 1.48$, respectively, which are the values closest to the reported $q = 1.32$. Using the stability analysis from §8.4.3, setting $(p, q) = (1, 1.30)$ does not result in an instability. Alternatively, setting $(p, q) = (1, 1.48)$, yields the unstable eigenvalue $\sigma = -0.363 + 0.00587i$, which is in fact the dominant class II instability, again provided that q is limited to the discrete values. This results in an oscillating period from (8.11) of $T^* = 2.82T$, and perturbation frequencies from (8.12) of $\omega'_1 = 1.64\omega_0$ and $\omega'_2 = 1.36\omega_0$, which are in very good agreement with the values $T^* = 3T$, $\omega'_1 = 1.64\omega_0$, and $\omega'_2 = 1.36\omega_0$ from the experiments. At this nonlinearity a symmetric class II instability (*i.e.* with $p = 0.5$) does exist, but is not dominant; setting $(p, q) = (0.5, 1.48)$ yields $\sigma = 0.00433i$. Hence, for a small range of parameters (again considering discrete q), it is possible for the dominant class II instability to result in oscillating crescent patterns similar to those observed in the experiments, which may help explain their selection. Although we have not been able to explain the emergence of oscillating patterns with exactly the same combination of parameters as reported by Collard & Caulliez (1999) ($q = 1.48$ versus $q = 1.32$), the values are reasonably close. We find it particularly encouraging that the perturbation frequencies match so closely with the experiments.

This does not, however, account for the lack of the class I instability in the experiments. At this nonlinearity, the dominant class I instability corresponds to $(p, q) = (0.35, 0)$, with $\sigma = -0.157 + 0.0156i$, which is clearly stronger than the previously mentioned class II mode. It therefore seems that the class I instability may somehow be suppressed in the experiments (or alternatively, the class II instability artificially excited). The most obvious explanation for such a suppression is the use of a plastic film on the water surface. Collard & Caulliez (1999) indeed report that, in addition to preventing wave breaking, the film damps longitudinal wave modulations (also that it is used to ‘isolate the three-dimensional wave pattern formation’). Bliven, Huang & Long (1986) also provide experimental evidence that the class I instability is suppressed by wind, which was also used in the experiments. As evidence of such a suppression, whatever the cause, we note that Collard & Caulliez (1999) report observing phase-locked L2 crescent patterns for waves exceeding a critical steepness $H/L = 0.16/\pi \approx 0.051$, far below where the class II instability is theoretically dominant. It is not clear why such a plastic film and/or the wind would suppress the class I modes more than their class II counterparts, though the experimental results seem to support this contention.

While this explanation is inevitably speculative, we do demonstrate a plausible scenario where class II instabilities resulting in oscillating crescent patterns similar to those observed in the experiments of Collard & Caulliez (1999) would indeed be likely to appear, while still working within the framework of existing theories. Additional experiments to gain a better understanding of the effects of the plastic film, as well as the wind, are probably necessary for a more complete understanding of the selection mechanism in the experiments.

For additional details on the potential dominance of oscillating crescent waves see Fuhrman & Madsen (2005).

8.5 Competition Between Unstable Modes

We now investigate the initial competition up to the breaking point between various resonant interactions. Each simulation in this section uses the fourth-order smoothing filter applied at each time step, to have a minimal effect on the growth of the respective modes. Each simulation is run to the point of breakdown due to steepening of one or more wave fronts caused by the resulting instabilities. All harmonic analyses in this section use data from the final $4T$, to give an indication of the final evolved state.

8.5.1 Competition between isolated class II modes

We first investigate the direct competition between the dominant (symmetric) class II modes (covered in §8.3) with the unsymmetric satellites (covered in §8.4). We consider a simulation with carrier waves having $H/L = 0.096$ on a 1025×17 computational grid. The simulation uses a double perturbation with $k'_{x1} = 1.5k_0$, $\omega'_1 = 1.5\omega_0$ and $k'_{x2} = k_0$, $\omega'_2 = 1.32\omega_0$. Both perturbations use $k'_y = 1.32k_0$ and $\epsilon = 0.01$. Note that the second perturbation excites only one mode from each of the (oscillating) unsymmetric pairs (the others *i.e.* with $k'_x = 2k_0$ and $\omega' = 1.68\omega_0$, are free to evolve via the resonant quintet interactions). Both processes are excited with equivalent strength, however, and in the absence of the other perturbation simulations have shown that they develop to the expected patterns.

Figure 8.17 (a) shows harmonic amplitudes corresponding to the various frequencies involved in the quintet resonant interactions. Clearly, both of the instabilities exhibit an initial growth, and as the strengths of the instabilities are nearly equivalent (see Tables 8.3 and 8.4), neither dominates the other. Figure 8.17 (b) shows the computed free surface at the end of the simulation involving the competing modes, where both instabilities are apparent. The overall pattern resembles the L2 pattern of §8.3, however clear deviations are noticeable at every other wave front. Recall that the resonant interaction with the unsymmetric pairs results in oscillating crescents aligned in straight rows. These in turn cause an oscillating increase and decrease in the steepness of successive wave fronts – the L2 waves having the same momentary arrangement are steepened, while those having opposite arrangement are

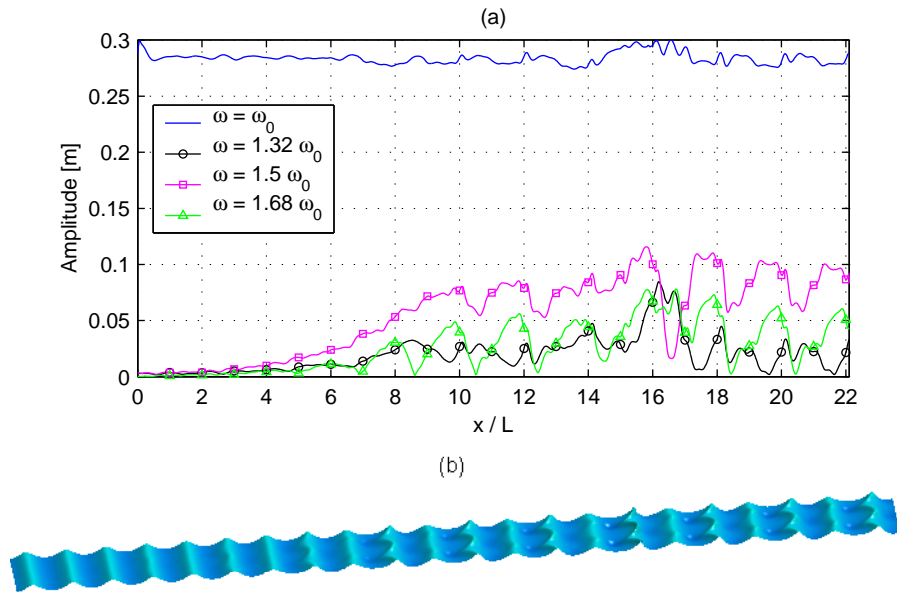


Figure 8.17: Computed (a) harmonic amplitudes and (b) free surface at $t = 24.4T$ for the simulation involving competition between symmetric (phase-locked) and unsymmetric (oscillating) class II instabilities with $H/L = 0.096$. In (b) the vertical scale is exaggerated two times.

diminished. This experiment demonstrates that multiple class II instabilities can develop simultaneously, with both contributing to the eventual breaking of the crescent waves. This is consistent with the findings of Annenkov & Shrira (1999, 2001), who also show the initial development of multiple class II instabilities.

8.5.2 Competition between isolated class I and II modes

We now use the model to investigate competition between isolated dominant class I and II instabilities. Three simulations are considered with incident waves having $H/L = 0.064$, 0.095 , and 0.111 . For each simulation the dominant high-frequency component for both class I and II instabilities (see Table 8.3) is excited with strength ϵ . The class II perturbations use the k'_y values from Table 8.1, while the class I perturbations use $k'_y = 0$. The case with $H/L = 0.064$ uses $\epsilon = 0.05$ while the other two simulations use $\epsilon = 0.01$, all on a 1025×17 computational grid. The simulations with $H/L = 0.064$, 0.095 , and 0.111 last for roughly $45T$, $21.25T$, and $13T$, respectively.

Figure 8.18 shows harmonic amplitudes along $y = L_y/2$ for the dominant frequencies involved in both the class I (quartet) and II (quintet) resonant interactions, while Figure 8.19 shows computed free surfaces near the final state of each simulation. Figure 8.18 (a) shows the case with $H/L = 0.064$, where the class I instability clearly dominates the class II instability, consistent with the expectation from the stability analysis of McLean (1982b) (as well as our

own analysis). In this case the dominant lower class I side-band actually grows to roughly the same strength as the primary wave before eventually leading to breaking. Although the class II mode does develop, it never reaches the considerable amplitudes of the class I modes. The free surface near the final model state is shown in Figure 8.19 (a), where the observed instability is only slightly three-dimensional. From Table 8.3, this class I instability involves wavenumbers $k'_{x1} = 1.32k_0$ and $k'_{x2} = 0.68k_0$. Using simple superposition arguments, we can expect that the pattern will repeat itself with a length of $\approx 3L$, which matches that seen in Figure 8.19 (a) (upon close examination roughly every third wave near the end of the domain is steepened).

The case with $H/L = 0.095$ is noticeably different. From Table 8.3, the strength of the class I and II instabilities is similar at this nonlinearity. From the harmonic analysis in Figure 8.18 (b) it is seen that both instabilities grow in strength to roughly equivalent magnitudes. As might be expected, neither process dominates the other. The resulting free surface is shown in Figure 8.19 (b), where both two- and three-dimensional effects are apparent. The three-dimensional class II instability is instantly recognizable from the crescent forms. The two-dimensional class I instability can be distinguished, as it steepens roughly every other wave front near the end of the domain. This is again consistent with the expectations from the wavenumbers involved $k'_{x1} = 1.47k_0$, $k'_{x2} = 0.53k_0$.

The case with $H/L = 0.111$ demonstrates relative dominance of the class II instability. The peak class I harmonic amplitudes shown in Figure 8.18 (c) are significantly lower than those of the class II mode, though they too certainly develop. The computed free surface at the end of the simulation is shown in Figure 8.19 (c), where the resulting pattern is predominantly three-dimensional in nature, closely resembling the previous plot in Figure 8.6 (b) having the same nonlinearity. Minor two-dimensional effects are also apparent, steepening roughly every other wave front near the end of the domain. These are of secondary importance, and are noticeably less pronounced than in Figure 8.19 (b).

8.5.3 Competition of random disturbances

All of the previously modeled crescent patterns have been generated using very deliberate two- and three-dimensional perturbations, as described in §8.2. These have proven to be a very efficient means for generating isolated instabilities, however it is perhaps not very representative of natural (or even laboratory) conditions resulting in such patterns. In this section we therefore consider the nonlinear evolution of randomly perturbed plane incident waves. Hence, the incident stream function solution values for the time stepping variables η , \tilde{U} , and \tilde{V} are multiplied individually at each grid point by a factor $(1 + \epsilon\mu)$, where μ is a uniformly distributed random number between -1 and 1. We consider simulations using three nonlinearities $H/L = 0.095$, 0.111, and 0.127. Each simulation uses a 1025×33 computational grid (*i.e.* a full wavelength of the dominant transversal class II mode), with $\epsilon = 0.02$. Discretizations are again taken from Table 8.1.

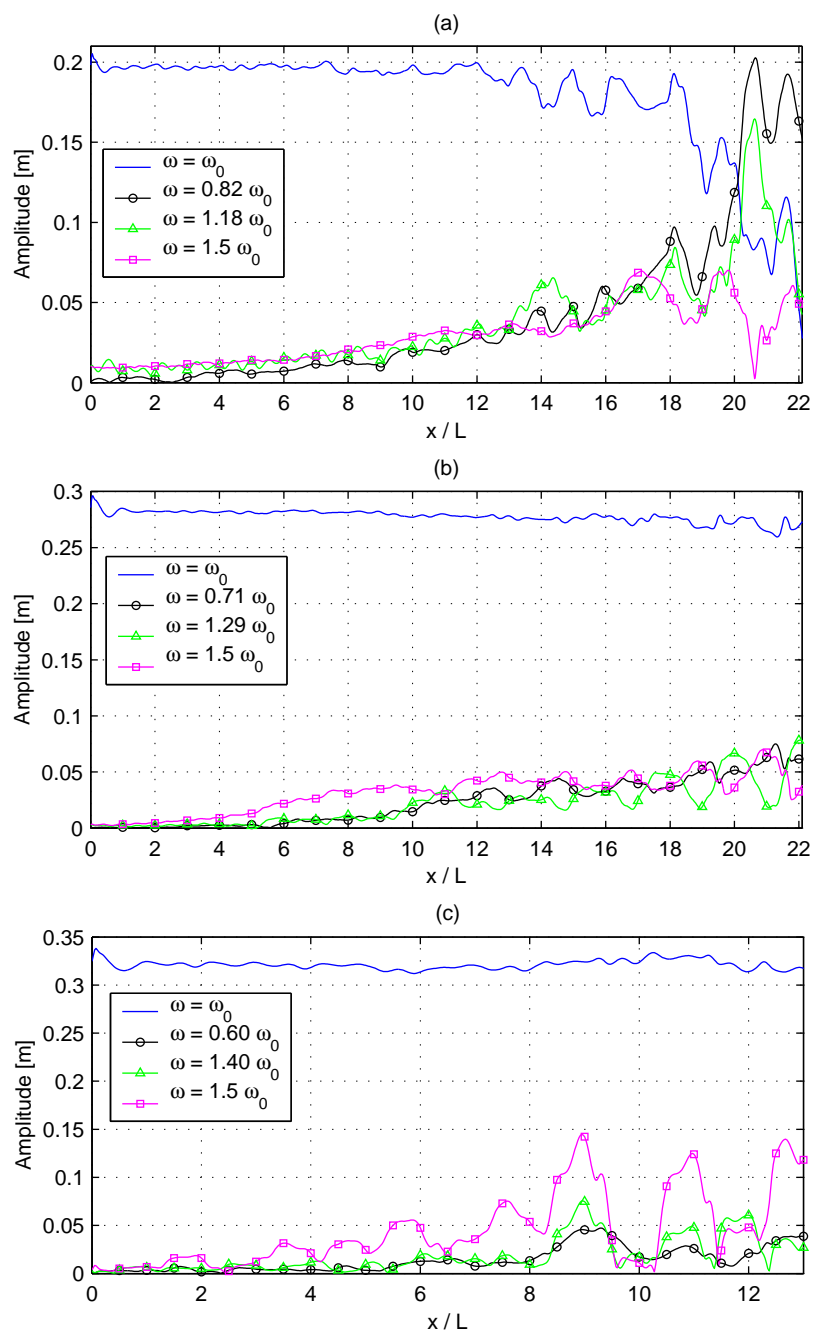


Figure 8.18: Computed harmonic amplitudes along $y = L_y/2$ for simulations with competing class I and II instabilities for (a) $H/L = 0.064$, (b) $H/L = 0.095$, and (c) $H/L = 0.111$.

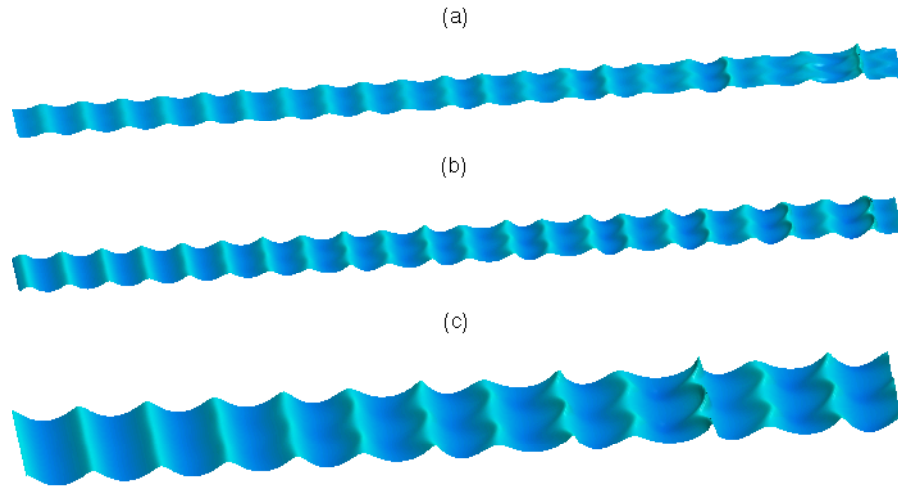


Figure 8.19: Computed free surfaces near the end state for simulations with competing class I and II instabilities for (a) $H/L = 0.064$ at $t = 43.75T$, (b) $H/L = 0.095$ at $t = 21.25T$, and (c) $H/L = 0.111$ at $t = 13T$. The vertical scale is exaggerated two times.

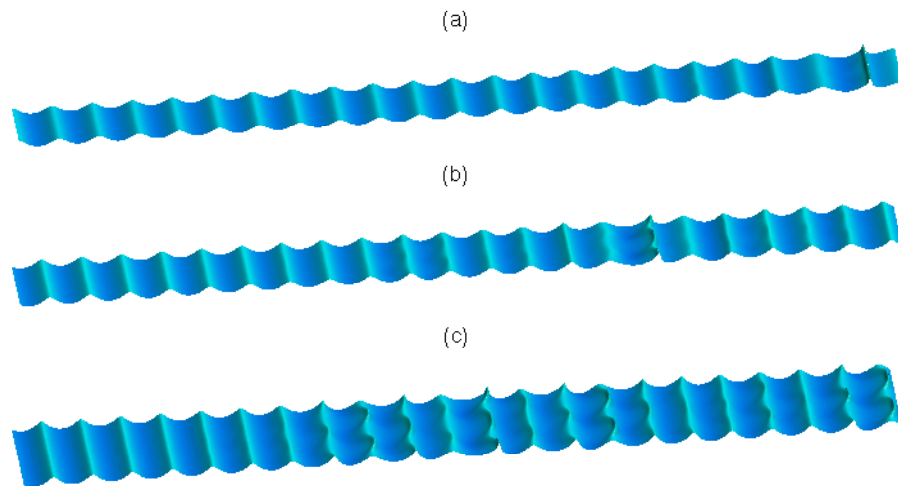


Figure 8.20: Computed wave patterns generated from simulations with random disturbances ($\epsilon = 0.02$) with (a) $H/L = 0.095$, $t = 34T$, (b) $H/L = 0.111$, $t = 23.75T$, and (c) $H/L = 0.127$, $t = 15.75T$. The vertical scale is exaggerated two times.

Computed free surfaces near the end of each simulation are shown in Figure 8.20. Figure 8.20 (a) shows the case with $H/L = 0.095$, which demonstrates a predominantly two-dimensional instability near the end of the computational domain. Minor three-dimensional effects are also apparent. Note that the class I instability does have a slightly larger linear growth rate than the corresponding class II instability at this nonlinearity (see McLean, 1982*b*, as well as Table 8.3). Interestingly, the resulting free surface is much less three-dimensional than in Figure 8.19 (b) having the same nonlinearity. This could suggest that the class II instability is suppressed more by the randomness than is the class I instability, at least at

this nonlinearity (the suppression of the class I instability by randomness is demonstrated in Alber, 1978). A more in-depth investigation would certainly be necessary before making any firm conclusions on this matter, however.

Figure 8.20 (b) shows the case with $H/L = 0.111$, which results in a predominantly three-dimensional steepening of the wave, again consistent with expectations from Table 8.3. Both Su *et al.* (1982) and Melville (1982) report dominance of the three-dimensional instability at $H/L \approx 0.10$, thus this is consistent with their observations. Two-dimensional effects are also clearly present, as every other wavefront around the crescent is slightly steepened. We also note that the emergence of the crescent at $x \approx 15L$ compares quite well with the observations of Melville (1982), who reports strong three-dimensional effects at $x \approx 10L$, as well as with Su *et al.* (1982), who report a first stage of wave evolution at $x \approx 19L$ (both with $H/L \approx 0.10$). We speculate that a continued evolution of the model beyond the breaking point might lead to clearer dominance of the class II instability at this nonlinearity.

Figure 8.20 (c) shows the case with $H/L = 0.127$. Here, multiple L2-like patterns emerge starting at $x \approx 7L$. There is no noticeable indication of two-dimensional instabilities. We also call attention to the series of wave fronts starting at $x \approx 15L$ in Figure 8.20 (c), with successive fronts having minor peaks at $y = 0, L_y,$ and $2L_y$. Such an arrangement deviates from the standard L2 pattern, and may be the beginnings of potential L3- or L4-like patterns, as observed in Su *et al.* (1982) and Su (1982) (Melville, 1982, also reports such deviations).

We finally mention a number of interesting experiments involving the competition of various modes in Annenkov & Shrira (1999, 2001) using a weakly-nonlinear model based on the Zakharov equation. Their experiments demonstrate sporadically occurring crescent patterns, occurring over long-term (*i.e.* $O(1000T)$) evolutions, whereas the experiments described here consider only the initial development to breaking, at significantly higher nonlinearities. Nevertheless, the experiments share some common tendencies. The results of Annenkov & Shrira (1999, 2001) also indicate the initial growth of multiple instabilities (as mentioned in §8.5.1), as well as a tendency for significantly stronger modes to exhibit dominance over weaker instabilities. The vast difference in both time scales and nonlinearity make a more meaningful comparison difficult, however. The onset of breaking in each of the experiments presented here will most likely change the long-term evolution of the waves dramatically, making such sporadic patterns unlikely at the nonlinearities where the class II instability is dominant. For example, Su *et al.* (1982) report observing spilling crescent breakers for roughly $10L$, after which the wave trains return to a more or less two-dimensional form. This process is later followed by a frequency downshift in the spectrum. The long-term fully nonlinear evolution of crescent waves remains relatively unstudied.

8.6 Computational Efficiency

In this section the issue of computational efficiency is briefly addressed. All previously described simulations have been run on a single 2.26 GHz processor, making use of the Intel

FORTTRAN compiler. A summary of computational results for selected simulations is given in Table 8.5. Here N refers to the number of spatial grid points, N_t is the number of time steps, and

$$E = \frac{CPU}{NN_t} \quad (8.14)$$

is a measure of relative computational expense in terms of CPU time per grid point per time step (allowing for easy comparison of the various simulations). From this table it can be seen that the numerical solutions for $\mathbf{Ax} = \mathbf{b}$ (which are the dominant computational expense) in the Boussinesq model are robust, even in the most nonlinear situations. Modeling crescent waves is in fact quite demanding, as simulations are inevitably in deep water, require fairly refined grids, and are highly nonlinear – all factors contributing to the ill-conditioning of the matrix \mathbf{A} . Recall that the matrix-free Fourier space preconditioning method from §4.6.3 is limited to solving flat bottom problems, due to the assumption of constant coefficients in Fourier space. Therefore some results using the generally applicable approximate Schur complement preconditioner developed in §4.6.4 (see also Fuhrman & Bingham, 2004) are also included. These solutions can be seen to be somewhat less efficient (roughly by a factor of three), but are still very acceptable. Consistent with the results shown in Chapter 4, the solutions for the Boussinesq model scale roughly linearly with N in these simulations. This study further confirms that the Boussinesq model is an efficient method for the study of highly nonlinear water waves at reasonably large space and time scales – the simulations presented here take hours, not days, on a modern processor. This efficiency has allowed for a quantitative study of crescent wave patterns at significantly larger spatial and temporal scales than have been previously presented.

8.7 Conclusions

This chapter presents a detailed numerical study of crescent (or horseshoe) water wave patterns using the fully nonlinear and highly dispersive Boussinesq model (again based on the formulation of Madsen *et al.*, 2002, 2003). The numerical model utilizes the efficient solution strategies developed in Chapter 4 (see also Fuhrman & Bingham, 2004). Herein, it is shown that the computed results for the most unstable phase-locked L2 crescent wave patterns compare both qualitatively and quantitatively well with observations, giving confidence in the model. The growth rate of the instability is shown to match closely with that predicted by the linear analysis of McLean (1982*b*) near the inception. At later stages of the evolution, however, the growth is significantly accelerated when uninhibited by dissipation. The model results suggest that it is the dissipative effects due to wave breaking that ultimately counteract the unstable growth, leading to the relatively steady forms described in physical experiments. We also use the model to investigate the effects of variable nonlinearity on these patterns. We demonstrate that increases in the nonlinearity generally result in wider crescent patterns (as predicted by McLean, 1982*b*) with less pronounced tails. Through Fourier analysis of both time and space series, we confirm the quintet resonant interaction

Table 8.5: Computational summary of selected crescent wave simulations. The reported iterations are the average in each simulation for solutions of $\mathbf{Ax} = \mathbf{b}$.

Simulation	\S	H/L	ϵ	N	N_t	Prec.	Iterations	CPU [hr]	$E \cdot 10^7$ [hr]
L2	8.3.5	0.096	0.16	8721	5000	Fourier	12.7	4.45	1.02
L2	8.3.3	0.105	0.16	8721	310	Fourier	12.4	0.32	1.18
L2	8.3.3	0.105	0.16	8721	260	Schur	21.9	0.63	2.78
L2	8.3.5	0.105	0.01	17,425	720	Fourier	7.9	1.13	0.90
L2	8.3.5	0.105	0.01	17,425	720	Schur	16.9	3.03	2.42
L2	8.3.5	0.131	0.05	8721	160	Fourier	14.2	0.20	1.43
Oscillating	8.4.1	0.096	2×0.08	8721	5000	Fourier	12.6	4.39	1.01
Oscillating	8.4.2	0.096	2×0.08	8721	5000	Fourier	12.0	4.30	0.99
Competition	8.5.2	0.064	2×0.05	17,425	1800	Fourier	8.1	2.65	0.84
Competition	8.5.2	0.111	2×0.01	17,425	530	Fourier	8.5	0.94	1.02
Competition	8.5.3	0.095	0.02	33,825	1370	Fourier	7.3	3.66	0.79
Competition	8.5.3	0.111	0.02	33,825	970	Fourier	8.4	2.89	0.88
Competition	8.5.3	0.111	0.02	33,825	970	Schur	17.9	8.99	2.74
Competition	8.5.3	0.127	0.02	33,825	640	Fourier	10.3	2.41	1.11
Competition	8.5.3	0.127	0.02	33,825	640	Schur	22.4	7.77	3.59

as the dominant physical process, involving the primary wave with a pair of symmetric satellites. A series of quadratic nonlinearities also force additional bound higher harmonics, giving definition to the crescent forms.

A numerical investigation of oscillating crescent waves, observed recently by Collard & Caulliez (1999), is also presented. The computed results provide a very close match with the oscillation period observed in the physical experiments, and a detailed account of the rather complicated oscillation cycle is presented. Through direct numerical simulation we also demonstrate distinct occurrences of L3 and L4 crescent patterns observed by Su *et al.* (1982) and Su (1982). These occur momentarily when the model is transitioning between various resonant interactions. The dominant physical processes in the oscillating crescent patterns are again demonstrated to be resonant quintet interactions, involving the primary wave with two unsymmetric satellite pairs. The arrangement of the patterns in straight rows as observed by Collard & Caulliez (1999) is further shown to be merely a special case (visually) of these oscillating crescent waves, which in general do not have such an arrangement. A re-investigation into the stability analysis of McLean (1982*b*) is undertaken, resulting in a quantitative explanation (including accurate predictions of the oscillation period) for each of the cases considered. A possible explanation of the selection of the oscillating patterns observed in the experiments is also provided.

Finally, the model is used to conduct a series of numerical experiments involving the competition of various unstable modes during the initial growth toward wave breaking. These include competition between isolated class II modes, between isolated class I and II modes, as

well as with random (white noise) disturbances. The results show that multiple instabilities can grow simultaneously, provided that they are of similar strength, with each contributing to the eventual breaking of the waves. The computed results involving the random disturbances compare well with observations in wave tank experiments both in the form (*i.e.* two- or three-dimensional) and location of the initial instability. Deviations from the dominant L2 pattern also arise naturally, consistent with observations.

The computations presented in this chapter are further demonstrations of deep-water, highly nonlinear (to the point of breaking), three-dimensional wave modeling with the high-order Boussinesq model. The model is shown to be an efficient computational method for the general study of highly nonlinear water waves at reasonably large space and time scales.

Chapter 9

Nonlinear Wave-Structure Interactions

Chapter Summary

This chapter describes the extension of the finite difference Boussinesq model to include domains having arbitrary piecewise-rectangular bottom-mounted structures. The resulting linearized system is analyzed for stability on a structurally divided domain, and it is shown that exterior corner points pose potential stability problems, as well as other numerical difficulties. These are mainly due to the discretization of high-order mixed-derivative terms near these points, where the velocity field is theoretically singular. Fortunately, the system is receptive to dissipation, and these problems can be overcome in practice using high-order filtering techniques. The resulting model is verified through numerical simulations involving classical linear wave diffraction around a semi-infinite breakwater, linear and nonlinear gap diffraction, and highly nonlinear deep water wave run-up on a vertical plate. These cases demonstrate the applicability of the model over a wide range of water depth and nonlinearity.

9.1 Introduction

This chapter describes the extension of the finite difference Boussinesq model to allow domains with arbitrary piecewise-rectangular bottom-mounted structures. Such an extension is conceptually trivial, but introduces several practical problems concerning the implementation, stability, and accuracy of the numerical scheme. Many of these difficulties owe to the considerable complexity of the underlying system of PDEs, which include numerous (up to fifth-order) mixed-derivative terms. This chapter therefore pays particular attention to these details. The method of discretization will be described in depth, and the numerical stability of this discretization is examined (on a structurally divided domain), revealing potential

negative effects due to high-order terms at exterior corner points (about which the velocity field is known to be theoretically singular). These details are felt to be widely-relevant, as the PDE system considered here readily simplifies to a number of other Boussinesq-type formulations in the literature when certain terms are neglected and/or certain coefficients are changed (see Madsen & Agnon, 2003). The resulting numerical model is verified using three test cases. These involve classical linear diffraction around a semi-infinite breakwater, linear and nonlinear gap diffraction, and highly nonlinear deep water wave run-up on a vertical plate. These demonstrate the applicability of the model over a wide range of both water depth and wave nonlinearity. The resulting simulations are demonstrated to be suitably accurate for modern engineering applications, even in very physically demanding circumstances.

The outline of the chapter is as follows. The method used for the discretization around structures is described in §9.2. The effects of structural corner points on the numerical stability are analyzed and discussed in §9.3. Numerical results for linear diffraction around a semi-infinite breakwater are provided in §9.4, for linear and nonlinear gap diffraction in §9.5, and for highly nonlinear deep water run-up (and diffraction) on a vertical bottom-mounted plate in §9.6. Conclusions are drawn in §9.7.

This chapter can be found in a similar form in Fuhrman, Bingham & Madsen (2005) (see also Bingham *et al.*, 2004; Fuhrman *et al.*, 2004*c*).

9.2 Discretization Around Structures

In this section we provide details on the extension of the basic finite difference model (on a rectangular domain) to include arbitrary piecewise-rectangular bottom-mounted structures. Structures are incorporated into the model by simply flagging (through an input file) those grid points immediately surrounding the desired structural boundary, as well as the points within the structure. For this purpose, we have identified 13 different point-types: four walls (facing up, down, left, or right in plan), four interior corners, four exterior corners, and ‘land’ points (*i.e.* points outside the fluid domain). Using these simple components it is possible to define quite arbitrary piecewise-rectangular structures within a basic rectangular region. To avoid direct discretization of exterior corner singularities, all structural walls are defined halfway between the existing grid points. Also, to avoid excessive book-keeping, our current implementation limits horizontal walls running in the x - and y -directions to minimum lengths of $3\Delta x$ and $3\Delta y$, respectively, corresponding to half the span of the finite difference stencil.

Due to the large number of (up to fifth-order) mixed-derivatives which must be approximated in the current model, we find it convenient to maintain the same basic finite difference structure throughout the domain, rather than *e.g.* changing to one-sided differences around the structures. Boundary conditions around the structures are thus again imposed by reflecting the coefficients across the structural boundaries, in a similar fashion as for the exterior domain. This is straight-forward, except for around exterior corner points.

Around exterior corner points, *e.g.* the one considered in Figure 9.1, the resulting finite difference approximations for mixed-derivatives depend on the order in which the various derivatives are conceptually taken. For example x -derivatives can be approximated at all stencil points lying along the centerline in y , with the remaining y -derivative then operating on these values; or the reverse. Examples of the discretizations used in our implementation are depicted in Figure 9.1. We first consider taking an arbitrary mixed-derivative at a point adjacent to a wall, as in Figure 9.1 (a). In this case the derivatives in the direction parallel to the wall are conceptually taken first (at points moving outward from the wall), with the remaining derivative (in the direction perpendicular to the wall) operating on these values. By adopting this strategy, derivatives on either side of a corner are approximated using only grid points lying on the same side of the wall, which intuitively seems advantageous. Analogous discretizations are used at all points adjacent to walls.

For points that are not adjacent to a wall, *e.g.* as shown in Figures 9.1 (b) and (c), we use a combination of the two possibilities. Depending on the order in which the derivatives are conceptually taken (*i.e.* whether x - or y -derivatives are taken first) the coefficients within the structure will be reflected across opposing walls, as illustrated in Figures 9.1 (b) and (c). Both approximations are formally consistent with the original continuous operator. However, as there is no reason to favor one over the other for these points, we simply take their average

$$\frac{\partial^{j+k}}{\partial x^j \partial y^k} = \frac{1}{2} \frac{\partial^k}{\partial y^k} \left(\frac{\partial^j}{\partial x^j} \right) + \frac{1}{2} \frac{\partial^j}{\partial x^j} \left(\frac{\partial^k}{\partial y^k} \right). \quad (9.1)$$

Thus, for the center-point considered in Figures 9.1 (b) and (c), the finite difference coefficients within the structure would be reflected across both walls (with sign still depending on the type of boundary condition) with a factor 0.5. Analogous discretizations are used for all center-points not adjacent to a wall having a finite difference stencil overlapping an exterior corner. This implementation conveniently leads to discretizations that are symmetric about the corner.

As an initial verification, linear deep water standing waves have been separately tested on L-shaped domains with each of the four exterior-type corners placed at the point of symmetry (*i.e.* the antinode). Hence, the problem becomes mathematically equivalent to using no structure at all. Inspection of the resulting time series at points near the corner results in visually perfect matches with the theoretical period, very similar to the previous demonstration without structures in §6.2. Hence, at least in ideal cases (*i.e.* where there are not steep velocity gradients about the corner), we obtain similar convergence as in the basic finite difference model.

9.3 Linear Stability Analysis

In this section we present a method of lines-type stability analysis to demonstrate the potential effects of discretizations around structures, particularly involving exterior corner points.

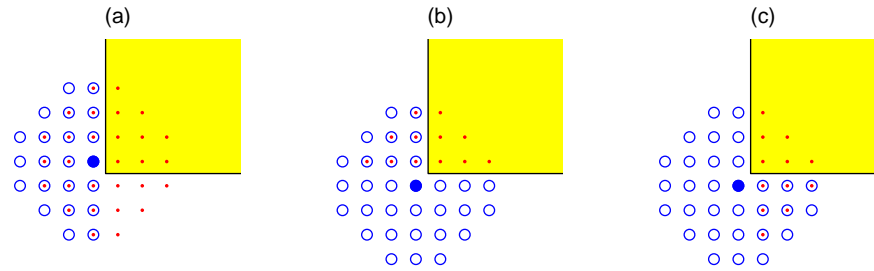


Figure 9.1: A demonstration of the treatment of mixed derivatives near an exterior corner. The shaded region is the structure, \bullet are the center-points, \cdot represent coefficients reflected across the walls to the \ominus points. Figure (a) shows the resulting stencil when conceptually taking the y -derivatives first for a center-point adjacent to a vertical (in plan) wall. Figures (b) and (c) show potential stencils for a center-point not adjacent to a wall, when first taking the x - and y -derivatives, respectively.

Analysis on even relatively simple, but irregular domains is in fact quite rare, since commonly used Fourier techniques are no longer applicable. By working directly with matrices, however, it is relatively straight-forward to perform such an analysis. Following Chapter 5 (see also Fuhrman *et al.*, 2004a), we consider the linearized system of PDEs in the semi-discrete form

$$\frac{\partial \mathbf{y}}{\partial t} = \mathbf{J} \mathbf{y}. \quad (9.2)$$

Here \mathbf{y} is a vector of the discrete time stepping variables, which for the linearized system are η and $\mathbf{u}_0 = (u_0, v_0)$, representing horizontal velocities taken at the still-water level $z = 0$. The determination of the linear Jacobian matrix \mathbf{J} for this system is somewhat involved, and complete details can again be found in Chapter 5, where the linear and nonlinear stability properties of the basic finite difference model are investigated (see also Appendix D). A necessary condition for the stability of such a system is, again, that the resulting eigenvalues λ of \mathbf{J} , when scaled by the time step Δt , lie within the stability region for the time-stepping scheme of interest. This approach is standard; for details see *e.g.* Fornberg (1998), Hirsch (1988), Iserles (1996), and Trefethen (2000), as well as Chapter 5. In the following we take a fairly general approach, not stressing any particular time stepping scheme. For completeness, however, we again mention that the explicit fourth-order, four-stage Runge-Kutta scheme used throughout this thesis has a stability region spanning the imaginary interval $(-2\sqrt{2}i, 2\sqrt{2}i)$, see Table 5.1. From a general stability standpoint it is desirable that no eigenvalues of the matrix \mathbf{J} lie to the right-half of the complex plane, as these correspond analytically to exponentially growing (*i.e.* unstable) modes for the semi-discrete system (9.2).

Figure 9.2 demonstrates computed scaled eigenvalue spectra for a series of systematically varied discretizations. All results use a 21×21 computational grid, with $\Delta x = \Delta y = 0.05$ m. In each case the time step Δt has been selected to result in a spread along the imaginary axis of $(-i, i)$ based on the previous analysis in Chapter 5. Figure 9.2 (a) shows the computed spectrum for the basic system on this domain (*i.e.* without structures) for a typical shallow

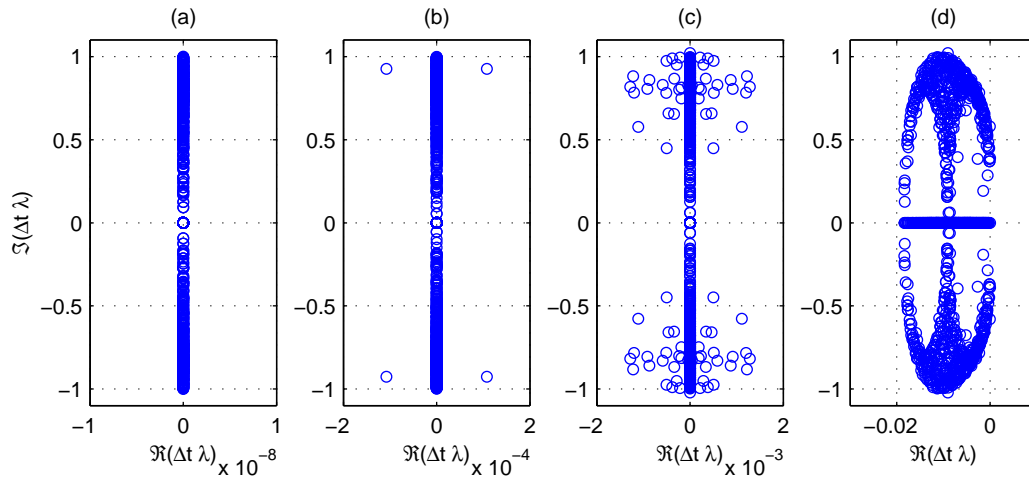


Figure 9.2: Computed eigenvalues of $\Delta t \mathbf{J}$ for (a) a square domain with $k_N h = 2\pi$, $\Delta t = 0.0484$ s, $D = 0$; (b) as in (a) but for a structurally divided domain including an exterior corner point; (c) as in (b) but with $k_N h = 20\pi$, $\Delta t = 0.0478$ s; and (d) as in (c) but with diffusion coefficient $D = 8 \cdot 10^{-5}$ m²/s.

water discretization with $k_N h = 2\pi$, where $k_N = \sqrt{(\pi/\Delta x)^2 + (\pi/\Delta y)^2}$ is the modulus of the Nyquist wavenumber vector. The dimensionless parameter $k_N h$ is important, as it governs the numerical significance of the high-order (Boussinesq-type) terms. Consistent with previous analyses, the eigenvalues are purely imaginary, and therefore do not suggest stability problems beyond those already described in Chapter 5. This is the case regardless of the parameter $k_N h$. Figure 9.2 (b) shows the computed spectrum for an otherwise identical problem, but where a simple structure has been added by placing an exterior corner at $(x, y) = (0.5025, 0.5025)$ m connecting thin walls extending positively in both x - and y -directions to the edge of the domain (thus the domain is now divided into separate L- and square-shaped sections). As can be seen, this discretization results in a single pair of analytically unstable eigenvalues. Likewise, Figure 9.2 (c) shows the spectrum for a typical deep water discretization on the same domain, now with $k_N h = 20\pi$, which results in numerous analytically unstable eigenvalues. The spread of the spectrum along the real axis is also seen to increase roughly linearly with $k_N h$.

Further inspection has shown that these potential instabilities arise from the discretization around exterior corner points when third-order or higher derivatives are included. Discretizations including only up to second-order derivatives or involving structures without exterior corners result in spectra similar to Figure 9.2 (a), regardless of the depth. The eigenvalues in the right-half of the complex plane are of course undesirable. However, additional analyses for this system have shown similar de-stabilizing effects arising from the nonlinear terms (locally demonstrated in §5.6), as well as variable depths. Thus, this effect is perhaps not altogether surprising, particularly given that the flow at these corners is theoretically singular. The spread along the real axis is typically many orders of magnitude smaller than along the imaginary axis, indicating that the instabilities are generally weak, even when $k_N h$ is

rather large. Fortunately, experience has shown that the system can generally be stabilized via the introduction of numerical dissipation. This is illustrated qualitatively in Figure 9.2 (d), where a diffusive term with diffusion coefficient $D = 8 \cdot 10^{-5} \text{ m}^2/\text{s}$ has been added to each of the linearized free-surface conditions. The discrete system is clearly receptive to these effects, and all eigenvalues now lie to the left-half of the complex plane. We stress that these diffusive terms are only used for demonstration purposes in this analysis, whereas more advanced filtering techniques are used in simulations, to be described in what follows.

On a related issue, simulations involving exterior corner points typically result in steep velocity gradients in the neighborhood of the corner, leading to numerical inaccuracies and convergence problems. Convergence difficulties due to corner singularities are also reported *e.g.* in Huang & Seymour (2000). The end result in our simulations is often high-frequency noise in the vicinity of the corner, even for schemes which are formally *linearly* stable. This can also quickly excite nonlinear instabilities, as well as pollute the rest of the domain. Furthermore, steep free surface gradients (*e.g.* those computed from a noisy water surface) create a local un-physical importance of the nonlinear terms, which can in turn lead to severe convergence difficulties for iterative solutions of $\mathbf{Ax} = \mathbf{b}$ (particularly since the preconditioning methods designed in Chapter 4 are based on the linearized formulation). As might be expected from Figure 9.2, all of these problems are compounded as $k_N h$ increases (*i.e.* as the depth becomes large or the grid is refined), and the high-derivative terms become more important. The sensitivity likewise increases with nonlinearity.

To combat these various de-stabilizing effects and numerical difficulties we employ a sixth-order, 57-point (octagon shaped) Savitzky & Golay (1964)-type smoothing filter throughout this chapter. For most of the domain this is applied incrementally, and only after full time steps. Alternatively, around structures (*i.e.* at points where the full filter overlaps a structural boundary) we use a simpler line-version (summing the coefficients first along an x -, and then a y -line), applied after each Runge-Kutta stage, often repeatedly. The resulting nine-point filter is given by the stencil

$$[-0.0043 \quad 0.0342 \quad -0.120 \quad 0.239 \quad 0.701 \quad 0.239 \quad -0.120 \quad 0.0342 \quad -0.0043].$$

An amplification portrait (created using standard Fourier analysis techniques described in Appendix C) for multiple applications of this filter is shown in Figure 9.3, where n_s refers to the number of successive smoothing applications. Also shown for comparison is the portrait for a single application of the classical three-point filter described *e.g.* in Abbott & Minns (1998) (p. 229), given by the stencil $[0.25 \quad 0.5 \quad 0.25]$. The differences between these two filters are quite dramatic. Multiple applications of the high-order filter effectively zero a wider range of poorly resolved modes, after which the amplification factor quickly approaches unity (*i.e.* no damping). Alternatively, the three-point filter damps a much broader portion of the wavenumber spectrum. Indeed, even after 100 applications of the high-order filter, the damping of lower wavenumber modes is still significantly less than with a single application of the three-point filter! This has also been confirmed in simulations.

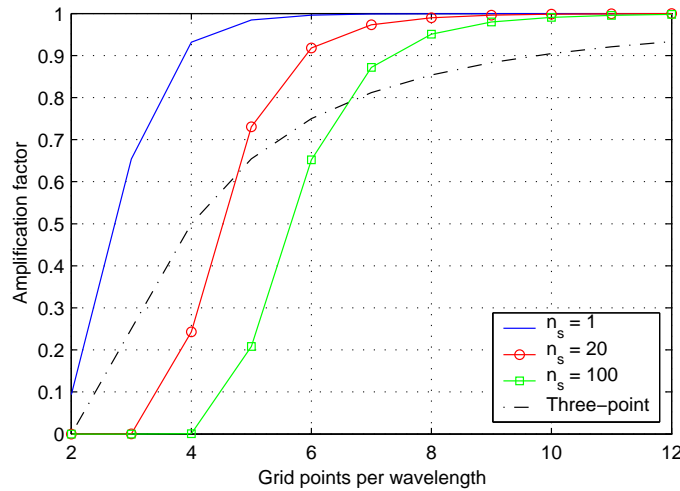


Figure 9.3: Amplification portrait for the nine-point filter (arising when the coefficients from the sixth-order, 57-point Savitzky-Golay smoothing filter are summed for an x - or a y -line) applied n_s times. Also shown for comparison is the portrait for a single application of the classical three-point filter.

We stress that the purpose of this analysis is merely to demonstrate that seemingly excessive applications of the high-order filter will not necessarily destroy modes of physical interest (and in fact will be less damaging than other commonly used lower-order filters). Other filtering techniques could also be used, and we adopt this particular strategy mainly out of convenience. As a reference value, we typically use a discretization of 20 points per primary wavelength (thus *e.g.* a bound second-harmonic would have 10 grid points per wavelength, and so on). As the repeated applications are only at points in the neighborhood of the structure, even seemingly large repetitions are insignificant with respect to the overall computational cost. Furthermore, the contact of a given wave with the structure is typically short, hence any added dissipation when compared to the rest of the domain is kept reasonable. While the necessity of such smoothing is of course not ideal, it has enabled us to compute wave structure interactions using the present model even in rather extreme physical situations (in particular see §9.6).

9.4 Linear Breakwater Diffraction

As a first means of model verification, we consider the classical problem of linear wave diffraction around a semi-infinite breakwater. We use linear incident waves with wavelength $L = 1$ m (*i.e.* wavenumber $k = 2\pi/L = 2\pi \text{ m}^{-1}$) propagating in the $+y$ -direction. We consider two depths $h = 0.25$ m ($kh = \pi/2$, with period $T = 0.835$ s, $\Delta t = T/20 = 0.0417$ s) and $h = 1$ m ($kh = 2\pi$, $T = 0.800$ s, $\Delta t = T/20 = 0.0400$ s). Both cases use a spatial discretization of $\Delta x = \Delta y = L/20 = 0.05$ m on a 400×221 grid, resulting in the computational domain shown in Figure 9.4. As described in §3.5, in all simulations

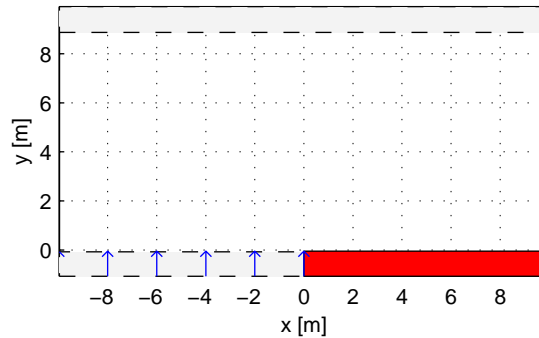


Figure 9.4: Model setup for linear breakwater diffraction simulations. The light shaded regions represent relaxation zones (wavemaker and sponge layer), the arrows indicate the incident wave direction, and the dark shaded region is the structure.

described in this chapter a wavemaker region relaxed over a single wavelength in the direction of propagation is used for wave generation, with a similar relaxation zone placed at the opposing end to absorb the outgoing wave-field. To mimic a semi-infinite breakwater, a rectangular structure covering the entire right half (positive x) of the wavemaker region is used, extending half a grid point beyond the region in y , with the exterior (diffracting) corner serving as the origin (see Figure 9.4). The smoothing filter is applied after every full time step for most of the domain, whereas around the structural boundary line applications are used after each stage evaluation (as described in §9.3), with $n_s = 1$ and $n_s = 20$ for the shallow and deep cases, respectively. As there are four stage evaluations per full time step, around the structure the filter is actually applied $4n_s$ times per time step. Simulations for 400 time steps required approximately 4.3 and 9.5 hr, respectively. Note that throughout this chapter the Intel compiler is used, and simulations are on a 2.26 GHz processor.

Diffraction diagrams for both simulations are presented in Figure 9.5. Also shown for comparison is the theoretical solution from Penny & Price (1952), based on the solution of Sommerfeld (1896). We note that relaxation zones are not used at the lateral boundaries, and we choose instead simply to take measurements before reflections off of these walls develop (this is done in part to demonstrate simulations on larger domains). As can be seen the numerical effects of the water depth create a varied response in the model. The shallow water simulation, Figure 9.5 (a), underestimates the waveheights in the shadow zone, but provides excellent results in the negative x region. Madsen & Warren (1984) found a similar under-estimation in the shadow zone with a lower-order Boussinesq model, thus this behavior is not unprecedented. Alternatively, the deep water simulation, Figure 9.5 (b), provides much improved results in the shadow zone, at the expense of minor errors in the negative x region. Numerical disturbances are much more apparent in this simulation, as can be seen in Figure 9.5 (b), just above the exterior corner.

To view these results in another light, computed and theoretical free surface envelopes are plotted in Figure 9.6 for both cases along $y = L$. The previously mentioned numerical disturbances are again evident for the deep water case in Figure 9.6 (b), causing an over-estimation of the modulations in the negative x -direction. Although not perfect, the results from both

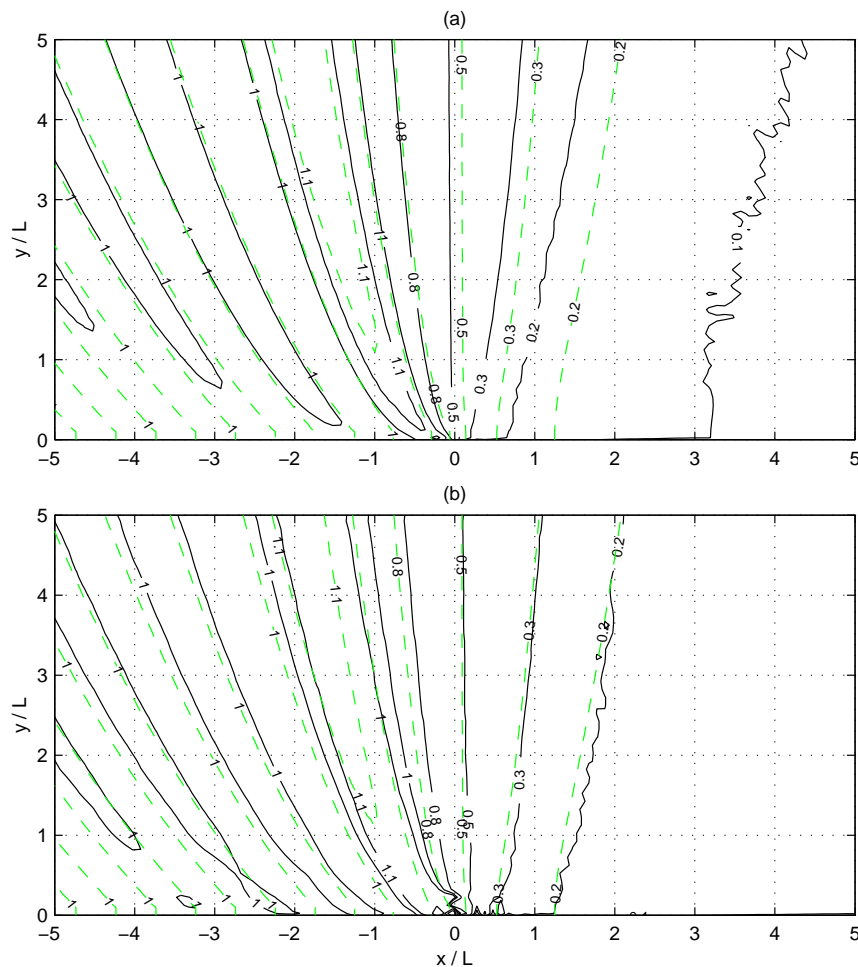


Figure 9.5: Computed (solid) and theoretical (dashed) linear diffraction diagrams with (a) $kh = \pi/2$ and (b) $kh = 2\pi$.

cases are seemingly acceptable for engineering purposes. These simulations demonstrate that the numerical difficulties described in §9.3 can be overcome over a wide range of water depths to produce reasonable results.

9.5 Linear & Nonlinear Gap Diffraction

As a second means of model verification we will consider linear and nonlinear gap diffraction. We use the setup from the symmetric gap diffraction experiment of Pos (1985), using incident waves with period $T = 0.67$ s and waveheight $H = 0.055$ m on a depth $h = 0.125$ m ($H/h = 0.444$). These waves diffract around a gap with width 0.99 m. For the linear simulation we use sinusoidal incident waves with wavelength $L = 0.604$ m (from the linear dispersion relation). For the nonlinear simulation we use stream function (Fenton, 1988) incident waves

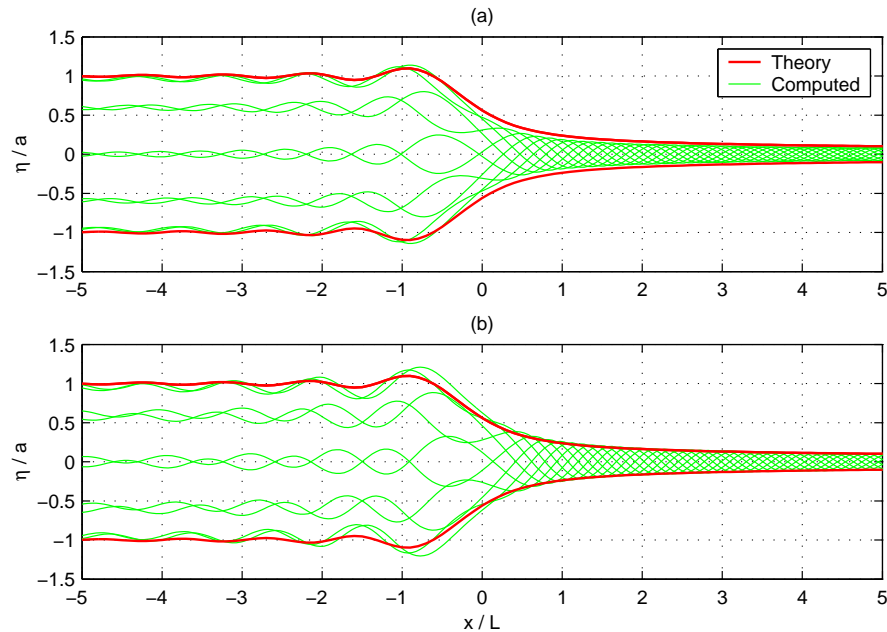


Figure 9.6: Computed and theoretical envelopes for linear diffraction around a breakwater along $y = L$ with (a) $kh = \pi/2$ and (b) $kh = 2\pi$. Here $a = H/2$ is the incident wave amplitude.

propagating in the $+x$ -direction with Stokes' drift (or mean transport) velocity $c_s = 0$ to match conditions of a closed flume, yielding a wavelength $L = 0.630$ m ($kh = 1.25$). Clearly these waves are nonlinear. For the discretization we use $\Delta x = \Delta y = 0.03$ m $\approx L/20$ and $\Delta t = T/20 = 0.0335$ s on a 201×221 computational grid. Due to symmetry only the lower half (in plan) of the physical domain is modeled. We match the gap width of the experiments and place the corner at the origin, just after the wavemaker region, as in §9.4. In both simulations the smoothing filter is applied after every five time steps throughout most of the domain. Around the structure line-smoothing is applied after each stage evaluation, with $n_s = 1$ for the linear simulation, and $n_s = 20$ for the nonlinear simulation. Both simulations were run for 300 time steps, taking roughly 1.0 and 3.9 hr, respectively.

Diffraction diagrams for this test case are presented in Figure 9.7. Figure 9.7 (a) shows computed results from the linear simulation as well as the theoretical results from Penny & Price (1952) for comparison. As might be expected from §9.4, the waveheights in the shadow zone are again under-predicted. The match in the far-field (only a few wavelengths away from the structure) is quite good, however. This figure is useful for comparison with the nonlinear simulation, described in the following.

Figures 9.7 (b) and (c) show the measured diffraction diagram of Pos (1985) and the computed results from the nonlinear simulation, respectively. The diffraction coefficients for the nonlinear simulation are calculated using the difference between maximum and minimum surface elevations at each grid point over a complete period, similar to what was done in the experiments. The computed free surface from the nonlinear simulation is also shown

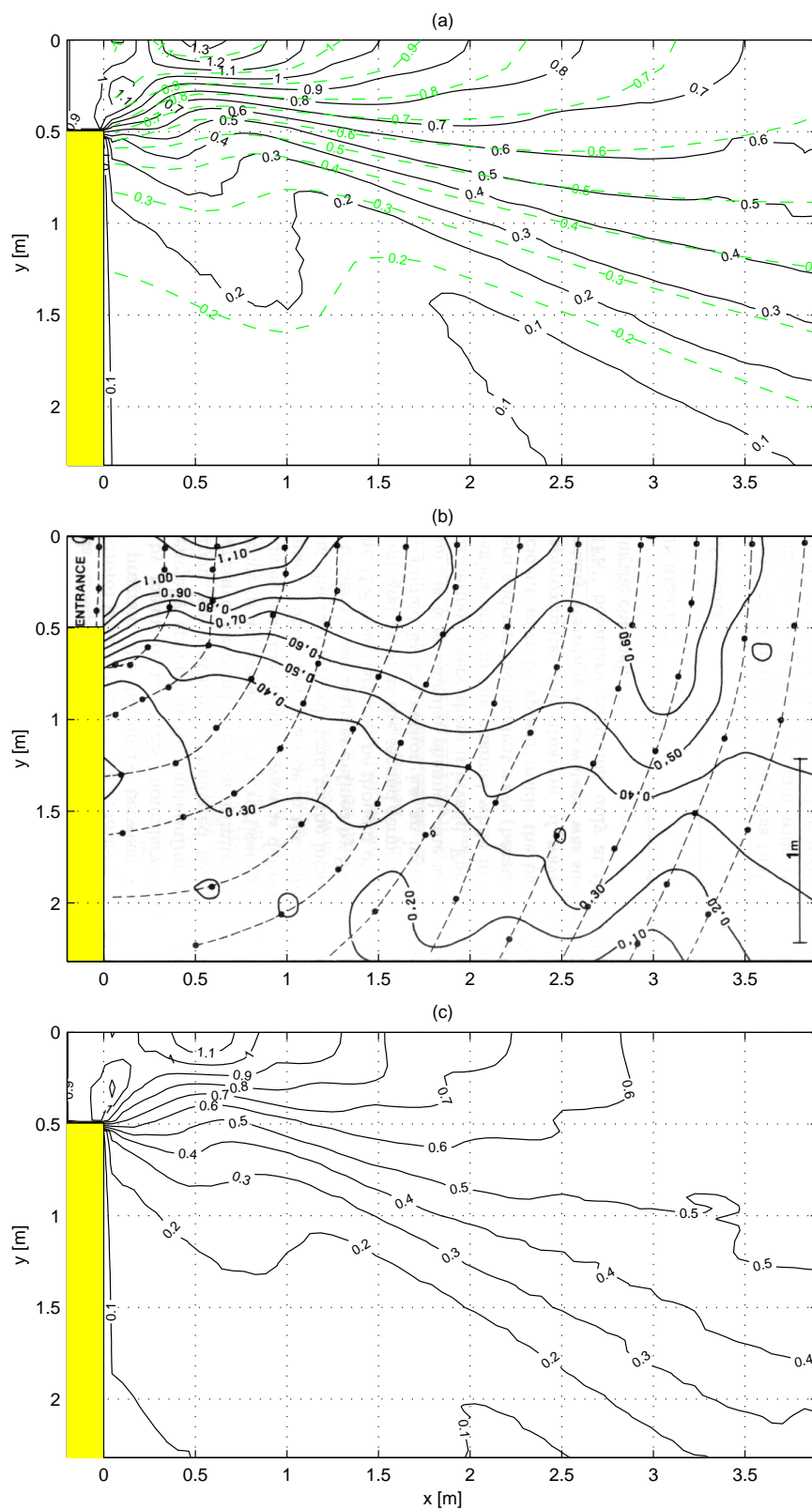


Figure 9.7: Gap diffraction diagrams ($t \approx 12T$) from (a) a linear simulation (solid) with linear theory (dashed), (b) the measurements of Pos (1985), and (c) a nonlinear simulation.

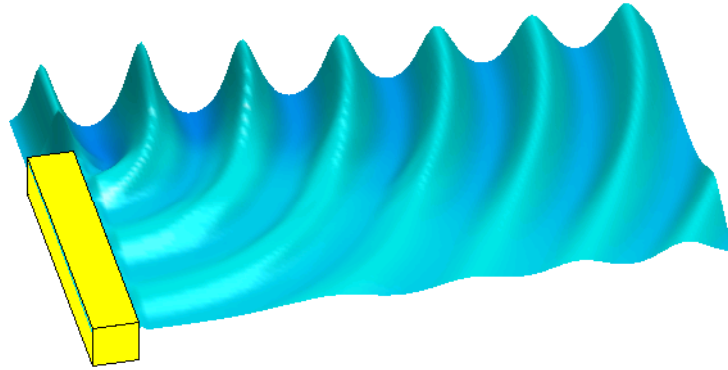


Figure 9.8: Computed free surface from the nonlinear gap diffraction simulation. The vertical scale is exaggerated 10 times.

in Figure 9.8. From Figure 9.7 (b) and (c), the waveheights in the shadow zone are again under-predicted. For the majority of the domain, however, the results match the measurements noticeably better than in the linear simulation, confirming the importance of nonlinear effects in this problem. In particular we note the focusing region directly behind the gap around $(x, y) = (0.6, 0)$, where the match is significantly improved. Other interesting features are qualitatively consistent with the experiments. For example, the weaving patterns of the 0.5–0.6 contours from the simulation are clearly present, though less exaggerated than in the measurements. Both the measured and computed 0.6–0.9 contours also demonstrate a clear tendency to turn upward (in plan) much earlier than predicted by linear theory, indicating reduced waveheights land-ward of the gap (there a general increase in the diffraction due to nonlinear effects). There is also a clear divide between contours turning upwards and running lengthwise in both diffraction diagrams. This is evident between the 0.4 and 0.5 contours in the measurements and between the 0.5 and 0.6 contours from the simulation. The extent of the 0.1 contour at $x \approx 2$ m even resembles the measurements rather closely.

We finally note that Abohadima & Isobe (1999) also simulated this case using a model based on weakly nonlinear time dependent mild slope equations. Their results (see their Figure 6) match the experiments better than those presented here in the extreme shadow zone. The present results are noticeably better in the far-field, however, likely due to the fully nonlinear capabilities of the current model.

9.6 Nonlinear Wave Run-Up on a Vertical Plate

As a final test case we consider a series of physical experiments presented by Molin *et al.* (2004, 2003, 2005) involving highly nonlinear deep water wave run-up on a vertical bottom-mounted plate. We consider the experiments with plane incident waves having period $T = 0.88$ s and waveheights $H = 0.038, 0.046,$ and 0.058 m on a depth $h = 3$ m. Using the linear dispersion relation this results in $L = 1.21$ m and $kh = 15.6$. The wavetank is 16 m wide,

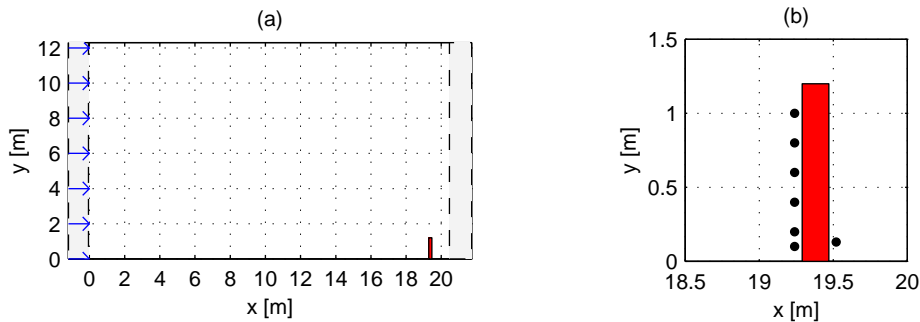


Figure 9.9: Model setup for the plate run-up simulations. The shaded regions are the same as in Figure 9.4. Figure (a) shows the entire domain, while (b) shows the approximate measurement locations around the plate.

with a 1.2 m plate (with thickness $b = 0.05$ m) extended perpendicularly from the bottom (in plan) sidewall 19.3 m from the wavemaker. By geometric symmetry this is equivalent to a 2.4 m wide plate in the middle of a 32 m tank. Time series measurements in front of the plate were recorded at $y = 0.1, 0.2, 0.4, 0.6, 0.8,$ and 1.0 m and behind the plate at $y = 0.13$ m, where the side-wall runs along $y = 0$.

The full computational domain used is shown in Figure 9.9 (a), with the approximate measurement locations around the plate shown in Figure 9.9 (b). For the numerical simulations we reduce the depth to $h = 0.6$ m, hence $kh \approx \pi$. Thus, we still solve a deep water problem, while easing the previously described numerical difficulties associated with large depths and nonlinearities. We use plane incident waves propagating in the $+x$ -direction computed from the stream function solution of Fenton (1988), giving wavelengths $L = 1.212, 1.216,$ and 1.223 m (with incident steepness $H/L = 0.0314, 0.0378,$ and $0.0474,$ respectively). For the discretization we use $\Delta x = 0.06$ m $\approx L/20$, $\Delta y = 0.0615$ m, and $\Delta t = T/20 = 0.044$ s on a 383×201 computational grid. A 1.2×0.18 m plate (the width is again limited to $3\Delta x$) is extended outward from $y = 0$ with the front face at $x = 19.29$ m, nearly matching the physical setup. To ease the computational burden, the width of the computational domain (12.3 m) is not quite large as in the physical experiments, but has been found to have negligible effects on the wave run-up near the plate. We also use a single precision variant of the Schur complement preconditioner from §4.6.4 for this problem. In each of the simulations the smoothing filter is applied every 5 full time steps throughout most of the domain. Line-smoothing is applied around the plate after each stage evaluation with $n_s = 20$ for the first two cases and $n_s = 100$ for the case with $H = 0.058$ m. As a reference, the simulation with $H = 0.046$ m was run for 1500 time steps, requiring roughly 20 hr. We are confident that similar results could be obtained using a significantly smaller model domain, however we present these simulations as demonstrations of the nonlinear model on a rather large computational domain.

For comparison we consider the time frame $55 < t < 60$ s for the first two cases and $50 < t < 55$ s for the case with $H = 0.058$ m (due to a breakdown from extreme nonlinearities at the end of the simulation). These windows correspond roughly to the time after the group

Table 9.1: Summary of maximum wave steepness, surface elevation, and elevation amplification factor (estimated as $2\eta_{max}/H$) from the envelopes in front of the plate and along $y = 0$ for the plate run-up simulations.

Incident		Plate envelope			$y = 0$ envelope		
H [m]	H/L	H/L_{max}	η_{max} [m]	Factor	H/L_{max}	η_{max} [m]	Factor
Linear		—	—	2.32	—	—	2.37
0.038	0.0314	0.085	0.0569	2.99	0.093	0.0629	3.31
0.046	0.0378	0.109	0.0755	3.28	0.131	0.0926	4.03
0.058	0.0474	0.173	0.128	4.41	0.203	0.1525	5.26

velocity has traveled to the plate and back to the wavemaker. In both the experiments and the simulations a clear peak is observed when the initial wave front reaches the plate, and for comparison purposes the measured time series have been shifted to coordinate this event at a single location.

Measured and computed free surface envelopes along the front of the plate are shown in Figure 9.10 for all three cases. The match with the experiments in each case is impressive. Both the model and experiments demonstrate a clear migration of the maximum surface elevation from roughly the middle of the plate to the plate-wall corner (at $y = 0$) as the nonlinearity is increased. The simulations also confirm the significant increase in the surface elevations due to the nonlinear effects involved in the run-up. The computed free surface near the plate from the simulation with $H = 0.058$ m is also shown in Figure 9.11.

To illustrate the run-up more clearly, and to further demonstrate the extreme nonlinearity involved in these simulations, we present computed envelopes from the wavemaker to the plate along $y = 0$ in Figure 9.12. From a comparison with the wavemaker regions (negative x), it is clear that the reflected wave has traveled all the way back to the wavemaker in Figures 9.12 (a) and (b), while this is nearly the case in (c). Note that in these simulations we are not using a second relaxation zone after the wavemaker, to match the experimental conditions. From these figures, it is seen that the maximum surface elevation actually occurs at a distance of $\approx L/2$ in front of the plate in each case, resulting in extremely steep nearly-standing waves.

The maximum wave steepness, surface elevation, and surface elevation amplification observed in Figures 9.10 and 9.12 are quantified in Table 9.1 for each of the cases. Also shown for comparison are the amplification results from a linear simulation. A very significant amplification is once again observed as the nonlinearity increases, consistent with the earlier observations (see Figure 9.10). In the most extreme case, the incident waves are amplified by a factor greater than 5 slightly in front of the plate, resulting in a local wave steepness exceeding $H/L = 0.2$! Slightly lower values are found at the plate. These observations support the contention of Molin *et al.* (2004, 2003), that the observed run-up involves (at least) third-order effects in the wave steepness.

To demonstrate that the relative phase is also correct about the plate, a comparison of selected time series measurements with the computed results for the case with $H = 0.046$

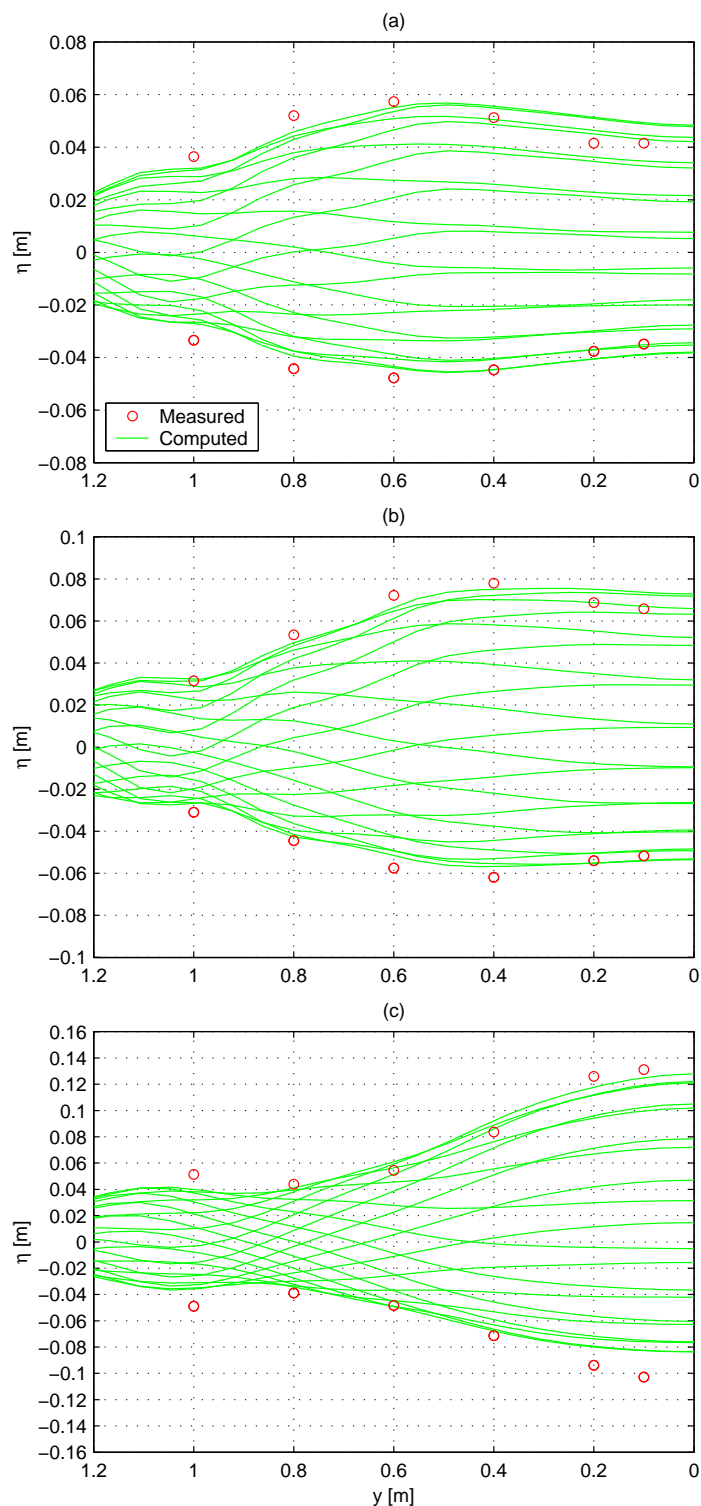


Figure 9.10: Computed and measured free surface envelopes in front of the plate for (a) $H = 0.038$ m, (b) $H = 0.046$ m, and (c) $H = 0.058$ m.

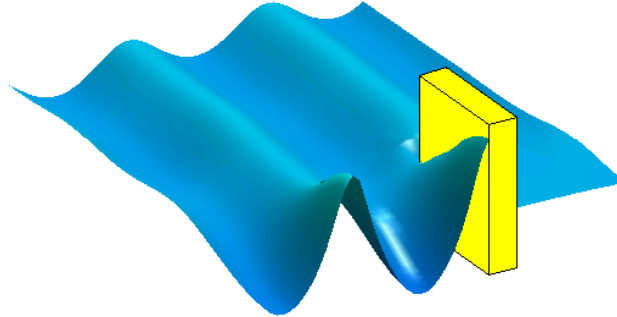


Figure 9.11: Computed free surface near the plate for the simulation with incident waves having $H = 0.058$ m. The vertical scale is exaggerated five times.

m is provided in Figure 9.13. As can be seen, during this time frame both experiments and simulation are near a steady state. The match between the computed and measured time series is again excellent. Indeed, even behind the plate the match is quite satisfactory, as seen in Figure 9.13 (d), confirming reasonable diffraction properties in this case. Note that at this location the computed solution has been shifted by a time of $(b - 3\Delta x)/c = -0.094$ s (where $c = L/T$ is the wave celerity) to compensate for the extra width of the plate. Time series comparisons at the other locations, as well as from the other cases are of similar quality as those presented in Figure 9.13.

This test case demonstrates an interesting and realistic situation where the interaction of moderately nonlinear incident waves with a structure results in rather extreme nonlinearities. The excellent nonlinear and dispersive properties of the present model have clearly been put to the test in this section. This case in particular represents a challenging physical situation which would likely be unamenable with most other Boussinesq-type models.

9.7 Conclusions

This chapter describes the extension of the basic finite difference model based on the high-order Boussinesq formulation of Madsen *et al.* (2002, 2003) to allow domains with arbitrary piecewise-rectangular bottom-mounted structures. While conceptually this is trivial, the practical difficulties are considerable. Due mainly to the necessity of discretizing high- (up to fifth-) order mixed derivative terms at theoretically singular exterior corner points, the model is prone to potential stability and convergence problems. These generally become more pronounced as the numerical importance of the high-derivative (Boussinesq-type) terms is increased (*i.e.* large water depths or refined grids). Fortunately, as we have demonstrated through analysis and direct numerical simulations, the system is receptive to dissipation. Repeated local applications of a high-order smoothing filter provide a simple and effective

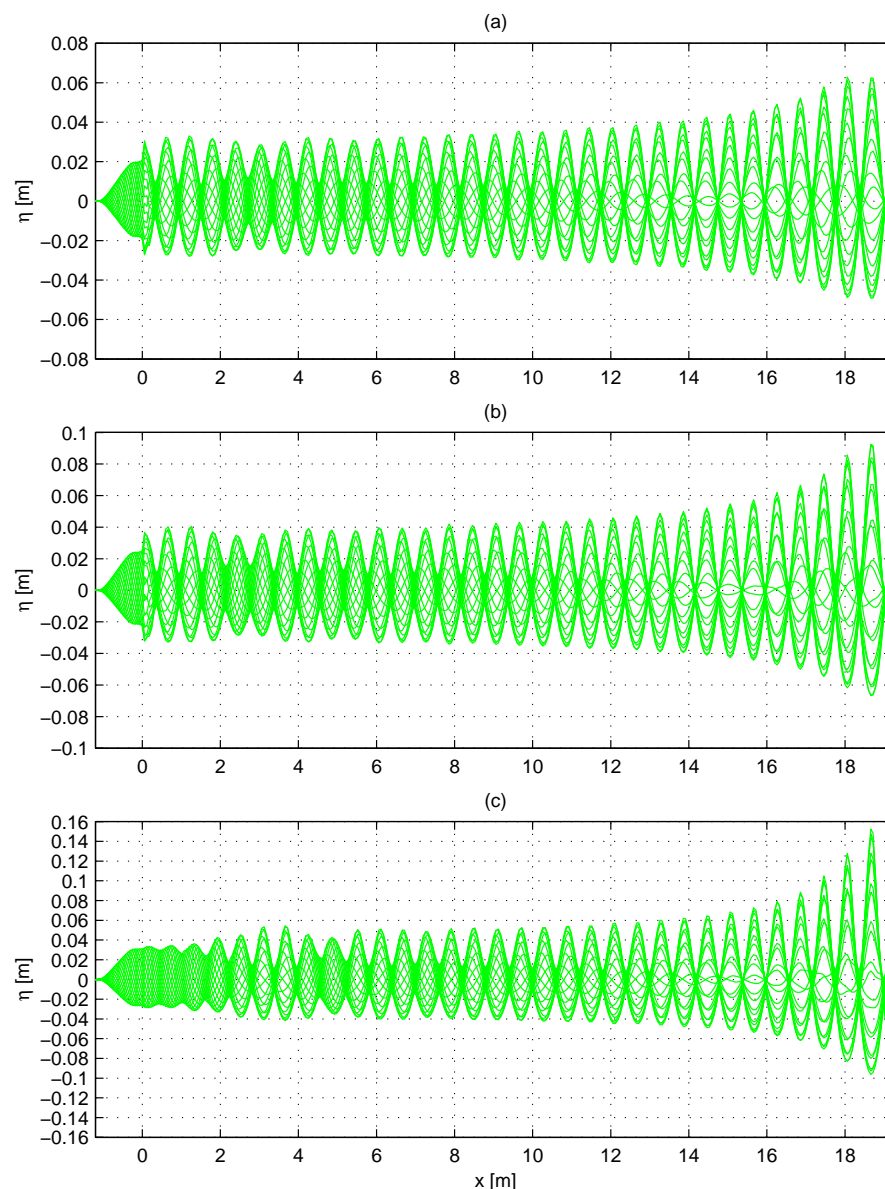


Figure 9.12: Computed free surface envelopes along $y = 0$ for (a) $H = 0.038$ m, (b) $H = 0.046$ m, and (c) $H = 0.058$ m.

means for managing these problems in practical situations, while minimizing damage to modes of physical interest.

The numerical model is verified using three different test cases. These involve classical linear diffraction around a semi-infinite breakwater (in both shallow and deep water), linear and nonlinear (shallow water) gap diffraction, and highly nonlinear deep water run-up on a vertical bottom-mounted plate. From the diffraction cases, there is unfortunately a tendency for an under-estimation of the waveheights in the extreme shadow zone. This is particularly apparent in the shallow water simulations presented herein, though our experience has shown

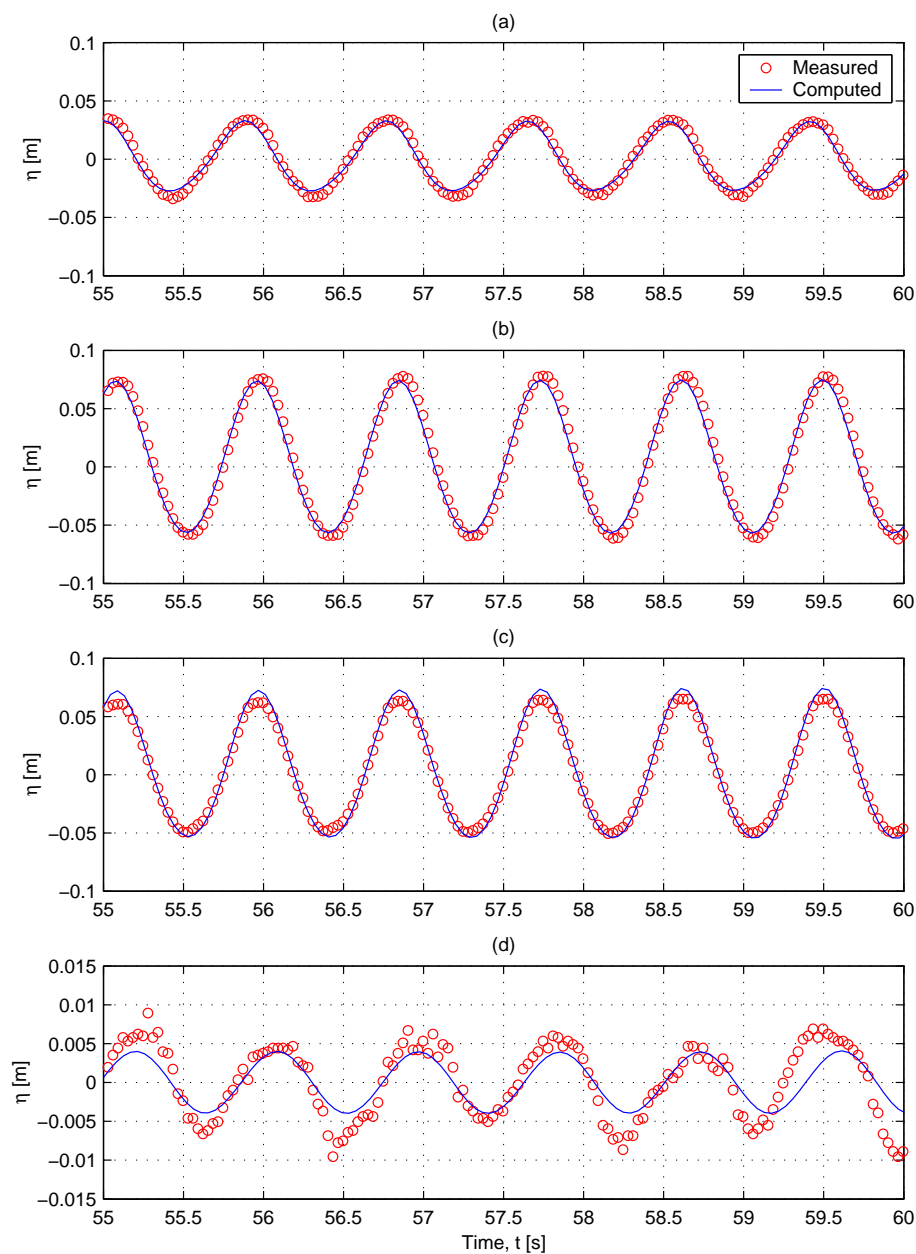


Figure 9.13: Measured and computed time series of surface elevations ($H = 0.046$ m) in front of the plate near (a) $y = 1$ m, (b) $y = 0.4$ m, and (c) $y = 0.1$ m; and (d) behind the plate near (d) $y = 0.13$ m.

that this tendency is reasonably wide-spread. The match in the far field is generally much better. Despite these acknowledged difficulties, the model has proven to be reasonably accurate in cases involving diffraction over a wide range of depth and nonlinearity.

The most impressive results presented are those involving the highly nonlinear deep water wave run-up on a vertical plate in §9.6. For the full range of incident wave steepness tested, the comparison with measurements proved to be excellent. The extreme nonlinearity in combination with the depth for these cases results in problems which would be difficult, if not impossible, for other Boussinesq-type models in the literature. The present model seems ideally suited for problems of this type.

While other, simpler, models (*e.g.* those based on the mild-slope equation of Berkhoff, 1972) would undoubtedly be better suited for simulations where the physics are not too extreme, the potentially wide applications of the present model (in terms of both water depth and nonlinearity) make it attractive for solving some extremely difficult, yet seemingly common, problems involving wave-structure interactions arising in the fields of coastal and offshore engineering.

Chapter 10

Extension to Rapidly Varying Bathymetry

Chapter Summary

New Boussinesq-type equations are given for fully nonlinear and highly dispersive water waves interacting with a rapidly varying bathymetry. The system is an extension of the high-order formulation used previously, which is limited to mildly sloping bottoms. The new formulation is again based on a series expansion from an arbitrary, spatially varying z -level $z = \hat{z}(x, y)$. Under the assumption that \hat{z} is slowly varying in space, *i.e.* $\hat{z} = \hat{z}(\delta x, \delta y)$, where $\delta \ll 1$, the exact velocity expressions are simplified to include up to low-order derivatives of \hat{z} . On the other hand, no mild-slope assumptions about the variation of the sea bottom $h(x, y)$ are made. The choice of the expansion level \hat{z} is an important key to the successful use of the model: For rapidly varying bathymetries it is necessary to smooth \hat{z} in order to reduce the magnitude of *e.g.* $\nabla \hat{z}$ and $\hat{z} \nabla^2 \hat{z}$ terms. In this process local deviations from the optimal $\hat{z} = -h/2$ are generally acceptable, as long as this ratio is within the interval $0.2 \leq \sigma \leq 0.55$, where $\sigma = -\hat{z}/h$. Numerical results are given for linear shoaling, confirming that the excellent embedded properties of the original formulation are retained. Simulations involving the linear reflection from a plane shelf are also included, which clearly demonstrate the superiority of the new formulation in cases involving partial reflection from rapid bathymetric changes. Furthermore, linear class I and II Bragg scattering from an undular sea bottom is simulated. The computations are verified against measurements, theoretical solutions, and numerical models from the literature. Finally, a detailed investigation of nonlinear class III Bragg scattering is made, and new results are given for the subharmonic and superharmonic interactions with the sea bed.

10.1 Introduction

One of the investigations made by Madsen, Bingham & Schäffer (2003), leading to the Boussinesq formulation presented in Chapter 2, addressed the importance of the first derivatives of \hat{z} appearing in the velocity formulation. They made a Fourier analysis of the linearized equations on a mildly sloping bottom and found that the terms proportional to $\nabla\hat{z}$ had no influence on linear shoaling of the wave amplitude, but merely a local (minor) influence on the velocity profile, leading to a phase shift relative to the surface elevation. This conclusion was found to be valid for the case of infinite series expansions, as well as for the Boussinesq formulation using truncated expansions. On this basis Madsen *et al.* (2003) concluded that these terms could be ignored for most practical purposes. The highly accurate numerical results for nonlinear shoaling on a slope of 1/35 presented by Madsen, Bingham & Liu (2002) confirmed this conclusion.

Unfortunately, recent investigations have proven that in general the $\nabla\hat{z}$ terms should not be left out. One classical example demonstrating the shortcomings of the original model is the partial reflection from a constant slope, which was originally investigated by Booij (1983) with the objective of checking the validity of the approximations in the mild-slope wave equation of Berkhoff (1972). We have recently simulated this case and found that without the explicit $\nabla\hat{z}$ terms in the velocity formulation, the computed reflection coefficients are significantly off, even when the slope is relatively mild. Other cases such as steep shelves, steep trenches, and undular sea bottoms call for further attention, as any mild slope approximation is violated for such rapidly varying bathymetries.

This is the motivation for the present chapter, in which we present a new high-order Boussinesq-type formulation for fully nonlinear waves interacting with a rapidly varying bathymetry. The derivation is similar to that presented in Chapter 2 (for full details see Madsen, Fuhrman & Wang, 2005). However, for the first time, this derivation has been made without invoking mild-slope approximations. In the final formulation we assume that the spatial variation of the expansion level $\hat{z}(x, y)$ is moderately varying so that higher derivatives of \hat{z} can be ignored. The resulting velocity formulation again includes up to fifth derivatives of the velocity variables. On this basis the kinematic condition at the sea bottom is also derived.

The remainder of this chapter is organized as follows. The extension of the basic Boussinesq formulation to be valid for rapidly varying bathymetries is described in §10.2. A linear Fourier analysis of the embedded dispersive properties is presented in §10.3. The results of numerical simulations involving linear shoaling are presented in §10.4, and for linear reflection from a plane shelf in §10.5. Finally, numerical simulations involving linear class I and II, and nonlinear class III Bragg scattering are presented in §10.6. Conclusions are formulated in §10.7.

The subject matter from this chapter can be found in a more extensive form in Madsen, Fuhrman & Wang (2005). There a rigorous derivation and analysis is presented, as are

numerous additional computational results. Some results are also presented in Madsen & Fuhrman (2004).

10.2 Extension to Rapidly Varying Bathymetry

The velocity formulation of Madsen *et al.* (2003) (see also Chapter 2) uses an expansion from an arbitrary z -level, which is assumed to be a constant fraction of the sea bed measured from the still water level, namely $\hat{z} = -h/2$. On an uneven bottom the resulting untruncated expressions in fact contain infinitely high derivatives of \hat{z} . Madsen *et al.* (2003) made a mild-slope approximation and finally ignored *all* spatial derivatives of \hat{z} , as was presented in Chapter 2. In order to allow for more dramatic bathymetric variations, we extend their derivation to a more flexible variation of \hat{z} , while keeping low-order derivatives of \hat{z} in this section.

By following a similar procedure as outlined in Chapter 2, but by assuming that \hat{z} is a mildly sloping function in space *i.e.* $\hat{z} = \hat{z}(\delta x, \delta y)$, Madsen *et al.* (2005) arrived at the general velocity formulation

$$\mathbf{u}(x, y, z, t) = J_I \hat{\mathbf{u}}^* + J_{II} \hat{w}^*, \quad (10.1)$$

$$w(x, y, z, t) = J_I \hat{w}^* - J_{II} \hat{\mathbf{u}}^*, \quad (10.2)$$

where

$$J_I = J_{01} + \delta \nabla \hat{z} J_{11} + \delta^2 \nabla^2 \hat{z} J_{21} + \delta^2 (\nabla \hat{z})^2 J_{31} + O(\delta^3), \quad (10.3)$$

$$J_{II} = J_{02} + \delta \nabla \hat{z} J_{12} + \delta^2 \nabla^2 \hat{z} J_{22} + \delta^2 (\nabla \hat{z})^2 J_{32} + O(\delta^3), \quad (10.4)$$

with

$$J_{01} \equiv 1 + \left(-\frac{\psi}{2} + \frac{\hat{z}^2}{18} \right) \nabla^2 + \left(\frac{\psi^4}{24} - \frac{\hat{z}^2 \psi^2}{36} + \frac{\hat{z}^4}{504} \right) \nabla^4, \quad (10.5)$$

$$J_{02} \equiv \psi \nabla + \left(-\frac{\psi^3}{6} + \frac{\hat{z}^2 \psi}{18} \right) \nabla^3 + \left(\frac{\psi^5}{120} - \frac{\hat{z}^2 \psi^3}{108} + \frac{\hat{z}^4 \psi}{504} \right) \nabla^5, \quad (10.6)$$

$$\begin{aligned} J_{11} \equiv & \psi \nabla + \left(-\frac{\psi^3}{2} - \frac{\hat{z} \psi^2}{9} + \frac{\hat{z}^2 \psi}{18} \right) \nabla^3 + \\ & \left(\frac{\psi^5}{24} + \frac{\hat{z} \psi^4}{54} - \frac{\hat{z}^2 \psi^3}{36} - \frac{\hat{z}^3 \psi^2}{126} + \frac{\hat{z}^4 \psi}{504} \right) \nabla^5, \end{aligned} \quad (10.7)$$

$$J_{12} \equiv \left(\psi^2 + \frac{\hat{z} \psi}{9} \right) \nabla^4 + \left(-\frac{\psi^4}{6} - \frac{\hat{z} \psi^3}{18} + \frac{\hat{z}^2 \psi^2}{18} + \frac{\hat{z}^3 \psi}{126} \right) \nabla^4, \quad (10.8)$$

and $\psi = (z - \hat{z})$. The J_{21} , J_{22} , J_{31} , and J_{32} operators can also be found in Madsen *et al.* (2005), however, as they are not used in the present chapter they are left out for brevity. Note that by setting $\delta = 0$ in (10.3) and (10.4), (10.1) and (10.2) become equivalent to the original expressions (2.40) and (2.41).

By inserting (10.1) and (10.2) into (2.14), the kinematic bottom condition then becomes

$$\begin{aligned}
& \left(1 + \left(\frac{\hat{z}^2}{18} - \frac{\psi_b^2}{2}\right) \nabla^2 + \left(\frac{\hat{z}^4}{504} - \frac{\hat{z}^2 \psi_b^2}{36} + \frac{\psi_b^4}{24}\right) \nabla^4\right) \hat{w}^* - \\
& \left(\psi_b \nabla + \left(\frac{\hat{z}^2 \psi_b}{18} - \frac{\psi_b^3}{6}\right) \nabla^3 + \left(\frac{\hat{z}^4 \psi_b}{504} - \frac{\hat{z}^2 \psi_b^3}{108} + \frac{\psi_b^5}{120}\right) \nabla^5\right) \hat{\mathbf{u}}^* + \\
\delta \nabla h \cdot & \left[\left(1 + \left(\frac{\hat{z}^2}{18} - \frac{\psi_b^2}{2}\right) \nabla^2 + \left(\frac{\hat{z}^4}{504} - \frac{\hat{z}^2 \psi_b^2}{36} + \frac{\psi_b^4}{24}\right) \nabla^4\right) \hat{\mathbf{u}}^* + \right. \\
& \left. \left(\psi_b \nabla + \left(\frac{\hat{z}^2 \psi_b}{18} - \frac{\psi_b^3}{6}\right) \nabla^3 + \left(\frac{\hat{z}^4 \psi_b}{504} - \frac{\hat{z}^2 \psi_b^3}{108} + \frac{\psi_b^5}{120}\right) \nabla^5\right) \hat{w}^* \right] + \\
\delta \nabla \hat{z} \cdot & \left[\left(\psi_b \nabla + \beta_{13} \left(\frac{\hat{z}^2 \psi_b}{18} - \frac{\hat{z} \psi_b^2}{9} - \frac{\psi_b^3}{2}\right) \nabla^3 + \right. \right. \\
& \left. \left. \beta_{15} \left(\frac{\hat{z}^4 \psi_b}{504} - \frac{\hat{z}^3 \psi_b^2}{126} - \frac{\hat{z}^2 \psi_b^3}{36} + \frac{\hat{z} \psi_b^4}{54} + \frac{\psi_b^5}{24}\right) \nabla^5\right) \hat{w}^* - \right. \\
& \left. \left(\beta_{12} \left(\frac{\hat{z} \psi_b}{9} + \psi_b^2\right) \nabla^2 + \beta_{14} \left(\frac{\hat{z}^3 \psi_b}{126} + \frac{\hat{z}^2 \psi_b^2}{18} - \frac{\hat{z} \psi_b^3}{18} - \frac{\psi_b^4}{6}\right) \nabla^4\right) \hat{\mathbf{u}}^* \right] + \\
& \delta^2 \nabla^2 \hat{z} \Gamma_1 + \delta^2 \nabla \hat{z} \cdot \nabla \hat{z} \Gamma_2 + \delta^2 \nabla \hat{z} \cdot \nabla h \Gamma_3 = O(\delta^3), \tag{10.9}
\end{aligned}$$

where $\psi_b = -(h + \hat{z})$. The $O(\delta^2)$ terms can again be found in Madsen *et al.* (2005), but are left out here for brevity. Note that here the β -coefficients are left as free parameters, similar to §2.6. By optimizing with respect to the liner shoaling gradient (with $\hat{z} = -h/2$), Madsen *et al.* (2005) recommend setting

$$\beta_{12} = 0.95583, \quad \beta_{14} = 0.51637, \quad \beta_{13} = 0.72885, \quad \beta_{15} = 0.28478, \tag{10.10}$$

which can be shown to provide highly-accurate shoaling properties out to $kh \approx 30$. This will be verified through direct numerical simulation in §10.4. Note that a similar optimization procedure was applied by *e.g.* Agnon *et al.* (1999); Madsen *et al.* (2002, 2003); Madsen & Schäffer (1998).

Thus the new fully nonlinear formulation now consists of (2.11) and (2.13), combined with (10.1), (10.2), and (10.9). The new expressions can be seen to be somewhat more lengthy than those originally used from Chapter 2. The terms involved are of essentially identical form, however, thus the implementation of this new formulation is not significantly more complicated than before.

10.3 Fourier Analysis of Linear Dispersion

By analyzing the linearized flat-bottom system, following the procedure described previously in §2.7, Madsen *et al.* (2005) arrived at the following embedded dispersion relation for arbitrary \hat{z}

$$\frac{\omega^2}{ghk^2} = \frac{1 + \mu_2(kh)^2 + \mu_4(kh)^4 + \mu_6(kh)^6 + \mu_8(kh)^8}{1 + \nu_2(kh)^2 + \nu_4(kh)^4 + \nu_6(kh)^6 + \nu_8(kh)^8 + \nu_{10}(kh)^{10}}, \quad (10.11)$$

where

$$\begin{aligned} \mu_2 &= \left(\frac{1}{6} - \frac{\sigma^2}{9} \right), & \mu_4 &= \left(\frac{1}{120} - \frac{\sigma^2}{54} + \frac{4\sigma^4}{567} \right), \\ \mu_6 &= \left(\frac{\sigma^2}{270} - \frac{\sigma^3}{72} + \frac{29\sigma^4}{1701} - \frac{\sigma^5}{135} + \frac{2\sigma^6}{2835} \right), \\ \mu_8 &= \left(\frac{\sigma^4}{7560} - \frac{\sigma^5}{1620} + \frac{17\sigma^6}{17010} - \frac{11\sigma^7}{17010} + \frac{8\sigma^8}{59535} \right), \end{aligned} \quad (10.12)$$

$$\begin{aligned} \nu_2 &= \left(\frac{1}{2} - \frac{\sigma^2}{9} \right), & \nu_4 &= \left(\frac{1}{24} - \frac{\sigma^2}{18} + \frac{4\sigma^4}{567} \right), \\ \nu_6 &= \left(\frac{\sigma}{120} - \frac{5\sigma^2}{216} - \frac{\sigma^3}{54} - \frac{5\sigma^4}{1134} + \frac{\sigma^5}{945} - \frac{\sigma^6}{2835} \right), \\ \nu_8 &= \left(\frac{\sigma^3}{1080} - \frac{\sigma^4}{252} + \frac{7\sigma^5}{1215} - \frac{\sigma^6}{315} + \frac{4\sigma^7}{8505} + \frac{\sigma^8}{59535} \right), \\ \nu_{10} &= \left(\frac{\sigma^5}{113400} - \frac{\sigma^6}{22680} + \frac{2\sigma^7}{25515} - \frac{\sigma^8}{17010} + \frac{\sigma^9}{59535} - \frac{\sigma^{10}}{893025} \right). \end{aligned} \quad (10.13)$$

This should be compared to Stokes' reference solution from (2.48). A contour plot showing the percentage error in the ratio $(c^2 - c_{Stokes}^2)/c_{Stokes}^2$ is shown in Figure 10.1 as a function of kh and $\sigma = -\hat{z}/h$. From this we conclude that less than 2.5% errors are observed for $kh < 15$ with $0.20 \leq \sigma \leq 0.55$. This flexibility is useful for cases involving rapidly varying bathymetries, where smoothing the expansion level \hat{z} (but not h) leads to local deviations from the optimal choice of $\sigma = 0.5$. Note that with $\sigma = 0.5$ the embedded linear dispersive properties are the same as shown previously in Figure 2.1.

It is important to emphasize that singularities in (10.11) start to develop within the range $0.524 < \sigma < 0.6832$. The roots $k_R h$ of the denominator of (10.11) are shown (as open circles) in Figure 10.2. Within this interval instabilities can in principle be triggered in the numerical model, if the highest resolved dimensionless wavenumber $k_N h$ exceeds $k_R h$. This conclusion, however, is only indicative, and to investigate the exact numerical aspects of this matter we make a matrix based stability analysis of the linearized system (similar to §5.5) in a single horizontal dimension. Thus, we express the linearized system in the semi-discrete form (5.1). We keep the depth constant, and for a particular σ gradually increase the

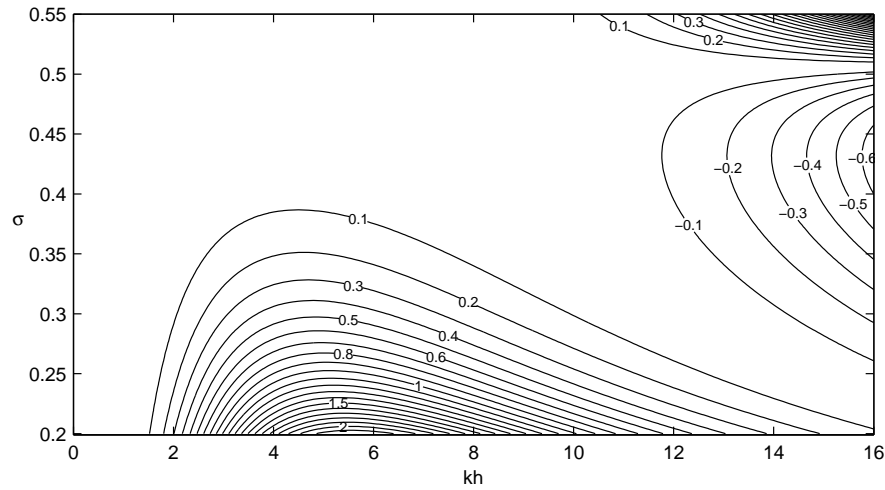


Figure 10.1: Percentage error in $(c^2 - c_{Stokes}^2)/c_{Stokes}^2$ based on the dispersion relation (10.11) as a function of kh and $\sigma = -\hat{z}/h$.

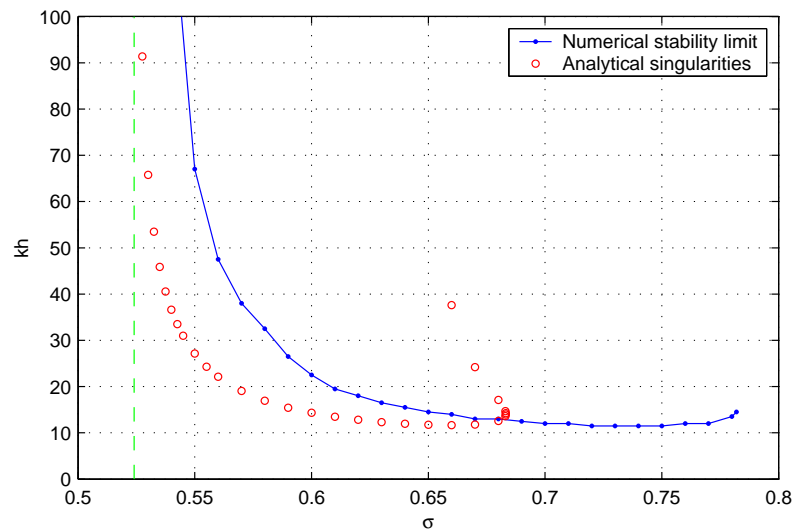


Figure 10.2: Limiting $k_N h$ for numerical stability for various values of σ . Also shown for comparison are calculated analytical singularities (*i.e.* poles) in the embedded dispersion relation. The dashed vertical line at $\sigma = 0.524$ corresponds to the maximum value of σ where no singularities exist, both analytically and numerically.

Nyquist wavenumber $k_N = \pi/\Delta x$ until an eigenvalue with a positive real part is encountered, corresponding to a numerical instability (recall from Chapter 5 that the eigenvalues of the linearized system are normally purely imaginary). The Nyquist wavenumbers just prior to an instability are also shown in Figure 10.2. They confirm the trend of the analytical poles at $k_R h$, while also allowing slightly more flexibility for applications of the model (*i.e.* the numerical curve lies slightly above the analytical curve). We can conclude that to completely avoid the possibility of singularities, we should choose $\sigma < 0.524$, but in practice it is possible to accept local values perhaps as high as $\sigma \approx 0.57$ as long as the grid size is not too fine. In general we recommend staying within the interval $0.20 \leq \sigma \leq 0.55$ for most practical cases. The stability analysis has been confirmed through testing with the numerical model.

10.4 Linear Shoaling

As the first test case of the new model we consider linear shoaling on a mildly sloping beach, similar to §6.4. The objective is to confirm that the numerical model follows the theoretical shoaling analysis made by Madsen *et al.* (2005). Contrary to results presented elsewhere in this thesis, all numerical results in the present chapter use a single horizontal dimension, using a numerical algorithm similar to that presented in Madsen *et al.* (2002).

We simulate the transformation of monochromatic linear waves running up a plane slope of $1/20$. We use a wave period of $T = 1.13$ s, with depths ranging from $h = 9.55$ m at the deep water entrance to 0.036 m at the shallow end. The simulation covers a transition from $kh = 30$ to $kh = 0.35$, which is an extreme range of wavenumbers. The shoaling analysis made in Madsen *et al.* (2005) indicates that it is feasible, however, when the optimized shoaling coefficients defined by (10.10) are used (as opposed to the default values of unity). For the discretization we use $\Delta x = 0.04$ m and $\Delta t = 0.03$ s.

The computed result is shown in Figure 10.3, and we notice a perfect agreement with the linear shoaling theory, which is shown as the full lines in the envelope. In contrast, when the non-optimized shoaling coefficients are applied, the result is very erroneous (not shown). We emphasize that the same accuracy can be achieved using the formulation by Madsen *et al.* (2002) (*i.e.* the formulation from Chapter 2) although only the J_{01} , J_{02} operators were included in the velocity formulation. This case hence demonstrates that the excellent embedded properties of the original formulation are retained in the new extended version presented in this chapter.

10.5 Reflection from a Plane Shelf

The next case deals with wave reflection from a plane shelf. We consider the classical benchmark originally suggested by Booij (1983). The topography, shown in Figure 10.4 (a),

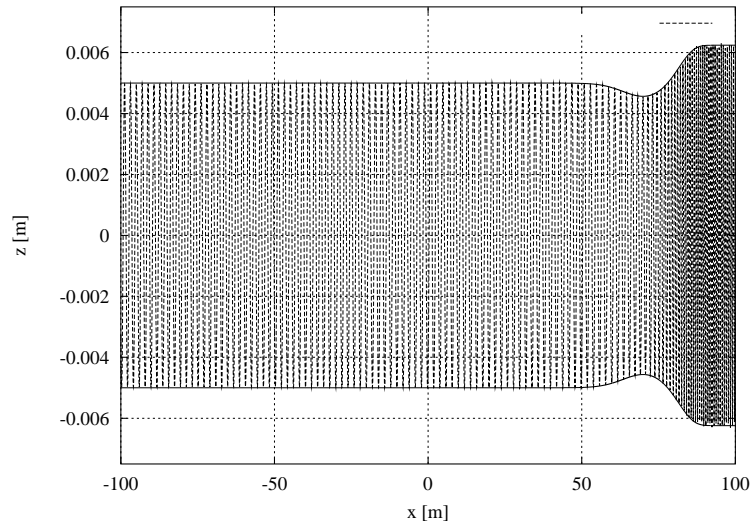


Figure 10.3: Linear shoaling on a 1:20 slope covering the range $0.35 < kh < 30$. The dashed line is the computed surface elevation, while the full line is the shoaling envelope based on linear theory.

consists of a plane slope connecting two constant depth regions, with an incoming depth of 0.6 m and a final depth of 0.2 m. The width of the plane slope b_0 is varied from case to case within the interval $6.4 \text{ m} \geq b_0 \geq 0.4 \text{ m}$, corresponding to slopes of 1/16 to 1.0. We study the reflection of monochromatic linear waves with a period $T = 2.0 \text{ s}$, which means that kh varies between 0.9 and 0.4 *i.e.* fairly shallow water. To resolve the steepest case we use a grid size of $\Delta x = 0.02 \text{ m}$ and a time step $\Delta t = 0.025 \text{ s}$. For all but the steepest slopes we use $\hat{z} = -0.5h$. For the slopes higher than 0.2, the upper and lower corners of \hat{z} are smoothed slightly using a Savitzky-Golay filter, to reduce detrimental effects caused by discontinuities in \hat{z} at the abrupt corner.

Two sets of simulations are made with the Boussinesq model. Firstly, we use the original Boussinesq model of Chapter 2 (also of Madsen *et al.*, 2002, 2003) *i.e.* excluding the $O(\delta)$ terms in (10.1) and (10.2). The results are shown in Figure 10.4 (b) (as open circles). In comparison with the reference solutions of Suh *et al.* (1997) using both a finite element method and an extended linear mild-slope equation, this result is clearly disappointing for steep as well as for mild bottom slopes. This poor result is in strong contrast to excellent results achieved for linear shoaling, which are essentially identical to those presented in §10.4, as well as the earlier variable bottom results from §6.4 and §6.5. Consequently, we can conclude that partial reflection is sensitive to the local phase differences between the velocity profile and the surface elevation, which are not correctly accounted for without the $O(\delta)$ terms. Secondly, we redo the simulations using the velocity formulation presented in §10.2 *i.e.* including the $O(\delta)$ terms. The result is also shown (as filled circles) in Figure 10.4 (b), and we notice a remarkable improvement of the reflection coefficients.

This case demonstrates the clear superiority of the new formulation presented in this chapter for cases involving rapidly varying bathymetry. A number of additional cases are also con-

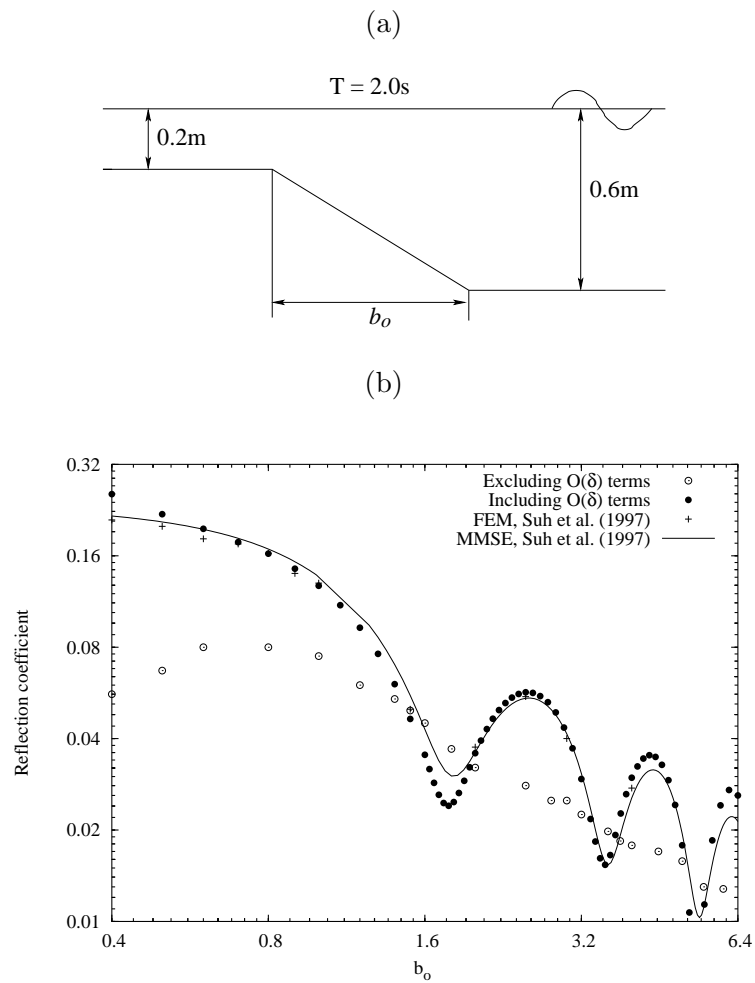


Figure 10.4: (a) Bathymetry used (waves propagating right to left) in the experiments of Booij (1983) involving reflection from a plane shelf and (b) comparison of computed results with previous simulations.

sidered in Madsen *et al.* (2005). These include reflection from a plane shelf in intermediate depths, as well as from both Gaussian shaped and symmetric trenches with sloped transitions (following cases from Bender & Dean, 2003). For details of these additional simulations the reader is referred to Madsen *et al.* (2005).

10.6 Bragg Scattering

In this section we study wave reflection and transmission in connection with surface waves propagating over a sea bottom with a patch of periodic undulations (ripples). When the wavenumbers of the bottom ripples and the incident waves satisfy certain conditions, the scattered waves will be significantly amplified. The mechanism of the wave-ripple interaction is in many ways analogous to the mechanism of nonlinear wave-wave interaction for surface waves traveling over a uniform depth. As first shown by Phillips (1960), resonance conditions for wave-wave interactions read

$$\mathbf{k}_1 \pm \mathbf{k}_2 \pm \cdots \pm \mathbf{k}_{M+1} = 0, \quad \omega_1 \pm \omega_2 \pm \cdots \pm \omega_{M+1}, \quad (10.14)$$

where $M \geq 2$, and where ω_j, \mathbf{k}_j satisfy the linear dispersion relation. Similarly, resonance conditions for wave-ripple interactions are called Bragg conditions, and they are obtained by replacing one or more of the free surface wave components in (10.14) by periodic bottom components with corresponding ripple wavenumbers, but with zero frequencies as the ripples are fixed in time.

The phenomenon of Bragg scattering goes back to Sir William Henry Bragg and his son William Lawrence Bragg, who were both awarded the Nobel Prize in 1915 for their pioneering work ‘X-rays and Crystal Structures’. However, in the context of water waves Davies (1982) was one of the first to develop a theoretical solution for backscattering from an undular sea-bed, while Davies & Heathershaw (1984) presented a detailed experimental study. Since then the problem has drawn considerable attention, and today the literature on this topic is quite rich. Recently, Liu & Yue (1998) discussed three different classes of Bragg scattering in one and two horizontal dimensions. In the following, we shall study examples of these three classes, but our work will be limited to a single horizontal dimension.

As a general approach to the problem, we define a bedform consisting of a sequence of sinusoidal ripples on an otherwise flat bathymetry, *i.e.*

$$h = h_0 + \sum_{j=1}^J d_j \sin K_j x, \quad (10.15)$$

where h_0 is the mean depth relative to the still water datum, d_j are the ripple amplitudes, and K_j are the ripple wavenumbers. Undular bottom variations are often rapidly varying, with bottom wave numbers being of the same order of magnitude as the surface wave numbers, meaning that any spatial derivative of h can be significant. This makes it impossible for

us to directly relate the expansion level \hat{z} to the rapidly varying bottom h , and instead we generally use a constant $\hat{z} = \sigma_0 h_0$, where h_0 is a spatially averaged depth, with $\sigma_0 \leq 0.5$. In the examples studied in the following subsections, we assume a constant h_0 , but in general it may also be slowly varying in space.

10.6.1 Class I Bragg resonance

Class I Bragg resonance defines the second-order triad interaction involving a single bottom wavenumber K and two surface waves having wavenumber \mathbf{k}_1 (incoming wave) and \mathbf{k}_2 (reflected wave). For this case (10.14) simplifies to

$$\mathbf{k}_1 \pm \mathbf{k}_2 \pm \mathbf{K} = 0, \quad \omega_1 \pm \omega_2 = 0. \quad (10.16)$$

In a single horizontal dimension (*i.e.* for normal incidence) this condition is satisfied with

$$k_1 = -k_2 = \frac{K}{2}, \quad \omega_1 = \omega_2, \quad (10.17)$$

i.e. the reflected wave (subscript 2) has the same wavenumber and frequency as the incoming wave (subscript 1). This is the classical linear Bragg resonance, which has been studied extensively in the literature: Experimentally by *e.g.* Davies (1982); Davies & Heathershaw (1984); Hara & Mei (1987); Heathershaw & Davies (1985); theoretically by *e.g.* Kirby (1986); Mei (1985); Mei *et al.* (1988); and numerically by *e.g.* Chamberlain & Porter (1995); Suh *et al.* (1997), to mention a few.

Davies & Heathershaw (1984) made experiments with three different ripple patches consisting of two, four, and 10 ripples. Of their experiments, the most demanding is the 10 ripple patch with $Kd = 0.31$ and $d/h = 0.16$. For this test case we use $\hat{z} = -0.44h_0$, which makes the ratio $\sigma = -\hat{z}/h$ vary between 0.379 and 0.524, which is acceptable for stability as well as accuracy. As the test case is linear, we solve the linearized surface conditions instead of the fully nonlinear set, as in the preceding sections. Simulations are made with $\Delta t = 0.0589$ s and $\Delta x = 0.162$ m, corresponding to a resolution of 20 points per bottom wave length. We determine the reflection coefficients for a range of wave periods corresponding to the interval $0.5 \leq 2k_1/K \leq 2.5$.

The results are shown in Figure 10.5, where a very good agreement between our computations and the measurements of Davies & Heathershaw (1984) can be observed. There is obviously a strong reflection near the theoretical point of resonance at $2k_1/K = 1$. Actually, the peak occurs for $2k_1/K$ slightly less than one. As discussed by Liu & Yue (1998), this downshift can be explained by taking into account that k_1 is spatially varying due to the finite bottom variations. They used a perturbation analysis of the linear dispersion relation to demonstrate that the spatially averaged wavenumber on the undular bottom is slightly larger than the wavenumber corresponding to the averaged water depth h_0 . This explains a downshift of the peak Bragg reflection when it is represented in terms of the averaged depth wavenumber.

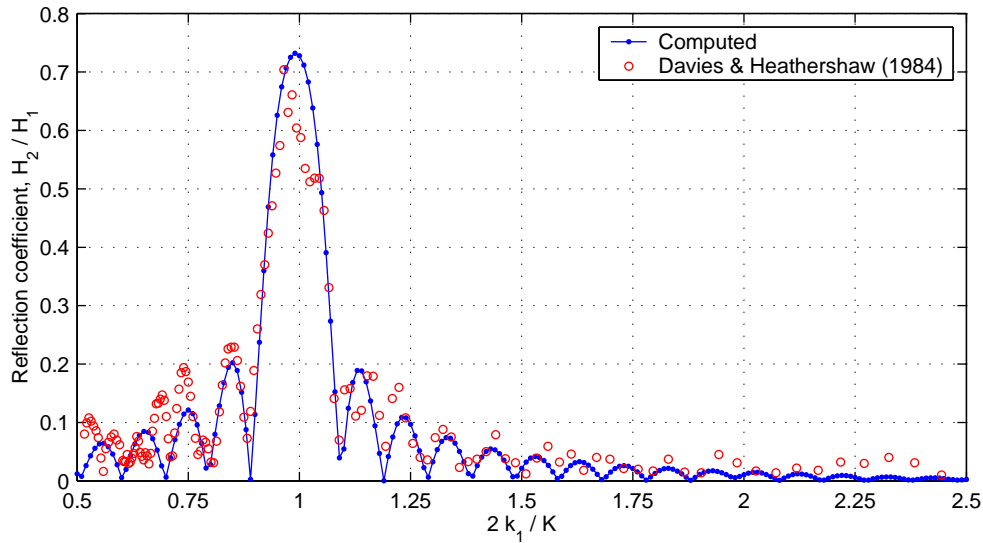


Figure 10.5: Results for class I Bragg scattering.

In Figure 10.5 we also notice an almost symmetrical tail of reflection peaks on both sides of the resonance point. We emphasize that the (potential) response at $2k_1/K = 2$ is actually a class II Bragg resonance as it occurs at the second harmonic of the bottom wavenumber K . However, the computed as well as the measured reflection is seen to be very small at this location. In general our linear Bragg results are almost identical to what was achieved by Kirby (1986) and Suh *et al.* (1997) solving their extended versions of the mild-slope equations. In contrast, the results of Chamberlain & Porter (1995) deviate slightly in two ways: Firstly, their tail of reflection peaks is less symmetrical around the resonance peak, and secondly they predict a more pronounced response at $2k_1/K = 2$.

10.6.2 Class II Bragg resonance

Class II Bragg resonance concerns higher-order Bragg effects arising from large amplitude (or slope) bottom undulations. It defines a third-order quartet wave-ripple interaction involving two different bottom wavenumbers \mathbf{K}_1 and \mathbf{K}_2 , and two surface wave numbers \mathbf{k}_1 (incoming wave) and \mathbf{k}_2 (reflected wave). In this case (10.14) simplifies to

$$\mathbf{k}_1 \pm \mathbf{k}_2 \pm \mathbf{K}_1 \pm \mathbf{K}_2 = 0, \quad \omega_1 \pm \omega_2 = 0. \quad (10.18)$$

In a single horizontal dimension (normal incidence), this condition is satisfied with

$$k_1 = -k_2 = \frac{K_1 \pm K_2}{2}, \quad \omega_1 = \omega_2. \quad (10.19)$$

Again the reflected wave (subscript 2) has the same wavenumber and frequency as the incoming wave (subscript 1), but this time the resonance involves the bottom superharmonics

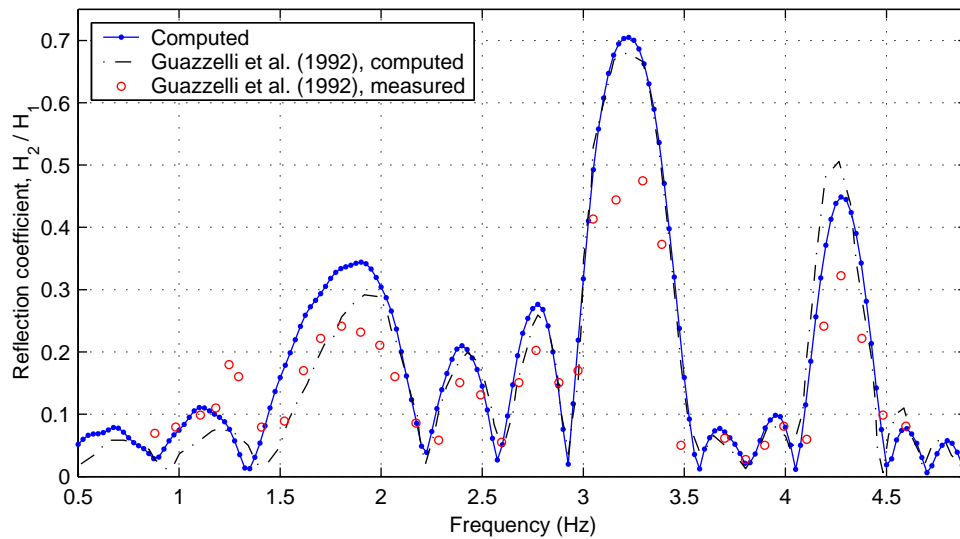


Figure 10.6: Results for class II Bragg scattering.

$K_1 + K_2$, $2K_1$, $2K_2$ and the bottom subharmonic $K_1 - K_2$. This problem has been studied experimentally and numerically by Guazzelli *et al.* (1992); O'Hare & Davies (1993); and numerically *e.g.* by Athanassoulis & Belibassakis (1999); Chamberlain & Porter (1995); Liu & Yue (1998); Suh *et al.* (1997).

We study the following case from Guazzelli *et al.* (1992): A doubly sinusoidal sea-bed with a mean depth $h_0 = 2.5$ cm, a ripple patch with length 48 cm, ripple amplitudes $d_1 = d_2 = 0.5$ cm, and ripple wavenumbers of $K_1 = \pi/3$, $K_2 = \pi/2$. In this case we apply the expansion level $\hat{z} = -0.275h_0$, which makes the ratio σ fluctuate between the limits of 0.2 and 0.43. The case is nonlinear in bottom amplitude but linear in surface amplitude, so we again apply the linear surface conditions. Simulations are made with $\Delta t = 0.0005$ s and $\Delta x = 0.002$, corresponding to a resolution of 20 points per minimum bottom wave length.

Figure 10.6 shows a fairly good agreement between our computations and the measurements of Guazzelli *et al.* (1992). First, we notice the distinct peaks occurring near the two class I resonance frequencies at $f_1 = 3.35$ Hz and $f_1 = 4.33$ Hz corresponding to $k_1 = 0.5K_1$ and $k_1 = 0.5K_2$, respectively. Second, we notice the peak near the subharmonic class II resonance frequency $f_1 = 1.93$ Hz corresponding to the wavenumber $k_1 = (K_1 - K_2)/2$. Guazzelli *et al.* (1992), in their Figure 6, present numerical computations (using the successive-application-matrix method, SAMM) with and without evanescent modes. For comparison, we have included their results with evanescent modes in Figure 10.6, and the agreement with our results is generally very good. In contrast, the results of Guazzelli *et al.* (1992) excluding the evanescent modes (not shown here) tend to significantly underestimate the subharmonic peak and to reduce the class I peaks to some extent. Similar underestimations were obtained by Suh *et al.* (1997) on the basis of the modified mild-slope equations (their Figure 8b). Obviously, we have done nothing to specifically account for the effect of evanescent modes in our approach, but our results turn out to be very similar to the best of Guazzelli *et al.* (1992). The likely explanation is that there is no need for evanescent modes as long as the exact

bottom condition is solved in combination with velocity profiles which directly incorporate the uneven bottom.

10.6.3 Class III Bragg resonance

Liu & Yue (1998) were the first to discuss and analyze the class III Bragg resonance, which occurs when nonlinear surface waves interact with an undular sea bottom. This class defines a third-order quartet wave-ripple interaction involving one bottom wavenumber K and three surface wavenumbers $\mathbf{k}_1, \mathbf{k}_2, \mathbf{k}_3$, in which case the resonance condition (10.14) reads

$$\mathbf{k}_1 \pm \mathbf{k}_2 \pm \mathbf{k}_3 \pm \mathbf{K} = 0, \quad \omega_1 + \omega_2 + \omega_3 = 0. \quad (10.20)$$

As discussed by Liu & Yue (1998), this condition can be satisfied by accounting for the incident wave twice *i.e.* with $\mathbf{k}_1 = \mathbf{k}_2$, in which case (10.20) leads to a reflected subharmonic $\mathbf{k}_3 = 2\mathbf{k}_1 - \mathbf{K}$ or a transmitted superharmonic $\mathbf{k}_3 = 2\mathbf{k}_1 + \mathbf{K}$, both generated at frequency $\omega_3 = 2\omega_1$. In a single horizontal dimension (normal incidence), this resonance condition simplifies to

$$k_3 = 2k_1 \pm K, \quad \omega_3 = 2\omega_1. \quad (10.21)$$

Further simplifications were introduced by Liu & Yue (1998), as they invoked the linear dispersion relation to obtain the approximations

$$\omega_3 \approx \sqrt{gk_3 \tanh(k_3 h_0)}, \quad \omega_1 \approx \sqrt{gk_1 \tanh(k_1 h_0)}. \quad (10.22)$$

Now (10.21) and (10.22) can be solved with respect to the surface wavenumbers k_1, k_3 for a given bottom wavenumber K and a given mean depth h_0 . As an example Liu & Yue (1998) consider a patch of 36 sinusoidal ripples on an otherwise flat bottom, with ripples defined by $Kd = 0.25$ and $Kh_0 = 2.642$. In this case (10.21) and (10.22) predict a subharmonic reflection at $k_3/K = 0.546$ for an incident wavenumber of $k_1/K = 0.227$, and a superharmonic transmission at $k_3/K = 2.195$ for an incident wavenumber of $k_1/K = 0.598$.

We simulate this example by invoking the fully nonlinear surface conditions and by applying the stream function theory of Fenton (1988) to describe the incident wave at the wavemaker. The expansion level is chosen to be $\hat{z} = -0.5h_0$, which makes the ratio σ fluctuate between 0.46 and 0.55, which is acceptable from a stability and accuracy point of view. Simulations are generally made with $h_0 = 1$ m, $\Delta t = 0.1$ s, and $\Delta x = 0.12$ m, corresponding to a resolution of 20 points per bottom wavelength.

Firstly, we concentrate on the reflected class III subharmonic. Figure 10.7 (a) shows the computed reflection coefficient defined by H_3/H_1 in the vicinity of $k_1/K = 0.227$ for three sets of incoming wave steepness $k_1 H_1 = 0.0609, 0.1272, \text{ and } 0.18$, respectively. Note that the first two of these values correspond to $k_1 a_1 = 0.03$ and 0.06 , respectively, where a_1 is the amplitude of the first harmonic in the stream function solution. These are the two test

cases simulated by Liu & Yue (1998), who extended the high-order spectral (HOS) method of Dommermuth & Yue (1987) to the case of an uneven bottom. Their results are also included in Figure 10.7 (a), and are seen to agree very well with our results, although a slight shift in the resonance location can be observed. With increasing nonlinearity two obvious trends can be observed from Figure 10.7 (a): 1) A gradual increase in the peak reflection coefficient, and 2) a gradual downshift of the location of the peak resonance. The first part of this observation is explained by the perturbation theory of Liu & Yue (1998), which predicts a linear growth rate of the reflection coefficient with peaks of 0.22, 0.42, and 0.54 for the three steepnesses considered in Figure 10.7 (a). As expected, the perturbation theory is quite accurate for weak nonlinearities, while it severely overestimates the reflection coefficient for stronger nonlinearity. With respect to the second observation, Liu & Yue (1998) did not provide an explanation. Madsen *et al.* (2005) explain and accurately predict this downshift of resonance, which will briefly be discussed at the end of this section.

Secondly, we concentrate on the transmitted class III superharmonic. In this particular case we reduce the time step to $\Delta t = 0.04$ s and the grid size to $\Delta x = 0.06$ m, as the waves involved in this process are shorter than experienced in connection with the subharmonic reflection. Figure 10.7 (b) shows the computed transmission coefficient defined by H_3/H_1 in the vicinity of $k_1/K = 0.598$ for four sets of incoming wave steepness $k_1 H_1 = 0.06, 0.12, 0.18,$ and 0.24 . With increasing nonlinearity two obvious trends can be observed from Figure 10.7 (b): 1) A gradual increase in the peak transmission coefficient, and 2) a gradual upshift of the location of the peak resonance. Again, the first part of this observation is explained by the perturbation theory of Liu & Yue (1998), which predicts a linear growth rate of the transmission coefficient with peaks of 0.074, 0.147, 0.22, and 0.29 for the four nonlinearities considered in Figure 10.7 (b). This time the perturbation theory is surprisingly accurate, even for the highly nonlinear cases.

Thirdly, we re-investigate the class I Bragg resonance, which is expected to occur in the vicinity of $k_1/K = 0.5$. In contrast to Figure 10.5, which was based on linear waves and linear wavenumbers, Figure 10.7 (c) shows the computed reflection coefficients as a function of the nonlinear wavenumber k_1 determined from stream function theory. We notice a slight downshift of the peak resonance for increasing nonlinearity, but the differences are actually quite small.

The remaining open question concerning the class III Bragg scattering is: Why does the reflection lead to a downshift and the transmission to an upshift of the resonance relative to the predictions provided by (10.21) and (10.22)? Not surprisingly, the explanation turns out to be amplitude dispersion in the interacting waves, and to quantify this effect we have developed a third-order theory for bichromatic waves on arbitrary depth. The resulting analysis is presented in Madsen *et al.* (2005) for the particular cases considered in this subsection, which predict the behavior observed in Figures 10.7 (a) and (b) quite accurately. For brevity, we do not present details of the analysis here. We mention that earlier work in this direction was made by Hogan *et al.* (1988); Longuet-Higgins & Phillips (1962); Zhang & Chen (1999), however their theories are limited to deep water waves and hence not applicable

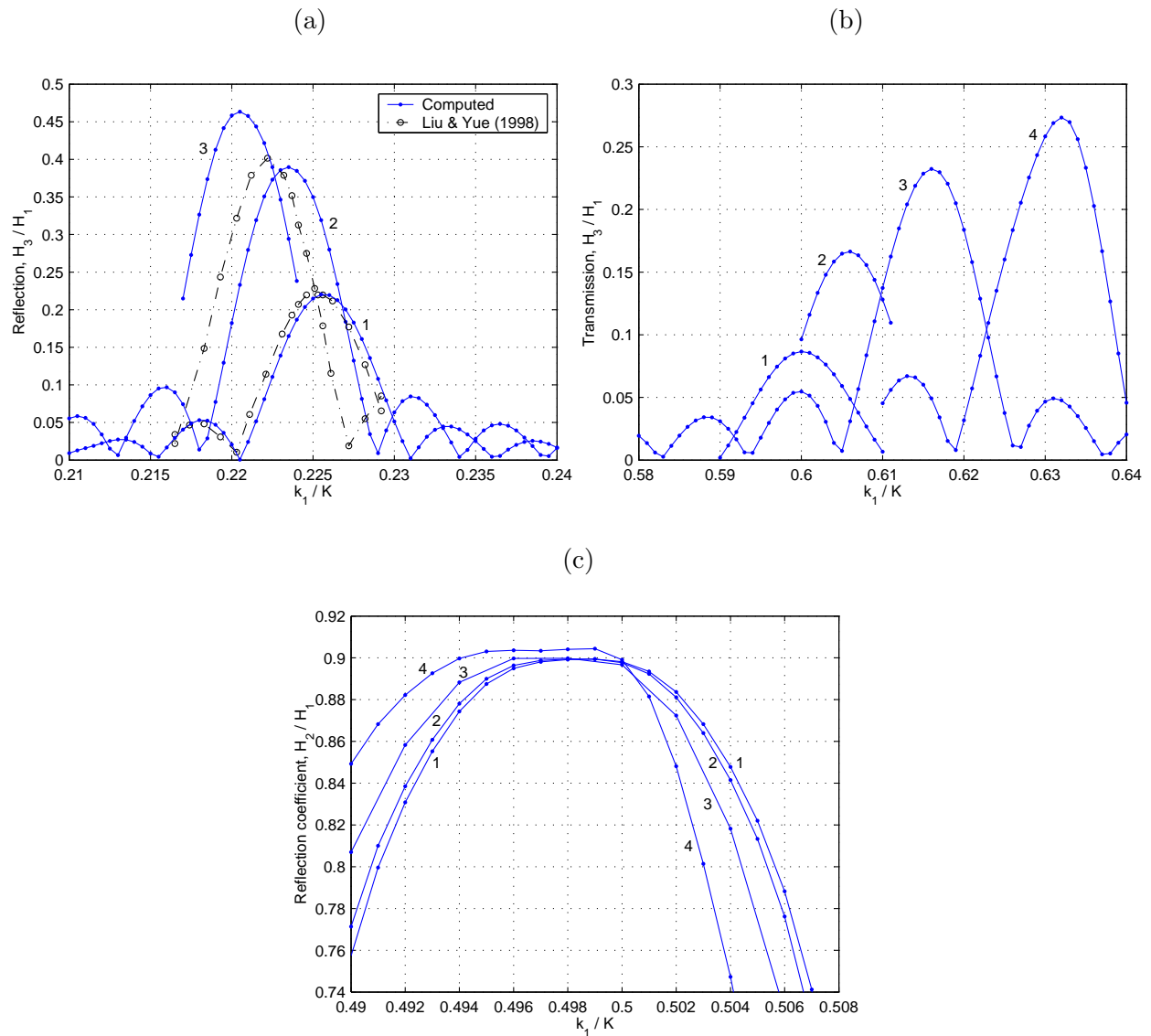


Figure 10.7: Results for class III Bragg scattering. Figure (a) shows the subharmonic reflection with 1–3: $k_1 H_1 = 0.0609, 0.1272, 0.18$. Figure (b) shows the superharmonic transmission with 1–4: $k_1 H_1 = 0.06, 0.12, 0.18, 0.24$. Figure (c) shows the reflection coefficient for nonlinear class I Bragg scattering with 1: Linear, 2–4: $k_1 H_1 = 0.06, 0.12, 0.18$.

to the present investigation. Full details on the third-order theory can be found in Madsen & Fuhrman (2005); Madsen *et al.* (2005).

10.7 Conclusions

In this chapter new Boussinesq-type equations are presented for fully nonlinear and highly dispersive water waves interacting with a potentially rapidly varying bathymetry. The derivation is an extension/generalization of the original Boussinesq formulation from Chapter 2, which is valid on a mildly sloping bottom. The resulting formulation involves the assumption that the expansion level $\hat{z}(x, y)$ is slowly varying in space. On the other hand, for the first time no mild-slope assumption about the variation of the sea bottom $h(x, y)$ is invoked. The final velocity expressions contain low-order derivatives of \hat{z} and up to fifth derivatives of the velocity variables. For a constant depth the new formulation simplifies to the original formulation of Madsen *et al.* (2002, 2003).

The choice of the expansion level \hat{z} is an important key to the successful use of the model. Madsen & Agnon (2003); Madsen *et al.* (2002, 2003) concluded that on a constant depth the best accuracy of the velocity profile, the linear dispersion relation and of nonlinear wave-wave interactions is obtained when $\hat{z} = -0.5h$. On an uneven bottom this condition is obviously generalized to $\hat{z} = -0.5h(x, y)$, and this choice also leads to the best accuracy for linear and nonlinear shoaling on a mildly sloping beach. Hence, this is the natural starting point for most applications. However, on a rapidly varying bathymetry this condition will violate the assumption of a slowly varying \hat{z} . As a result it becomes necessary to smooth \hat{z} so that its higher derivatives and products of derivatives rapidly become insignificant. Undular sea bottoms, in principle offer the most challenging situation, as the bottom wavenumbers are often of the same order of magnitude as the surface wavenumbers. In this case it is typically not feasible to relate \hat{z} to the rapidly varying bottom contours. Instead we use $\hat{z} = -\sigma_0 h_0$ with $\sigma_0 \leq 0.5$, where h_0 is a spatially averaged depth (in all cases presented herein this corresponds to using a constant \hat{z} level).

As a consequence of smoothing \hat{z} for rapidly varying bathymetries, the ratio $\sigma = -\hat{z}/h$ will locally deviate from the optimal choice of 0.5. Fortunately, the formulation is relatively robust, and errors in the linear dispersion relation will be limited to less than 2.5% for $kh < 15$ when $0.20 \leq \sigma \leq 0.55$. These bounds should generally not be violated, however. If the upper bound is exceeded singularities appear in the dispersion relation, and these may lead to numerical instabilities if the Nyquist wavenumber is sufficiently large. Alternatively, relatively large dispersive errors will occur in quite shallow water if the lower bound is violated.

The resulting numerical model is verified on a wide range of test cases, only some of which are presented here. Firstly, a linear shoaling case involving the range of dimensionless depths $0.35 \leq kh \leq 30$ is considered, and the perfect match with linear theory confirms that the new formulation maintains the excellent properties of the original formulation. Secondly,

we consider reflection from a plane shelf in shallow water with slopes varying from 1/16 to 1.0. Numerical results are compared to Suh *et al.* (1997), and we conclude that accurate results can be obtained for slopes up to 1.0. This case has also been used to show the clear superiority of the new formulation (retaining $\nabla\hat{z}$ terms) in cases involving partial reflection from rapid changes in bathymetry. We also simulate cases involving linear class I and II Bragg scattering. The computed results compare very well with the measurements of Davies & Heathershaw (1984), and the previous computations of Guazzelli *et al.* (1992), respectively.

Finally, we make fully nonlinear computations of class III Bragg scattering, recently discovered and discussed by Liu & Yue (1998). New results are given for the subharmonic and superharmonic interactions with the sea bed leading to reflection and transmission, respectively. We observe a clear downshift/upshift of the peak reflection/transmission with increasing nonlinearity, which can be explained from the third-order amplitude dispersion in the resulting bichromatic wavefield.

It is the author's opinion that the new (extended) system of equation presented in this chapter should be the basis of future applications of this high-order Boussinesq formulation. It contains embedded properties of equal quality to the original system presented in Chapter 2, while also extending the range of applications to cases involving rapidly varying bathymetries, at minimal added computational expense.

Chapter 11

Conclusions & Recommendations

As a wide number of topics have been touched upon, ranging from sparse matrix preconditioning, to stability analyses (both numerical and physical), to various nonlinear wave phenomena, the conclusions from this thesis are many. The most important of these are highlighted in §11.1, with some additional reflections also provided. Particular attention is paid here to new advancements/achievements in this thesis. Some recommendations for further research are also provided in §11.2.

11.1 Conclusions

First and foremost, it has been established through initial testing, and (more importantly) further applications, that the new and somewhat complicated high-order Boussinesq formulation of Madsen *et al.* (2002, 2003) can indeed be solved efficiently and scalably in two horizontal dimensions using the largely case-specific preconditioned iterative strategies developed in Chapter 4. This accomplishment alone is no small feat, as methods for efficiently solving this (or reasonably similar) systems of PDEs seem to be lacking in the literature. This issue was in fact a source of major concern for roughly the first half of the (three year) project, as idea after idea (most not covered in the thesis for brevity) failed quite miserably in deep water. This sparse matrix problem, for which efficient solutions were crucial for the overall success of the project, finally fell with the development of the matrix free Fourier space preconditioner in §4.6.3 (limited to solving flat-bottom problems or regular domains) and the generally applicable approximate Schur complement preconditioner in §4.6.4. These two methods in particular have proven their robustness throughout this thesis, and were well worth their considerable time investment. Most notably, these methods provide an elusive combination of robustness, efficiency, scalability, and reasonable storage demands, which are essential elements for large scale applications. It is important to stress that, as shown throughout Chapter 4, these methods are particularly adept at solving the irrotational version of the equations (see §4.2).

Secondly, the discrete system of PDEs has been thoroughly analyzed for numerical stability in both one and two horizontal dimensions in Chapter 5. A first analysis of the linearized system has provided a simple means for obtaining the fundamentally important time step limitations for a given discretization. Linear analysis alone was found to not adequately explain our experience with the nonlinear model, however, and the matrix-based analysis is subsequently extended to include the local effects of the nonlinear terms in §5.6. While such an approach is reasonably common (though certainly not standard) for simple nonlinear systems, such an extension for the present high-order Boussinesq formulation is again a non-trivial task. Despite this complexity, the local nonlinear analysis was able to show distinct differences in the numerical stability of the rotational and irrotational formulations; namely that the irrotational formulation has much better stability properties when high nonlinearity is combined with large depths or refined grids, confirming our own general experience. This is an important conclusion, as many of the practical applications of the model involve highly nonlinear waves in deep water. Given that the rotational system was also significantly more difficult to precondition, it can be concluded that the irrotational version seems most attractive for applications of the numerical model, and has consequently been used throughout most of this work.

With efficient and numerically stable solution strategies firmly in place, and after a thorough validation procedure described in Chapter 6, it was finally possible to realize the true objective of this project: To simulate various two and (especially) three-dimensional nonlinear water wave phenomena, with the added hope of providing further insight into the complicated physical processes involved. This work begins by considering the nonlinear interaction of symmetric wave fronts at oblique incident angles in Chapter 7, resulting in various short-crested wave patterns. Here simulations in both shallow and deep water are considered, resulting in the characteristic hexagonal and rectangular shapes observed in experiments as well as in previous computations. Simulations of the deep water (rectangular) surface patterns demonstrate a number of interesting phenomena. Notably, there is a modulation along the propagating direction, resulting in crest forms varying from peaked (at the center) to flat, to having dips along the centerline. This behavior was also observed in physical experiments, but not properly explained. It is demonstrated that these modulations are in fact third-order artifacts of using first-order wavemaker conditions, resulting in a parasitic release of free first harmonics. These effects are due to the three-dimensionality of the problem, and disappear at the plane wave limit. This new explanation makes apparent the need for a third-order (three-dimensional) wavemaker theory before steady short-crested waves of moderate to large wave steepness can be produced experimentally.

Applications of the numerical model are continued in Chapter 8 where an extensive fully nonlinear numerical study of the fascinating phenomenon of crescent (or horseshoe) waves is undertaken. These occur on the water surface due to the (class II, see McLean, 1982*b*) instability of steep Stokes waves to three-dimensional periodic perturbations, corresponding to a five-wave resonant interaction. The most unstable (phase-locked) L2 crescent patterns are firstly studied, where, among other things, the growth rate of the instability is investigated. The simulations suggest that accelerated growth rates (compared to the linear theory) are possible at later stages of crescent development, as well as during the evolution into a pre-

existing crescent wave train. The model is also used to demonstrate the effects of variable nonlinearity on these patterns.

Secondly, the related oscillating crescent patterns, observed recently by Collard & Caulliez (1999), are studied. The simulations match their observations well both qualitatively and quantitatively. Furthermore, the original analysis of McLean (1982*b*) is extended to cases involving unsymmetric (unstable) satellite pairs, and it is demonstrated that this analysis is useful in providing accurate quantitative estimates of the observed oscillation periods. Further investigation with this analysis also leads to a possible explanation for the inception mechanism of the oscillating patterns in the experiments, which has not been previously explained. It is demonstrated that for a certain space of parameters it is possible for the dominant class II instability to result in oscillating patterns similar to those observed in the experiments. The new explanation suggests that the observed patterns were in part an artifact of the tank width combined with a suppression of the class I (Benjamin & Feir, 1967) instability. Computed L3 and L4 patterns (as denoted in Su, 1982) are also demonstrated, which occur momentarily during model transitional states.

Finally, the model is used to conduct a number of experiments involving the initial competition of various unstable modes to the breaking point. These generally demonstrate that multiple unstable modes can grow simultaneously, consistent with previous findings. Simulations involving random disturbances also show good agreement with physical experiments, both in the form (*i.e.* two or three dimensional) as well as in the location of the initial instability. Deviations from the standard L2 crescent pattern also arise naturally, consistent with observations. Chapter 8, in the author's opinion, represents a significant step forward in the study of these phenomena. With the exception of Xue *et al.* (2001), whose simulations were limited to small domains and short time scales, all previous numerical studies were limited to weakly nonlinear simulations. It will be interesting in the future to hopefully see other fully nonlinear studies on these phenomena, which build further on our results.

Chapter 9 tackles the challenging task of implementing piecewise-rectangular bottom-mounted structures into the basic finite difference model. While conceptually this task is trivial, the practical difficulties are considerable. This is mainly due to the necessity of discretizing high (up to fifth-) order derivatives around theoretically singular exterior corner points, resulting in potential stability and convergence problems. Fortunately, the system is receptive to dissipation, and repeated local applications of high-order smoothing filters are a simple yet effective means for managing these difficulties in practice, while minimizing damage to modes of physical interest. The model is used to provide reasonably accurate (though not perfect) results involving both linear and nonlinear diffraction. The most impressive of the results are those involving highly nonlinear deep water wave run-up on a vertical bottom-mounted plate, previously studied experimentally and analytically by Molin *et al.* (2004, 2003). For the entire range of incident wave steepness considered the match with experimental measurements is demonstrated to be excellent, resulting in wave amplifications much greater than predicted from linear theory. In the most extreme case a local wave steepness of $H/L > 0.20$ is observed in front of the plate, presenting physical situations beyond the capabilities of most (if not all) previous Boussinesq-type formulations.

Finally, the original Boussinesq formulation described in Chapter 2 is extended and generalized in Chapter 10 to allow for applications with rapidly varying bathymetry. Simulations involving linear shoaling, reflection from a plane shelf, and class I and II Bragg scattering demonstrate the accuracy of the new formulation in its linearized form. Nonlinear simulations involving class III Bragg scattering are also shown, and new results extending the previous simulations of Liu & Yue (1998) are presented. These simulations demonstrate a clear downshift/upshift for the reflected/transmitted class III Bragg resonance. These observations can be attributed to the third-order interaction between the incoming and reflected wavefields. This new formulation contains linear and nonlinear properties equal in quality to the original formulation, while extending the range of applicability to cases with rapidly varying bathymetry, at a minimal increase in the computational expense. Therefore, in the author's opinion this new formulation should be the focus of future research with this high-order Boussinesq model.

This thesis establishes the high-order Boussinesq-type approach of Madsen *et al.* (2002, 2003) as an attractive method for the study of highly nonlinear and dispersive water waves in two horizontal dimensions. The developed model is capable of efficiently treating three-dimensional fully nonlinear waves over a large range of (now rapidly) varying water depths, including on piecewise rectangular domains. The wide variety of nonlinear wave phenomena investigated herein is a testament to the versatility of this approach. Numerical simulations with the model, in combination with ever-important analysis, have led to a deeper understanding of many complicated physical processes within the field of nonlinear wave hydrodynamics.

11.2 Recommendations

It finally seems appropriate to provide some recommendations for further research in the areas touched upon in this thesis. The author can truly think of a large number of interesting directions to turn, furthering the work presented here. Below are some ideas for future research, which the author finds particularly stimulating.

Firstly, given that the irrotational version seems to be more attractive numerically than the rotational version, it seems logical to replace the horizontal velocities with a velocity potential, hence reducing the number of unknowns. Based on the number of nonzeros in the resulting matrix this might be expected to require a work load of only $4/9$ (*i.e.* roughly half) of the current implementation. It should be stressed, however, that this figure does not account for any loss of numerical accuracy, which might be expected due to an increase in the order of derivatives that must be taken (a similar velocity potential model would require a sixth-derivative).

From the numerical side of things, it seems doubtful that the preconditioning methods developed in Chapter 4 can be significantly improved in terms of their robustness and iteration

counts. However, it would be interesting in the future to investigate parallel solution strategies, particularly for the Schur complement preconditioner, which would allow for even larger domains than those presented in this work. This would essentially require parallel implementations of the sparse matrix-vector product and the direct factorization methods. These components are known to be parallelizable, and can be found in various software packages.

It would also be interesting to pursue various alternative spatial discretizations, to further reduce the required resolution for a given problem, which is especially important when two horizontal dimensions are considered. Spectral discretizations using Fast Fourier Transforms might be of interest, which would also directly incorporate periodic boundary conditions, which are beneficial for certain types of problems.

Similarly, higher-order finite difference discretizations might also be attractive. In particular, it should be possible to implement a corresponding high-order sparse matrix-vector product without actually constructing the matrix, which would also significantly reduce the storage demands. Furthermore, each of the high-order mixed derivatives could be built up using successive line applications of pure x - and y -derivatives, generally simplifying the implementation. Such a matrix-free method is particularly attractive in combination with the Fourier space preconditioner (*i.e.* on flat bottom problems), which should then allow for very large domains to be simulated with very low (perhaps negligible) storage requirements. Indeed, the only remaining (potential) storage burden would be that from the GMRES algorithm. In cases where this were limiting, preliminary testing has already shown that the BiCGSTAB algorithm of van der Vorst (1992), which has minimal storage demands, requires only slightly more matrix-vector products for convergence.

There are also many obvious extensions of the nonlinear simulations treated within this thesis, which involve a number of interesting nonlinear wave phenomena. Extending the work of Chapter 7, it would certainly be of interest to simulate truly steady three dimensional short-crested waves. This should be possible using any of the various perturbation theories from the literature (*e.g.* Hogan *et al.*, 1988; Hsu *et al.*, 1979) as incident waves, and would provide further verification that the observed phenomena are indeed artifacts of the first-order wavemaker conditions used here, though the author does not consider this to be in question. Given the demonstrated inadequacies of current wavemaking practice for these patterns, as pointed out in this thesis, numerical investigations into these phenomena seem to currently be the best method for studying these particular steady forms.

While the numerical study of crescent waves in Chapter 8 is rather extensive, there is still an additional need to study the long term evolution of these patterns, beyond the initial breaking point. This would of course, also require a breaking model, which is currently being developed.

Furthering the work of Chapter 9, where bottom-mounted structures were incorporated, it would be interesting to investigate other discretization strategies around the exterior corner points, with the hope of improving the general numerical stability. This might best be pursued in the context of a previously mentioned velocity potential formulation. This work

is currently under investigation by researchers at the Hydrodynamics Department, Ecole Supérieure d'Ingénieurs de Marseille, France; see *e.g.* Jamois *et al.* (2004). Incorporating floating bodies into the model might also be interesting.

There are indeed numerous additional nonlinear water wave phenomena which still need to be studied. An area currently receiving much attention is that of *freak waves*: extremely large waves appearing on the sea surface, often from nowhere; see *e.g.* the recent review of Kharif & Pelinovsky (2003). Given the fully nonlinear capabilities of the the present high-order Boussinesq model, in combination with its demonstrated computational efficiency, this seems like a natural area to pursue. It is expected that the Boussinesq model could be quite useful in studying these phenomena, especially in combination with some of the other improvements discussed in this section.

References

- ABBOTT, M. B. 1979 *Computational Hydraulics: Elements of the Theory of Free Surface Flows*. London: Pitman.
- ABBOTT, M. B. & BASCO, D. R. 1989 *Computational Fluid Dynamics: An Introduction for Engineers*. New York: John Wiley & Sons.
- ABBOTT, M. B., MCCOWAN, A. & WARREN, I. R. 1984 Accuracy of short-wave numerical models. *J. Hydr. Eng. ASCE* **110**, 1287–1301.
- ABBOTT, M. B. & MINNS, A. W. 1998 *Computational Hydraulics*, 2nd edn. Brookfield USA: Ashgate.
- ABBOTT, M. B., PETERSEN, H. M. & SKOVGAARD, O. 1978 On the numerical modelling of short waves in shallow water. *J. Hydr. Res.* **16**, 173–203.
- ABOHADIMA, S. & ISOBE, M. 1999 Linear and nonlinear wave diffraction using the non-linear time dependent mild slope equations. *Coast. Eng.* **37**, 175–192.
- AGNON, Y. & GLOZMAN, M. 1996 Periodic solutions for a complex hamiltonian system: New standing water waves. *Wave Motion* **24**, 139–150.
- AGNON, Y., MADSEN, P. A. & SCHÄFFER, H. A. 1999 A new approach to high order Boussinesq models. *J. Fluid Mech.* **399**, 319–333.
- ALBER, I. E. 1978 The effects of randomness on the stability of two-dimensional surface wavetrains. *Proc. R. Soc. Lond. A* **363**, 525–546.
- AMESTOY, P. R., DAVIS, T. A. & DUFF, I. S. 1996 An approximate minimum degree ordering algorithm. *SIAM J. Matrix Anal. Appl.* **17**, 886–905.
- ANNENKOV, S. Y. & SHRIRA, V. I. 1999 Sporadic wind wave horse-shoe patterns. *Nonlin. Proc. Geophys.* **6**, 27–50.
- ANNENKOV, S. Y. & SHRIRA, V. I. 2001 Numerical modelling of water-wave evolution based on the Zakharov equation. *J. Fluid Mech.* **449**, 341–372.

- ATHANASSOULIS, G. A. & BELIBASSAKIS, K. A. 1999 A consistent coupled-mode theory for the propagation of small-amplitude water waves over variable bathymetry regions. *J. Fluid Mech.* **389**, 275–301.
- BABOVIC, V. & FUHRMAN, D. R. 2002 Data assimilation of local model error forecasts in a deterministic model. *Int. J. Numer. Meth. Fluids* **39**, 887–918.
- BAGGETT, J. S., DRISCOLL, T. A. & TREFETHEN, L. N. 1995 A mostly linear model of transition to turbulence. *Phys. Fluids* **7**, 833–838.
- BAGGETT, J. S. & TREFETHEN, L. N. 1995 Low-dimensional models of subcritical transition to turbulence. *Phys. Fluids* **9**, 1043–1053.
- BATEMAN, W. J. D., SWAN, C. & TAYLOR, P. H. 2001 On the efficient numerical simulation of directionally spread surface water waves. *J. Comput. Phys.* **174**, 277–305.
- BENDER, C. J. & DEAN, R. G. 2003 Wave transformation by two-dimensional bathymetric anomalies with sloped transitions. *Coast. Eng.* **50**, 61–84.
- BENJAMIN, T. B., BONA, J. L. & MAHONY, J. J. 1972 Model equations for long waves in non-linear dispersive systems. *Phil. Trans. R. Soc. Lond. A* **272**, 47–78.
- BENJAMIN, T. B. & FEIR, J. E. 1967 The disintegration of wave trains on deep water. Part 1. Theory. *J. Fluid Mech.* **27**, 417–430.
- BENZI, M. 2002 Preconditioning techniques for large linear systems: A survey. *J. Comput. Phys.* **182**, 418–477.
- BERKHOFF, J. C. W. 1972 Computation of combined refraction-diffraction. In *Proc. 13th Coastal Engineering Conf.*, , vol. 1, pp. 471–490. Vancouver, Canada.
- BINGHAM, H. B. & AGNON, Y. 2005 A Fourier-Boussinesq method for nonlinear water waves. *Eur. J. Mech. B/Fluids* **24**, 255–274.
- BINGHAM, H. B., FUHRMAN, D. R., JAMOIS, E. & KIMMOUN, O. 2004 Nonlinear wave interaction with bottom-mounted structures by a high-order Boussinesq method. In *Proc. 19th Int. Workshop on Water Waves and Floating Bodies*. Cortona, Italy.
- BLIVEN, L. F., HUANG, N. E. & LONG, S. R. 1986 Experimental study of the influence of wind on Benjamin-Feir sideband instability. *J. Fluid Mech.* **162**, 237–260.
- BOCZAR-KARAKIEWICZ, B. 1972 Transformation of wave profile in shallow water—a Fourier analysis. *Arch. Hydrotechnik* **19**, 197–210.
- BOOLJ, N. 1983 A note on the accuracy of the mild-slope equation. *Coast. Eng.* **7**, 191–203.
- BOUSSINESQ, J. V. 1872 Théorie des ondes et des remous qui se propagent le long d'un canal rectangulaire horizontal, en communiquant au liquide contenu dans ce canal des vitesses sensiblement pareilles de la surface au fond. *J. Math. Pures Appl.* **17**, 55–108.

- BREDMØSE, H. 2002 Deterministic modelling of water waves in the frequency domain. PhD thesis, Technical University of Denmark, Lyngby, Denmark.
- BRIGGS, W. L., HENSON, V. E. & MCCORMICK, S. F. 2000 *A Multigrid Tutorial*, 2nd edn. Philadelphia: SIAM.
- BRYANT, P. J. 1973 Periodic waves in shallow water. *J. Fluid Mech.* **59**, 625–644.
- BRYANT, P. J. 1985 Doubly periodic progressive permanent waves in deep water. *J. Fluid Mech.* **161**, 27–42.
- BUHR-HANSEN, J. & SVENDSEN, I. A. 1974 Laboratory generation of waves of constant form. In *Proc. 14th Coastal Engineering Conf.*, pp. 320–338. Copenhagen.
- CASH, J. R. & KARP, A. H. 1990 A variable order Runge-Kutta method for initial value problems with rapidly varying right-hand sides. *ACM Trans. Math. Software* **16**, 201–222.
- CHAMBERLAIN, P. G. & PORTER, D. 1995 The modified mild-slope equation. *J. Fluid Mech.* **291**, 393–407.
- CHAPALAIN, G., COINTE, R. & TEMPERVILLE, A. 1992 Observed and modelled resonantly interacting progressive water waves. *Coast. Eng.* **16**, 267–301.
- CHEN, Y. & LIU, P. L.-F. 1995 Modified Boussinesq equations and associated parabolic models for water wave propagation. *J. Fluid Mech.* **288**, 351–381.
- CLAMOND, D. & GRUE, J. 1995 A fast method for fully nonlinear water-wave computations. *J. Fluid Mech.* **447**, 337–355.
- COLLARD, F. & CAULLIEZ, G. 1999 Oscillating crescent-shaped water wave patterns. *Phys. Fluids* **11**, 3195–3197.
- CRAIG, W. 2001 On the Badulin, Kharif and Shrira model of resonant water waves. *Physica D* **152–153**, 434–450.
- CRAIG, W. & NICHOLLS, D. P. 2000 Traveling two and three dimensional capillary gravity water waves. *SIAM J. Math. Anal.* **32**, 323–359.
- CRAIG, W. & NICHOLLS, D. P. 2002 Traveling gravity water waves in two and three dimensions. *Eur. J. Mech. B/Fluids* **21**, 615–641.
- CRAIG, W. & SULEM, C. 1993 Numerical simulation of gravity waves. *J. Comput. Phys.* **108**, 73–83.
- DAVIES, A. G. 1982 The reflection of wave energy by undulations on the seabed. *Dyn. Atmos. Oceans* **6**, 207–232.
- DAVIES, A. G. & HEATHERSHAW, A. D. 1984 Surface-wave propagation over sinusoidally varying topography. *J. Fluid Mech.* **144**, 419–443.

- DOMMERMUTH, D. G. & YUE, D. K. P. 1987 A high-order spectral method for the study of nonlinear gravity waves. *J. Fluid Mech.* **184**, 267–288.
- DUFF, I. S. 1986 Parallel implementation of multifrontal schemes. *Parallel Comput.* **3**, 193–204.
- DUFF, I. S. 1989 Multiprocessing a sparse matrix code on the Alliant FX/8. *J. Comput. Appl. Math.* **27**, 229–239.
- DUFF, I. S., ERISMAN, A. M. & REID, J. K. 1986 *Direct methods for sparse matrices*. Oxford: Oxford University Press.
- DUFF, I. S. & REID, J. K. 1984 The multifrontal solution of unsymmetric sets of linear systems. *SIAM J. Sci. Stat. Comput.* **5**, 633–641.
- EMBREE, M. & TREFETHEN, L. N. 2004 Pseudospectra Gateway. Web site: <http://www.comlab.ox.ac.uk/pseudospectra>.
- FENTON, J. D. 1988 The numerical solution of steady water wave problems. *Comput. Geosci.* **14**, 357–368.
- FISCHER, G. 1959 A numerical method for tidal computations in inner seas (in German). *Tellus* **11**, 60–76.
- FORNBERG, B. 1998 *A Practical Guide to Pseudospectral Methods*. Cambridge: Cambridge University Press.
- FREILICH, M. H. & GUZA, R. T. 1984 Nonlinear effects on shoaling surface gravity waves. *Phil. Trans. R. Soc. Lond. A* **311**, 1–41.
- FUHRMAN, D. R. & BINGHAM, H. B. 2003 Preconditioning methods for a high-order Boussinesq water wave model. In *Proc. Third Int. Conf. on Preconditioning Techniques for Large Sparse Matrix Problems in Scientific and Industrial Applications*. Napa USA.
- FUHRMAN, D. R. & BINGHAM, H. B. 2004 Numerical solutions of fully non-linear and highly dispersive Boussinesq equations in two horizontal dimensions. *Int. J. Numer. Meth. Fluids* **44**, 231–255.
- FUHRMAN, D. R., BINGHAM, H. B. & MADSEN, P. A. 2005 Nonlinear wave-structure interactions with a high-order Boussinesq model. *Coast. Eng.* (to appear).
- FUHRMAN, D. R., BINGHAM, H. B., MADSEN, P. A. & THOMSEN, P. G. 2004a Linear and non-linear stability analysis for finite difference discretizations of high-order Boussinesq equations. *Int. J. Numer. Meth. Fluids* **45**, 751–773.
- FUHRMAN, D. R. & MADSEN, P. A. 2005 Potential dominance of oscillating crescent waves in finite width tanks. *Phys. Fluids* **17**, 038102.

- FUHRMAN, D. R., MADSEN, P. A. & BINGHAM, H. B. 2004*b* Computation of nonlinear water waves with a high-order Boussinesq model. In *Proc. 29th Int. Conf. on Coastal Engineering*. Lisbon, Portugal.
- FUHRMAN, D. R., MADSEN, P. A. & BINGHAM, H. B. 2004*c* Numerical modeling of water waves with a fully nonlinear and highly dispersive Boussinesq model. In *Proc. Fields Institute Workshop on Free Surface Water Waves*. Toronto, Canada, poster presentation.
- FUHRMAN, D. R., MADSEN, P. A. & BINGHAM, H. B. 2004*d* A numerical study of crescent waves. *J. Fluid Mech.* **513**, 309–341.
- GOBBI, M. F., KENNEDY, A. B. & KIRBY, J. T. 1998 A comparison of higher order boussinesq and local polynomial approximation models. In *Proc. 26th Int. Conf. on Coastal Engineering*, pp. 631–644. Copenhagen, Denmark.
- GOBBI, M. F., KIRBY, J. T. & WEI, G. 2000 A fully non-linear Boussinesq model for surface waves. Part 2. Extension to $O(kh^4)$. *J. Fluid Mech.* **405**, 181–210.
- GOLUB, G. H. & VAN LOAN, C. F. 1996 *Matrix Computations*. Baltimore: Johns Hopkins University Press.
- GUAZZELLI, E., REY, V. & BELZONS, M. 1992 Higher-order Bragg reflection of gravity surface waves by periodic beds. *J. Fluid Mech.* **245**, 301–317.
- HAMMACK, J., HENDERSON, D. M. & SEGUR, H. 2005 Deep-water waves with persistent, two-dimensional surface patterns. *J. Fluid Mech.* (in press).
- HAMMACK, J., MCCALLISTER, D., SCHEFFNER, N. & SEGUR, H. 1995 Two-dimensional periodic waves in shallow water. Part 2. Asymmetric waves. *J. Fluid Mech.* **285**, 95–122.
- HAMMACK, J., SCHEFFNER, N. & SEGUR, H. 1989 Two-dimensional periodic waves in shallow water. *J. Fluid Mech.* **209**, 567–589.
- HAMMACK, J., SCHEFFNER, N. & SEGUR, H. 1991 A note on the generation and narrowness of periodic rip currents. *J. Geophys. Res.* **96**, 4909–4914.
- HAMMACK, J. L. & HENDERSON, D. M. 2002 Experiments on deep-water waves with two-dimensional surface patterns. In *Proc. 21st Int. Conf. Offshore Mechanics and Arctic Engineering*. Oslo, Norway.
- HAMMACK, J. L. & HENDERSON, D. M. 2003 Experiments on deep-water waves with two-dimensional surface patterns. *J. Offshore Mech. Arctic Eng.* **125**, 48–53.
- HARA, T. & MEI, C. C. 1987 Bragg scattering of surface waves by periodic bars: theory and experiment. *J. Fluid Mech.* **178**, 221–241.
- HEATHERSHAW, A. D. & DAVIES, A. G. 1985 Resonant wave reflection by transverse bedforms and its relation to beaches and offshore bars. *Mar. Geol.* **62**, 321–338.

- HIRSCH, C. 1988 *Numerical Computation of Internal and External Flows. Volume 1: Fundamentals of Numerical Discretization*. New York: John Wiley & Sons.
- HOGAN, S. J., GRUMAN, I. & STIASSNIE, M. 1988 On the changes in phase speed of one train of water waves in the presence of another. *J. Fluid Mech.* **192**, 97–114.
- HOUWEN, P. J. V. D., MOOIMAN, J. & WUBS, F. W. 1991 Numerical analysis of time-dependent Boussinesq models. *Int. J. Numer. Meth. Fluids* **13**, 1235–1250.
- HSU, J. R., TSUCHIYA, Y. & SILVESTER, R. 1979 Third-order approximation to short-crested waves. *J. Fluid Mech.* **90**, 179–196.
- HUANG, H. & SEYMOUR, B. R. 2000 Finite difference solutions of incompressible flow problems with corner singularities. *J. Sci. Comput.* **15**, 265–292.
- IPSEN, I. C. F. 2001 A note on preconditioning nonsymmetric matrices. *SIAM J. Sci. Comput.* **23**, 1050–1051.
- ISERLES, A. 1996 *A First Course in the Numerical Analysis of Differential Equations*. Cambridge: Cambridge University Press.
- JAMOIS, E., KIMMOUN, O., MOLIN, B. & STASSEN, Y. 2004 Nonlinear interactions and wave run-up near a gravity base structure. In *Proc. 29th Int. Conf. Coastal Engineering*. Lisbon, Portugal.
- KENNEDY, A., KIRBY, J., CHEN, Q. & DALRYMPLE, R. 2001 Boussinesq-type equations with improved nonlinear performance. *Wave Motion* **33**, 225–243.
- KHARIF, C. & PELINOVSKY, E. 2003 Physical mechanisms of the rogue wave phenomenon. *Eur. J. Mech. B/Fluids* **22**, 603–634.
- KHARIF, C. & RAMAMONJIARISOA, A. 1988 Deep water gravity wave instabilities at large steepness. *Phys. Fluids* **31**, 1286–1288.
- KHARIF, C. & RAMAMONJIARISOA, A. 1990 On the stability of gravity waves on deep water. *J. Fluid Mech.* **218**, 163–170.
- KIMMOUN, O., BRANGER, H. & KHARIF, C. 1999 On short-crested waves: experimental and analytical investigations. *Eur. J. Mech. B/Fluids* **18**, 889–930.
- KIRBY, J. T. 1986 A general wave equation for waves over rippled beds. *J. Fluid Mech.* **162**, 171–186.
- KIRBY, J. T. 1990 Modelling shoaling directional wave spectra in shallow water. In *Proc. 22nd Int. Conf. Coastal Engineering*, pp. 109–122. Delft, The Netherlands.
- KORTEWEG, D. J. & DE VRIES, F. 1895 On the change of form of long waves advancing in a rectangular canal, and on a new type of long stationary waves. *Philos. Mag.* **39**, 422–443.

- KUSABA, T. & MITSUYASU, H. 1986 Nonlinear instability and evolution of steep water waves under wind action. *Rep. Res. Inst. Appl. Mech. Kyushu University* **33**, 33–64.
- LI, B. & FLEMING, C. A. 1997 A three dimensional multigrid model for fully nonlinear water waves. *Coast. Eng.* **30**, 235–258.
- LIU, P. L. F. & TSAY, T. K. 1984 Refraction-diffraction model for weakly nonlinear water waves. *J. Fluid Mech.* **141**, 265–274.
- LIU, P. L. F., YOON, S. B. & KIRBY, J. T. 1985 Nonlinear refraction-diffraction of waves in shallow water. *J. Fluid Mech.* **153**, 185–201.
- LIU, Y. & YUE, D. K. P. 1998 On generalized Bragg scattering of surface waves by bottom ripples. *J. Fluid Mech.* **356**, 297–326.
- LOGHIN, D. & WATHEN, A. J. 2002 Schur complement preconditioners for the Navier-Stokes equations. *Int. J. Numer. Meth. Fluids* **40**, 403–412.
- LOGHIN, D. & WATHEN, A. J. 2003 Schur complement preconditioning for elliptic systems of partial differential equations. *Numer. Lin. Alg. Appl.* **10**, 423–443.
- LONGUET-HIGGINS, M. S. 1975 Integral properties of periodic gravity waves of finite amplitude. *Proc. R. Soc. Lond. A* **342**, 157–174.
- LONGUET-HIGGINS, M. S. & COKELET, E. D. 1978 The deformation of steep surface waves on water II: Growth of normal-mode instabilities. *Proc. R. Soc. Lond. A* **364**, 1–28.
- LONGUET-HIGGINS, M. S. & PHILLIPS, O. M. 1962 Phase velocity effects in tertiary wave interactions. *J. Fluid Mech.* **12**, 333–336.
- LYNETT, P. & LIU, P. L.-F. 2004a Linear analysis of the multi-layer model. *Coast. Eng.* **51**, 439–454.
- LYNETT, P. & LIU, P. L.-F. 2004b A two-layer approach to wave modelling. *Proc. R. Soc. Lond. A* **460**, 2637–2669.
- MADSEN, O. S. & MEI, C. C. 1969 The transformation of a solitary wave over an uneven bottom. *J. Fluid Mech.* **39**, 781–791.
- MADSEN, P. A. & AGNON, Y. 2003 Accuracy and convergence of velocity formulations for water waves in the framework of Boussinesq theory. *J. Fluid Mech.* **477**, 285–319.
- MADSEN, P. A., BANIJAMALI, B., SCHÄFFER, H. A. & SØRENSEN, O. R. 1996 Boussinesq type equations with high accuracy in dispersion and nonlinearity. In *Proc. 25th Int. Conf. on Coastal Engineering*, pp. 95–108. Orlando, USA.
- MADSEN, P. A., BINGHAM, H. B. & LIU, H. 2002 A new Boussinesq method for fully nonlinear waves from shallow to deep water. *J. Fluid Mech.* **462**, 1–30.

- MADSEN, P. A., BINGHAM, H. B. & SCHÄFFER, H. A. 2003 Boussinesq-type formulations for fully nonlinear and extremely dispersive water waves: derivation and analysis. *Proc. R. Soc. Lond. A* **459**, 1075–1104.
- MADSEN, P. A. & FUHRMAN, D. R. 2004 Recent progress in modelling of non-linear water waves. In *Proc. Fields Institute Workshop on Free Surface Water Waves*. Toronto, Canada.
- MADSEN, P. A. & FUHRMAN, D. R. 2005 Third order multidirectional irregular waves (in preparation).
- MADSEN, P. A., FUHRMAN, D. R. & WANG, B. 2005 A Boussinesq-type method for fully nonlinear waves interacting with a rapidly varying bathymetry. *Coast. Eng.* (submitted).
- MADSEN, P. A., MURRAY, R. & SØRENSEN, O. R. 1991 A new form of the Boussinesq equations with improved linear dispersion characteristics. Part 1. *Coast. Eng.* **15**, 371–388.
- MADSEN, P. A. & SCHÄFFER, H. A. 1998 Higher order Boussinesq-type equations for surface gravity waves—derivation and analysis. *Phil. Trans. R. Soc. Lond. A* **356**, 3123–3181.
- MADSEN, P. A. & SCHÄFFER, H. A. 1999 A review of Boussinesq-type equations for gravity waves. In *Advances in Coastal and Ocean Engineering* (ed. P. Liu), , vol. 5, pp. 1–95. World Scientific.
- MADSEN, P. A., SIMONSEN, H. J. & PAN, C.-H. 2004 Numerical simulation of tidal bores and hydraulic jumps. *Coast. Eng.* (to appear).
- MADSEN, P. A. & SØRENSEN, O. R. 1990 Extension of the Boussinesq equations to include wave propagation in deeper water and wave-ship interaction in shallow water. In *Proc. 22nd Int. Conf. Coastal Engineering*, pp. 3112–3125.
- MADSEN, P. A. & SØRENSEN, O. R. 1992 A new form of the Boussinesq equations with improved linear dispersion characteristics. Part 2. A slowly-varying bathymetry. *Coast. Eng.* **18**, 183–204.
- MADSEN, P. A. & SØRENSEN, O. R. 1993 Bound waves and triad interactions in shallow water. *Ocean Eng.* **20**, 359–388.
- MADSEN, P. A., SØRENSEN, O. R. & SCHÄFFER, H. A. 1997a Surf zone dynamics simulated by a Boussinesq type model. Part 1: Model description and cross-shore motion of regular waves. *Coast. Eng.* **32**, 255–283.
- MADSEN, P. A., SØRENSEN, O. R. & SCHÄFFER, H. A. 1997b Surf zone dynamics simulated by a Boussinesq type model. Part 2: Surf beat and swash oscillations for wave groups and irregular waves. *Coast. Eng.* **32**, 289–320.
- MADSEN, P. A. & WARREN, I. R. 1984 Performance of a numerical short-wave model. *Coast. Eng.* **8**, 73–93.

- MAYER, S., GARAPON, A. & SØRENSEN, L. S. 1998 A fractional step method for unsteady free-surface flow with applications to non-linear wave dynamics. *Int. J. Numer. Meth. Fluids* **28**, 293–315.
- MAYER, S. & MADSEN, P. A. 2000 Simulations of breaking waves in the surf zone using a navier-stokes solver. In *Proc. 25th Int. Conf. Coastal Engineering*, pp. 928–941. Sydney, Australia.
- MCLEAN, J. W. 1982*a* Instabilities of finite-amplitude gravity waves on water of finite depth. *J. Fluid Mech.* **114**, 331–341.
- MCLEAN, J. W. 1982*b* Instabilities of finite-amplitude water waves. *J. Fluid Mech.* **114**, 315–330.
- MCLEAN, J. W., MA, Y. C., MARTIN, D. U., SAFFMAN, P. G. & YUEN, H. C. 1981 Three-dimensional instability of finite-amplitude water waves. *Phys. Rev. Lett.* **46**, 817–820.
- MEI, C. C. 1983 *The Applied Dynamics of Ocean Surface Waves*. New York: John Wiley & Sons.
- MEI, C. C. 1985 Resonant reflection of surface water waves by periodic sand-bars. *J. Fluid Mech.* **152**, 315–335.
- MEI, C. C., HARA, T. & NACIRI, M. 1988 Note on Bragg scattering of water waves by parallel bars on the sea bed. *J. Fluid Mech.* **186**, 147–162.
- MEI, C. C. & LEMÉHAUTÉ, B. 1966 Note on the equations of long waves over an uneven bottom. *J. Geophys. Res.* **71**, 393–400.
- MEI, C. C. & ÜNLÜATA, U. 1972 Harmonic generation in shallow water waves. In *Waves on Beaches and Resulting Sediment Transport* (ed. R. E. Meyer), pp. 181–202. New York: Academic Press.
- MELVILLE, W. K. 1982 The instability and breaking of deep-water waves. *J. Fluid Mech.* **115**, 165–185.
- METCALF, M. & REID, J. 1996 *FORTRAN 90/95 Explained*. Oxford: Oxford Science Publications.
- MEURANT, G. 1999 *Computer Solution of Large Linear Systems*. Amsterdam: Elsevier.
- MOLIN, B., REMY, F. & KIMMOUN, O. 2004 Experimental study of the non-linear wave interaction with a vertical plate. In *Proc. Int. Society of Offshore and Polar Engineering Conf.*. Toulon, France.
- MOLIN, B., REMY, F., KIMMOUN, O. & FERRANT, P. 2003 Third-order interactions and wave run-up. In *Proc. 18th Int. Workshop on Water Waves and Floating Bodies*. Le Croisic, France.

- MOLIN, B., REMY, F., KIMMOUN, O. & JAMOIS, E. 2005 The role of tertiary wave interactions in wave-body problems. *J. Fluid Mech.* **528**, 323–354.
- MURPHY, M. F., GOLUB, G. H. & WATHEN, A. J. 2000 A note on preconditioning for indefinite linear systems. *SIAM J. Sci. Comput.* **6**, 1969–1972.
- NICHOLLS, D. P. 1998 Traveling water waves: Spectral continuation methods with parallel implementation. *J. Comput. Phys.* **142**, 224–240.
- NICHOLLS, D. P. 2001 On hexagonal gravity water waves. *Math. Comput. Simulation* **55**, 567–575.
- NIELSEN, K. B. 2003 Numerical prediction of green water loads on ships. PhD thesis, Technical University of Denmark, Lyngby, Denmark.
- NIELSEN, K. B. & MAYER, S. 2004 Numerical prediction of green water incidents. *Ocean Eng.* **31**, 363–399.
- NWOGU, O. 1993 Alternative form of Boussinesq equations for nearshore wave propagation. *J. Waterw. Port C-ASCE* **119**, 618–638.
- O’HARE, T. J. & DAVIES, A. G. 1993 A comparison of two models for surface-wave propagation over rapidly varying bathymetry. *Appl. Ocean Res.* **15**, 1–11.
- PENNY, W. G. & PRICE, A. T. 1952 Part I. The diffraction theory of sea waves and the shelter afforded by breakwaters. *Phil. Trans. R. Soc. Lond. A* **244**, 236–253.
- PEREGRINE, D. H. 1967 Long waves on a beach. *J. Fluid Mech.* **27**, 815–827.
- PHILLIPS, O. M. 1960 On the dynamics of unsteady gravity waves of finite amplitude, Part 1. Elementary interactions. *J. Fluid Mech.* **9**, 193–217.
- POS, J. D. 1985 Asymmetrical breakwater gap wave diffraction using finite and infinite elements. *Coast. Eng.* **9**, 101–123.
- PRESS, W. H., TEUKOLSKY, S. A., VETTERLING, W. T. & FLANNERY, B. P. 1992 *Numerical Recipes in FORTRAN: The Art of Scientific Computing*, 2nd edn. Cambridge: Cambridge University Press.
- RAKHA, K. A. & KAMPHUIS, J. W. 1997 A morphology model for an eroding beach backed by a seawall. *Coast. Eng.* **30**, 53–75.
- RAYLEIGH 1876 On waves. *Philos. Mag.* **5**, 257–279.
- ROBERTS, A. J. 1983 Highly nonlinear short-crested water waves. *J. Fluid Mech.* **135**, 301–321.
- RYGG, O. B. 1988 Nonlinear refraction-diffraction of surface waves in intermediate and shallow water. *Coast. Eng.* **12**, 191–211.

- SAAD, Y. 1994a ILUT: a dual threshold incomplete ILU factorization. *Numer. Lin. Alg. Appl.* **1**, 387–402.
- SAAD, Y. 1994b SPARSKIT: A basic tool kit for sparse matrix computations, Version 2. Available: www.cs.umn.edu/research/arpa/SPARSKIT/sparsekit.html.
- SAAD, Y. 2003 *Iterative Methods for Sparse Linear Systems*, 2nd edn. PWS Publishing Co.
- SAAD, Y. & SCHULTZ, M. H. 1986 GMRES: a generalized minimal residual algorithm for solving nonsymmetric linear systems. *SIAM J. Sci. Stat. Comput.* **7**, 856–869.
- SAAD, Y. & VAN DER VORST, H. A. 2000 Iterative solution of linear systems in the 20th century. *J. Comput. Appl. Math.* **123**, 1–33.
- SAVITZKY, A. & GOLAY, M. J. E. 1964 Smoothing and differentiation of data by simplified least squares procedures. *Anal. Chem.* **36**, 1627–1639.
- SCHÄFFER, H. A. 1996 Second-order wavemaker theory for irregular waves. *Ocean Eng.* **23**, 47–88.
- SCHÄFFER, H. A. & MADSEN, P. A. 1995 Further enhancements of boussinesq-type equations. *Coast. Eng.* **26**, 1–15.
- SCHÄFFER, H. A., MADSEN, P. A. & DEIGAARD, R. A. 1993 A Boussinesq model for wave breaking in shallow water. *Coast. Eng.* **20**, 185–202.
- SCHÄFFER, H. A. & STEENBERG, C. M. 2003 Second-order wavemaker theory for multidirectional waves. *Ocean Eng.* **30**, 1203–1231.
- SEGUR, H. & FINKEL, A. 1985 An analytical model of periodic waves in shallow water. *Stud. Appl. Math.* **73**, 183–220.
- SERRE, P. F. 1953 Contribution à l'étude des écoulements permanents et variables dans les canaux. *La Houille Blanche* pp. 374–388; 830–872.
- SHRIRA, V. I., BADULIN, S. I. & KHARIF, C. 1996 A model of water wave 'horse-shoe' patterns. *J. Fluid Mech.* **318**, 375–404.
- SHRIRA, V. I., BADULIN, S. I. & VORONOVICH, A. G. 2000 EM scattering from sea surface in the presence of wind wave patterns. *Int. Geoscience and Remote Sensing Symposium* **2**, 926–928.
- SKANDRANI, C. 1997 Contribution à l'étude de la dynamique non linéaire des champs de vagues tridimensionnels en profondeur infinie. PhD thesis, Université de la méditerranée, Aix-Marseille II, Marseille, France.
- SMITH, R. A. 1998 An operator expansion formalism for nonlinear surface waves over variable depth. *J. Fluid Mech.* **363**, 333–347.

- SOMMERFELD, A. 1896 Mathematische theorie der diffraktion. *Math. Ann.* **47**, 317–374.
- SU, C. H. & GARDNER, C. S. 1969 Korteweg-de Vries equation and generalizations. III. Derivation of the Korteweg-de Vries equation and Burgers equation. *J. Math. Phys.* **10**, 536–539.
- SU, M. Y. 1982 Three-dimensional deep-water waves. Part 1. Experimental measurement of skew and symmetric wave patterns. *J. Fluid Mech.* **124**, 73–108.
- SU, M. Y., BERGIN, M., MARLER, P. & MYRICK, R. 1982 Experiments on nonlinear instabilities and evolution of steep gravity-wave trains. *J. Fluid Mech.* **124**, 45–72.
- SUH, K. D., LEE, C. & PARK, W. S. 1997 Time-dependent equations for wave propagation on rapidly varying topography. *Coast. Eng.* **32**, 91–117.
- SVENDSEN, I. A. & JONSSON, I. G. 1976 *Hydrodynamics of Coastal Regions*. Lyngby, Denmark: Technical University of Denmark.
- TREFETHEN, A. E., TREFETHEN, L. N. & SCHMID, P. J. 1999 Spectra and pseudospectra for pipe Poiseuille flow. *Comput. Meth. Appl. Mech. Eng.* **175**, 413–420.
- TREFETHEN, L. N. 1996 *Finite Difference and Spectral Methods for Ordinary and Partial Differential Equations*. Available: <http://web.comlab.ox.ac.uk.oucl/work/nick.trefethen/pdetext.html>: Unpublished text.
- TREFETHEN, L. N. 1997 Pseudospectra of linear operators. *SIAM Rev.* **39**, 383–406.
- TREFETHEN, L. N. 2000 *Spectral methods in Matlab*. Philadelphia: SIAM.
- TREFETHEN, L. N. & BAU, D. 1997 *Numerical Linear Algebra*. Philadelphia: SIAM.
- TREFETHEN, L. N., TREFETHEN, A. E., REDDY, S. C. & DRISCOLL, T. A. 1993 Hydrodynamic stability without eigenvalues. *Science* **261**, 578–584.
- VAN DER VORST, H. A. 1992 Bi-CGSTAB: a fast and smoothly converging variant of Bi-CG for the solution of nonsymmetric linear systems. *SIAM J. Sci. Stat. Comput.* **13**, 631–644.
- WEI, G. & KIRBY, J. T. 1995 Time dependent numerical code for extended Boussinesq equations. *J. Waterw. Port C-ASCE* **121**, 251–261.
- WEI, G., KIRBY, J. T., GRILLI, S. T. & SUBRAMANYA, R. 1995 A fully nonlinear Boussinesq model for surface waves. Part 1. Highly nonlinear unsteady waves. *J. Fluid Mech.* **294**, 71–92.
- WEISSTEIN, E. W. 2004 Eric Weisstein's world of Biography. Web site: <http://scienceworld.wolfram.com/biography/Boussinesq.html>.
- WHALEY, R. C., PETITET, A. & DONGARRA, J. J. 2000 Automated empirical optimization of software and the ATLAS project. Available: <http://math-atlas.sourceforge.net/>.

- WHALIN, R. W. 1971 *The limit of applicability of linear wave refraction theory in a convergence zone. Res. Rep. H-71*. Vicksburg, MS: U.S. Army Corps of Engineers, Waterways Expt. Station.
- WIEGEL, R. L. 1964 Water wave equivalent of mach reflection. In *Proc. 9th Conf. Coastal Engineering*, pp. 82–102.
- WILLIAMS, J. M. 1985 *Tables of Progressive Gravity Waves*. Pitman.
- WITTING, J. M. 1984 A unified model for the evolution of nonlinear water waves. *J. Comput. Phys.* **56**, 203–239.
- WRIGHT, T. G. 2002 Algorithms and software for pseudospectra. PhD thesis, Oxford University, Oxford.
- WRIGHT, T. G. & TREFETHEN, L. N. 2001 Large-scale computation of pseudospectra using ARPACK and EIGS. *SIAM J. Sci. Comput.* **23**, 591–605.
- WU, T. Y. 1999 Modelling nonlinear dispersive water waves. *J. Eng. Mech.* **125**, 747–755.
- WU, T. Y. 2001 A unified theory for modelling water waves. *Adv. Appl. Mech.* **37**, 1–88.
- XUE, M., XÜ, H., LIU, Y. & YUE, D. K. P. 2001 Computations of fully nonlinear three-dimensional wave-wave and wave-body interactions. Part 1. Dynamics of steep three-dimensional waves. *J. Fluid Mech.* **438**, 11–39.
- YOON, S. B. & LIU, P.-F. 1989 Interactions of currents and weakly nonlinear water waves in shallow water. *J. Fluid Mech.* **205**, 397–419.
- ZAKHAROV, V. E. 1968 Stability of periodic waves of finite amplitude on the surface of a deep fluid. *J. Appl. Mech. Tech. Phys.* **9**, 190–194.
- ZHANG, J. & CHEN, L. X. 1999 General third-order solutions for irregular waves in deep water. *J. Eng. Mech.* **125**, 768–779.

Appendix A

Differential Operators

This section includes the various operators in the system of PDEs denoted herein as \mathcal{A} . The enhanced free surface operators from the rotational system (4.6) are

$$\mathcal{A}_1 = 1 - \alpha_2 \left(\frac{\partial^2}{\partial x^2} + \frac{\partial^2}{\partial y^2} \right) + \alpha_4 \left(\frac{\partial^4}{\partial x^4} + 2 \frac{\partial^4}{\partial x^2 \partial y^2} + \frac{\partial^4}{\partial y^4} \right), \quad (\text{A.1})$$

$$\mathcal{A}_{11} = 1 - \alpha_2 \left(\frac{\partial^2}{\partial x^2} \right) + \alpha_4 \left(\frac{\partial^4}{\partial x^4} + \frac{\partial^4}{\partial x^2 \partial y^2} \right), \quad (\text{A.2})$$

$$\mathcal{A}_2 = -\alpha_2 \left(\frac{\partial^2}{\partial x \partial y} \right) + \alpha_4 \left(\frac{\partial^4}{\partial x^3 \partial y} + \frac{\partial^4}{\partial x \partial y^3} \right), \quad (\text{A.3})$$

$$\mathcal{B}_{11} = (\eta - \hat{z}) \left(\frac{\partial}{\partial x} \right) - \beta_3 \left(\frac{\partial^3}{\partial x^3} + \frac{\partial^3}{\partial x \partial y^2} \right) + \beta_5 \left(\frac{\partial^5}{\partial x^5} + 2 \frac{\partial^5}{\partial x^3 \partial y^2} + \frac{\partial^5}{\partial x \partial y^4} \right), \quad (\text{A.4})$$

$$\mathcal{A}_{22} = 1 - \alpha_2 \left(\frac{\partial^2}{\partial y^2} \right) + \alpha_4 \left(\frac{\partial^4}{\partial x^2 \partial y^2} + \frac{\partial^4}{\partial y^4} \right), \quad (\text{A.5})$$

$$\mathcal{B}_{12} = (\eta - \hat{z}) \left(\frac{\partial}{\partial y} \right) - \beta_3 \left(\frac{\partial^3}{\partial x^2 \partial y} + \frac{\partial^3}{\partial y^3} \right) + \beta_5 \left(\frac{\partial^5}{\partial x^4 \partial y} + 2 \frac{\partial^5}{\partial x^2 \partial y^3} + \frac{\partial^5}{\partial y^5} \right), \quad (\text{A.6})$$

with the α and β coefficients in (2.42) applied at $z = \eta$. The basic bottom operators are

$$\mathcal{A}_{01} = (h + \hat{z}) \left(\frac{\partial}{\partial x} \right) - \frac{1}{9} (h + \hat{z})^3 \left(\frac{\partial^3}{\partial x^3} + \frac{\partial^3}{\partial x \partial y^2} \right) + \frac{1}{945} (h + \hat{z})^5 \left(\frac{\partial^5}{\partial x^5} + 2 \frac{\partial^5}{\partial x^3 \partial y^2} + \frac{\partial^5}{\partial x \partial y^4} \right), \quad (\text{A.7})$$

$$\mathcal{A}_{02} = (h + \hat{z}) \left(\frac{\partial}{\partial y} \right) - \frac{1}{9} (h + \hat{z})^3 \left(\frac{\partial^3}{\partial x^2 \partial y} + \frac{\partial^3}{\partial y^3} \right) + \frac{1}{945} (h + \hat{z})^5 \left(\frac{\partial^5}{\partial x^4 \partial y} + 2 \frac{\partial^5}{\partial x^2 \partial y^3} + \frac{\partial^5}{\partial y^5} \right), \quad (\text{A.8})$$

$$\mathcal{B}_0 = 1 - \frac{4}{9}(h + \hat{z})^2 \left(\frac{\partial^2}{\partial x^2} + \frac{\partial^2}{\partial y^2} \right) + \frac{1}{63}(h + \hat{z})^4 \left(\frac{\partial^4}{\partial x^4} + 2\frac{\partial^4}{\partial x^2 \partial y^2} + \frac{\partial^4}{\partial y^4} \right). \quad (\text{A.9})$$

The bottom slope operators (in the x -direction) are

$$\mathcal{C}_{11} = 1 - c_2(h + \hat{z})^2 \left(\frac{\partial^2}{\partial x^2} \right) + c_4(h + \hat{z})^4 \left(\frac{\partial^4}{\partial x^4} + \frac{\partial^4}{\partial x^2 \partial y^2} \right), \quad (\text{A.10})$$

$$\mathcal{C}_{12} = -c_2(h + \hat{z})^2 \left(\frac{\partial^2}{\partial x \partial y} \right) + c_4(h + \hat{z})^4 \left(\frac{\partial^4}{\partial x^3 \partial y} + \frac{\partial^4}{\partial x \partial y^3} \right), \quad (\text{A.11})$$

$$\mathcal{C}_{13} = (h + \hat{z}) \left(\frac{\partial}{\partial x} \right) - s_3(h + \hat{z})^3 \left(\frac{\partial^3}{\partial x^3} + \frac{\partial^3}{\partial x \partial y^2} \right) + s_5(h + \hat{z})^5 \left(\frac{\partial^5}{\partial x^5} + 2\frac{\partial^5}{\partial x^3 \partial y^2} + \frac{\partial^5}{\partial x \partial y^4} \right), \quad (\text{A.12})$$

and in the y -direction

$$\mathcal{C}_{21} = \mathcal{C}_{12}, \quad (\text{A.13})$$

$$\mathcal{C}_{22} = 1 - c_2(h + \hat{z})^2 \left(\frac{\partial^2}{\partial y^2} \right) + c_4(h + \hat{z})^4 \left(\frac{\partial^4}{\partial x^2 \partial y^2} + \frac{\partial^4}{\partial y^4} \right), \quad (\text{A.14})$$

$$\mathcal{C}_{23} = (h + \hat{z}) \left(\frac{\partial}{\partial y} \right) - s_3(h + \hat{z})^3 \left(\frac{\partial^3}{\partial x^2 \partial y} + \frac{\partial^3}{\partial y^3} \right) + s_5(h + \hat{z})^5 \left(\frac{\partial^5}{\partial x^4 \partial y} + 2\frac{\partial^5}{\partial x^2 \partial y^3} + \frac{\partial^5}{\partial y^5} \right). \quad (\text{A.15})$$

The additional bottom slope operator used in the irrotational system (4.8) is

$$\mathcal{C}_1 = 1 - c_2(h + \hat{z})^2 \left(\frac{\partial^2}{\partial x^2} + \frac{\partial^2}{\partial y^2} \right) + c_4(h + \hat{z})^4 \left(\frac{\partial^4}{\partial x^4} + 2\frac{\partial^4}{\partial x^2 \partial y^2} + \frac{\partial^4}{\partial y^4} \right). \quad (\text{A.16})$$

Appendix B

Finite Difference Approximations

This appendix provides the various finite difference approximations used in the Boussinesq model, as introduced in §3.2.

B.1 One-Dimensional Derivative Approximations

Second-order accurate finite difference approximations for the first five pure x -derivatives are:

$$\frac{\partial f}{\partial x} = \frac{1}{\Delta x} \left(\frac{-1}{2} f_{j-1} + \frac{1}{2} f_{j+1} \right) + O(\Delta x^2), \quad (\text{B.1})$$

$$\frac{\partial^2 f}{\partial x^2} = \frac{1}{\Delta x^2} (f_{j-1} - 2f_j + f_{j+1}) + O(\Delta x^2), \quad (\text{B.2})$$

$$\frac{\partial^3 f}{\partial x^3} = \frac{1}{\Delta x^3} \left(\frac{-1}{2} f_{j-2} + f_{j-1} - f_{j+1} + \frac{1}{2} f_{j+2} \right) + O(\Delta x^2), \quad (\text{B.3})$$

$$\frac{\partial^4 f}{\partial x^4} = \frac{1}{\Delta x^4} (f_{j-2} - 4f_{j-1} + 6f_j - 4f_{j+1} + f_{j+2}) + O(\Delta x^2), \quad (\text{B.4})$$

$$\frac{\partial^5 f}{\partial x^5} = \frac{1}{\Delta x^5} \left(-\frac{1}{2} f_{j-3} + 2f_{j-2} - \frac{5}{2} f_{j-1} + \frac{5}{2} f_{j+1} - 2f_{j+2} + \frac{1}{2} f_{j+3} \right) + O(\Delta x^2). \quad (\text{B.5})$$

Similarly, seven-point approximations for the first five derivatives are

$$\frac{\partial f}{\partial x} = \frac{1}{\Delta x} \left(-\frac{1}{60} f_{j-3} + \frac{3}{20} f_{j-2} - \frac{3}{4} f_{j-1} + \frac{3}{4} f_{j+1} - \frac{3}{20} f_{j+2} + \frac{1}{60} f_{j+3} \right) + O(\Delta x^6), \quad (\text{B.6})$$

$$\frac{\partial^2 f}{\partial x^2} = \frac{1}{\Delta x^2} \left(\frac{1}{90} f_{j-3} - \frac{3}{20} f_{j-2} + \frac{3}{2} f_{j-1} - \frac{49}{18} f_j + \frac{3}{2} f_{j+1} - \frac{3}{20} f_{j+2} + \frac{1}{90} f_{j+3} \right) + O(\Delta x^6), \quad (\text{B.7})$$

$$\frac{\partial^3 f}{\partial x^3} = \frac{1}{\Delta x^3} \left(\frac{1}{8} f_{j-3} - f_{j-2} + \frac{13}{8} f_{j-1} - \frac{13}{8} f_{j+1} + f_{j+2} - \frac{1}{8} f_{j+3} \right) + O(\Delta x^4), \quad (\text{B.8})$$

$$\frac{\partial^4 f}{\partial x^4} = \frac{1}{\Delta x^4} \left(-\frac{1}{6} f_{j-3} + 2f_{j-2} - \frac{13}{2} f_{j-1} + \frac{28}{3} f_j - \frac{13}{2} f_{j+1} + 2f_{j+2} - \frac{1}{6} f_{j+3} \right) + O(\Delta x^4), \quad (\text{B.9})$$

$$\frac{\partial^5 f}{\partial x^5} = \frac{1}{\Delta x^5} \left(-\frac{1}{2} f_{j-3} + 2f_{j-2} - \frac{5}{2} f_{j-1} + \frac{5}{2} f_{j+1} - 2f_{j+2} + \frac{1}{2} f_{j+3} \right) + O(\Delta x^2). \quad (\text{B.10})$$

Finite difference approximations for pure y -derivatives are analogous to those listed previously.

B.2 Mixed Derivative Approximations

For the remainder of this appendix finite difference approximations for mixed derivative terms are given with the following stencil notation

$$\frac{\partial^{m+n}}{\partial x^m \partial y^n} \approx \frac{1}{\Delta x^m \Delta y^n} \mathbf{F}_{m,n}. \quad (\text{B.11})$$

Here the truncation error will be written under the assumption that $O(\chi) \equiv O(\Delta x) \equiv O(\Delta y)$ for simplicity. Second-order mixed finite difference approximations are

$$\frac{\partial^2}{\partial x \partial y} = \frac{1}{\Delta x \Delta y} \begin{bmatrix} -1/4 & 0 & 1/4 \\ 0 & 0 & 0 \\ 1/4 & 0 & -1/4 \end{bmatrix} + O(\chi^2), \quad (\text{B.12})$$

$$\frac{\partial^3}{\partial x^2 \partial y} = \frac{1}{\Delta x^2 \Delta y} \begin{bmatrix} 1/2 & -1 & 1/2 \\ 0 & 0 & 0 \\ -1/2 & 1 & -1/2 \end{bmatrix} + O(\chi^2), \quad (\text{B.13})$$

$$\frac{\partial^4}{\partial x^2 \partial y^2} = \frac{1}{\Delta x^2 \Delta y^2} \begin{bmatrix} 1 & -2 & 1 \\ -2 & 4 & -2 \\ 1 & -2 & 1 \end{bmatrix} + O(\chi^2), \quad (\text{B.14})$$

$$\frac{\partial^4}{\partial x^3 \partial y} = \frac{1}{\Delta x^3 \Delta y} \begin{bmatrix} -1/4 & 1/2 & 0 & -1/2 & 1/4 \\ 0 & 0 & 0 & 0 & 0 \\ 1/4 & -1/2 & 0 & 1/2 & -1/4 \end{bmatrix} + O(\chi^2), \quad (\text{B.15})$$

$$\frac{\partial^5}{\partial x^3 \partial y^2} = \frac{1}{\Delta x^3 \Delta y^2} \begin{bmatrix} -1/2 & 1 & 0 & -1 & 1/2 \\ 1 & -2 & 0 & 2 & -1 \\ -1/2 & 1 & 0 & -1 & 1/2 \end{bmatrix} + O(\chi^2), \quad (\text{B.16})$$

$$\frac{\partial^5}{\partial x^4 \partial y} = \frac{1}{\Delta x^4 \Delta y} \begin{bmatrix} 1/2 & -2 & 3 & -2 & 1/2 \\ 0 & 0 & 0 & 0 & 0 \\ -1/2 & 2 & -3 & 2 & -1/2 \end{bmatrix} + O(\chi^2). \quad (\text{B.17})$$

Note that finite difference approximations for $\frac{\partial^3}{\partial x \partial y^2}$, $\frac{\partial^4}{\partial x \partial y^3}$, $\frac{\partial^5}{\partial x \partial y^4}$, and $\frac{\partial^5}{\partial x^2 \partial y^3}$ derivatives can readily be found using (B.11) combined with the identity $\mathbf{F}_{m,n} = \mathbf{F}_{n,m}^T$, and are thus not explicitly given here.

With the full 25-point (diamond) stencil the following finite difference approximations change to

$$\frac{\partial^2}{\partial x \partial y} = \frac{1}{\Delta x \Delta y} \begin{bmatrix} & 1/24 & 0 & -1/24 & \\ 1/24 & -5/12 & 0 & 5/12 & -1/24 \\ 0 & 0 & 0 & 0 & 0 \\ -1/24 & 5/12 & 0 & -5/12 & 1/24 \\ & -1/24 & 0 & 1/24 & \end{bmatrix} + O(\chi^4), \quad (\text{B.18})$$

$$\frac{\partial^3}{\partial x^2 \partial y} = \frac{1}{\Delta x^2 \Delta y} \begin{bmatrix} & -1/12 & 1/6 & -1/12 & \\ -1/24 & 5/6 & -19/12 & 5/6 & -1/24 \\ 0 & 0 & 0 & 0 & 0 \\ 1/24 & -5/6 & 19/12 & -5/6 & 1/24 \\ & 1/12 & -1/6 & 1/12 & \end{bmatrix} + O(\chi^4), \quad (\text{B.19})$$

$$\frac{\partial^4}{\partial x^2 \partial y^2} = \frac{1}{\Delta x^2 \Delta y^2} \begin{bmatrix} & -1/12 & 1/6 & -1/12 & \\ -1/12 & 5/3 & -19/6 & 5/3 & -1/12 \\ 1/6 & -19/6 & 6 & -19/6 & 1/6 \\ -1/12 & 5/3 & -19/6 & 5/3 & -1/12 \\ & -1/12 & 1/6 & 1/12 & \end{bmatrix} + O(\chi^4). \quad (\text{B.20})$$

Mixed finite difference approximations for the 37-point (octagon) stencil are

$$\frac{\partial^2}{\partial x \partial y} = \frac{1}{\Delta x \Delta y} \begin{bmatrix} & & -1/120 & 0 & 1/120 & & \\ & -1/144 & 4/45 & -19/36 & 0 & -4/45 & 1/144 \\ & 0 & 0 & 0 & 0 & 0 & 0 \\ & 1/120 & -4/45 & 19/36 & 0 & -19/36 & 4/45 & -1/120 \\ & & 1/144 & -4/45 & 0 & 4/45 & -1/144 & \\ & & & 1/120 & 0 & -1/120 & & \end{bmatrix} + O(\chi^6), \quad (\text{B.21})$$

$$\frac{\partial^3}{\partial x^2 \partial y} = \frac{1}{\Delta x^2 \Delta y} \begin{bmatrix} & & & 1/60 & -1/30 & 1/60 & & \\ & 1/180 & -4/45 & 19/18 & -35/18 & 19/18 & -4/45 & 1/180 \\ & 0 & 0 & 0 & 0 & 0 & 0 & 0 \\ & -1/180 & 4/45 & -19/18 & 35/18 & -19/18 & 4/45 & -1/180 \\ & & -1/144 & 8/45 & -41/120 & 8/45 & -1/144 & \\ & & & -1/60 & 1/30 & -1/60 & & \end{bmatrix} + O(\chi^6), \quad (\text{B.22})$$

$$\frac{\partial^4}{\partial x^2 \partial y^2} = \frac{1}{\Delta x^2 \Delta y^2} \begin{bmatrix} & & & & 1/90 & -1/45 & 1/90 & & \\ & & 1/144 & -8/45 & 41/120 & -8/45 & 1/144 & & \\ & 1/90 & -8/45 & 19/9 & -35/9 & 19/9 & -8/45 & 1/90 & \\ & -1/45 & 41/120 & -35/9 & 257/36 & -35/9 & 41/120 & -1/45 & \\ & 1/90 & -8/45 & 19/9 & -35/9 & 19/9 & -8/45 & 1/90 & \\ & & 1/144 & -8/45 & 41/120 & -8/45 & 1/144 & & \\ & & & 1/90 & -1/45 & 1/90 & & & \end{bmatrix} + O(\chi^6), \quad (\text{B.23})$$

$$\frac{\partial^4}{\partial x^3 \partial y} = \frac{1}{\Delta x^3 \Delta y} \begin{bmatrix} & & 1/24 & -1/12 & 0 & 1/12 & -1/24 & & \\ & 1/16 & -7/12 & 47/48 & 0 & -47/48 & 7/12 & -1/16 & \\ & 0 & 0 & 0 & 0 & 0 & 0 & 0 & \\ & -1/16 & 7/12 & -47/48 & 0 & 47/48 & -7/12 & 1/16 & \\ & & -1/24 & 1/12 & 0 & -1/12 & 1/24 & & \end{bmatrix} + O(\chi^4), \quad (\text{B.24})$$

$$\frac{\partial^5}{\partial x^4 \partial y} = \frac{1}{\Delta x^4 \Delta y} \begin{bmatrix} & & & & & & & & \\ & -1/12 & -1/12 & 1/3 & -1/2 & 1/3 & -1/12 & -1/12 & \\ & 0 & 0 & 0 & 0 & 0 & 0 & 0 & \\ & 1/12 & -7/6 & 47/12 & -17/13 & 47/12 & -7/6 & 1/12 & \\ & & 1/12 & -1/3 & 1/2 & -1/3 & 1/12 & & \end{bmatrix} + O(\chi^4), \quad (\text{B.25})$$

$$\frac{\partial^5}{\partial x^3 \partial y^2} = \frac{1}{\Delta x^3 \Delta y^2} \begin{bmatrix} & 1/24 & -1/12 & 0 & 1/12 & -1/24 & \\ 1/8 & -7/6 & 47/24 & 0 & -47/24 & 7/6 & -1/8 \\ -1/4 & 9/4 & -15/4 & 0 & 15/4 & -9/4 & 1/4 \\ 1/8 & -7/6 & 47/24 & 0 & -47/24 & 7/6 & -1/8 \\ & 1/24 & -1/12 & 0 & 1/12 & -1/24 & \end{bmatrix} + O(\chi^4). \quad (\text{B.26})$$

Finally, mixed finite difference approximations for the 49-point (square) stencil are

$$\frac{\partial^2}{\partial x \partial y} = \frac{1}{\Delta x \Delta y} \begin{bmatrix} 1/3600 & -1/400 & 1/80 & 0 & -1/80 & 1/400 & -1/3600 \\ -1/400 & 9/400 & -9/80 & 0 & 9/80 & -9/400 & 1/400 \\ 1/80 & -9/80 & 9/16 & 0 & -9/16 & 9/80 & -1/80 \\ 0 & 0 & 0 & 0 & 0 & 0 & 0 \\ -1/80 & 9/80 & -9/16 & 0 & 9/16 & -9/80 & 1/80 \\ 1/400 & -9/400 & 9/80 & 0 & -9/80 & 9/400 & -1/400 \\ -1/3600 & 1/400 & -1/80 & 0 & 1/80 & -1/400 & 1/3600 \end{bmatrix} + O(\chi^6), \quad (\text{B.27})$$

$$\frac{\partial^3}{\partial x^2 \partial y} = \frac{1}{\Delta x^2 \Delta y} \begin{bmatrix} 1/5400 & 1/400 & -1/40 & 49/1080 & -1/40 & 1/400 & -1/5400 \\ 1/600 & -9/400 & 9/40 & -49/120 & 9/40 & -9/400 & 1/600 \\ -1/120 & 9/80 & -9/8 & 49/24 & -9/8 & 9/80 & -1/120 \\ 0 & 0 & 0 & 0 & 0 & 0 & 0 \\ 1/120 & -9/80 & 9/8 & -49/24 & 9/8 & -9/80 & 1/120 \\ -1/600 & 9/400 & -9/40 & 49/120 & -9/40 & 9/400 & -1/600 \\ -1/5400 & -1/400 & 1/40 & -49/1080 & 1/40 & -1/400 & 1/5400 \end{bmatrix} + O(\chi^6), \quad (\text{B.28})$$

$$\frac{\partial^4}{\partial x^2 \partial y^2} = \frac{1}{\Delta x^2 \Delta y^2} \begin{bmatrix} 1/8100 & -1/600 & 1/60 & -49/1620 & 1/60 & -1/600 & 1/8100 \\ -1/600 & 9/400 & -9/40 & 49/120 & -9/40 & 9/400 & -1/600 \\ 1/60 & -9/40 & 9/4 & -49/12 & 9/4 & -9/40 & 1/60 \\ -49/1620 & 49/120 & -49/12 & 2401/324 & -49/12 & 49/120 & -49/1620 \\ 1/60 & -9/40 & 9/4 & -49/12 & 9/4 & -9/40 & 1/60 \\ -1/600 & 9/400 & -9/40 & 49/120 & -9/40 & 9/400 & -1/600 \\ 1/8100 & -1/600 & 1/60 & -49/1620 & 1/60 & -1/600 & 1/8100 \end{bmatrix} + O(\chi^6), \quad (\text{B.29})$$

$$\frac{\partial^4}{\partial x^3 \partial y} = \frac{1}{\Delta x^3 \Delta y} \begin{bmatrix} -1/480 & 1/60 & -13/480 & 0 & 13/480 & -1/60 & 1/480 \\ 3/160 & -3/20 & 39/160 & 0 & -39/160 & 3/20 & -3/160 \\ -3/32 & 3/4 & -39/32 & 0 & 39/32 & -3/4 & 3/32 \\ 0 & 0 & 0 & 0 & 0 & 0 & 0 \\ 3/32 & -3/4 & 39/32 & 0 & -39/32 & 3/4 & -3/32 \\ -3/160 & 3/20 & -39/160 & 0 & 39/160 & -3/20 & 3/160 \\ 1/480 & -1/60 & 13/480 & 0 & -13/480 & 1/60 & -1/480 \end{bmatrix} + O(\chi^4), \quad (\text{B.30})$$

$$\frac{\partial^5}{\partial x^4 \partial y} = \frac{1}{\Delta x^4 \Delta y} \begin{bmatrix} 1/360 & -1/30 & 13/120 & -7/45 & 13/120 & -1/30 & 1/360 \\ -1/40 & 3/10 & -39/40 & 7/5 & -39/40 & 3/10 & -1/40 \\ 1/8 & -3/2 & 39/8 & -7 & 39/8 & -3/2 & 1/8 \\ 0 & 0 & 0 & 0 & 0 & 0 & 0 \\ -1/8 & 3/2 & -39/8 & 7 & -39/8 & 3/2 & -1/8 \\ 1/40 & -3/10 & 39/40 & -7/5 & 39/40 & -3/10 & 1/40 \\ -1/360 & 1/30 & -13/120 & 7/45 & -13/120 & 1/30 & -1/360 \end{bmatrix} + O(\chi^4), \quad (\text{B.31})$$

$$\frac{\partial^5}{\partial x^3 \partial y^2} = \frac{1}{\Delta x^3 \Delta y^2} \begin{bmatrix} 1/720 & -1/90 & 13/720 & 0 & -13/720 & 1/90 & -1/720 \\ -3/160 & 3/20 & -39/160 & 0 & 39/160 & -3/20 & 3/160 \\ 3/16 & -3/2 & 39/16 & 0 & -39/16 & 3/2 & -3/16 \\ -49/144 & 49/18 & -637/144 & 0 & 637/144 & -49/18 & 49/144 \\ 3/16 & -3/2 & 39/16 & 0 & -39/16 & 3/2 & -3/16 \\ -3/160 & 3/20 & -39/160 & 0 & 39/160 & -3/20 & 3/160 \\ 1/720 & -1/90 & 13/720 & 0 & -13/720 & 1/90 & -1/720 \end{bmatrix} + O(\chi^4). \quad (\text{B.32})$$

Appendix C

Fourier Analysis of Savitzky-Golay Smoothing Filters

This appendix provides details for the standard Fourier analysis of the various Savitzky-Golay smoothing filters in §3.6 (see also §9.3). Note that the method described is similarly valid for the analysis of any operation that constitutes a convolution in a single dimension. Summing the rows (or columns) of a given two-dimensional filter is firstly used to simplify the problem to a single dimension, as described *e.g.* in §3.6. A single application of such a one-dimensional smoothing filter s spanning $2\alpha + 1$ grid points centered about grid point j can be written as

$$f^*(j) = \sum_{q=j-\alpha}^{j+\alpha} s_{q-j} f(q), \quad (\text{C.1})$$

where s_i refers to the coefficient of the smoothing filter at index i , where $-\alpha \leq i \leq \alpha$. Here the $*$ superscript refers to the function value after the smoothing filter is applied on the original discrete function f . This operation can be analyzed in Fourier space simply by inserting the individual Fourier components

$$f(j) \Rightarrow \check{f} e^{ij\theta}, \quad f^*(j) \Rightarrow \check{f}^* e^{ij\theta}, \quad (\text{C.2})$$

where $\theta = 2\pi/N$, with $N = L/\Delta x$ the number of grid points per wavelength, and where \check{f} and \check{f}^* represent the respective Fourier amplitudes. This leads directly to

$$\check{f}^* e^{ij\theta} = \sum_{q=j-\alpha}^{j+\alpha} s_{q-j} \check{f} e^{iq\theta}. \quad (\text{C.3})$$

By arbitrarily setting $j = 0$, dividing both sides by \check{f} , and taking the absolute value, this can be written in terms of the amplification factor $|A|$ as

$$|A| = \left| \frac{\check{f}^*}{\check{f}} \right| = \left| \sum_{q=-\alpha}^{\alpha} s_q e^{iq\theta} \right|, \quad (\text{C.4})$$

which describes the relative amplification of a given mode discretized with N grid points per wavelength resulting from a single application of the filter \mathbf{s} . The resulting expression for a given filter can often be simplified further, however this general form can easily be evaluated *e.g.* in MATLAB[®] or *Mathematica*[™]. Using (C.4) it is straight-forward to produce amplification portraits for the various smoothing filters, *e.g.* as shown in Figure 3.3, simply by varying N .

Note that if the effects of multiple applications are desired, *e.g.* as in Figure 9.3, the value for $|A|$ in (C.4) should simply be raised to the power n_s , the number of successive smoothing applications.

Appendix D

The Jacobian Matrix

This appendix provides a complete description for the computation of the individual components of the Jacobian matrix from (5.27), which is used in the local nonlinear stability analysis in §5.6. Direct differentiation of (5.23)-(5.25) as implied by the elements in (5.27) leads to

$$\frac{\partial}{\partial \eta} \left(\frac{\partial \eta}{\partial t} \right) = -\tilde{U} \frac{\partial}{\partial x} - \tilde{V} \frac{\partial}{\partial y} + 2\tilde{w} \left(\frac{\partial \eta}{\partial x} \frac{\partial}{\partial x} + \frac{\partial \eta}{\partial y} \frac{\partial}{\partial y} \right) + D\nabla^2, \quad (\text{D.1})$$

$$\frac{\partial}{\partial \tilde{U}} \left(\frac{\partial \eta}{\partial t} \right) = -\frac{\partial \eta}{\partial x} + \left(1 + \left(\frac{\partial \eta}{\partial x} \right)^2 + \left(\frac{\partial \eta}{\partial y} \right)^2 \right) \frac{\partial \tilde{w}}{\partial \tilde{U}}, \quad (\text{D.2})$$

$$\frac{\partial}{\partial \tilde{V}} \left(\frac{\partial \eta}{\partial t} \right) = -\frac{\partial \eta}{\partial y} + \left(1 + \left(\frac{\partial \eta}{\partial x} \right)^2 + \left(\frac{\partial \eta}{\partial y} \right)^2 \right) \frac{\partial \tilde{w}}{\partial \tilde{V}}, \quad (\text{D.3})$$

$$\begin{aligned} \frac{\partial}{\partial \eta} \left(\frac{\partial \tilde{U}}{\partial t} \right) &= -g \frac{\partial}{\partial x} + 2\tilde{w} \frac{\partial \tilde{w}}{\partial x} \left(\frac{\partial \eta}{\partial x} \frac{\partial}{\partial x} + \frac{\partial \eta}{\partial y} \frac{\partial}{\partial y} \right) + \\ &\quad \tilde{w}^2 \left(\frac{\partial^2 \eta}{\partial x \partial y} \frac{\partial}{\partial y} + \frac{\partial \eta}{\partial y} \frac{\partial^2}{\partial x \partial y} + \frac{\partial^2 \eta}{\partial x^2} \frac{\partial}{\partial x} + \frac{\partial \eta}{\partial x} \frac{\partial^2}{\partial x^2} \right), \end{aligned} \quad (\text{D.4})$$

$$\begin{aligned} \frac{\partial}{\partial \tilde{U}} \left(\frac{\partial \tilde{U}}{\partial t} \right) &= -\frac{\partial \tilde{U}}{\partial x} - \tilde{U} \frac{\partial}{\partial x} + \left(1 + \left(\frac{\partial \eta}{\partial x} \right)^2 + \left(\frac{\partial \eta}{\partial y} \right)^2 \right) \left(\frac{\partial \tilde{w}}{\partial x} \frac{\partial \tilde{w}}{\partial \tilde{U}} + \tilde{w} \frac{\partial}{\partial \tilde{U}} \left(\frac{\partial \tilde{w}}{\partial x} \right) \right) + \\ &\quad 2\tilde{w} \left(\frac{\partial \eta}{\partial y} \frac{\partial^2 \eta}{\partial x \partial y} + \frac{\partial \eta}{\partial x} \frac{\partial^2 \eta}{\partial x^2} \right) \frac{\partial \tilde{w}}{\partial \tilde{U}} + D\nabla^2, \end{aligned} \quad (\text{D.5})$$

$$\begin{aligned} \frac{\partial}{\partial \tilde{V}} \left(\frac{\partial \tilde{U}}{\partial t} \right) &= -\frac{\partial \tilde{V}}{\partial x} - \tilde{V} \frac{\partial}{\partial x} + \left(1 + \left(\frac{\partial \eta}{\partial x} \right)^2 + \left(\frac{\partial \eta}{\partial y} \right)^2 \right) \left(\frac{\partial \tilde{w}}{\partial x} \frac{\partial \tilde{w}}{\partial \tilde{V}} + \tilde{w} \frac{\partial}{\partial \tilde{V}} \left(\frac{\partial \tilde{w}}{\partial x} \right) \right) + \\ &\quad 2\tilde{w} \left(\frac{\partial \eta}{\partial y} \frac{\partial^2 \eta}{\partial x \partial y} + \frac{\partial \eta}{\partial x} \frac{\partial^2 \eta}{\partial x^2} \right) \frac{\partial \tilde{w}}{\partial \tilde{V}}, \end{aligned} \quad (\text{D.6})$$

$$\begin{aligned} \frac{\partial}{\partial \eta} \left(\frac{\partial \tilde{V}}{\partial t} \right) &= -g \frac{\partial}{\partial y} + 2\tilde{w} \frac{\partial \tilde{w}}{\partial y} \left(\frac{\partial \eta}{\partial x} \frac{\partial}{\partial x} + \frac{\partial \eta}{\partial y} \frac{\partial}{\partial y} \right) + \\ &\quad \tilde{w}^2 \left(\frac{\partial^2 \eta}{\partial y^2} \frac{\partial}{\partial y} + \frac{\partial \eta}{\partial y} \frac{\partial^2}{\partial y^2} + \frac{\partial^2 \eta}{\partial x \partial y} \frac{\partial}{\partial x} + \frac{\partial \eta}{\partial x} \frac{\partial^2}{\partial x \partial y} \right), \end{aligned} \quad (\text{D.7})$$

$$\begin{aligned} \frac{\partial}{\partial \tilde{U}} \left(\frac{\partial \tilde{V}}{\partial t} \right) &= -\frac{\partial \tilde{U}}{\partial y} - \tilde{U} \frac{\partial}{\partial y} + \left(1 + \left(\frac{\partial \eta}{\partial x} \right)^2 + \left(\frac{\partial \eta}{\partial y} \right)^2 \right) \left(\frac{\partial \tilde{w}}{\partial y} \frac{\partial \tilde{w}}{\partial \tilde{U}} + \tilde{w} \frac{\partial}{\partial \tilde{U}} \left(\frac{\partial \tilde{w}}{\partial y} \right) \right) + \\ &\quad 2\tilde{w} \left(\frac{\partial \eta}{\partial y} \frac{\partial^2 \eta}{\partial y^2} + \frac{\partial \eta}{\partial x} \frac{\partial^2 \eta}{\partial x \partial y} \right) \frac{\partial \tilde{w}}{\partial \tilde{U}}, \end{aligned} \quad (\text{D.8})$$

$$\begin{aligned} \frac{\partial}{\partial \tilde{V}} \left(\frac{\partial \tilde{V}}{\partial t} \right) &= -\frac{\partial \tilde{V}}{\partial y} - \tilde{V} \frac{\partial}{\partial y} + \left(1 + \left(\frac{\partial \eta}{\partial x} \right)^2 + \left(\frac{\partial \eta}{\partial y} \right)^2 \right) \left(\frac{\partial \tilde{w}}{\partial y} \frac{\partial \tilde{w}}{\partial \tilde{V}} + \tilde{w} \frac{\partial}{\partial \tilde{V}} \left(\frac{\partial \tilde{w}}{\partial y} \right) \right) + \\ &\quad 2\tilde{w} \left(\frac{\partial \eta}{\partial y} \frac{\partial^2 \eta}{\partial y^2} + \frac{\partial \eta}{\partial x} \frac{\partial^2 \eta}{\partial x \partial y} \right) \frac{\partial \tilde{w}}{\partial \tilde{V}} + D\nabla^2, \end{aligned} \quad (\text{D.9})$$

where (similar to §5.5)

$$\tilde{w} = \mathcal{A}_1 \mathcal{Z}_{31} \tilde{U} + \mathcal{A}_1 \mathcal{Z}_{32} \tilde{V} - \mathcal{B}_{11} \mathcal{Z}_{11} \tilde{U} - \mathcal{B}_{11} \mathcal{Z}_{12} \tilde{V} - \mathcal{B}_{12} \mathcal{Z}_{21} \tilde{U} - \mathcal{B}_{12} \mathcal{Z}_{22} \tilde{V}, \quad (\text{D.10})$$

$$\frac{\partial \tilde{w}}{\partial \tilde{U}} = \mathcal{A}_1 \mathcal{Z}_{31} - \mathcal{B}_{11} \mathcal{Z}_{11} - \mathcal{B}_{12} \mathcal{Z}_{21}, \quad (\text{D.11})$$

$$\frac{\partial \tilde{w}}{\partial \tilde{V}} = \mathcal{A}_1 \mathcal{Z}_{32} - \mathcal{B}_{11} \mathcal{Z}_{12} - \mathcal{B}_{12} \mathcal{Z}_{22}. \quad (\text{D.12})$$

Note that while η is included (via the operators \mathcal{A}_i , \mathcal{B}_i , and \mathcal{Z}_i) in the local determination for \tilde{w} in (D.10), there are formally $\frac{\partial \tilde{w}}{\partial \eta}$ terms missing in (D.1), (D.4), and (D.7). The neglect of these terms is justified by the weak dependence of the operators on η (particularly in deep water), and by the extreme complexity of doing otherwise.

Finally, it is again implied that to form the actual Jacobian matrix \mathbf{J} the continuous operators specified in this appendix must be considered respectively in their discrete forms.

Appendix E

Stability Analysis of Finite Amplitude Deep Water Waves

This appendix describes the stability analysis of plane finite amplitude deep water waves to three-dimensional periodic perturbations. The analysis follows closely the original work of McLean (1982*b*) (note also the similar work of McLean, 1982*a*, for finite depth gravity waves). Results from this analysis can be found throughout Chapter 8, especially in Tables 8.3 and 8.4 from §8.4.3. The analysis is also used in §8.4.4.

E.1 Governing Equations

Consider surface gravity waves on an inviscid, irrotational, incompressible fluid of great depth. In a frame of reference moving with constant speed c (taken to be the speed of the unperturbed wave $\bar{\eta}$, here assumed to be periodic in x and plane in y), the basic equations are (McLean, 1982*b*)

$$\left. \begin{aligned} \nabla^2 \phi &= 0, & -\infty < z < \eta \\ \phi &\sim -cx, & z \rightarrow -\infty, \end{aligned} \right\} \quad (\text{E.1})$$

$$\left. \begin{aligned} \phi_t + \eta + \frac{1}{2} (\phi_x^2 + \phi_y^2 + \phi_z^2) &= \frac{1}{2} c^2 \\ \eta_t + \phi_x \eta_x + \phi_y \eta_y - \phi_z &= 0 \end{aligned} \right\} \quad z = \eta. \quad (\text{E.2})$$

Following McLean (1982*b*), without loss of generality, we have here taken the gravitational acceleration g to be unity. We consider the stability of two-dimensional steady waves to an

infinitesimal three-dimensional disturbance. Let

$$\eta = \bar{\eta} + \epsilon\eta', \quad \phi = \bar{\phi} + \epsilon\phi', \quad (\text{E.3})$$

where it is assumed that $\epsilon \ll 1$. Inserting (E.3) into (E.2) and neglecting terms of $O(\epsilon^2)$ gives

$$\left. \begin{aligned} \bar{\eta} + \frac{1}{2}(\bar{\phi}_x^2 + \frac{1}{2}\bar{\phi}_z^2) + \epsilon(\phi'_t + \eta' + \bar{\phi}_x\phi'_x + \bar{\phi}_z\phi'_z) &= \frac{1}{2}c^2 \\ \bar{\phi}_x\bar{\eta}_x - \bar{\phi}_z + \epsilon(\eta'_t + \bar{\phi}_x\eta'_x + \phi'_x\bar{\eta}_x - \phi'_z) &= 0 \end{aligned} \right\} z = \eta. \quad (\text{E.4})$$

We wish to express the equations at $z = \bar{\eta}$ rather than at $z = \eta$. This can be achieved via the use of the following Taylor series expansions

$$\bar{\phi}_z|_{z=\eta} = \bar{\phi}_z + \epsilon\eta'\bar{\phi}_{zz}|_{z=\bar{\eta}} + O(\epsilon^2), \quad \bar{\phi}_x|_{z=\eta} = \bar{\phi}_x + \epsilon\eta'\bar{\phi}_{xz}|_{z=\bar{\eta}} + O(\epsilon^2). \quad (\text{E.5})$$

Inserting (E.5) into (E.4), and collecting terms of $O(\epsilon)$ gives

$$\left. \begin{aligned} \phi'_t + \eta' + \bar{\phi}_x\phi'_x + \bar{\phi}_z\phi'_z + (\bar{\phi}_x\bar{\phi}_{xz} + \bar{\phi}_z\bar{\phi}_{zz}) &= 0 \\ \eta'_t + \bar{\phi}_x\eta'_x + \phi'_x\bar{\eta}_x + (\bar{\phi}_{xz}\bar{\eta}_x - \bar{\phi}_{zz})\eta' - \phi'_z &= 0 \end{aligned} \right\} z = \bar{\eta}. \quad (\text{E.6})$$

Similarly, inserting (E.3) into (E.1) and collecting the $O(\epsilon)$ term leads directly to

$$\nabla^2\phi' = 0, \quad -\infty < z < \bar{\eta}, \quad (\text{E.7})$$

which is again just the Laplace equation for ϕ' .

E.2 The Eigenvalue Problem

We will now describe the formulation of an eigenvalue problem for analyzing the stability of the unperturbed wave $\bar{\eta}$ subject to the infinitesimal perturbation η' . We look for non-trivial solutions to (E.6) and (E.7) of the form

$$\eta' = e^{-i\sigma t} e^{i(px+qy)} \sum_{j=-\infty}^{\infty} a_j e^{ijx}, \quad (\text{E.8})$$

$$\phi' = e^{-i\sigma t} e^{i(px+qy)} \sum_{j=-\infty}^{\infty} b_j e^{ijx} e^{\gamma z}, \quad (\text{E.9})$$

where p and q are arbitrary real numbers and $\gamma = \sqrt{(p+j)^2 + q^2}$. The physical disturbance corresponds to the real part of (E.8) and (E.9). Substituting (E.8) and (E.9) into (E.6) gives

$$(1 + \bar{\phi}_x \bar{\phi}_{xz} + \bar{\phi}_z \bar{\phi}_{zz}) \sum_{j=-\infty}^{\infty} a_j e^{ijx} + \sum_{j=-\infty}^{\infty} (\rho \bar{\phi}_x + \gamma \bar{\phi}_z) \cdot b_j e^{ijx} e^{\gamma \bar{\eta}} = i\sigma \sum_{j=-\infty}^{\infty} b_j e^{ijx} e^{\gamma \bar{\eta}}, \quad (\text{E.10})$$

$$\sum_{j=-\infty}^{\infty} (\bar{\phi}_{xz} \bar{\eta}_x - \bar{\phi}_{zz} + \rho \bar{\phi}_x) a_j e^{ijx} + \sum_{j=-\infty}^{\infty} (\bar{\eta}_x - \gamma) \cdot b_j e^{ijx} e^{\gamma \bar{\eta}} = i\sigma \sum_{j=-\infty}^{\infty} a_j e^{ijx}, \quad (\text{E.11})$$

where $\rho = i(p+j)$. Note that the left hand sides of (E.10) and (E.11) arise from the spatial derivative terms in (E.6), while the right hand sides arise from the time derivative terms.

The analysis proceeds by firstly calculating the unperturbed wave $\bar{\eta}$, $\bar{\phi}$, which is assumed here to have a wavenumber k_0 of unity, with wavelength $L = 2\pi$. Truncating (E.8) and (E.9) at M modes, and applying (E.10) and (E.11) at $2M+1$ equidistant grid points within $0 \leq x \leq L$ then yields a generalized eigenvalue problem of order $4M+2$ of the form

$$(\mathbf{A} - \sigma \mathbf{B}) \mathbf{u} = 0, \quad (\text{E.12})$$

where the eigenvector is $\mathbf{u} = \{a_{-M}, \dots, a_M, b_{-M}, \dots, b_M\}$. The present analysis is made using *Mathematica*TM, which unfortunately does not have a generalized eigenvalue solver. Therefore (E.12) is first converted to the standard eigenvalue problem

$$(\mathbf{Z} - \mathbf{I}\sigma) \mathbf{u} = 0, \quad (\text{E.13})$$

where $\mathbf{Z} = \mathbf{B}^{-1} \mathbf{A}$, before solving.

E.3 Analysis of Linear Waves

For a linear carrier wave $\bar{\eta} = 0$, $\bar{\phi} = -x$, and $c = 1$. The system comprised of (E.10) and (E.11) can be written in the form (E.12) with

$$\mathbf{A} = \begin{bmatrix} e^{ijx} & -\rho e^{ijx} \\ -\rho e^{ijx} & -j - p \end{bmatrix}, \quad \mathbf{B} = \begin{bmatrix} 0 & i e^{ijx} \\ i e^{ijx} & 0 \end{bmatrix}, \quad (\text{E.14})$$

giving

$$\mathbf{Z} = \mathbf{B}^{-1} \mathbf{A} = \begin{bmatrix} -2 - p & i\gamma \\ -i & -2 - p \end{bmatrix}. \quad (\text{E.15})$$

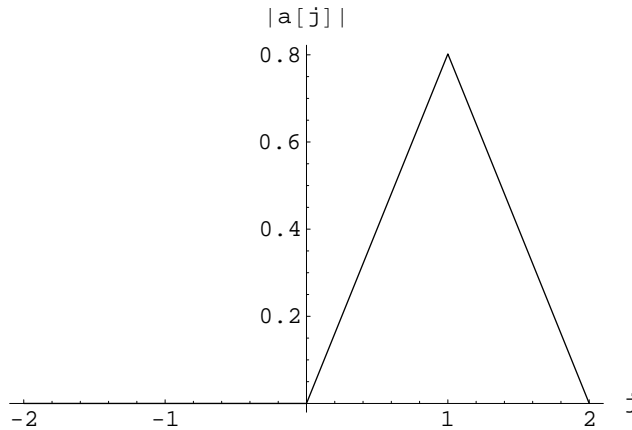


Figure E.1: An example of an eigenvector corresponding to a stable eigenvalue from an analysis of a linear (infinitesimal) unperturbed wave.

This gives the eigenvalues

$$\sigma_j = -(p + j) \pm ((p + j)^2 + q^2)^{0.25}, \quad (\text{E.16})$$

for each integer j . These correspond to infinitesimal modes with wavenumber $\mathbf{k}' = (k'_x, k'_y) = (p + j, q)$ and frequencies $\sigma_j = -k'_x \pm |\mathbf{k}'|^{0.5}$. This is in fact just the (deep water) linear dispersion relation in a frame of reference moving with speed $c = \sqrt{g/k} = 1$, which should be expected.

We may use this linear result as an initial test for the numerical eigenvalue solver for a specific value of p and q . We set the discrete free surface to be flat *i.e.* $\bar{\eta} = 0$ with $\bar{\phi} = -x$ everywhere. As an example, with $p = 0.5$, $q = 1$, and $M = 2$ the computed $j = 1$ eigenvalues are $\sigma = \{-2.8427, -0.1573\}$, in perfect agreement with (E.16). As the eigenvalues are real, the linear carrier wave is stable to this perturbation. The absolute values of the a_j coefficients from the eigenvector corresponding to the second eigenvalue is given in Figure E.1. As should be expected, this has a peak at $j = 1$, with all other components equal to zero. This indicates that there is no interaction between the various modes, which should also be expected in the linear case.

E.4 Analysis of Finite Amplitude Waves

We will now describe the analysis of finite amplitude steady waves. For the unperturbed wave we use the stream function solution of Fenton (1988), with $kh = 4\pi$ (*i.e.* very deep), and with Stokes' drift velocity $c_s = 0$. The solution is typically truncated at M Fourier modes, matching the earlier truncations of (E.8) and (E.9). Once the matrices are constructed and the eigenvalues computed, we can restrict our attention to those eigenvalues having non-zero imaginary part, as these correspond to a physical instability. This can readily

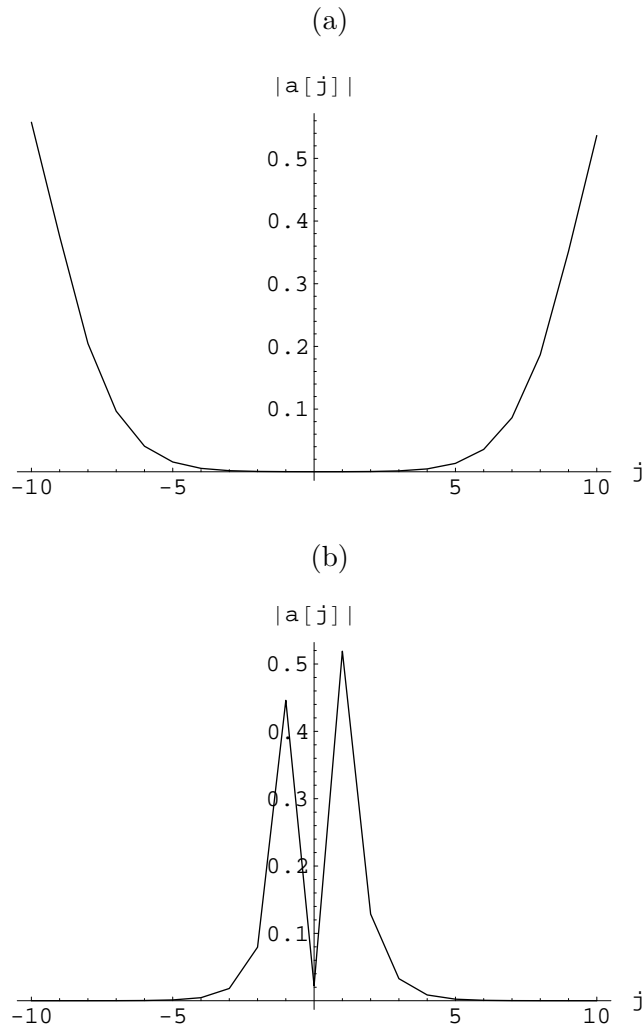


Figure E.2: Computed class I eigenvector components ($H/L = 0.064$, $M = 10$, $p = 0.32$, $q = 0$) corresponding to (a) an unconverged eigenvalue and (b) a converged class I eigenvalue.

be seen *e.g.* by considering the assumed form of the perturbations (E.8) and (E.9). The analysis is more complicated than simply choosing the ‘most unstable’ eigenvalue (*i.e.* with the largest imaginary part), however. The eigenvector must also be used to interpret the physical significance of each eigenvalue.

As an example, we consider a case with $H/L = 0.064$, $M = 10$, $p = 0.32$, and $q = 0$ (hence these perturbations are two-dimensional). The analysis yields two unstable eigenvalues: $-0.207 + 3.504i$ and $-0.146 + 0.0134i$, with the first eigenvalue having a significantly larger imaginary part than the second. Eigenvector components for each case are plotted in Figure E.2. In Figure E.2 (a) eigenvector components corresponding to the first eigenvalue are shown. Clearly this does not represent a converging expansion, as the expansion coefficients a_j are actually growing as $|j|$ becomes larger. Furthermore, the peaks of the shown eigenvector are at $j = \pm 10$, which suggests an interaction between modes having

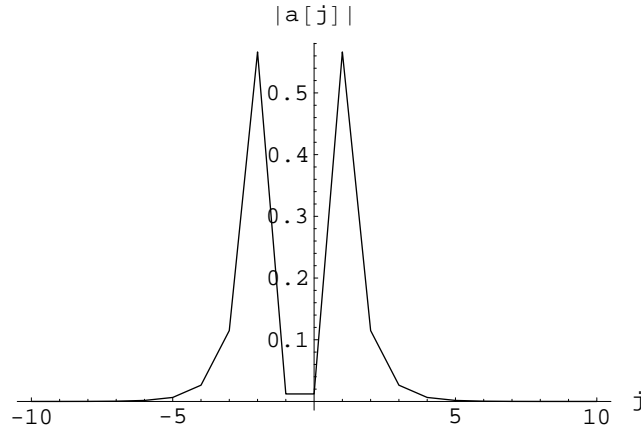


Figure E.3: Converged class II eigenvector components from a case with $H/L = 0.064$, $M = 10$, $p = 0.5$, and $q = 1.54$.

wavenumbers $\mathbf{k}'_1 = (p + 10, q)$ and $\mathbf{k}_2 = (10 - p, -q)$ *i.e.* large wavenumbers, implying poor resolution. Hence the first eigenvalue is physically meaningless, and can be discarded. Alternatively, the eigenvector components in Figure E.2 (b) indicate a converged expansion, thus the second eigenvalue is physically significant. The eigenvector has peaks at $j = \pm 1$, indicating a resonant interaction involving wavenumbers $\mathbf{k}'_1 = (p + 1, q)$ and $\mathbf{k}'_2 = (1 - p, -q)$. Seen in the fixed frame of reference, and requiring the angular frequencies ω_i to be positive, the resonance conditions may generally be written as

$$n\mathbf{k}_0 = \mathbf{k}'_1 + \mathbf{k}'_2, \quad n\omega_0 = \omega'_1 + \omega'_2, \quad (\text{E.17})$$

which is a generalization of (8.8), corresponding to a $(n + 2)$ -wave resonant interaction. For this example (E.17) is clearly satisfied with $n = 2$. Hence this corresponds to a four-wave resonant interaction, and is thus a typical example of a class I Benjamin & Feir (1967)-type instability. Note that McLean (1982*b*) suggests that the last eigenvector component can be used to determine the convergence of the detected instabilities, which we find is a useful strategy for narrowing the investigation to those eigenvalues which are physically relevant.

As a demonstration of a class II instability we will consider a case with $H/L = 0.064$, $M = 10$, $p = 0.5$, and $q = 1.54$. Note that with $q \neq 0$, the perturbation is now three-dimensional. This also yields two unstable eigenvalues, the first of which is again clearly unconverged, and will not be considered for brevity. The second is $\sigma = 0.00531i$, with corresponding eigenvector components shown in Figure E.3. This has peaks at $j = 1$ and -2 , indicating a resonant interaction between wavenumbers $\mathbf{k}'_1 = (p + 1, q)$ and $\mathbf{k}'_2 = (2 - p, -q)$. This clearly satisfies (E.17) with $n = 3$, corresponding to a five-wave resonant interaction. This is a typical example of a class II instability, responsible for the various crescent wave patterns studied throughout Chapter 8. Note that as the eigenvalue in this example is purely imaginary, this represents modes that are bound to the unperturbed wave, and would therefore result in a phase-locked L2 crescent pattern. Note that for $p \neq 0.5$ this is generally not the case.

Finally, recall that in the present analysis we have assumed $k_0 = g = 1$, following McLean (1982*b*). From the deep water linear dispersion relation this yields the angular frequency

$\omega = \sqrt{gk} = 1$, on which the perturbation frequencies σ are relative. Equivalently, the unstable perturbation frequencies σ from this analysis may be considered as dimensionless, requiring a scaling of \sqrt{gk} (using the actual dimensional values) to gain physical relevance, which is the view taken throughout Chapter 8 for consistency.

Appendix F

Linear Accuracy Analysis

This appendix provides a Fourier-based accuracy analysis of the discrete linearized flat-bottom Boussinesq formulation in a single horizontal dimension. As shown in §5.4, the system can be expressed in the form

$$\frac{\partial}{\partial t} \begin{bmatrix} \eta \\ u_0 \end{bmatrix} = \begin{bmatrix} 0 & \frac{\mathcal{A}_1 \mathcal{A}_{01} + \mathcal{B}_0 \mathcal{B}_{11}}{\mathcal{A}_{01} \mathcal{B}_{11} - \mathcal{A}_1 \mathcal{B}_0} \\ \mathcal{D}_1 & 0 \end{bmatrix} \begin{bmatrix} \eta \\ u_0 \end{bmatrix}, \quad (\text{F.1})$$

where $\mathcal{D}_1 = -g \frac{\partial}{\partial x}$, and the $\mathcal{A}_i, \mathcal{B}_i$ operators are one-dimensional representations of those given in Appendix A. The eigenvalues of this system are symbolically

$$\lambda = \pm \sqrt{\frac{\mathcal{D}_1 (\mathcal{A}_{01} \mathcal{A}_1 + \mathcal{B}_0 \mathcal{B}_{11})}{\mathcal{A}_{01} \mathcal{B}_{11} - \mathcal{A}_1 \mathcal{B}_0}}. \quad (\text{F.2})$$

The analysis follows closely that from §5.4, and proceeds by replacing each of the continuous derivative operators in (F.2) with their discrete Fourier representations. For a given physical water depth kh and spatial resolution $N = L/\Delta x$ (*i.e.* the number of grid points per wavelength) the corresponding eigenvalues can be computed, which are again purely imaginary conjugates for the centered spatial discretizations considered in this work. After amplifying the eigenvalues by the chosen time step Δt , we can insert these into the polynomial

$$\rho(\Delta t \lambda) \equiv 1 + \Delta t \lambda + \frac{(\Delta t \lambda)^2}{2} + \frac{(\Delta t \lambda)^3}{6} + \frac{(\Delta t \lambda)^4}{24}, \quad (\text{F.3})$$

which from (5.3) defines the evolution in the eigenvector basis for a single time step with the explicit fourth-order, four stage Runge-Kutta method described in §3.4. This will result in a relative amplification, given by $|\rho(\Delta t \lambda)|$, as well as a change in phase, given by $\phi = \arg(\rho(\Delta t \lambda))$. Note that for numerical stability we formally require that $|\rho(\Delta t \lambda)| \leq 1$. We here define the amplification factor A as the relative change in amplitude over a period, which gives

$$A \equiv |\rho(\Delta t \lambda)|^{N_t}, \quad N_t = \frac{T}{\Delta t}. \quad (\text{F.4})$$

A full period, of course, involves a rotation of 2π radians, hence the actual numerical period is given by $T_{num} = 2\pi\Delta t/\phi$. This corresponds to a mode having wavelength $L = N\Delta x$, thus the numerical celerity is

$$c_{num} \equiv \frac{L}{T_{num}} = \frac{\Delta x\phi}{\theta\Delta t}, \quad \theta = \frac{2\pi}{N}. \quad (\text{F.5})$$

The relative phase speed Q then simplifies to

$$Q \equiv \frac{c_{num}}{c} = \frac{\Delta x\phi}{\theta\Delta tc} = \frac{\phi}{\theta Cr}, \quad (\text{F.6})$$

where c is the embedded celerity of the Boussinesq formulation, as indicated *e.g.* in (5.12), and $Cr = \frac{c\Delta t}{\Delta x}$ is the Courant number. Hence, for a given Courant number Cr , dimensionless depth kh , and spatial resolution N it is possible to determine both A and Q . In this appendix finite difference approximations are considered with each derivative accurate to second order, along with stencils having seven and nine points. For the seven- and nine-point stencils, each approximation again has the maximum possible formal accuracy for the given number of points, as before.

A number of so-called *amplification* and *phase portraits* are shown in Figure F.1, which demonstrate the general effects of varying the spatial finite difference approximations, the Courant number Cr , and depth kh . The top pair demonstrates the effects of varying the finite difference stencil with constant $Cr = 0.5$ and $kh = 6$. From the amplification portrait (left) it is seen that the larger stencils generally result in more dissipation for poorly resolved modes, after-which each of the discretizations converge reasonably similarly. The dispersion portrait (right) shows much more dramatic differences between the strictly second-order approximations and the higher-order stencils. Clearly, the larger stencils are much more adept in achieving high dispersive accuracy. This is consistent with the linear standing wave results shown *e.g.* in §6.2, Figure 6.2, which show little dissipation, but large dispersive errors *e.g.* with the strictly second-order scheme (*i.e.* the period is visually off). The differences between the seven- and nine-point stencils do not appear to be so pronounced from Figure F.1, and consequently the seven-point stencil is used on the remaining figures. It is also interesting to note that with these schemes the Nyquist mode (with $N = 2$) is always undamped, but has $c_{num} = 0$ (*i.e.* it remains stationary!).

The second (middle) pair in Figure F.1 demonstrates the effects of variable Cr with constant $kh = 6$. Here the use of larger Cr expectedly results, rather generally, in larger dissipation of the wavenumber spectrum. There are also differences in the relative phase speed Q , with lower Cr resulting in noticeably better accuracy for a given N .

The third (bottom) pair in Figure F.1 demonstrates the effects of variable kh with a constant $Cr = 0.5$. The accuracy is (somewhat surprisingly) rather insensitive to these depth variations. The most notable difference is apparent for the largest depth considered ($kh = 20$), where the relative celerity is seen to converge more slowly, though the error is clearly converged to a relative accuracy better than 0.01 in the shown dispersion portrait. This is

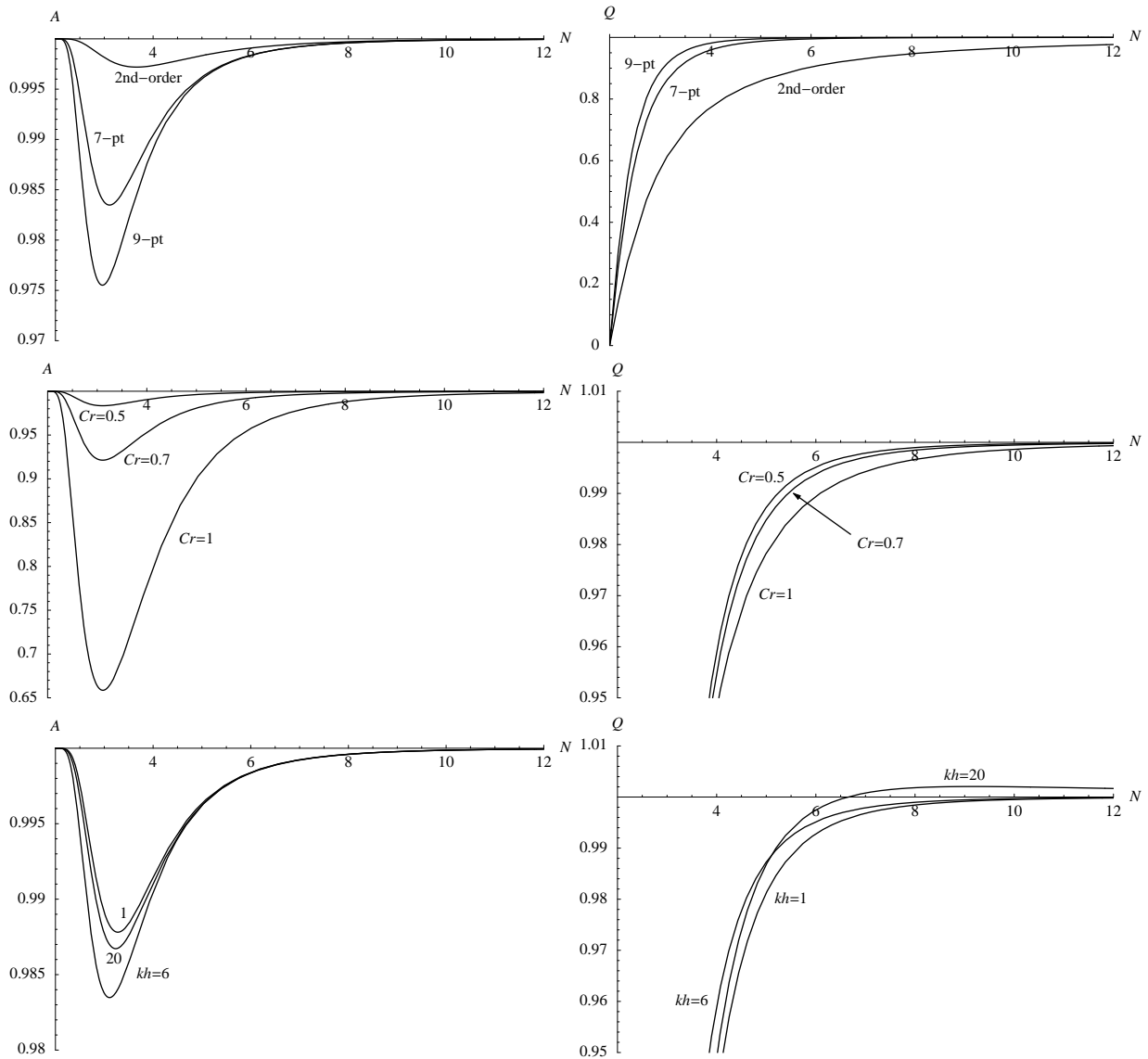


Figure F.1: Amplification (left) and phase portraits (right) for (top) variable finite difference approximations with $Cr = 0.5$, $kh = 6$; (middle) variable Cr with seven-point approximations and $kh = 6$; and (bottom) variable kh with seven-point approximations and $Cr = 0.5$.

therefore not of great concern, as the embedded dispersive properties of the Boussinesq formulation likewise become rather inaccurate in this range (*e.g.* at $kh = 20$ the relative embedded dispersive error is $(1 - c/c_{Stokes}) \approx 0.003$, while $kh = 25$ gives roughly 0.008). The results in these figures of course vary somewhat depending on the precise combination of parameters used, however the trends seen throughout Figure F.1 are representative and remain consistent.

To present results from this analysis in another light, Table F.1 provides the resolution N required to give amplitude/dispersive errors below a given error threshold ϵ , which should

Table F.1: Number of grid points per wavelength $N = L/\Delta x$ necessary to achieve a desired relative error tolerance ϵ with respect to dissipation and dispersion for two values of Cr with $kh = 6$.

Cr	ϵ	Dissipation			Dispersion		
		2nd-order	7-pt	9-pt	2nd-order	7-pt	9-pt
0.5	0.01	2	3.9	4.1	18.2	5.2	4.4
	0.001	5.8	6.6	6.6	57.5	8.0	6.4
	0.0001	10.2	10.6	10.6	182	12.6	9.9
1.0	0.01	7.7	8.3	8.3	18.3	6.1	5.5
	0.001	13.0	13.3	13.3	57.5	10.8	10.4
	0.0001	20.9	21.1	21.1	182	19.2	18.8

serve as a useful guide for discretizing various cases. The results use constant $kh = 6$, however results *e.g.* with $kh = 12$ have been found to be very similar, consistent with expectations from Figure F.1. Note that within the field of coastal engineering it is standard practice to use the (three-digit) approximation $g = 9.81 \text{ m/s}^2$, rather than *e.g.* the more precise worldwide-averaged value $g = 9.80665 \text{ m/s}^2$ (local values may deviate even more). Hence the modeled wave celerity is typically only accurate within the relative bound $(1 - \sqrt{9.80665/9.81}) \approx 0.0002$ due to inherent uncertainties/inaccuracies in the assumed gravitational acceleration g . This threshold then serves as a lower limit for the relative dispersive error which can justifiably be sought from a practical perspective. (This argument is, of course, moot in the non-dimensional sense.) In Table F.1 relative accuracy down to $\epsilon = 0.0001$ is considered, which in any event is highly accurate, corresponding *e.g.* to a 1% phase error after 100 periods. This table again demonstrates the significant improvement with the seven-point stencil over the strictly second-order discretization. The additional improvements with the nine-point stencil are again rather modest, and would not appear to justify its added computational expense (and other potential complexities). The spatial discretizations used throughout this thesis therefore seem most appropriate.

Table F.1 also suggests that lowering Cr (*i.e.* reducing the time step Δt) can be effective in reducing the spatial resolution required for a desired accuracy, which would in turn lead to significant savings in terms of the required storage. Recall that throughout much of this thesis $Cr = 1$ has been used. This is further demonstrated in Figure F.2, which shows the relative dissipative error $(1 - A)$ for seven-point discretizations versus the spatial resolution N for Courant numbers ranging within $0.25 \leq Cr \leq 1.5$. Analysis has shown that the amplification error is practically independent of the depth kh , thus this figure may be globally used to estimate the level of dissipation.

Finally, the relative dispersive error $|1 - Q|$ for spatial resolutions $N = 10, 20,$ and 40 is shown as a function of kh for $Cr = 0.5$ and 1.0 in Figure F.3. Also shown is the relative embedded dispersive error of the Boussinesq formulation with respect to Stoke's first-order theory. As already discussed, this curve is relevant since even a perfectly converged numerical

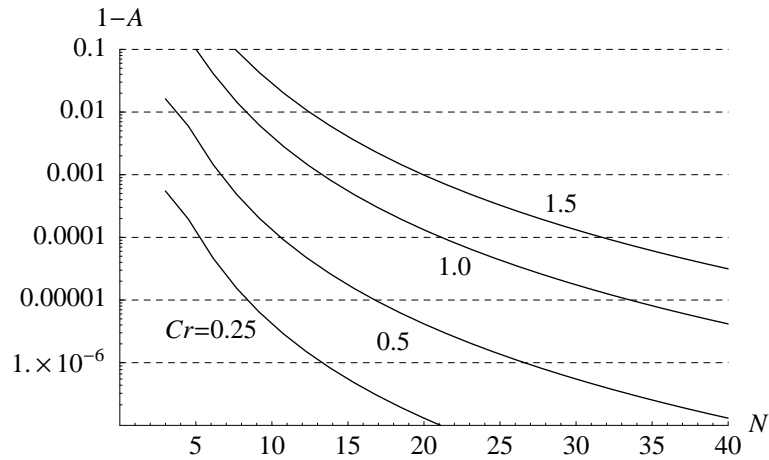


Figure F.2: Relative amplitude error ($1 - A$) for seven-point discretizations versus the spatial resolution N for various Courant number Cr .

model will be no more accurate physically than the underlying system of PDEs on which it is based. It should be noted that the poles in the curves in Figure F.3 correspond to locations where the numerical celerity transitions from being under to over estimated. Thus, for a certain resolution N and depth kh , the numerical scheme will in fact provide the *exact* embedded celerity, which has been confirmed directly through numerical simulations. Generally speaking, the discretizations hold their accuracy surprisingly well versus increases in kh , with a resolution of $N = 20$ seeming to provide acceptable accuracy for most practical circumstances.

The accuracy analysis presented in this appendix should allow for intelligent discretizations to be made with the Boussinesq model, while also generally confirming the adequacy of those used throughout this thesis.

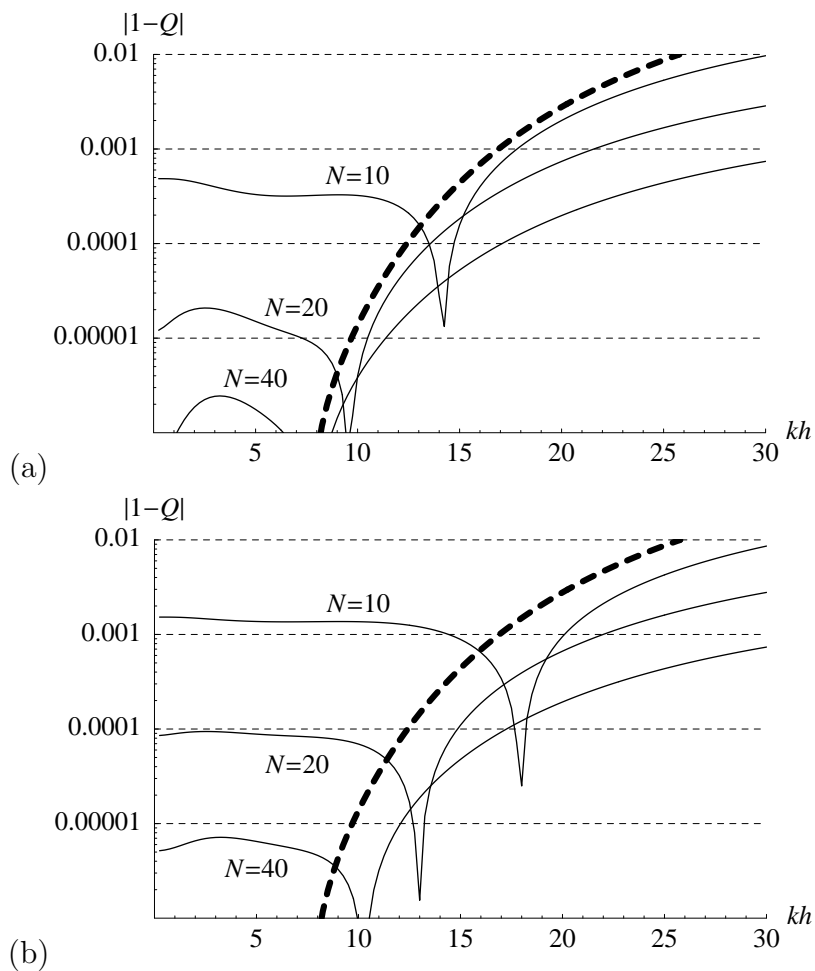


Figure F.3: Relative dispersive error $|1 - Q|$ for seven-point discretizations versus kh for resolutions $N = 10, 20,$ and 40 ; with (a) $Cr = 0.5$ and (b) $Cr = 1.0$. Also shown (bold dashed lines) is the embedded relative dispersive error of the Boussinesq formulation (with respect to Stoke's first-order theory).

PhD Theses
Department of Naval Architecture and Offshore Engineering
Technical University of Denmark · Kgs. Lyngby

- 1961 **Strøm-Tejsen, J.**
Damage Stability Calculations on the Computer DASK.
- 1963 **Silovic, V.**
A Five Hole Spherical Pilot Tube for three Dimensional Wake Measurements.
- 1964 **Chomchuenchit, V.**
Determination of the Weight Distribution of Ship Models.
- 1965 **Chislett, M.S.**
A Planar Motion Mechanism.
- 1965 **Nicordhanon, P.**
A Phase Changer in the HyA Planar Motion Mechanism and Calculation of Phase Angle.
- 1966 **Jensen, B.**
Anvendelse af statistiske metoder til kontrol af forskellige eksisterende tilnærmelsesformler og udarbejdelse af nye til bestemmelse af skibes tonnage og stabilitet.
- 1968 **Aage, C.**
Eksperimentel og beregningsmæssig bestemmelse af vindkræfter på skibe.
- 1972 **Prytz, K.**
Datamatorienterede studier af planende bådes fremdrivningsforhold.
- 1977 **Hee, J.M.**
Store sideportes indflydelse på langskibs styrke.
- 1977 **Madsen, N.F.**
Vibrations in Ships.
- 1978 **Andersen, P.**
Bølgeinducerede bevægelser og belastninger for skib på lægt vand.
- 1978 **Römeling, J.U.**
Buling af afstivede pladepaneller.
- 1978 **Sørensen, H.H.**
Sammenkobling af rotations-symmetriske og generelle tre-dimensionale konstruktioner i elementmetode-beregninger.
- 1980 **Fabian, O.**
Elastic-Plastic Collapse of Long Tubes under Combined Bending and Pressure Load.

- 1980 **Petersen, M.J.**
Ship Collisions.
- 1981 **Gong, J.**
A Rational Approach to Automatic Design of Ship Sections.
- 1982 **Nielsen, K.**
Bølgeenergimaskiner.
- 1984 **Nielsen, N.J.R.**
Structural Optimization of Ship Structures.
- 1984 **Liebst, J.**
Torsion of Container Ships.
- 1985 **Gjersøe-Fog, N.**
Mathematical Definition of Ship Hull Surfaces using B-splines.
- 1985 **Jensen, P.S.**
Stationære skibsbølger.
- 1986 **Nedergaard, H.**
Collapse of Offshore Platforms.
- 1986 **Yan, J.-Q.**
3-D Analysis of Pipelines during Laying.
- 1987 **Holt-Madsen, A.**
A Quadratic Theory for the Fatigue Life Estimation of Offshore Structures.
- 1989 **Andersen, S.V.**
Numerical Treatment of the Design-Analysis Problem of Ship Propellers using Vortex Lattice Methods.
- 1989 **Rasmussen, J.**
Structural Design of Sandwich Structures.
- 1990 **Baatrup, J.**
Structural Analysis of Marine Structures.
- 1990 **Wedel-Heinen, J.**
Vibration Analysis of Imperfect Elements in Marine Structures.
- 1991 **Almlund, J.**
Life Cycle Model for Offshore Installations for Use in Prospect Evaluation.
- 1991 **Back-Pedersen, A.**
Analysis of Slender Marine Structures.

-
- 1992 **Bendiksen, E.**
Hull Girder Collapse.
- 1992 **Petersen, J.B.**
Non-Linear Strip Theories for Ship Response in Waves.
- 1992 **Schalck, S.**
Ship Design Using B-spline Patches.
- 1993 **Kierkegaard, H.**
Ship Collisions with Icebergs.
- 1994 **Pedersen, B.**
A Free-Surface Analysis of a Two-Dimensional Moving Surface-Piercing Body.
- 1994 **Hansen, P.F.**
Reliability Analysis of a Midship Section.
- 1994 **Michelsen, J.**
A Free-Form Geometric Modelling Approach with Ship Design Applications.
- 1995 **Hansen, A.M.**
Reliability Methods for the Longitudinal Strength of Ships.
- 1995 **Branner, K.**
Capacity and Lifetime of Foam Core Sandwich Structures.
- 1995 **Schack, C.**
Skrogudvikling af hurtiggående færger med henblik på sødygtighed og lav modstand.
- 1997 **Simonsen, B.C.**
Mechanics of Ship Grounding.
- 1997 **Olesen, N.A.**
Turbulent Flow past Ship Hulls.
- 1997 **Riber, H.J.**
Response Analysis of Dynamically Loaded Composite Panels.
- 1998 **Andersen, M.R.**
Fatigue Crack Initiation and Growth in Ship Structures.
- 1998 **Nielsen, L.P.**
Structural Capacity of the Hull Girder.
- 1999 **Zhang, S.**
The Mechanics of Ship Collisions.
- 1999 **Birk-Sørensen, M.**
Simulation of Welding Distortions of Ship Sections.

- 1999 **Jensen, K.**
Analysis and Documentation of Ancient Ships.
- 2000 **Wang, Z.**
Hydroelastic Analysis of High-Speed Ships.
- 2000 **Petersen, T.**
Wave Load Prediction—a Design Tool.
- 2000 **Banke, L.**
Flexible Pipe End Fitting.
- 2000 **Simonsen, C.D.**
Rudder, Propeller and Hull Interaction by RANS.
- 2000 **Clausen, H.B.**
Plate Forming by Line Heating.
- 2000 **Krishnaswamy, P.**
Flow Modelling for Partially Cavitating Hydrofoils.
- 2000 **Andersen, L.F.**
Residual Stresses and Deformations in Steel Structures.
- 2000 **Friis-Hansen, A.**
Bayesian Networks as a Decision Support Tool in Marine Applications.

PhD Theses
Maritime Engineering · Department of Mechanical Engineering
Technical University of Denmark · Kgs. Lyngby

- 2001 **Lützen, M.**
Ship Collision Damage.
- 2001 **Olsen, A.S.**
Optimisation of Propellers Using the Vortex-Lattice Method.
- 2002 **Rüdinger, F.**
Modelling and Estimation of Damping in Non-linear Random Vibration.
- 2002 **Bredmose, H.**
Deterministic Modelling of Water Waves in the Frequency Domain.
- 2003 **Urban, J.**
Crushing and Fracture of Lightweight Structures.

-
- 2003 Lazarov, B.S.**
Slepian Simulations of Plastic Displacement of Randomly Excited Hysteretic Structures.
- 2003 Ravn, E.S.**
Probabilistic Damage Stability of Ro-Ro Ships.
- 2003 Törnqvist, R.**
Design of Crashworthy Ship Structures.
- 2003 Nielsen, K.B.**
Numerical Prediction of Green Water Loads on Ships.
- 2004 Folsø, R.**
Comfort Monitoring of High Speed Passenger Ferries.
- 2004 Fuhrman, D.R.**
Numerical Solutions of Boussinesq Equations for Fully Nonlinear and Extremely Dispersive Water Waves.

Maritime Engineering
Department of
Mechanical Engineering
Technical University
of Denmark

Niels Koppels Allé, Building 403
DK-2800 Kgs. Lyngby
Denmark
Phone + 45 4525 1360
Fax + 45 4588 4325
info.mt@mek.dtu.dk
www.mek.dtu.dk

ISBN 87-89502-41-8

